Etude computationnelle de la formation d'un film ultra-mince de Nafion à l'intérieur d'une couche catalytique de PEMFC

Daiane Damasceno Borges Damasceno Borges

UNIVERSITÉ DE GRENOBLE

THÈSE

Pour obtenir le grade de

DOCTEUR DE L'UNIVERSITÉ DE GRENOBLE

Spécialité : **Matériaux, Mécanique, Génie Civil, Electrochimie**

Arrêté ministériel : 7 août 2006

Présentée par

Daiane DAMASCENO BORGES

Thèse dirigée par **Gerard Gebel**
et codirigée par **Alejandro A. Franco et Stefano Mossa**

préparée au sein **Laboratoire des Composants pour Piles à combustibles et Electrolyseurs et de Modélisation (CEA LITEN)**
et de **Ecole Doctorale I-MEP**^{2}

Computational Studies of the formation of Nafion ultra-thin films inside PEMFC Catalyst Layer

Thèse soutenue publiquement le **12 Avril 2013**,
devant le jury composé de :

Gerald Pourcelly
Professeur, Université de Montpelier 2, Montpelier-FR, Président

Kunal Karan
Professeur, Queen's University, Kingston-CA, Rapporteur

Mathieu Salanne
Maître de Conférences, Université Pierre et Marie Curie, Paris-FR, Rapporteur

David Brown
Professeur, Université de Savoie, Chambery-FR, Examinateur

Gerard Gebel
Chercheur, CEA/INAC/SPrAM, Grenoble-FR, Directeur de thèse

Alejandro A. Franco
Chercheur, LRCS/CNRS Univeristé de Picardie Jules Verne, Amiens-FR, Co-Directeur de thèse

Fall in love with some activity, and do it! Nobody ever figures out what life is all about, and it does not matter. Explore the world. Nearly everything is really interesting if you go into it deeply enough. Work as hard and as much as you want to on the things you like to do the best. Don't think about what you want to be, but what you want to do. Keep up some kind of a minimum with other things so that society does not stop you from doing anything at all.

Richard P. Feynman

Acknowledgement

I would like to express my sincere thanks to my supervisors. I thank to my thesis director, Dr. Gerard Gebel for all support he provided me when necessary. Equally thank to my co-director, Dr. Alejandro A. Franco for his high motivation, enthusiasm and encouragement. I thank him the trust and freedom he gave me to pursue independent work. My sincere gratitude to Dr. Stefano Mossa for his help and scientific support indispensable for the accomplishment of this work. I thank him to his scientific advice and knowledge and many insightful discussions. I am very grateful for his thoughtful and detailed comments in reviewing this thesis. I also would like to thank Dr. Kourosh Malek for his collaboration on this work with his great ideas.

My sincere thanks also goes to the laboratory director, Dr. Olivier Lemaire for his kindness and comprehension. I thank very much to Dr. Valentina Vetere for her help, wise advices and friendship. *Grazie mille Valentina!* Thanks also to the members of INAC/SPrAM for hosting me in their laboratory. I thank to the secretaries Geraldine, Aline, Charlene and Celine. I thank to all members of my Ph.D jury for accepting reading this manuscript, especially to Dr. Mathieu Salanne and to Prof. David Brown for very constructive comments and corrections.

I would like to thank to those people who made my road much less hard. I thank to MEMEheroes: to Rodrigo, for his long-time friendship; to Romain, for his humour and for introducing me the "black side" of french culture; to Yoshinori, for the great time together in the marathon and also for the high level scientific discussions; Chea and Mohamed, for the adventures time in the ski, Pablo and Daniela (mi hermanos latinos) for amazing time we pass together. Thank to many others from the lab who helped to make a funny and friendly ambience of work. My heartfelt gratitude to my best friends: Luiz, Paula and Chico for their endless encouragement and support throughout the whole period. *Muito obrigada meus amigos!* Finally, I have no words to express my grateful to my dear Benjamin for his day-to-day support in all moments.

I thank to his strongly encouragement and unconditional helps. I also thank him for correcting the French texts of this manuscript. I immensely thank to his patience, companionship and love. *Merci beaucoup mon cherie!*

Last but not the least, I would like to thank my family: my parents Maria José and Aladim and brothers, Pablo, Glênio and Saulo who always trusted and supported in all my projects. I thank in especial to my parents for their unconditional love. *Dedico esta tese à vocês. Muito obrigada!*

Abstract

In recent years, Polymer Electrolyte Membrane Fuel Cells (PEMFC) have attracted much attention due to their potential as a clean power source for many applications. Among the fuel cell developers, the formation of Nafion ultra-thin films inside the PEMFC catalyst layer has been a "hot" topic for two reasons: first, it has significant impact on the electrochemical activities and transport phenomena inside catalyst layer; second, the structure and properties of these films significantly differ from those in the ionomer membrane. The hydrophobic/hydrophilic character of the substrate appears to be a key parameter dictating the interaction between the hydrated ionomer and the substrate. The purpose of this thesis is to investigate in an unique framework a variety of environments peculiar of the catalyst layer, taking into account the substrate hydrophilicity and the film hydration level. We propose a simple approach base on classical Molecular Dynamics simulations that allows us to precisely control the hydrophilic character of the substrate by using an unique tunable control parameter. We perform a complete investigation of the substrate effects on the morphology and transport properties of the ionomer film at different hydration levels. Finally, we discuss about the implications of our results for the PEM fuel cell technology.

Keywords. Nafion ultra-thin film; PEM fuel cell; catalyst layer; hydrophilicity

Résumé

Au cours des dernières années, les piles à combustible à membrane échangeuse de protons (PEMFC) ont attiré beaucoup d'attention en raison de leur potentiel en tant que source d'énergie propre dans de nombreuses applications. Parmi les principaux développements sur ce sujet, la formation de films ultra-minces de Nafion à l'intérieur de la couche catalytique est un sujet "chaud" pour deux raisons: il a un impact significatif sur l'activité électrochimique et sur les phénomènes de transport à l'intérieur de la couche catalytique; et la structure et les propriétés de ces films peuvent différer significativement de ceux de la membrane ionomère. La morphologie de l'ionomère de Nafion à l'intérieur de la CL se trouve être fortement sensible à la nature du matériau utilisé, et en particulier son caractère hydrophobe/hydrophile. L'objectif de ma thèse de doctorat est d'effectuer une étude en profondeur des effets du substrat sur la morphologie et les propriétés de transport du film ultra-mince de l'ionomère pour différents niveaux d'hydratation lorsque l'on considère seulement les propriétés de mouillabilité du système. Nous avons développé un modèle simple, d'approche champ moyen, qui permet de changer continuellement l'hydrophilicité du substrat en contact avec le film. La méthode choisie pour ce travail est basée sur des simulations de Dynamique Moléculaire classique. Enfin, nous ferons une projection de l'impact que pourrai avoir notre travail sur l'évolution des technologies de piles à combustible PEM.

Keywords. film ultra-mince de Nafion; piles à combustible PEM; couche catalytique; hydrophilicité

Contents

List of Figures

List of Tables

Chapter 1

Introduction

The increasing global demand for energy together with the growing environmental concerns encourage scientists and industrialists to invest in innovative technology for new energies production. Over the last decades, great efforts have been deployed on the common quest for an alternative to the depleting natural source of fossil fuel. For the design of a new technology, the quantity of energy that can be produced, the cost, and the impact on the environment (especially the quantity of emission of CO_2) are of major concerns. Legitimately, such a technology is expected to be competitive over the whole range of applications of the energy conversion device market: transportation (in other terms the automotive market), stationary power generation (for residence, public buildings), and portable applications (like cell phones, portable computers, auxiliary power unit in cars, *etc.*).

Fuel Cells are considered one of the most promising electrical energy conversion devices. The basic operating principle of fuel cells was first reported by Schoenbein and Grove in 1839, when they managed to generate electricity from hydrogen and oxygen by reversing water electrolysis [Schoenbein 1839, Grove 1839]. During nearly one hundred years, there were almost no progresses on the development of this technology. Only in 1950's, W. Thomas Grubb further modified the original fuel cell design by using a polymeric ion-exchange membrane as the electrolyte [Grubb 1959]. In the following, Leonard Niedrach was the first to devise a way of depositing platinum onto the membrane, which served as the catalyst for the necessary cell reactions[Niedrach 1967]. At that time, the first application of fuel cell as an auxiliary power source in the NASA's Gemini space flights was accomplished.

During the development of fuel cell technologies, the *Proton Exchange Membrane Fuel Cells* (PEMFC), also called *Polymer Electrolyte Membrane Fuel Cells* have been highlighted. This type of fuel cell has high power density and numerous advantages (*e.g.* relative low operating temperature, low weight, *etc.*) compared to the others.

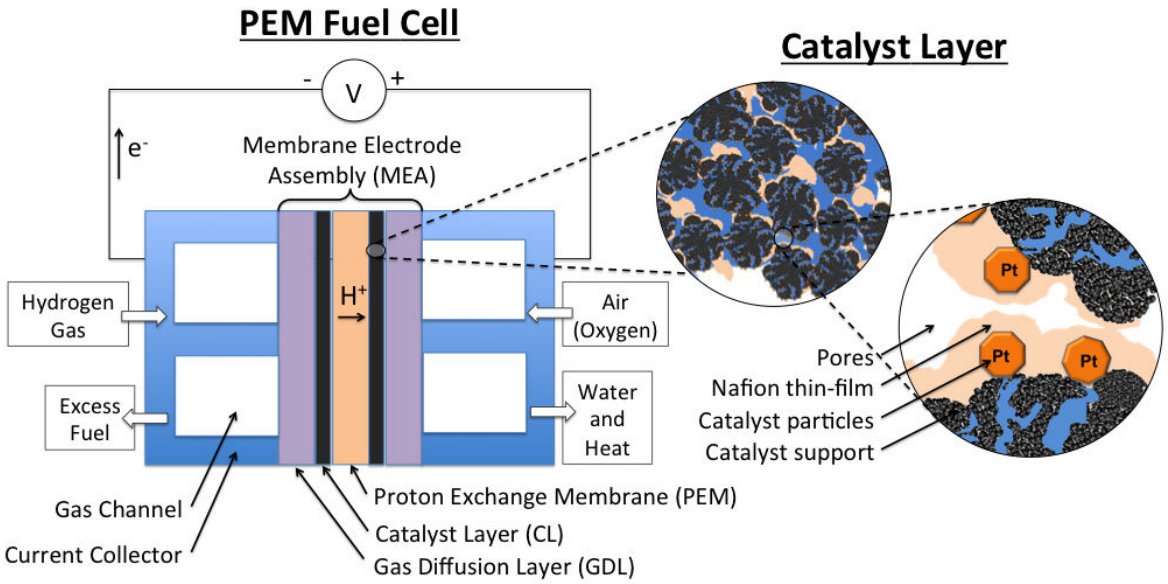

Figure 1.1: Schematic view of Proton Exchange Membrane Fuel Cell (PEMFC). The Catalyst Layer (CL) structure consists of: carbon particles or agglomerates decorated with catalyst particles (Pt/C); Nafion ionomer dispersed on Pt/C; and porous phase.

Typically, their components are the Membrane Electrode Assembly (MEA), which consists of two electrodes (anode and cathode) separated by the electrolyte membrane, and the Gas Channels placed on each side of the MEA (see figure 1.1). The electrode components are: the Catalyst Layer (CL), where the electrochemical reactions take place, and the Gas Diffusion Layer (GDL), through where the reactants diffuse from the channels to the active sites in CL.

The PEMFC working principle consists in continuously converting chemical energy from a hydrogen oxidation reaction into electric energy, for as long as fuel and oxidant are supplied. The process is illustrated in figure 1.1 and it consists in the following: the hydrogen fuel is supplied to the anode (negative terminal) while oxygen is supplied to the cathode (positive terminal); through oxidation reaction, hydrogen is separated into an electron (electricity production) and a proton; protons cross the electrolyte membrane and reach the cathode, where they react with the electrons and oxygen by means of reduction mechanisms to form water byproduct.

An important mark on the PEMFC history was in 1960's when *Nafion*, a proton conducting polymer invented by DuPont company was introduced as the membrane

electrolyte [Connolly 1966]. This polymer demonstrates excellent proton conductivity when hydrated. At that time, fuel cells with high power and energy densities were achieved under the condition of being extremely expensive to manufacture, due the high platinum utilization. This drawback was the main reason limiting the wide utilization of this technology. More significant progress became possible only after the 1980, when new designs contributed to significant reconfiguration of the cell components.

Nowadays, further development of PEMFCs is targeted by directly understanding the material properties at the molecular level for each component. In particular, Nafion membranes have received much attention due to the high complexity structure at nanoscale level. This polymer is the result of the copolymerisation of a tetrafluoroethylene backbone (Teflon) and perfluorovinyl ether groups terminated with sulfonate group side-chains. The main feature of Nafion structure is the heterogeneity at the nanoscale. When the polymer is hydrated, the *hydrophobic* backbone and *hydrophilic* side chains lead to spontaneous phase separation. Several models, such as inverted-micelles, cluster-networks, polymer bundles, have been proposed to describe the phase-separation morphology of the hydrated Nafion membrane [Mauritz 2004]. However, these models are very often inefficient and contradictory, and, therefore, the Nafion structure remains unclear. Likewise, there is still a debate about the relation of Nafion nano-structure with its transport properties, such as proton conduction and water management inside the membrane [Kreuer 2004].

The Catalyst Layer (CL) also presents a very heterogeneous and complex structure. The current CL fabrication approaches are highly empirical and use poorly controlled processing methods. The result is a random heterogeneous structure formed with platinum nanoparticles dispersed on a carbon matrix with impregnated Nafion ionomer (see figure 1.1). Nafion has been introduced as one of its constituents for two reasons: first, during the fabrication process Nafion acts as a binder, having an important role on the dispersion of Pt/C aggregates and, consequently on the Pt utilization. Second, during fuel cell operation, it forms an important proton-conductor network for the proton migration from/to the membrane to/from the catalyst sites. Nafion presents an inhomogeneous and non-continuous phase inside the CL. It can be found as a well-dispersed *ultra-thin film* on the surface of carbon supports and Pt particles (see figure 1.1). Typically, this film is not uniformly distributed and has thickness spanning the range $\sim$4 to 20 nm [More 2006].

Recently, the formation of Nafion ultra-thin films inside the catalyst layer has been a "hot" topic among the fuel cell developers. The structure and properties of these films might significantly differ from those in the ionomer membrane [Paul 2011a]. Focusing on the heterogeneity of the CL, the ionomer thin-film is expected to self-organize in different forms, depending on the properties of the substrate it is interacting. These interactions would depend on the chemical composition (*e.g.* , Pt and C materials oxidation state) and the geometry (curvature) of the substrate [Modestino 2012]. In particular, there is experimental evidence that the change of wetting properties of the substrate is sufficient to affect Nafion film morphology [Wood 2009]. Understanding the effects of such interactions on ionomer morphology is a crucial step to control the functional properties, such as proton conductivity and water transport inside CL.

The effective adsorption of the ionomer on the catalyst surface has also an important impact on CL activities. Until recently, the most accepted view considers Nafion as a non-adsorbing electrolyte in PEMFC catalyst layer. This general picture has changed when it was demonstrated that specific adsorption of sulfonate groups on the catalyst can occur and strongly affects the reactivity and stability of the oxygen-reduction mechanisms [Subbaraman 2010a, Ma 2007, Ohma 2011]. Moreover, the nature of the ionomer adsorption can be potentially dependent on the ionomer organization, including formation of ionic clusters, in the very near-surface region. Finally the adsorption should indirectly depend on the substrate properties, as for instance the hydrophilic/hydrophobic character.

Inside the CL, the use of different materials leads to the CL having an inhomogeneous hydrophilic/hydrophobic character. The platinum surface is more hydrophilic, while the carbon supports tend to be more hydrophobic. Also, the wettability properties of these surfaces can be affected during fuel cell operation. The variation of the cathode/anode potential can impact materials properties, especially the degree of surface coverage of both platinum and carbon, and the hydrophobicity of the surfaces [Borup 2007]. In the same way, the degradation mechanisms for these materials include ripening and compositional changes of catalyst due to corrosion, catalysts poisoning by adsorbed impurities, ageing of the proton exchange electrolyte membrane, changes in the hydrophobic/hydrophilic properties of catalyst layer surfaces [Chen 2006, Wang 2009]

Within this context, a simple question arises: what happens to Nafion thin-film

when it is deposited on surfaces with different hydrophilic/hydrophobic characters? A particularly interesting discussion is whether there is any preferred association of hydrophobic or hydrophilic Nafion domains with the surface. Which type of structures the ionomer can form depending on the wettability properties of the surface? If indeed the ionomer morphology is sensible to this parameter, the following step would be to investigate how this feature affects important functional properties, like proton conduction, water transport, ionomer adsorption. These questions can be addressed by performing computer simulations. The most prominent of computational methods for simulating this type of systems are Monte Carlo (MC) and Molecular Dynamics (MD). The main advantage of MD over MC is the availability of the time-dependency.

The purpose of our work is to perform a complete investigation of the substrate effects on the ionomer ultra-thin film morphology at different hydration levels, considering as the control parameter the wettability properties of the substrate only. The numerical method chosen for this work is classical Molecular Dynamics simulations. The investigation of such systems via computer simulations remains particularly challenging. Indeed, the system should be large enough to mimic the length scale of the film, which demands costly computational sources. Furthermore, the characterization of the substrate hydrophilicity and an adequate determination of the interaction parameters between the substrate and the ionomer is a crucial point of this work. Our idea was to develop a simple model within a mean field approach that allows us to continuously change the hydrophilicity of the substrate in contact with the film at reasonable computational time.

Finally, we note here that despite the fact that the formation of thin-film inside PEMFC catalyst layer is the main motivation for this work, we have aimed at understanding the Nafion thin-film formation in contact with any type of substrate. Therefore, due to the generality of this work, we believe that contribution goes beyond the PEM fuel cell applications. This study could help in understanding Nafion thin-films formed on several substrates, such as Au, Pt(hkl), Ru(hkl), SiO_2-terminated surface, which are materials widely used in ionomer-modified electrodes for various electrochemical applications.

The Thesis

The aim of my Ph.D. thesis is to perform computer simulation studies of the hydrated Nafion polyelectrolyte ultra-thin film formation when in contact with hydrophobic/hydrophilic surfaces. The physical properties of such system, including self-organization and dynamics of polymer and water complexes were investigated by using Molecular Dynamics simulations. Finally, the manuscript, including state-of-the-art, methods used, results as well as conclusions, is organized as follows:

- **Chapter 2: Scientific background: experiments and theory**

  The goal of this chapter is to present a selection of experimental and theoretical works that we have considered necessary for making the reader aware of the context in which our work is included. We introduce general concepts about Nafion and PEMFC catalyst layer, and present the state-of-the-art of the activities focusing on Nafion at interfaces, both frame an experimental and a theoretical point of view.

- **Chapter 3: Computational methods**

  In this chapter, we describe the computational methods used in this work. We discuss the main ideas behind Molecular Dynamics simulations, including algorithms and concepts from elemental statistical physics.

- **Chapter 4: The Model**

  This chapter is dedicated to the description of the model adopted to mimic Nafion and water, including parameters and simulation details. We report our results from simulations of Nafion-water system in the bulk phase, which was requested in order to validate the model. In addition, we introduce in details the model we have developed to mimic the interaction of ionomer and water with different substrates characterized by different hydrophilicity degrees. We also give technical details employed during the simulations of ionomer thin-film.

- **Chapter 5: Analysis of the structure of Nafion ultra-thin films**

  In this chapter, we explore self-assembly and nanostructures formation of a realistic model for the Nafion ionomer (introduced in chapter 4) when deposited

on surfaces with hydrophobic and hydrophilic surfaces. We show how thin-film structure depends on substrate hydrophilicity and ionomer film hydration.

- **Chapter 6: Water and hydronium dynamics in Nafion ultra-thin films**

  In this chapter, we complete our study focusing on the explanation of the effect of film morphology on the dynamics of water and proton complexes inside the hydrated ionomer film.

Chapter 2

Scientific background: experiments and theory

Contents

2.1 Introduction

The main motivation for investigating Nafion ultra-thin films systems is to contribute to the development of PEM fuel cell catalyst layer (CL). A good understanding of the CL system, including the physical-chemical mechanisms and how they are affected by the material environment is fundamental to achieve improvements on CL performance. In this context, a huge number of publications have been devoted to explore important issues in the range from nano to macro scales, using experimental and theoretical approaches and being performed by both engineers and fundamental researchers. Among these issues, the study of nano-structures of Nafion within CL has received less attention, although there is a general agreement that Nafion directly and indirectly impacts the CL activities.

In addition, there is an even more fundamental question: should Nafion in CL have properties significantly different from the ones in the membrane? Nafion membrane, also referred to as Nafion in the bulk phase, is still a matter of controversy concerning its morphology and physical properties. This can be justified due the technical limitations found in experiments and the high complexity of this material to be accurately accessed by computer simulations. As a result, one can find in the literature of the last decades, an extremely extended number of publications addressed to understand structure and properties of Nafion.

Due to this complex and rich context, we introduce general aspects about Nafion polymer and CL together with their state-of-the-art, before proposing a literature review on Nafion thin-films. Therefore, in the first part of this chapter we present Nafion, focusing on morphology and main properties. In the second part, we introduce the concept of CL in PEMFC, its components and functions, as well as the progresses achieved with new material designs through different fabrication methods. In the third part we dedicate to Nafion thin-films. We make a review of relevant experimental and theoretical studies that have addressed fundamental questions concerning properties of Nafion at interfaces at the molecular level. Finally, the challenges encountered in studying these types of systems and the motivations to perform a detailed study of thin-film formation on hydrophobic and hydrophilic substrates are discussed in the last part.

2.2 Nafion polymer: a complex nano-phase separated structure

2.2.1 General aspects

Nafion is a perfluorinated polymer discovered and developed by the DuPont de Nemours company. It is a result of the co-polymerization of non-polar tetrafluoroethylene, constituting the backbone, and polar perfluorosulfonic vinylether chain fragments attached to the backbone, as side chains. It is the first of a class of synthetic polymers with ionic properties, which are called *ionomers*. The chemical structure of Nafion is the following:

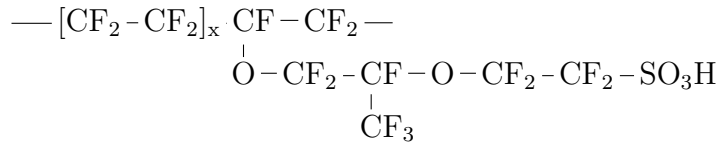

where x is the average value resulting from the unknown co-monomer sequence distribution. Usually, x varies from 6 to 8, which results in a distance between adjacent side chains of around 20 Å . The typical length of each side chain is about 10 Å while the backbone length can vary from 0.1 μm to 1 μm. During the co-polymerization the parameter x can be modified, which changes the number of sulfonate groups per mass unit. This is quantified by introducing the concept of *equivalent weight* (EW), defined as the weight of dry Nafion per mol of sulfonate acid groups. EW has a direct relation with the parameter x via the following equation:

$$EW = 100x + 446 \tag{2.1}$$

An EW of 1100 is typical of the standard commercialized *Nafion® 117*, where the designation '117' refers to a film having EW=1100 and a thickness of 0.007 in, *i.e.* 0.18 mm.

Nafion has many features that make it the best ionic polymer used in electrolyte membranes for electrochemical devices. The most important are the high intrinsic proton conductivity when the polymer is hydrated and water permeability with only

moderate water uptake. The hydration is usually quantified in terms of the *water content* - λ, defined as the number of water molecules per sulfonic acid groups. Water content varies from 0 to 22 as a function of relative humidity. When Nafion is fully hydrated the sulfonic acid groups dissociate to free protons H^+ for conduction. Nafion also exhibits excellent mechanical properties including flexibility, ductility and water-swelling capacity, as well as, good thermal stability. At last, it is relatively resistant to degradation, unless it is under aggressive conditions such as in presence of alkali metals and peroxide groups [Coulon 2012].

The main feature of Nafion structure is the heterogeneity at the nanoscale. When the polymer is hydrated, the *hydrophobic backbone* and *hydrophilic side chains* lead to spontaneous phase separation at the nano-structural level [Mauritz 2004]. The hydrophobic regions form semi-crystalline domains, while the hydrophilic regions, sulfonate groups with water uptake, form a continuous ionic network. The complexity of this interlaced domains, *i.e.* Nafion morphology, is a matter of continuing theoretical and experimental studies. In the following, we will report in more details about the models proposed to explain Nafion structure and its related properties (*e.g.* proton conductivity, water management).

2.2.2 Models for Nafion morphology based on scattering experiments

Experimentally, morphological characterization of Nafion is in large part based on small-angle X-ray scattering (SAXS) and wide-angle X-ray diffraction experiments. In the late 1970's, emerged from such experiments the evidence of the presence of ionic clusters within Nafion. The hydrated Nafion self-organization produces a clear peak in the scattering spectra, the so called *ionomer peak*, which has been attributed to the presences of these clusters. However, Nafion yields very little characteristic detail in the dimensions probed by these methods. Therefore, the information gathered is inherently indirect and limited by the need of employing morphological models that involve specific assumptions on the structure.

Several morphological models have been proposed for the interpretation of these scattering patterns. All of them are able to explain the presence of ionomer peak and describe how ionic groups form a network of clusters that allows for significant swelling

by solvents and efficient ionic transport within the polymer matrix. However, the models differ significantly in the geometry and spatial distribution of the ionic clusters. Here, we restrict our review to the most cited models and make a brief exposition only about the morphological proposed without going in details of experiments. This brief review is in parts based on the work by K. A. Mauritz and R. B. Moore [Mauritz 2004].

The most widely referenced model is the one proposed in 1981 by Gierke and co-workers [Gierke 1981, Hsu 1983]. In this model, the authors suggest that the morphology of Nafion is best described by ionic clusters that are approximately spherical in shape with diameter of $\sim 3-5$ nm and with an inverted micellar structure (see figure 2.1). The spherical ionic clusters are interconnected by cylindrical channels of ~ 1 nm in diameter. This model could explain the high permeability and the requirement of a percolation pathway for ionic transport in Nafion membranes. With increasing water content, the changes on the morphology are attributed to the increase in cluster size and redistribution of the sulfonate sites to yield fewer clusters in the fully hydrated material.

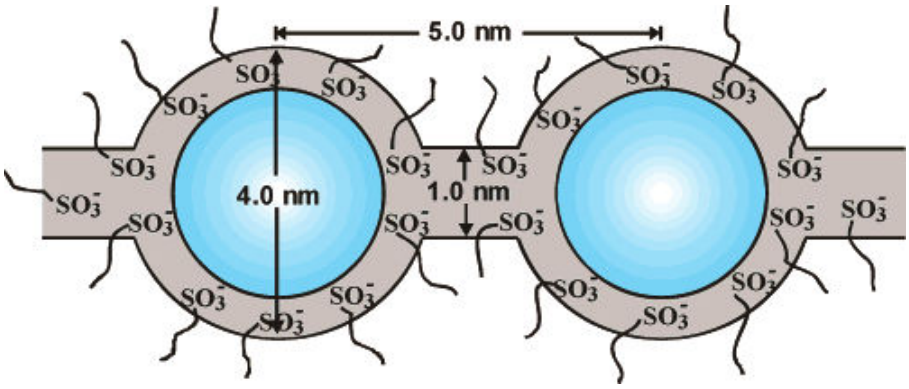

Figure 2.1: The cluster-network model, proposed by Gierke *et al.* [Gierke 1981, Hsu 1983] consist of spherical inverted micelles interconnected by cylindrical channels. Figure from reference [Mauritz 2004].

Another pioneering model is the one proposed by Yeager and Steck [Yeager 1981]. The authors suggest a three-phase model that identify the polymer matrix within three regions: *i)* a fluorocarbon backbone, some of which is microcrystalline; *ii)* an interfacial region of relatively large fractional void volume containing a few pendant side chains, some water; and *iii)* sulfate or carboxylic groups and counter ions which are not in clusters, and the clustered regions where the majority of the ionic exchange

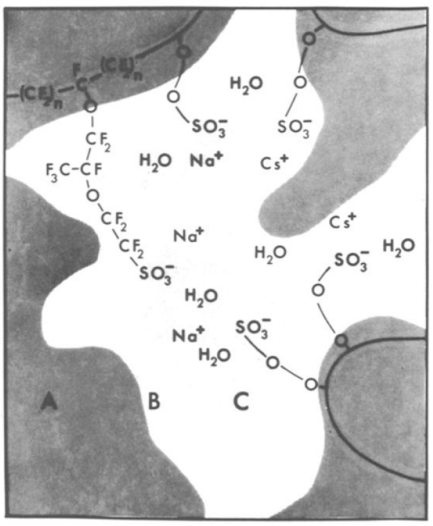

Figure 2.2: Three phase model proposed by Yeager *et al.* [Yeager 1981]: (A) a fluorocarbon backbone, (B) an interfacial region containing some pendant side chains, some water, and (C) the clustered regions where the majority of the ionic exchange sites, counter ions, and sorbed water exists. Figure from reference [Yeager 1981].

sites, counter ions, and sorbed water exists (see figure 2.2). This model significantly differs from the one of Gierke *et al.* [Gierke 1981], given to the fact that the clusters do not have a strict geometrical definition and their geometrical distribution has a lower degree of order. Although this model is not the most widely accepted, it has given an important contribution introducing the idea of the existence of transitional interfaces between hydrophilic and hydrophobic regions.

Through the analysis of the structural behaviour during Nafion swelling and de-swelling processes, Litt *et al.* [Litt 1997] propose a lamellar structural model, that consists of ion domains defined as hydrophilic "micelle" layers separated by thin lamellar PTFE-like crystallites. During the hydration process, as water absorbs between the lamellae, the increase in spacing between ionic domains is expected to be proportional to the volume fraction of water in the polymer. In this model the swelling behaviour is completely reversible, without morphological reorganization. Later, this model appeared to be an oversimplification of the global description of Nafion. Other works have shown that the interlamellar spacings shift with water content in a manner significantly different from that of parallel shift [Gebel 2000b, Young 2002].

An alternative to the lamellar model was later proposed by Haubold *et al.*

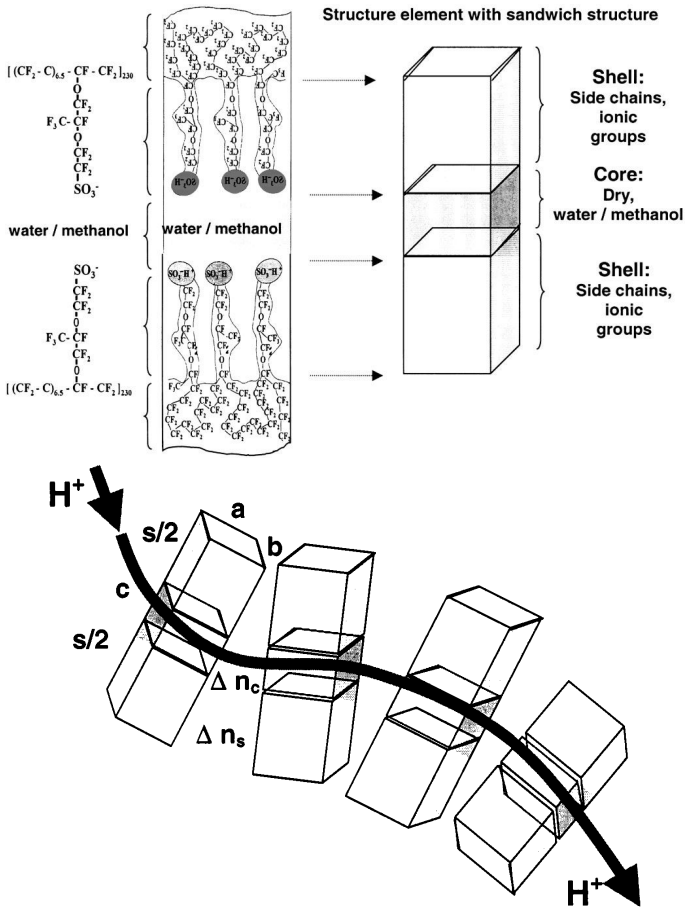

Figure 2.3: Sandwich-like model for Nafion morphology proposed by Haubold *et al.* [Haubold 2001]. The model consist on sandwich-like structural basic elements (shown at the top of the figure) that compose the complex channel structures. Figures from reference [Haubold 2001]

[Haubold 2001]. They suggest that Nafion is composed by basic rectangular parallelepiped elements with lateral dimensions around 1.5-4.5 nm and height around 6.0 nm. Each element consists of a sandwich structure constituted by a sequence of layers: polymer, ionic groups, solvent (core region), ionic groups and polymer. In order to provide channels for the proton transport along the membrane, the "sandwiches" are linearly piled forming a continuous water phase, as shown in figure 2.3. This simple structure model is able to describe the swelling behavior of Nafion on a nanometer scale. During swelling there is a shrinking of the core region and a swelling of the shell region, which contains the side-chains of the Nafion molecule.

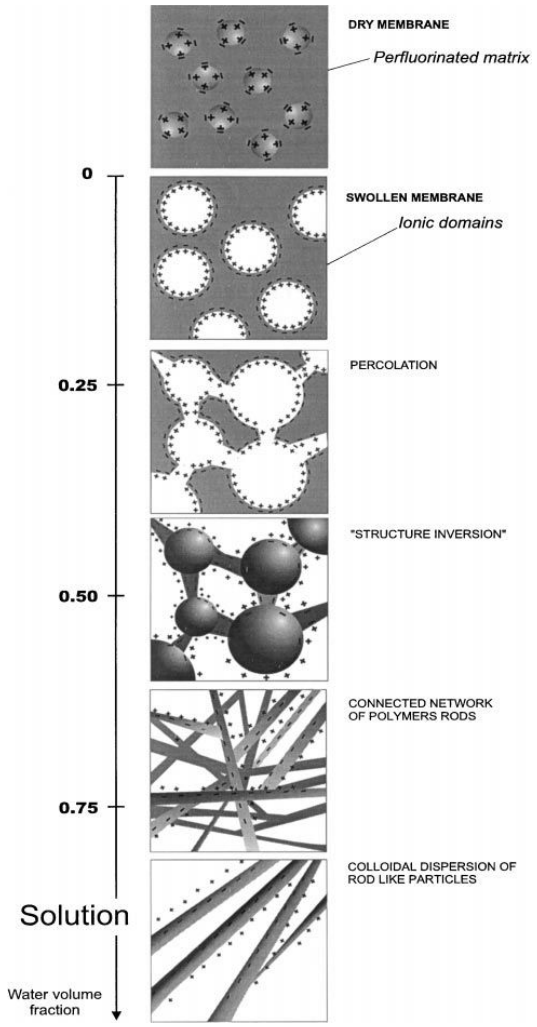

Figure 2.4: Model proposed by Gebel for the morphological reorganization when the dry Nafion membrane is swollen with water to the state of complete dissolution. Figure from reference [Gebel 2000a]

Gebel [Gebel 2000a] also has dedicated to study the morphological changes depending on polymer hydration. He proposes a general scheme for the evolution of the Nafion structure from the dry state through the water-swollen state (see figure 2.4). According to this author, spherical aggregates (inverted micelles) of diameters of 1.5 nm and with a center-to-center separation distance of 2.7 nm are formed at low hydration. When hydration increases, a continuous "cluster network" is first formed through the connecting cylinders of water between the swollen spherical clusters. At high hydration the continuous perfluorinated matix breaks up to a network of rod-like micelles. Finally, as the membrane dissolves into solution, the rodlike structures separate to yield a colloidal dispersion of isolated rods.

These ideas where further developed in collecting scattering data from Nafion samples at various water contents [Rubatat 2002, Rubatat 2004]. The observations included in those papers support the hypothesis that the swelling process involves a dilution of basic entities, and not a strong structural reorganization as previously proposed by Gebel. This dissociation was partial and continuous over the whole swelling process. Such entities have an intrinsic fibrillar structure which corresponds to elongated polymeric aggregates surrounded with the ionic charges (see figure 2.5). In the Nafion membrane, the fibrils are entangled and collapsed with a certain degree of orientational order at the mesoscopic scale. Moreover, water is not confined

Figure 2.5: Schematic representation of an entangled network of elongated rodlike aggregates in Nafion. Long-range heterogeneities arising from bundles of locally ordered aggregates. Figure from reference [Rubatat 2004]

in spherical cavities but between fibrillar objects. They assume the morphology of Nafion as a mixture between amorphous phases and ordered phases.

More recently, a new model was proposed by Schmidt-Rohr and Chen [Schmidt-Rohr 2008]. They compared the scattering profiles predicted by several popular morphological models of Nafion by using a novel continuum-level modelling algorithm. Their results suggest a new picture named the parallel water-channel model. The structure is made up of aligned water channels (cylinders) of ∼2.4 nm diameter with hydrophilic side groups pointing inward and the polymer backbone on the outside. The channels are locally parallel and can be considered as cylindrical inverted micelles (see figure 2.6). The cylinders are apparently stabilized by the stiffness of the helical backbone segments and partial crystallinity of the matrix polymer.

Recently, Elliott *et al.* [Elliott 2011] proposed a unified morphological description of Nafion membranes on the basis of SAXS experiments and mesoscale simulations (Dissipative Particle Dynamics (DPD)). They show that the most plausible morphology consists of independent bicontinuous networks of ionic clusters and backbone chains. Their results show that Nafion does not seem to conform to any of the models discussed above. However, this new model does retain the network of ionic aggregates found in cluster-network and fibrilar models, but rejects the existence of extended parallel channels. The authors draw attention to the problem of using structural models devised to interpret SAXS data. They argue that a good agreement of

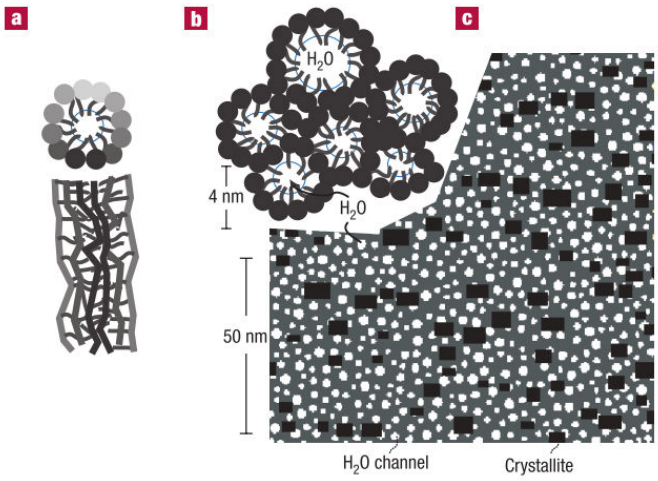

Figure 2.6: Parallel cylindrical water nanochannels. (a) Top and side view of a inverted micelle cylinder; (b) Several cylinders packing; (c) Cylindrical water channels (black) and Nafion crystallites (white). Figure from reference [Schmidt-Rohr 2008].

such models with scattering curve is a necessary but not sufficient condition of validity and additional information about statistical probability and thermodynamic stability of the model must be used to establish the validity of a model.

In summary, the debate about which one of the models mentioned above is most suitable and effective in representing ionomer's morphology is still open. The main controversy concerns the structural description of the ionic domains, such as size, shape and spatial distribution. Consensus has been reached on the idea that ionic domains in hydrated Nafion present anisotropy in shape and heterogeneity in their spatial distribution. It is also well accepted that such structures depend on the pretreatment methods used in the polymer sample preparation. Although we did not discuss in detail experimental procedures, it is important to mention here that the preparation, such as swelling and/or boiling in solvents, annealing, addition of water, drying in vacuum/air, and the order of theses steps, affects the ionomer morphology. In the following, we discuss how computational and theoretical studies based on fundamental thermodynamic principles can contribute to elucidate Nafion properties.

2.2.3 Computational studies of hydrated Nafion

As a complement to experimental work, computer simulations studies of Nafion polymer are helpful to clarify how chemical structure of hydrated ionomers, at the molecular level, control the polymer self-organization and, ultimately, the relation with the membrane properties. Computational modelling approaches that aim at solving this issue are in large part based on Molecular Dynamics simulations. Through this method, a Nafion system can be virtually reproduced and investigated under several external thermodynamic conditions (*e.g.* temperature, pressure) and polymer features, such as chemical architecture of monomers, length and separation of side-chains, equivalent weight (EW), ionomer concentration (or water content), *etc.* . The majority of heterogeneous structures reproduced by this method do exhibit nanophase segregation between polymer and aqueous phases in qualitative agreement with experimental results. Since a huge number of MD simulation studies of Nafion can be found in the literature, in the following, we select the works that we found the most interesting in the context of the present work.

Vishnyakov and Neimark [Vishnyakov 2001a, Vishnyakov 2001b] were pioneers in performing MD simulations to generate self-organized Nafion membranes. The authors applied united-atom representation of backbone monomers and include K^+ as counterions. They studied water clustering within Nafion matrix for three different water contents (5.0, 12.5 and 17 wt%, that correspond to a maximum value for $\lambda \sim 8.7$). They found that on increasing water content, water clusters do not form a stable continuous subphase, but they are connected through short lived bridges. This structural picture is in contrast with other authors who found evidences of the existence of a continuous aqueous phase for λ lower than 8 [Devanathan 2010]. This peculiar result could be due to the short oligomeric units used in their simulations [Eikerling 2009].

Several other authors also investigated the Nafion morphology by similar atomistic simulations [Allahyarov 2009, Devanathan 2007a]. All of them reported a strong dependence of water clustering and percolation on the water content. At low water content, only isolated small water clusters were formed. As the water content increased, it became possible that a predominant majority of water molecules formed a single cluster [Cui 2007]. Venkatnathan *et al.* [Venkatnathan 2007] have reported that water network percolation occurs between $\lambda = 5$ and 6. Close to the percolation

threshold, clusters are intermittently connected by mobile water molecules, so that transient spanning clusters form and disappear. At high hydration, spanning cluster permeates the membrane and creates water channels.

The local order formed within Nafion structure was also investigated. Through computing the pair correlation function, Urata *et al.* [Urata 2005] showed that sulfonic acid groups aggregate within short distances from 4.6-7.7 Å , despite electrostatic repulsions. Moreover, side chains are oriented perpendicular to the hydrophilic-hydrophobic interface, with a continuous aqueous phase bridging the sulfonic acid groups. The quantity of water molecules near H_3O^+ and SO_3^- , *i.e.* the degree of solvation, shows strong dependence on water content. The degree of solvation has been referred to explain the effects of Nafion nanostructure on the dynamics of water molecules and hydronium ions. Moreover, the poor conductivity observed in the membrane at low hydration levels is, in part, attributed to the poor hydration of H_3O^+ ion, which hampers proton transfer in the aqueous phase [Cui 2007].

Another parameter largely explored is the effect of ionomer architecture on Nafion morphology. Jang *et al.* [Jang 2004] studied properties of two samples of hydrated Nafion with the same equivalent weight, but using different monomeric sequences: a "dispersed" case with the side chains uniformly distributed along the backbone; and a "blocky" sequence with all the side chains located at the end of the backbone. Their main observation is that the blocky geometry presents larger degree of segregation, with the sulfonate groups in the dispersed case slightly more hydrated than in the blocky case. Also, the water has higher diffusion in the blocky case, which is explained by the fact that hydrophilic clusters are larger in this case.

Allahyarov and Taylor [Allahyarov 2011] also analysed different ionomer architectures, ranging from Nafion-like to ionomer structures with extremely long side chains and backbone segments (two and three times longer than Nafion). They compared two ionomers with different side-chain segment lengths, keeping the equivalent weight constant. They observed improvement on proton diffusion in the membrane with longer side chains, which are characterized by larger sulfonate clusters when compared with the one of short chain. When keeping the backbone length constant and changing the side-chain length and, therefore, the equivalent weight, Devanathan *et al.* [Devanathan 2012] found no appreciable changes on the structural or dynamics properties of the membrane. These observation is supported by experimental results

[Kreuer 2008].

The above atomistic simulations all support the similar idea of irregularly shaped ionic clusters of sulfonic groups and water connected by small channels. However, according to various morphological models interpreted by scattering experiments, the size of the individual ionic clusters and the average distance between them are larger than the usual simulation box size. Therefore, atomistic modelling would not be able to capture the distribution, size, shape and connectivity of such clusters, which motivates several authors to use mesoscale simulations instead of atomistic ones. One of them is the coarse-grain MD (CGMD) simulations performed by Dorenbos *et al.* [Dorenbos 2009]. The authors studied the impact of equivalent weight on pores morphology. They found that on increasing equivalent weight water clusters become larger and separated further apart, leading to a significant decrease in water diffusion.

Malek *et al.* [Malek 2008] also performed CGMD simulations and observed that Nafion structures exhibit sponge-like morphologies. Sizes of hydrophilic domains increase from 1 to 3 nm as a result of linear microscopic swelling. At low water content, hydrophilic domains are roughly spherical and poorly connected. At higher water content, they convert into elongated cylindrical shapes with high connectivity. Moreover, they predicted a percolation threshold at $\lambda \sim 4$. For water contents larger than 4, they observed the formation of continuous aqueous pathways for proton and water transport.

Another interesting work is the one performed by Knox and Voth [Knox 2010], who examined six of the most popular morphological models, *i.e.* cluster-channel, parallel cylinder, local order, lamellar, rod network, and a "random" model (some of them we have discussed in the previous section). To this end, they applied fully atomistic MD simulation at length scales quite large. Their simulations reveal fast intercluster bridge formation and network percolation in all systems. Furthermore, SO_3^- groups are located inside these bridges and play an important role in the percolation phenomenon. Moreover, the authors demonstrated that, all models, excepted the "random" one, exhibit scattering profiles in agreement with experiments, despite their very different geometries. Their work supports the idea of the inability of scattering data alone in elucidating the real structure of Nafion, and hence the need for more detailed measurements.

Several other models appeared in the literature focusing on different additional

parameters. These models also support the same idea of low order structure for hydrated Nafion and similar transport dependence on water content and temperatures. The models we discussed above only account for classical mechanisms. Although they can finally provide relevant insights on transport properties, other mechanisms that require quantum description exists, such as structural diffusion in the case of protons [Kreuer 2000]. In what follows, we discuss the state-of-the-art of water and proton transport properties inside hydrophilic domains at the molecular level, based on experimental, theoretical and computational studies.

2.2.4 Water and proton transport within Nafion hydrophilic domains

On the basis of extensive investigations of transport of water and proton within Nafion membrane, there is consensus on the idea that efficient transport is achieved only when Nafion is hydrated. The proton transport is strongly coupled with the distribution and transport of water, which is confined to hydrophilic domains. Once hydrophilic phases are swelled by water sorption and interconnected along the membrane, a volume for water transport is available [Kreuer 2000]. The boundaries of the two phases, which are characterized by a complex polymer/water interface, additionally impact water and proton transport. In this subsection, we review the works dedicated to understand the impact of water content on the polymer/water interface structure, and the consequence on water and proton transport. Therefore, the interesting question to be asked is how the transport mechanism of both water and proton is affected by water uptake and hydrophilic domains configuration such as geometrical shape, connectivity and water/polymer interface.

The water uptake alters molecular packing (SO_3^- agglomeration) and topology of the hydrophilic domains, and, consequently the water diffusion. According to Zhao *et al.* [Zhao 2011], initial water sorption disrupts SO_3^- packing that tends to be interdigitated by electrostatic dipole interactions. At this stage water creates free volume, as it pushes upon the hydrophobic matrix to allow incorporation. The greater the free volume the more effective is diffusion. As more water molecules are absorbed, the packing becomes more efficient and the free volume per molecule decreases. Then, the rate of increase of diffusivity with water content shows a transition at $\lambda = 4$,

which they identified as the number of water molecules forming the primary hydration shell of the sulfonic acid groups. The strength of the electrostatic interactions between sulfonic acids and water molecules will decrease between the first hydration shell and subsequent hydration shells. The weaker electrostatic interactions between sulfonic acid groups and the second hydration shell permit more efficient motion of water. Also, the mobility is facilitated due the connectivity of the hydrophilic network appears to be more fully established after the first four waters per sulfonic acid are sorbed.

At large water content, the topology of the hydrophilic domains changes, forming a bulk-like water in confinement. The confinement boundaries correspond to water/polymer interfaces characterized by pendant side chains terminating with sulfonic acid groups submerged in the aqueous phase. The velocities of the water molecules are found to increase steadily from the polymer backbone/water interface toward the center of the water channels. Kim *et al.* [Kim 2003] characterized water molecules into three groups: "free water", water that is not intimately bound to the polymer chain and behaves like bulk water; "loosely bounded water" water that is weakly bound to the side-chain; and "bounded water", water that is strongly bound to the side-chains. Urata *et al.* [Urata 2005] found that at high hydration, the short residence time of the bound water reveals that water molecules can frequently move away from the sulfonic groups alternating their state between bounded and more free molecules.

Selvan *et al.* [Selvan 2011] used an analytical model for water and charge transport in highly acidic and highly confined environments. They found that three factors control most part of the effect in determining the self-diffusivity in Nafion: acidity, confinement and connectivity. When increasing acidity, *e.g.* the molar concentration of hydronium ions in the system, the self-diffusivity of water should decrease. Confinement in the absence of high acidity is sufficient to slow water dynamics [Kim 2003]. Acidity and confinement together influence the intrinsic diffusivity, and the connectivity lowers that intrinsic diffusivity to the observed diffusivity through a well-understood percolative mechanism.

The state or nature of the water adsorbed in Nafion has direct consequences on the proton transport properties. Proton transport is characterized by dissociation of sulfonic acid group ($-SO_3H$), followed by a non-classical charge transfer mechanisms in combination with classical diffusion. Electronic structure calculations have shown that only 2-3 water molecules per sulfonic acid group are necessary for proton dissociation

from SO_3H and when 6 water molecules are added, separation of the dissociated proton from the sulfonate anion is observed [Paddison 2003]. After dissociation, the transfer of protons (short and long range) takes place through acid groups interacting with non-bulk water molecules in combination with structural diffusion, the so-called Grotthus mechanisms. In short, proton transport is described through three mechanism: *i)* surface diffusion, occurring close to sulfonate groups at ionomer/water interfaces *ii)* Grotthuss diffusion, occurring mainly in the middle of the water pores (bulk-like water) and *iii)* vehicular diffusion, through proton-carrying self-diffusion (H_3O^+) [Choi 2005].

Kreuer *et al.* [Kreuer 2008] have shown that the proton mobility mechanism is mainly vehicular at lower levels of hydration, with its magnitude increasing slowly with water concentration up to λ around 10-13, where it exceeds the water diffusion value due to the added effect of the Grotthuss mechanism. The Grotthuss mechanism in an aqueous environment consists in an excess protons-transfer through the hydrogen bond network formed by water molecules. It is generally accepted that this mechanism depend on the proton solvation structure, which is idealized in terms of Zundel ion ($H_5O_2^+$) and Eigen ion (H_9O^+) [Kreuer 2004]. Also, strong hydrogen bonding is considered to be a precursor of proton-transfer reactions. However, proton transport also requires rapid bond breaking and forming processes, which is only expected to occur in weakly hydrogen bonded systems. Thus, dynamical hydrogen bonding have long been recognized crucial for long-range proton transport [Kreuer 2000].

Density Functional Theory (DFT) calculations of an array of short side chains in the hydrated region showed that proton transport depends on the presence of weakly bound water molecules, flexibility of the side-chain and separation between SO_3^- groups [Roudgar 2006]. In order to promote long-range proton transport along minimally hydrated arrays, the surface groups should be sufficiently correlated but at the same time they should remain sufficiently flexible. Spohr *et al.* [Spohr 2002] analysed the correlation between the proton mobility and the degree of proton confinement in proton-carrying cluster near SO_3^- . They list three factors that facilitate proton transfer: charge de-localization within the SO_3^- groups; fluctuation motions of SO_3^- and side-chains, and water content.

2.3 PEMFC Catalyst Layer

2.3.1 General aspects

The core of a PEM Fuel Cell is the Membrane Electrode Assembly (MEA), which consists of two electrodes (anode and cathode) and the proton exchange membrane. The electrode is considered to be the Catalyst Layer (CL) and the Gas Diffusion Layer (GDL). The CL is the composite layer of about 10 μm in thickness where the electrochemical reactions take place for electric power generation. The electrochemical conversion combines hydrogen and oxygen to produce electricity, heat, and water. The reactions that occur in the anode and cathode CL are, respectively, the Hydrogen Oxidation Reaction (HOR) and the Oxygen Reduction Reaction (ORR). The half-cell reactions are given by the following equations

$$\mathrm{H_2} \longrightarrow 2\,\mathrm{H^+} + 2\,\mathrm{e^-} \qquad \text{HOR}$$

$$\mathrm{O_2} + 4\,\mathrm{H^+} + 4\,\mathrm{e^-} \longrightarrow 2\,\mathrm{H_2O} \qquad \text{ORR}$$

The reactant gases (*e.g.* $\mathrm{H_2}$, $\mathrm{O_2}$), protons and electrons inside CL, react on the top of the *catalyst surface*. Both HOR and ORR occur via several intermediate reactions. The HOR mechanism involves the adsorption of the $\mathrm{H_2}$ onto the catalyst surface, followed by dissociation of the molecule and the electrochemical reaction to $\mathrm{H^+}$. In the cathode, the ORR has a much more complex mechanism for the adsorption and dissociation of $\mathrm{O_2}$ [Damjanovic 1967]. In order to explain the oxygen reduction coupled with formation of water molecules and peroxide groups, a series of mechanisms have been suggested and intensive work based on *ab initio* calculation have been performed to determine the most thermodynamically favourable ORR steps [Jacob 2003, de Morais 2011b]. The intermediate steps could be formation of peroxide groups, such as $\mathrm{H_2O_2}$, OH and $\mathrm{HO_2}$, with a relative degree of formation which depends on the nature of the chemical composition and structural properties of the catalyst used [de Morais 2011a].

The rates of those reaction mechanisms determine the efficiency of electrochemical conversion, which is directly related to the CL performance. The kinetics of HOR

reactions is very fast and is usually controlled by mass-transfer limitations when the operating fuel cell reaches high current densities. In contrast, the kinetics of ORR is much slower and is the most responsible for cell activation losses. The choice of the type of catalyst particles to be employed is crucial for enhancing reaction rates. The catalyst particles for intermediating HOR and ORR reactions is the pure platinum. The high cost associated to the amount of platinum required as a catalyst, especially in the cathode, is one of drawback of fuel cells. The combination of platinum with different metals (*e.g.* PtNi, PtCo) have been thought as possible a solution to decrease costs without losing stability and performance [Stamenkovic 2007].

The ORR and HOR are governed by the nature of electrochemical interface found within a few angstroms from the catalyst surface. As it is well know in fundamental electrochemistry, electrode/electrolyte interface is formed by an electronic phase (catalyst surface) and the reactant phase components ('solution' environment comprised of reactants and reaction intermediates). This interface is characterized by the presence of *electrical double layer* (EDL) arising from the strong interactions between the ions/molecules in solution and the electrode surface. EDL strongly depends on the nature and distribution of ion/molecules in the reactant phase. At some more complex systems such as in the presence of ionomer in reactant phase, EDL remains not fully explained and sometimes contradictory [Zembala 2004]. Ultimately, EDL produces a gradient in electrical and chemical potentials at the vicinities of catalyst surface that constitute the driving force for electrochemical reactions.

Moreover, the reaction rates do not depend only on the nature of the catalyst used but also on transport conditions for reactants and products moving from/to catalytic sites. In other words, a high cathode CL performance (similarly in anode CL) may depend on: transport of protons from the membrane to the catalyst; electron conduction from the current collector to the catalyst; reactant gases from gas channels to the catalyst; and correct removal of water from the catalyst layer. In order to meet all requirements, a complex structure with interconnected pores phase for gas diffusion, a metallic phase for electron conduction and a path for proton transport are fundamental elements to build a CL. In the following, we give more details on the CL structure and the influence of manufacturing.

2.3.2 Pt-based Catalyst layer: manufacturing and structure

The necessity of having a heterogeneous structure to satisfy all catalyst layer (CL) functionalities, drives the quest for new material designs [Litster 2004]. Such designs attempt to optimize the distribution of transport media, in order to reduce transport losses and produce the highest current density with a minimum amount of catalyst particles. The success mainly depends on the type of material used and fabrication process applied. Therefore, many experimental and theoretical studies have been performed in order to understand the detailed CL structure and thus, be able to further develop new materials and fabrication methods.

The first attempt to design a CL for PEM fuel cells consisted on using a fine powder of platinum with good catalytic properties (Pt black), and hydrophobic polytetrafluoroethylene PTFE (Teflon) as a binder [Wilson 1995]. Although this type of CL demonstrates excellent long-term performances, it is excessive costly due the high platinum loadings (4 mg/cm^2). A significant improvement was achieved when the pure Pt black was replaced by the carbon supported Pt catalysts, which significantly reduced the Pt loading from 4 mg/cm^2 down to 0.4 mg/cm^2. A major advance came with the CL fabrication method, proposed and patented by Wilson in 1993 [Wilson 1993]. In this method, the hydrophobic PTFE was replaced by the hydrophilic PFSA ionomer (Nafion). This idea was successful and the CL was found to operate at almost twice the power density of previous method, due to a significant enhancement of catalyst active area from 22 to 45.4%.

Wilson's method is the base for the most used CL design, so-called thin-film CL. The basic fabrication process consists in preparing catalyst ink by mixing the Pt/C agglomerates with a polymer electrolyte and solvent. Next, the ink is deposited on a porous support (in the case of catalyst-coated gas diffusion electrode) or on a membrane (in the case of catalyst-coated membrane). Basically, the thin-film fabrication processes differ according to the nature of catalyst ink (*e.g.* , type of solvent, ionomers) and the ink deposition method. Without going into details we can mention several techniques that have been invented, such as decal transfer, brush painting, spray coating, doctor blade coating, screen printing, ink-jet printing, and rolling [Litster 2004, Yu 2011, Xiao 2012].

Although several fabrication methods have been proposed, very little can be

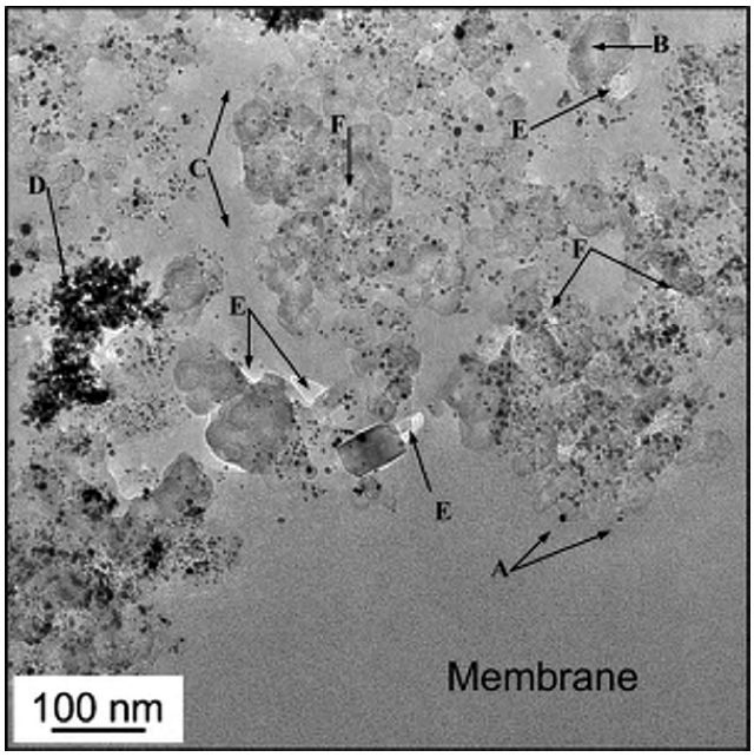

Figure 2.7: TEM image showing the cross-section of Pt_3Cr catalyst layer and Nafion membrane. The arrows point to: (A) the Pt_3Cr alloy catalyst particles, 4-12 nm diameter; (B) carbon aggregates, $\approx$ 340 nm diameter; (C) recast Nafion ionomer network; (D) coalesced Pt_3Cr particles; (E) secondary pores, 40-80 nm in diameter; and (F) primary pores, $<$ 17 nm in diameter. Figure from reference [Xie 2010].

done in order to control the formation of CL. Therefore, CL is characterized by a random heterogeneous structure. More precisely, it consists of a solid phase comprised of carbon particles or agglomerates decorated with catalyst nanoparticles, a proton-conducting network of Nafion ionomer, and an open-porous network. This can be visualized by Transmission Electron Microscope (TEM), as shown in the figure 2.7 [Xie 2010]. It shows a cross-section image of Nafion membrane and the thin-film CL with Pt_3Cr alloy as catalyst particles. This image clearly shows the typical phases that one can find inside the CL. One can see the Pt_3Cr alloy catalyst particles of 4-12 nm in diameter attached to the carbon support (arrow A) and agglomerated without catalyst supports (arrow D). The ionomer is found embedded as network (arrow C) and as physical binding structures for the carbon aggregates (arrow B). The pores, classified as primary ($<$ 17 nm in diameter) and secondary (40-80 nm in diameter),

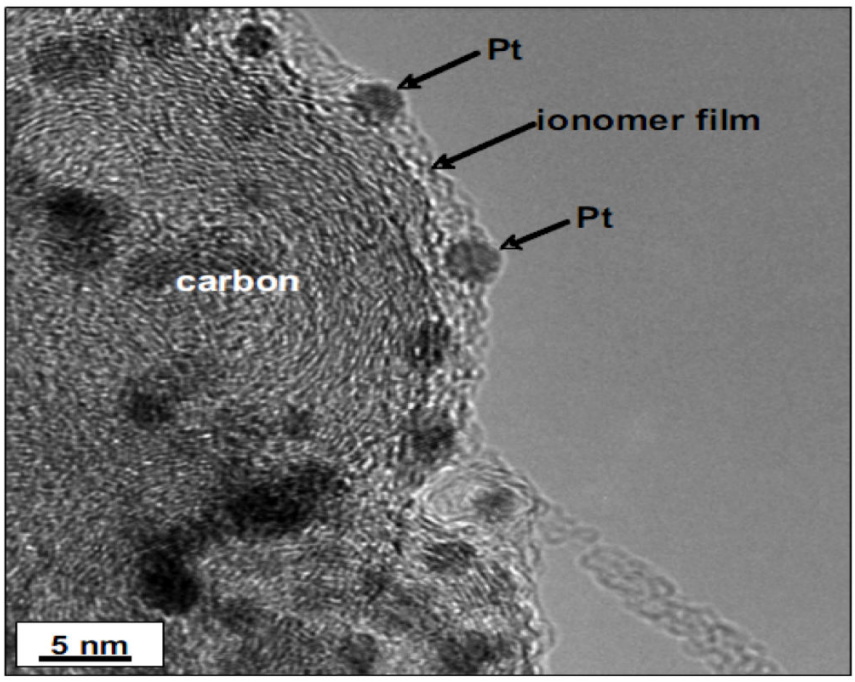

Figure 2.8: TEM image showing Pt/ionomer/C interfaces. This image clearly shows the formation of ionomer thin-film covering carbon and Pt particles. Figure from reference [More 2006]

are the white areas denoted by arrows F and E respectively.

The Nafion ionomer distributed within the CL presents an inhomogeneous and non-continuous phase. Through a high spacial resolution of TEM image shown in figure 2.8, we can clearly see the Nafion ionomer phase that embedded carbon-supported Pt. According to More *et al.* [More 2006], the ionomer can be found into three morphologies: well dispersed thin film layers on the surface of carbon supports and Pt particles; separate uncorrelated domains of ionomer agglomerates and Pt/C agglomerates; and rod-like fibrils bridging between Pt/C agglomerates. At this length scale, Nafion ionomer mediates the proton migration and water transport inside pores. Moreover, the presence of the ionomer film covering active catalyst sites would result in reactants, which must diffuse through the film. This diffusion process is greatly affected by the thickness and the local nanostructure of the film.

The thickness of the Nafion ionomer films surrounding the catalyst/carbon aggregates, as well as the dispersion of these aggregates, are affected by Nafion loading. Although Nafion provides important improvements concerning Pt utilization and

proton conductivity within CL, it exists a non-linear relationship between CL performance and Nafion loading. It was observed that when Nafion loading increases from 0.2 to 1.75 mg/cm^2, performances improve significantly. This indicates a better utilization of platinum. However, the performance is diminished at high current densities, when Nafion loading increases beyond 2.0 mg/cm^2 (33 % of CL weight). This is because of mass-transport losses. In this case, the excess Nafion could obstruct reactant gases diffusing, and hydrophilic Nafion segments could retain water inside CL [Paganin 1996, Song 2001].

A relevant factor that can deeply influence the CL structure during fabrication process is the choice of the solvent used during ink preparation. The different dielectric constants of the solvents and the corresponding interactions between ionomer and solvents, determine whether the ionomer is found in solubilized, colloidal or precipitated forms [Shin 2002]. In the so called "solution method", the ionomer totally dissolves and forms a solution state. The solvent could be water or additional organic solvent such as ethylene glycol, isopropanol, hexanol or glicerol that can improve ink paintability [Chun 1998]. This method can have the result ionomer excessively covers carbon particles, blocking electron conduction between Pt and carbon. In the "colloidal method" the ionomer is found in a colloidal state and form a continuous network of ionomer, that enhance proton transport and outperform the solution method at high current densities. Moreover, colloidal method could better control the sizes of the Pt particles and prevent Pt agglomeration [Lim 2008].

Several other factors can influence the microstructure formation in CLs. A detailed structural description, including agglomeration of Pt-decorated carbon, formation of ionomer domains, emergence of the porous network and formation of interfaces between the distinct phases, remain unclear. Consensus has been reached on the idea that CL presents highly heterogeneous structure that involves structures at different length scales. In what follows, we discuss the importance of hydrophobic character of CL for the global CL performance (water management). Also, we discuss the formation of hydrophilic and hydrophobic domains at nano and meso-scale inside CL and its importance on ionomer domain formation.

2.3.3 Hydrophobic and hydrophilic character of Catalyst Layer

The hydrophilic and/or hydrophobic feature of catalyst layers (CL) plays an important role in water management inside the fuel cell. Water produced within the cathode via the ORR, is found primarily in the liquid phase when PEM fuel cell operates under normal conditions (temperatures less than 80°C). Removal of liquid water from the cathode must be effective, when water in excess fills up the pores, and consequently, obstructs gas transport. Hydrophobic materials could lower the rate of water saturation in the flow field, thus preventing the water flooding in the cathode side [Yang 2010]. However, the presence of water is needed to humidify the ionomer, which is crucial to enhance proton transport inside CL. Therefore, the appropriate amount of water is an important factor affecting CL performance, and it is controlled by the wetting properties of the pore surfaces in the CL.

During the fabrication process, hydrophobicity of CL can be enhanced by simply adding extra components (*e.g.* dimethyl silicone oil) into the catalyst ink solution [Li 2009, Li 2010]. The choice of the type of carbon used as a catalyst support is also important in determining hydrophobicity (*e.g.* VULCAN carbon type are partially hydrophobic, with contact angle $\sim 90°$ [Kinoshita 1988]). During fuel cell utilization, the hydrophobicity of CL significantly changes due to degradation processes, as well as impurity effects. Viewed from the inside of CL, Yu and Ziegler [Yu 2006] showed that the CL has indeed non-uniform hydrophobicity. Through micro-contact angle measurements by environmental scanning electron microscopy (ESEM), the authors observed that the value of the surface contact angle depends on the local composition of the CL. Also, during degradation process they observed non-uniform hydrophobicity, despite that globally the CL becomes more hydrophilic.

At the nanoscale, the CL hydrophobicity becomes even more heterogeneous. Coarse-grained MD simulations showed that the nanostructure in CLs segregates into hydrophobic and hydrophilic regions. The hydrophobic region is constituted by the carbon particles, the ionomer backbone, and solvent. The hydrophilic region contains catalyst particles, water clusters, hydronium ions, solvent, and the ionomer side-chains [Malek 2007, Malek 2011b]. The hydrophilic/phobic character of catalyst and catalyst-support particles, can be modified during chemical processes. For example, it has been shown that graphitized carbon sheets functionalized with carboxyl or carbylate groups

enhance the capacity of wetting the surface [Mashio 2010]. In the same way, the oxidation process on the catalyst and the catalyst support could eventually increase the hydrophilicity of the surface. This effect can be observed during fuel cell operation (instantaneous changes) or it can be a phenomena related to degradation process (long-term changes).

The hydrophobicity and hydrophilicity of this material has strong impact on formation of CL structure. Malek *et al.* [Malek 2011b] demonstrated that the final microstructure depends on material wetting properties and the strength of ionomer-CL material interactions. Moreover, they showed that the surface wettability affects the distribution and morphology of ionomer, influencing its thickness and side-chain orientation. From experiments, there is evidence that surface wettability in addition with increased uptake of free water, cause a morphological rearrangement between Nafion hydrophobic backbone and hydrophilic side chains [Wood 2009]. In the next section, we present the state-of-art of Nafion morphology and transport properties of Nafion thin-films formed on different metal surfaces. We also include a discussion on ionomer adsorbed on catalyst surfaces and its impacts on CL chemical reactions.

2.4 Nafion at interfaces

In contrast to the extensive studies of the bulk Nafion membrane, very few studies have been devoted to ionomer adsorbed on solid electrode surfaces. From experimental and theoretical studies, one finds much evidence that the interfacial interactions can affect the structure and properties of ionomer. In particular, the formation of thin-films inside PEMFC catalyst layer (CL), is expected to have significant impact on proton conductivity, diffusion of reactants and products and the kinetics of electrochemical reactions occurring on catalytic surfaces. In this section, we review the experimental and theoretical works devoted to study the structure and dynamics of thin-films adsorbed on electrode surfaces and the impacts on physical-chemical CL activities.

2.4.1 Nafion thin-films: structure and proton transport

The structure of thin-films adsorbed on electrode surfaces has been investigated. A particularly interesting question is whether there is any preferred association of hydrophobic or hydrophilic parts of the ionomer with the electrode surface and whether such effects might depend upon the nature of the electrode material. Ma *et al.* [Ma 2007] have investigated the interaction between the Nafion ionomer and catalysts or carbon supports at ambient temperature. Through Nuclear Resonance Spectroscopy (NMR) experiments, the adsorption equilibrium constant and maximum surface coverage were used to compare affinities of Nafion dissolved in water with carbon, Pt and PtRu. Their conclusions were that Nafion has a higher affinity to carbon than to noble metal catalyst. Also, interaction of Nafion with PtRu is stronger than with Pt, which might be due to a favourable adsorption on hydrophilic ruthenium sites with chemisorbed hydroxide groups.

Masuda *et al.* [Masuda 2009] have investigated the formation of Nafion thin films on a highly oriented pyrolytic graphite (HOPG) surface by using atomic force microscopy (AFM) techniques. Their results show that the formation of this film involves unfolding/extension process of the micellar PFSA aggregates under the influence of atomic arrangement of the HOPG surface, which is characterized by a threefold symmetry. This conclusion comes from the observation of the adsorbed ionomer forming two-dimensionally ordered domains (oriented at 60° to each other) composed of unidirectionally aligned ribbon-like wires. This is a variance with what they found when the ionomer is placed on amorphous carbon surfaces, such as glassy carbon.

Also via AFM experiments, Koestner *et al.* [Koestner 2011] have observed adsorption of dissolved Nafion chains at a slow and rapid deposition rate on mica and graphite (HOPG) surfaces with and without autoclave treatment. The authors trace the ionomer conformation depending the imposed solution, deposition conditions and the type of substrate. The different conformations of adsorbed Nafion chains are: a collapsed sphere (globule), segmented rod, and expanded coil.

Eastman *et al.* [Eastman 2012] have given attention to the thickness of the ionomer adsorbed. They measured through several experimental techniques the equilibrium structure and effective diffusion coefficient of water in a series of Nafion thin-films of thickness ranging from 20 to 220 nm when exposed to water vapour. They

observed that the film thickness interferes in the manner some properties (*e.g.* water uptake, swelling, water diffusion), respond to the relative humidity. The authors identify the critical thickness around 60 nm, where there is a transition from a bulk-like to confined ionomer. This indicates that the nanostructure is greatly affected by film thickness. Also, this work alludes to a typical length scale of the interfacial region affected by the underlying substrate.

Wood *et al.* [Wood 2009] have found multilayer structures of nafion in contact with smooth flat surfaces. These structures showed separate hydrophobic and hydrophilic domains formed within the Nafion layer when equilibrated with saturated D_2O vapor. Any strong interaction between a flat surface and Nafion is likely to lead to the polymer chains lying flat on that surface, which is completely different from any bulk Nafion morphologies proposed. When Nafion was in contact with a bare Pt surface, the hydrophobic Nafion region was found to form adjacent to a Pt film. However, when a PtO monolayer was present, the hydrophobic backbone was pushed outward and the hydrophilic side chains were in contact with the PtO surface. These restructuring processes were reversible and strongly influenced by the polymer hydration.

Dura *et al.* [Dura 2009] have performed Neutron Refractometry (NR) measurements in order to investigate the structure of Nafion at the interface with SiO_2, Au and Pt surfaces. They have shown that lamellar structures composed of thin alternating water-rich and Nafion-rich layers exist at the interface between SiO_2 and the hydrated Nafion film. However, multilamellar structures do not exist at the Pt/Nafion or Au/Nafion interfaces, but a single thin layer rich in water occurs at the interface with these metalic surfaces. This difference indicates that Au and Pt surfaces have a lower affinity to the sulfonic acid/water phase than the more hydrophilic Si_2O surface. The authors interpreted these structures in terms of an interface induced ordering of the ribbon-like aggregates or lamellae observed in SAXS experiments of bulk Nafion. Therefore, the first Nafion-rich layer could be formed by closely packed ribbons or lamellae, oriented with their faces parallel to the substrate, and with successive layers of increasingly disordered character.

Modestino *et al.* [Modestino 2012] have investigated how to control Nafion structure and properties only via wetting interactions. They have prepared Nafion thin-films deposited on hydrophobic (OTS passivated substrates) and hydrophilic (Silicon sub-

strate) surfaces, and investigated the impact that internal morphology of these films has on water uptake. They found that thin films cast on hydrophobic substrates result in parallel orientation of ionomer channels that retards the absorption of water from humidified environments. On the other hand, films prepared on SiO_2 result in isotropic orientation of these domains, thus favouring water sorption and swelling of the polymer.

Bass *et al.* [Bass 2011] have investigated by grazing incidence SAXS (GISAXS) techniques, the morphology of Nafion thin films on hydrophobic silanized Si. The authors studied the features of the external surface of Nafion films, *i.e.* the interface of Nafion and the external phase (*e.g.* vapour or liquid water). They showed that the external surface is hydrophobic when the film is exposed to water vapour whereas it becomes hydrophilic when the film is equilibrated in liquid water. The authors attributed this difference to the orientation of Nafion micelles. In vapour environment Nafion micelle at the surface preferentially align parallel to the surface, while under water they are oriented normal to the surface. Moreover, the authors showed that the substrate where the film is deposited affects the micelles orientation adjacent to the subtrate. The orientation varies from parallel micelles, when the film is on hydrophilic native SiO_2 of Si substrate, to perpendicular micelles when it is on hydrophobic C18-capped Si substrate.

Furthermore, the proton transport properties in Nafion thin-films may also differ from those in the ionomer membrane. Paul *et al.* [Paul 2011b, Paul 2011a] have showed lower proton conductivity in thin-films adsorbed on Si_2O-terminated surface when compared with bulk membrane. The authors suggest that the conduction mechanisms in adsorbed thin films occurs mainly via surface diffusion, while, in bulk membrane, it occurs mainly via Grotthuss mechanism. Another reason could be due to the strong sulfonate groups interaction with the substrate, lessening water adsorption.

Iden *et al.* [Iden 2008] measured the effects of different carbon supports on the proton conductivity for pseudo-CL sandwiched between two Nafion membranes. They found that the pseudo CLs with the carbon support that had lower surface area and lower surface groups showed higher proton conductivity. Siroma et al. [Siroma 2009] have reported that the proton conductivity decrease and the apparent activation energy increase with decreasing thickness. This dependence is likely due to the dependence of the water content on thickness. Based on the finding that a dry membrane has a

low conductivity and a high apparent activation energy, it is assumed that a thin film does not absorb sufficient water.

2.4.2 Ionomer adsorption: effects on catalyst layer activity

Nafion thin-films coating catalyst surfaces in PEMFC should have an important impact on the kinetics of electrochemical reaction (*e.g.* ORR and HOR). Some experimental and theoretical studies suggest that Nafion could adsorb or interact with catalyst surfaces modifying the electrochemical double layer (EDL) structure [Jiang 2004]. Although standard electrochemical theories are largely used to describe the EDL under equilibrium conditions, the presence of a heterogeneous structure like Nafion may modify the EDL structure in a still unknown fashion.

Zhdanov and Kasemo [Zhdanov 2006, Zhdanov 2004] and Franco [Franco 2005] were pioneers to explore this issue. Zhdanov and Kasemo proposed a lattice-gas model using Monte Carlo simulation in order to mimic the phase separation of the Nafion matrix at the vicinity of catalyst surface. In this Nafion matrix they performed the charge and potential distribution inside the double layer. They have shown that the phase separation of Nafion may cause appreciable spatial fluctuation of the potential near the surface therefore influencing the rate of electrochemical reactions. Franco *et al.* [Franco 2006, Franco 2007b] have proposed a multiscale model describing the non equilibrium structure of the EDL for both PEMFC anodes and cathodes, explicitly accounting for the presence of the sulfonate groups of Nafion in the diffuse layer region.

The reaction kinetics are also strongly dependent on the catalyst surface coverage of spectator species, *i.e.* species that do not participate on the reaction. In other words, for the case of catalyst surface without Nafion, it has been proved that the catalytic activity of the ORR is almost completely determined by the availability of free metal surface sites. In the presence of the ionomer, it has been recognized that electrochemical process can take place only at domains where hydrophilic segments of Nafion are in contact with the electrode surface, while the regions where the Pt surface is exposed to the fluorocarbon backbone are inactive [Maruyama 1998].

The adsorption of Nafion on catalyst surface tends to occur through the sulfonate groups, which was observed by cyclic voltammetric experiments reported in a number of papers and also supported by in situ surface-enhanced Raman spectroscopy (SERS)

experiments [Zeng 2012]. Despite the adsorption of sulfonic groups, Kendrick *et al.* [Kendrick 2010] through spectroscopy techniques correlated with DFT calculations have suggested that the CF_3 in the side-chain are direct adsorbed on Pt surface. Such adsorption partially orders the Nafion backbone and side-chains relative to the Pt surface. The adsorption of polymer chains interferes on the adsorption of other species. Sonsudin *et al.* [Sonsudin 2010] compared the electrochemical behaviour of a bare and Nafion-coated Pt(111) in $HClO_4$ and H_2SO_4 solutions. They observed that specific adsorption/desorption of anions occurring in bare Pt(111) but not ionomer-coated electrode, possibly due to strong adsorption of polymer chains on the Pt surface and/or the prevention of anion penetration into Nafion film.

Subbaraman *et al.* [Subbaraman 2010a, Subbaraman 2010b] have compared the nature of Pt(*hkl*)-Nafion interfaces with the corresponding Nafion-free Pt(*hkl*) surface through voltammetric fingerprinting approach in order to clarify the nature of ionomer adsorption. They proposed a "spring model" to explain the adsorption of sulfonate anion on the Pt(*hkl*) surface. They suggest that the sulfonate anions are kept in the double layer by two thermodynamic driving forces, one trying to pull the anions to the surface (metal-sulfonate bonding) and a counter spring force with a strong tendency to return the sulfonate anions back to its native (state sulfonate-cation and/or sulfonate-backbone bonding). This balance will determine the nature of the sulfonate adsorption. The model of Subbaram *et al.* is relevant to explain how the environment immediately adjacent to the electrode surface can affect sulfonic acid group adsorption. They suggest that clustering of anions within the ionomer, spacing between the clusters, ionic cluster size, and the local anion-counter cation non-covalent interaction, play a major role in determining the overall surface coverage of sulfonate anions on the surface.

2.4.3 Computational studies of Nafion at interfaces

Molecular dynamics (MD) simulations can provide valuable insights in clarifying nanoscale structure and transport properties of Nafion at interfaces. Despite this potentially powerful contribution, very few works have been dedicated to this issue by using computer simulations. A possible reason for that could be the difficulty to correctly parametrize the interaction forces between Nafion and other materials. In

this subsection, we review the computational work focusing on the behaviour of Nafion in presence of carbon and platinum based materials.

The first work we consider here is that performed by Balbuena, Lamas *et al.* [Balbuena 2005, Lamas 2006]. They have applied MD methods to simulate the ionomer in the vicinity of graphite decorated with Pt particles. The system consists of Pt_{256} clusters attached to a graphite surface with addition one-by-one of Nafion chains followed by water molecules. In the equilibrium state, Nafion appears to strongly interact with Pt nanoparticle, mainly through its hydrophilic sulfonic chains. Water nucleates at the Nafion hydrophilic sites, forming ionic clusters on the platinum surface. The connectivity of these clusters depends on the water contents. They can be found either totally disconnected, partially connected or forming a continuum phase through the formation of multiple water bridges. The authors also showed that Nafion distribution depends on thermal preparation of the system. When doing a thermal relaxation through annealing procedure, the system ends up with a less organized distribution of the hydrophilic sites which reduces the connectivity among water clusters.

Liu *et al.* [Liu 2008] performed MD simulations of three-phase interface comprised of the hydrated PEM in contact with the vapor phase and with either the catalyst surface or the catalyst support surface. Their idea was to mimic the wetting behaviour of hydrated Nafion when it penetrates the CL pores (*e.g.* when the PEM membrane is in contact with CL). Characterization and analysis of the structural and dynamic properties of such system indicate that there is no wetting of the catalyst support surface (graphite) and significant wetting of the catalyst surface (Pt[100]). The velocity of hydrated Nafion wetting the catalyst surface was quantified for different membrane hydration level. A mixture composed of water, Nafion, and hydronium ions forms a monolayer coating the platinum surface. Additional analysis of water molecules and hydronium ions adsorbed at the Pt surface shows a long-range structure characterized by the formation of hydrogen bonds.

Selvan *et al.* [Selvan 2008] examined the structural and transport properties of water and hydronium ions at the Nafion/vapor phase interface. They found that in the interfacial region, the hydronium and water diffusivity parallel to the interface remains very similar to that in the bulk membrane, while the diffusivity perpendicular to the interface increases due to local decrease in density. On the basis of these diffusivities, they conclude that there is no observable additional resistance to mass transport of

the vehicular component of water and hydronium ions due to the interface. These finds are in contradiction with the morphology at the Nafion/vapor interface observed by Bass *et al.* [Bass 2010].

The studies of Selvan *et al.* [Selvan 2012] focus mainly on the structural changes of the polymer electrolyte membrane due to the presence of a Pt cubic nanoparticle. MD simulations of a single nanoparticle of platinum surrounded by Nafion at different hydration levels were performed. The authors investigated the changes in density and orientation distribution of sulfonic acid groups in the side-chains, water, and hydronium as a function of distance from platinum surface following changes of water contents of the ionomer film. The orientation of the side-chain containing the sulfonic acid group might play a significant role in the water density distribution near the platinum surface.

Mashio *et al.* [Mashio 2010] analysed by MD simulations the morphology of Nafion ionomer and water at the graphite surface. Because of the hydrophobic nature of the graphite sheet and ionomer backbones, Nafion ionomer interacts with the graphite sheet mainly via the backbone, whereas side chains are oriented away from the graphite sheet, adsorbing water at sulfonic acid groups. By using the system structures obtained, they also investigated transport of water and hydronium ions by computing the residence time ratios and the diffusion coefficients of water and hydronium. They observed that water mobility is limited by the electrostatic interactions with sulfonic acid groups or hydronium ions even if a continuous stable water cluster has formed.

Moreover, they explored the effect on structural and transport properties of the functionalization of graphitized carbon sheet with carboxyl ($COOH$) or carboxylate (COO^-) groups. The most significant effect on the water and ionomer distributions comes from the graphite sheet fuctionalize with ion groups. They observed that the number of water molecules, hydronium ions and sulfonic acid groups in the vicinity of the graphite sheet increases with the application of the ionized functional groups. The structure and surface properties of carbon supports clearly affect the transport properties of proton and water.

2.5 Challenges and thesis proposal

In the view of the optimization of PEMFC technology, the CL has shown to be the component that still presents opportunity for significant performance improvement and cost reduction. The reasons for that were discussed above and can be highlighted in two points: CL structure is not deeply understood; and CL efficiency strongly depends on fabrication processes; However, the search for more efficient CL consists of trial and error methods of manufacturing, without a good control of the final CL structure. Therefore, an obvious challenge is to understand the relation between manufacturing processes and the micro and nano-structure of CL. In particular, the morphology of the Nafion ionomer inside CL shows to be strongly sensitive to the type of material employed, especially the hydrophobic/philic character of these materials. Understanding the ionomer nanostructure, precisely the ionomer thin-films structure at molecular level is the major concern of our work.

The challenges for performing molecular studies of Nafion ionomer sytems include: the unavailability of experimental techniques to probe the details of morphology; and the computational limitations for simulating very large systems. The most adequate computational methods to be employed are Molecular Dynamics and Monte Carlo simulations. These methods have the crucial difficulty for parametrizing the interactions between the unit entities. This difficulty becomes even more challenging when the ionomer found in contact with a solid substrate. Interactions between the Nafion and substrate are still very hard to devise, especially in the case of metal surfaces. In addition, the simulation of substrate with different wettability character requires a comprehension of the principles, such as surface polarity and atomic rearrangement, that affect the water wetting behaviour.

Finally, very few works have been aimed at understanding ionomer in deposited on different types of substrate. Our work aims to contribute for understanding the interplay of water/substrate and polymer chains/substrate interactions on the ionomer film structure. Therefore, we propose a simple approach base on Molecular Dynamics simulations, which focuses very little on chemical details but aims at grasping the main general physical features. We consider here a mean-field-like interaction ionomer/substrate, that allows us to precisely control the hydrophilic character of the substrate by using an unique tunable control parameter. Before going into more details

on the model we propose, in the next chapter we present the idea and practical aspects of Molecular Dynamics simulations aiming to give an introduction for the reader who is not familiar with this method.

Chapter 3

Computational methods

Contents

3.1 Introduction

Computer simulation has proven to be a powerful and effective tool to describe molecular systems. The growth of computer power together with significant progress achieved on algorithm development are the main reasons of increasing utilization of computers to perform fundamental research in materials science. Moreover, a crucial motivation for performing computer simulations is the possibility to capture detailed information at atomistic level, which is very often impossible to probe in experiments.

Many computational methods are nowadays available and the method of choice depends on the length scale of the system and the scientific questions considered. In particular, for studies of polymers and molecular liquids like water, relevant in our case, Molecular Dynamics (MD) and Monte Carlo (MC) techniques are the most adequate and widely applied. Both methods rest on the principles of statistical mechanics and they allow rationalizing macroscopic system behaviour in terms of microscopic description. The major difference between them is that the first can simulate the time evolution of the particles of the system, thus compute time-dependent properties, which makes the MD method the tool of choice for the simulations of Nafion systems reported in this manuscript.

In this chapter we briefly discuss the classical MD simulation methodologies which have been used in the context of the present thesis. The chapter is divided into two parts: in the first we discuss the main ideas behind MD algorithms; the second part we discuss practical aspects, *e.g.* the use of boundary conditions, the different thermodynamic ensembles, etc., which have been relevant for our simulations on bulk and confined systems. A complete introduction to MD methods including fundamental concepts and detailed algorithms is beyond the goal of this chapter and can be easily found in text books [Frenkel 2002, Rapaport 2009, Allen 1989]. Moreover, a number of popular computational packages for MD simulations exist including LAMMPS [Plimpton 1995], GROMACS, AMBER, CHARMM, GROMOS, NAMD.

3.2 Molecular Dynamics simulations: the idea

A Molecular Dynamics simulation, also referred to as a “computer experiment”, is in some aspects close to a real experiment, where a scientist prepares a sample

and performs measurements. Indeed, in a MD simulation, the sample is prepared by selecting a particular topology and forces for the interacting units (the model). Next the system evolves according to these forces conforming to the laws of classical mechanics until it reaches a "good" thermodynamic equilibrium. Following this initial equilibration step, one follows the trajectory of the system including positions and velocities of all units, during a long period of time ranging from fs to hundreds of ns. By knowing the positions and velocities one can explicitly calculate virtually any observable probed in experiments.

A model system is constituted of atoms and molecules that are represented by classical particles, *i.e.* point masses or rigid bodies subject to the laws of classical mechanics and interacting through known potentials. The parameters that define these interactions are often derived based on quantum mechanics calculations or experimental data. The set of equations defining the interaction potentials with the appropriate parameters define the *force field*. Solving Newton equations of motions subjected to these forces generates the trajectory of the system units. In this section, we discuss the force field we have chosen to simulate our system and we introduce the algorithm used to integrate equation of motions. Next, we introduce general concepts of statistical mechanics used to extract the observables.

3.2.1 The force field

The force field usually subdivides the potential function in two classes: *bonded interactions*, including covalent bond-stretching, angle-bending, torsion potentials when rotating around bonds, and out-of-plane improper torsion potentials; and *non-bonded interactions*, consisting of Van der Waalls and electrostatics potentials. Therefore, total potential energy U is given by

$$U = U_{bonded} + U_{non-bonded} = U_b + U_\theta + U_\phi + U_\chi + U_{LJ} + U_{coul}. \tag{3.1}$$

Here, U_b, U_θ, U_ϕ and U_χ are, respectively, bond, angle, dihedral and improper bonded interaction potential, while U_{LJ} and U_{coul} are, respectively, Lennard-Jones and Coulomb non-bonded interaction potential. Each term in equation 3.1 that we have adopted for the simulations of Nafion polymer are specified in the following.

Bonded Interactions

The bonded interactions, also called intramolecular interactions, describe the forces between atoms within the same molecule. They are not exclusively pair interactions, and can also include interactions among 3 or 4 particles. These potentials are non-reactive, *i.e.* they do not allow making or breaking of bonds, and they are often modelled by harmonic terms (quadratic). Bonded interactions include: bond stretching (2 particles), bond angles (3 particles) and dihedral angles (4 particles), including a special type of dihedral terms called improper.

The simplest way to describe the bond stretching between two covalent bonded atoms *i*-*j* is to treat the bond as a "spring". Thus, the energy U_b is given by the Hook's law (harmonic potential), which is expressed by

$$U_b = k_b(r - r_0)^2. \tag{3.2}$$

Here, r is the distance between atoms i and j, r_0 is the equilibrium bond length and k_b is the spring constant. This harmonic approximation is reasonable for small bond length deformations. At large deformation the covalent bond would break, an effect that is not captured by this potential.

The bond angle interaction between a triplet of atoms *i*-*j*-*k* is also often represented by a harmonic potential U_θ given by

$$U_\theta = k_\theta(\theta - \theta_0)^2, \tag{3.3}$$

where θ is the angle between the bonds *i*-*j* and *j*-*k* and can be expressed in terms of scalar products involving the two bonds. θ_0 is the equilibrium bond angle and k_θ is the energy constant.

The dihedral potential, also referred to as torsion potential, accounts for torsional forces around the bonds. The dihedral angle between quadruplet of atoms *i*-*j*-*k*-*l* is conventionally defined as the angle between the planes *i*-*j*-*k* and *j*-*k*-*l*. A common form for the dihedral potential U_ϕ is

$$U_\phi = k_\phi[1 + d\cos(n\phi)], \tag{3.4}$$

where k_ϕ an energy scale corresponding to the energy barrier to rotation; d admits

values $+1$ and -1 and n is the "multiplicity", corresponding to the number of points of energy minimum in the function as the bond is rotated in the range $[0, 2\pi[$. U_ϕ plays a crucial role in the local structure of macromolecules like polymers and proteins. Indeed it constrains the rotation around a bond, which in turn controls the rigidity of the molecule. Although the physical origin of dihedral interaction is not completely understood, the repulsive interactions between overlapping bond orbitals and steric repulsion between atoms appear to be contributing factors.

The improper dihedral angle is a special type of dihedral angle. This potential term includes 3 atoms centred around a fourth one instead of four consecutive bonded atoms. If we consider four atoms i,j,k,l with j linked covalently bonded to i,k,l the improper angle is defined as the angle between j-i line and the k-j-l plane. The harmonic improper dihedral potential is

$$U_\chi = k_\chi(\chi - \chi_0)^2, \tag{3.5}$$

where χ_0 is value of the improper angle in equilibrium, and k_χ determines the rigidity of the potential. The improper torsion is used to select the correct molecular geometry. It is meant to keep atomic groups (e.g. aromatic rings) planar, or to prevent molecules from flipping over to their mirror images. Note that in our formulation spring constants (k_b, k_θ, k_ϕ and k_χ) include the $1/2$ factor, which is usually expressed explicitly.

Non-bonded interactions

In addition to the bonded interactions between atoms described above, force fields also contain non-bonded interactions, which act between atoms pertaining to the same molecule or different molecules. The non-bonded interactions arise due to van der Waals and electrostatic forces. Van der Waals forces are both repulsive and attractive depending on the interaction distance. The most common form that encompasses this behaviour is the Lennard-Jones (LJ) potential. This potential vanishes at long distances, is characterized by a potential well at intermediate distance and strongly repulsive when they approach too close. The repulsive part is the so-called hard-core term and results from the fact that one atom cannot diffuse through another. The attractive term results from the induced dipole-dipole moment interaction of the particles. The pairwise LJ potential is expressed by

$$U_{LJ}(r) = 4\varepsilon_{\alpha\beta}\left[\left(\frac{\sigma_{\alpha\beta}}{r}\right)^{12} - \left(\frac{\sigma_{\alpha\beta}}{r}\right)^{6}\right], \tag{3.6}$$

where $r = r_{ij}$ is the distance between pairs i and j of type α and β respectively. $\varepsilon_{\alpha\beta}$ is the energy constant that corresponds to the potential well depth and $\sigma_{\alpha\beta}$ is the length scale constant that corresponds to the distance at which $U_{LJ} = 0$. The LJ potential reaches the minimum at distance $r = 2^{\frac{1}{6}}\sigma_{\alpha\beta}$.

The parameters $\varepsilon_{\alpha\beta}$ and $\sigma_{\alpha\beta}$ are often determined only when i and j are of the same type, say $\varepsilon_{\alpha\alpha}$ and $\varepsilon_{\beta\beta}$. To estimate the potential between the non-identical particles α and β, the Lorentz-Berthelot mixing rules are frequently used [Lorentz 1881, Berthelot 1898]. This rule set the cross parameters as

$$\sigma_{\alpha\beta} = \frac{\sigma_{\alpha\alpha} + \sigma_{\beta\beta}}{2} \tag{3.7a}$$

$$\varepsilon_{\alpha\beta} = \sqrt{\varepsilon_{\alpha\alpha}\varepsilon_{\beta\beta}}. \tag{3.7b}$$

The Lennard-Jones potential decays rapidly (it decays faster than $1/r^6$). Such type of interactions are classified as short-range interactions and can be truncated, *i.e.* one can impose a cut-off to the potential, r_c, beyond which $U_{LJ}(r)$ is set to 0. The safe choice to truncate the LJ potential is use a cut-off distance of $r_c = 2.5\sigma$. To avoid a jump discontinuity at r_c, the LJ potential is shifted to $U_{LJ}(r_c) = 0$.

Other non-bonded interactions are electrostatic forces, which arise due to the unequal distribution of charge in a molecule. The electronic polarization in a molecule cannot be properly described in classical molecular dynamics simulations. In this case, it is treated implicitly by assigning to each atom a fixed partial charge obtained from quantum chemistry calculations. The electrostatic pairwise interaction is therefore calculated via the Coulomb potential

$$U_{coul} = k_e \frac{q_i q_j}{\varepsilon r}, \tag{3.8}$$

where $k_e = 1/4\pi\varepsilon_0$ is an energy-conversion constant, q_i and q_j are the charges on the two atoms, and ε is the relative permittivity constant. The difficulty in computing the electrostatic forces is the slow decay rate of the interaction as a function of distance r. In such type of interaction the long-range forces cannot be neglected, which means

that the potential cannot be simply truncated and alternative approaches must be found to deal with the long-range part of the interactions.

3.2.2 Integrating the equations of motion

Once the force field is established, the next step consists in solving numerically the equations of motion. Positions and velocities of a given particle i are determined from the conservative forces acting on it, which can be derived from the interaction potential as,

$$\vec{F}_i = -\vec{\nabla}_i U, \tag{3.9}$$

where U is given by equation 3.1. Thus, the molecular trajectory is calculated by

$$\frac{\vec{F}_i}{m_i} = \frac{\partial^2 \vec{r}_i}{\partial t^2}. \tag{3.10}$$

The equations 3.9 and 3.10 cannot be solved analytically, therefore numerical finite difference methods based on Taylor series expansions are used. The simplest and most efficient method is the so-called Verlet algorithm. It provides numerical stability and meets important criteria such as time-reversibility and the conservation of law of energy and linear momentum. The basic forms of Verlet algorithm are

$$\vec{r}(t+\Delta t) + \vec{r}(t-\Delta t) = 2\vec{r}(t) + \frac{\vec{F}(t)}{m}\Delta t^2 + O(\Delta t^4) \tag{3.11a}$$

$$\vec{r}(t+\Delta t) - \vec{r}(t-\Delta t) = 2\vec{v}(t)\Delta t + O(\Delta t^3) \tag{3.11b}$$

Here, $\vec{r}(t)$ and $\vec{v}(t)$ are the position and velocity of the particle at time t, and Δt is the time step which is of the order of few fs. The value of time step is chosen to be short enough to ensure a correct behaviour of the numerical algorithms and large enough to make affordable the generation of long-times trajectories.

3.2.3 Computer experiments

Above we have discussed how we can numerically solve the dynamics of the system based on force fields. Here, we will discuss how to use the simulated trajectory for "measuring" the properties of interest. The trajectory consists of a series of system

configurations (snapshots), which are correctly sampled given the imposed macroscopic external thermodynamic conditions. The properties are always related to statistical predictions, as an average value with statistical fluctuations. Therefore, the sample must be as representative as possible in order to lead to satisfactory results, *i.e.* with a statistical uncertainty small enough to draw the desired conclusions.

Statistical averages over the simulated sample trajectory can be computed as

$$\langle A \rangle = \langle A \rangle_t = \frac{1}{M} \sum_{i=1}^{M} A(\vec{r}_i, \vec{v}_i) \tag{3.12}$$

for any quantity A that can be obtained from the positions $\vec{r}$ and velocities $\vec{v}$ of one or several equivalent particles. M is the number of time steps and $\langle ... \rangle$ means the ensemble average while $\langle ... \rangle_t$ means the time average. $\langle A \rangle = \langle A \rangle_t$ means that the time average of a given quantity is equal to its ensemble average. This is true only if the system satisfies the ergodic hypothesis of thermodynamics. Strictly speaking, the configurations must be statistically uncorrelated, which means that they are independent of each others and of the initial configuration. In principle, if the simulation is performed over a sufficiently long time, an average computed property does not depend on the initial positions and velocities.

Here, we consider two very simple examples: temperature and pressure. According to the equipartition theorem the temperature of a system is related to its average kinetic energies. The temperature is measured by computing the average kinetic energy per degree of freedom.

$$k_B T = \frac{\left\langle m \vec{v}_i^{\,2} \right\rangle}{f}. \tag{3.13}$$

Here f is the degree of freedom, k_B is the Boltzman's constant, m is the mass and $\vec{v}_i$ is the velocity of particle i.

The most common method to compute the pressure is based on the Virial equation and it is given by

$$P = \rho k_B T + \frac{1}{dV} \left\langle \sum_{i<j} \vec{f}(\vec{r}_{ij}) \cdot \vec{r}_{ij} \right\rangle, \tag{3.14}$$

where ρ is the number density, d is the dimensionality of the system, V is the volume,

$\vec{f}(\vec{r}_{ij})$ is the force on particles i due to particle j, and $\vec{r}_{ij}$ is the vector separation.

3.3 Practical aspects

In this section are included additional informations that we found necessary in order to perform Molecular Dynamics simulations. Here, we discuss the boundary conditions used for simulating bulk phase and confined systems. Also, we give a brief introduction of the techniques for solving long range interactions and we discuss the use of thermostat and barostat for simulating the system in different thermodynamic ensembles.

3.3.1 Spatial boundary conditions

Molecular Dynamics simulations aim at reproducing the properties of a macroscopic sample. The "thermodynamic limit" of statistical mechanics quantities can be reached for small (less than 100) numbers of particles [Lustig 1998]. For such small systems, the effects of the hard boundaries of simulation box are not negligible. Therefore, in order to simulate bulk phases, it is essential to choose boundary conditions that mimic the presence of an infinite bulk. This is achieved by employing the so-called *periodic boundary conditions* (PBC).

In PBC, the simulation box and all the particles (the primitive cell) are replicated infinitely in all directions (infinite images). There are no physical boundaries, so that the particles are free to move between the box and its images. Consequently, a particle that leaves the simulation box through a particular bounding face immediately re-enters the region through the opposite face. Also, each particle interacts with the nearest image of all the other particles (minimum-image convention). When using PBC, it is important to pay attention to the size of the simulation box must be large enough to prevent a molecule from interacting with its own image. In other words, interaction range should not be larger than half of the simulation box size.

PBC are particularly useful for simulating homogeneous bulk system. But, it is also possible to simulate isolated clusters/molecules if consider the simulation box size sufficiently large that no atom interactions cross a box boundary. When the interest is to simulate planar surfaces or interfacial systems, it is very often applied

slab boundary conditions. Slab boundaries are periodic in two dimensions (*e.g.* x and y), while leaving the third (z) direction with open boundary conditions.

3.3.2 Long-range interactions

In long-range interactions, *e.g.* Coulomb interactions, each particle interacts not only with the other particles in the simulation box but also with all other replica particles in the infinite periodic lattice. In order to avoid computing (infinite) all pair interactions, one must use alternative approaches that are able to compute the interactions between particles at long distances efficiently, while reducing or avoiding truncation artefacts. The most common method is based on the Ewald summation techniques. The main idea is to take advantage of the periodic lattice structure to reformulate the expression for the total electrostatic energy into a form that can be easily solved.

The central problem is to solve Poisson equation for the electrostatic potential. Ewald method reformulates this potential as the sum of two terms: the short-range part, *i.e.* it is equally zero beyond some cut-off radius and is calculated by the real space pairwise interactions; and the long-range part, which is defined by a 'smooth' function and it is efficiently calculated in Fourier space. The physical interpretation of this is that the short-range contributions come from the original point charges, each screened by a Gaussian charge density of opposite sign. The smooth part is just the sum of these artificial Gaussians with the signs of the original point charges.

Although this method proves to have good efficiency and accuracy, the standard Ewald summation becomes computationally very expensive for very large systems, especially due to inefficiency to solve the Fourier part. To overcome this restriction, an alternative is to apply particle-mesh scheme. Such scheme exploits the fact that, through Fast Fourier Transform (FFT), the Poisson equation can be solved much more efficiently if the charges are distributed on a mesh. The oldest and most accurate mesh-based Ewald method is the so-called Particle-Particle/Particle-Mesh (PPPM) method developed by Eastwood and Hockney [Eastwood 1974]. Other similar methods are Particle Mesh Ewald (PME) [Darden 1993] and Smooth Particle Mesh Ewald (SPME) [Essmann 1995].

In PPPM method, three steps are required to compute the reciprocal space

part: charge assignment, solving Poisson equation, and force assignment. In the first step, the charge is assigned onto a mesh using interpolation scheme. Several charge assignments can be used depending on the accuracy desired, *e.g.* triangle-shaped charge function (TSC), cloud-in-cell (CIC). However, for a charge assignment function to be feasible, it has to cover a relatively small number of grid points. Moreover, the assignment should vary smoothly with the particle's location, which requires adequate grid spacing.

In the second step, the Poisson equation is solved by fast Fourier transforming the meshed charge density given by

$$\hat{\rho}_{\mathbf{jkl}}(k) = \frac{1}{L^3} exp\left(-\frac{k^2}{4\alpha^2}\right) \sum_i q_i exp(i\mathbf{k}\cdot\mathbf{r}_i), \tag{3.15}$$

where α is an arbitrary parameter, and L is the size of simulation box. Then, the long-range potential in k space is given by

$$\hat{\psi}_{long} = \hat{\rho}(k)\hat{G}(k), \tag{3.16}$$

where the symbol $\hat{}$ indicates the Fourier transform of a function. $\hat{G}(k)$ is the influence function, where the optimal function is the Green's function which makes the mesh calculation as close as possible to the continuum solution. Then, apply the inverse Fourier Transform to obtain ψ_{long} evaluated at the grid points. In the third and last step, the forces have to be calculated and assigned back to the particles of the system. Then, grid-defined forces are obtained by differentiating the potential. Electric fields on the mesh points are interpolated back to particle locations, using the same charge assignment function (this preserves Newton's 3rd law).

The computation effort for solving PPPM scales as $O(Nlog(N))$, compared to $O(N^{3/2})$ of standard Ewald summation. To increase the accuracy of potential/force computations, one needs to either refine the mesh, or use a better weighing/interpolation scheme; both choices can be computationally expensive. Frequently, Ewald method is recommended for systems of a few hundred particles per processor or less. For larger systems the PPPM method is suggested.

Slab Geometry

Both Ewald summation and PPPM methods described above, use Fourier summation, which implicitly assume that the system under study is infinitely periodic. Alternative methods must be used to compute the long-range interactions for systems with slab geometry that are periodic in two dimensions and have a finite length in the third dimension. One of the methods proposed, is the two-dimensional Ewald summation (EW2D) introduced by Parry [Parry 1975]. This method is found to be the most accurate, but computationally very expensive. Another widely used method is to apply the conventional three-dimensional Ewald summation (EW3D) technique to a simulation cell elongated in z direction so that a sufficiently large empty space between periodic replicas in z direction is created. The inclusion of empty space into the unit cell is done to avoid an artificial influence from the periodic images in z direction. Later, Yeh and Berkowitz [Yeh 1999] modified EW3D through addition of a correction term to remove the forces due to the net dipole of the periodically repeating slabs. More recently, Arnold and Joannis [Arnold 2002, de Joannis 2002] proposed the method that constitutes a generalized "electrostatic layer correction" (ELC) which adapts any standard 3D summation method to slab-like conditions. The method employs layer correction terms to eliminate the inter-slab interaction, in addition to the correction term responsible for net dipole, all mixed with mesh-based methods. In terms of speed and accuracy, this method seems to be the best choice.

3.3.3 Thermodynamic ensembles

Standard Molecular Dynamics simulations are performed in the so-called microcanonical ensemble, in which the number of particles N, the volume V, and the total energy E of the system are kept constant. However, it is often more convenient to perform MD simulations in other ensemble like canonical ensemble (NVT) or isotherm-isobaric ensemble (NPT) at constant temperature or pressure, respectively. The temperature control might be necessary for several reasons. For example, to match experimental conditions, to study temperature-dependent processes, to enhance the efficiency of equilibration (*e.g.* , high-temperature dynamics, simulated annealing), *etc.* The pressure control can also be important, especially for simulation of large systems as polymeric membranes where a fixed volume leads to inflexible boundaries that can

be considered unphysical. Appropriate methods exist to couple the simulation box to an artificial thermostat and/or barostat. In what follows, we introduce the most used methods.

Thermostat

The simplest way to control the temperature is based on velocity rescaling [Bussi 2007]. The method consists in rescaling all velocities, so that the kinetic energy correspond to the desired temperature according to equation 3.13. The velocities are multiplied at each time step by the factor λ given by

$$\lambda^2 = \frac{T_0}{T(t)}, \tag{3.17}$$

where $T(t)$ is the instantaneous temperature and T_0 is the desired temperature.

Temperature may also be controlled using the method of weak coupling to a thermal bath proposed by Berendsen [Berendsen 1984]. In this case coupling either removes or adds energy to the system to maintain constant temperature. The velocities are scaled at each step, such that the rate of change of temperature is proportional to the difference in temperature:

$$\frac{dT}{dt} = \frac{1}{\tau}(T_0 - T), \tag{3.18}$$

where τ is the coupling parameter which determines the time interval between heat exchanges with the bath. The scaling factor λ for the velocities is

$$\lambda^2 = 1 + \frac{\delta t}{\tau}\left\{\frac{T_0}{T\left(t - \frac{\delta t}{2}\right)} - 1\right\}, \tag{3.19}$$

where δt is the time step. In the limit $\tau \to \infty$ the Berendsen thermostat is inactive and the run is sampling a microcanonical ensemble, while if τ is too small it will cause unrealistically low temperature fluctuations. If $\tau = \delta t$, Berendsen thermostat reduces to the velocity rescaling method in equation 3.18. This thermostat does not strictly fix the temperature, but leads to exponential relaxation of instantaneous temperatures to a target one. The repetitive rescaling of the particle velocities during long simulations can introduce the "flying ice cube" effect, which leads to unphysical translations and rotations of the simulated system [Harvey 1998]. Another inconvenient is that the

ensemble generated when using the Berendsen thermostat or simple rescaling velocities is not a canonical ensemble. Nevertheless, these methods are very efficient for relaxing a system to the target temperature. Once the system has reached equilibrium, it might be important to probe a correct canonical ensemble.

The canonical ensemble can be generated by using an Andersen thermostat [Andersen 1980], devised by mixing deterministic MD with stochastic collisions. In this method, the system is coupled to a heat bath via stochastic impulsive forces (collisions with the heat bath) that act occasionally on randomly selected particles. The frequency of collisions should be chosen as a result of a compromise between two factors: rare collisions do not create sufficient temperature fluctuations and the system remains close to microcanonical; exceedingly frequent collisions effectively turn Andersen scheme into velocity reassignment. It has been rigorously shown that this method corresponds to canonical ensemble. However, it is important to keep in mind that Andersen thermostat breaks the continuity of particles trajectories and does not preserve energy and momentum.

It is also possible to perform deterministic MD at constant temperature by using Nosé-Hoover [Nose 1984, Hoover 1985] thermostat based on clever use of an extended Lagrangian. The idea of this method is to consider the heat bath as an integral part of the system by using an extended Lagrangian, which contains an additional artificial coordinate (s) and velocity ($\dot{s}$), associated with a "mass" $Q > 0$. Then, the Lagrangian for the extended system is written as

$$\mathcal{L}_{NH} = \sum_{i=1}^{N} \frac{m_i}{2} s^2 \dot{\mathbf{r}}_i^2 - U(\mathbf{r}^N) + \frac{Q}{2}\dot{s}^2 - g\frac{lns}{\beta}, \tag{3.20}$$

The first two terms of the Lagrangian represent the kinetic energy minus the potential energy of the real system. The additional terms are the kinetic and potential energy associated to s, which are chosen to ensure that the algorithm evolves configurations conforming to the canonical ensemble. The parameter g is equal to the number of degrees of freedom of the system. The value of Q should be chosen carefully and determines the coupling between the bath and the real system, influencing the temperature fluctuations. Although any finite (positive) mass is acceptable, if Q is too large, the canonical distribution will only be obtained after very long simulation times, while if it is too small, it may cause high-frequency temperature oscillations.

Barostat

Many of the methods used to control pressure are analogous to those used for the constant temperature. The most common methods are the scaling algorithm of Berendsen [Berendsen 1984], which, in fact does not reproduce correct NPT ensemble, and the Nose-Hoover method, which reproduces NPT ensemble by coupling the system to an external pressure and temperature bath. The Berendsen barostat modifies the simulation box size and scales the coordinates within the system by a scale factor μ given by

$$\mu = \left[1 - \frac{k\delta t}{\tau_P}(P - P_0)\right]^{1/3}. \tag{3.21}$$

Here τ_P is the relaxation constant, δt is time step, P_0 is the desired pressure and P is the instantaneous pressure. The Nosé-Hoover barostat can be applied using an external piston as additional degree of freedom. The use of barostat can be useful for pre-equilibrating the system at some P prior to beginning an NVE or NVT simulation during which one hopes the instantaneous pressure fluctuates about the previous setpoint.

Chapter 4

The Model

Contents

4.1 Introduction

The methodology for performing Molecular Dynamics simulations used in the present work is described in this chapter. We aim to simulate the formation of ultra-thin films of hydrated Nafion (*i.e.* ionomer, water molecules and counterion) when confined by a substrate characterized by different wetting properties. Therefore, we need first to implement the model, which consists in two major steps: we determine the most appropriate representation for the interacting units and the geometry of confinement; and then we set up the force field that governs the behaviour of these constituents. Of course, it is important that the model represents the real system in the most realistic way. Therefore, it is unavoidable to perform some tests to assure the validity of the model. Also, one should be aware of the eventual limitations of the model.

Therefore, this chapter is dedicated to describe the MD model used in this work as well as the results for validating the model. In the first part we introduce the ionomer model, including the ionomer architecture and the force field parameters. Then, we report some results on the simulation of hydrated ionomer system in the bulk (membrane). We compare our data with experimental ones and other results present in the literature in order to check the validity of the model. The following section is dedicated to describe the interfacial model (ionomer films). Also, we explain the hydrophilic control parameter whose physical meaning is discussed in terms of water droplet contact angle. The reader will also find in this chapter all details of the simulations we have carried out, as well as the reason behind the choice of a few particular methodological approaches. Moreover, we discuss advantages and limitations of the model adopted.

4.2 Modelling the Nafion membrane

4.2.1 Ionomer model

The Nafion polymer, as discussed in chapter 2, is composed by a hydrophobic polytetrafluorothylene backbone ($[-CF_2 - CF_2]$) and intercalated perfluorinated side-chains, terminated by a strongly hydrophilic SO_3^- group. The model used to simulate this polymer consists of a mixed all-atoms and coarse-grained representation. A united-

atom approach is used for CF, CF_2 and CF_3 groups as single interaction centres and a fully atomistic model to describe the radical sulfonic acid (SO_3^-) in the side-chain. This mixed modelling scheme is commonly used to represent complex polymer systems. It has been shown that partial united-atom description allows us to simulate large system sizes on the long time scales of interest here, without loosing any relevant information coming from atomic details [Urata 2005]. The gain on computing cost is mainly associated to a substantial decrease of the number of charged units in the system.

The representation of a single Nafion chain adopted in our simulations is schematically illustrated in figure 4.1. The polymer backbone is formed by a linear chain of 160 bonded monomers, which corresponds to a length of approximately 24 nm. 10 side-chains were uniformly distributed along the backbone, which amounts to a separation between adjacent side chains of 16 backbone monomers. Each side-chain comprises 11 atoms and has a length of approximately 1 nm. This particular topology has been chosen in order to match an equivalent weight of Nafion $\sim$ 1143.05 g/mol of SO_3^- , a typical value of the commercial Nafion 117.

4.2.2 Force field parameters

The total interaction energy of the system is the sum of both bonded and non-bonded terms. Intramolecular bonded interactions include harmonic bonds, angles, dihedrals and improper potentials, as detailed in the section 3.2.1. The intramolecular and intermolecular non-bonded interactions are described in terms of Lennard-Jones potentials and long-range Coulombic interactions. The choice of the set of potential parameters is the tricky part of such type of modelling and a careful choice must be done. These parameters can be derived from experimental work or high-level quantum mechanical calculations that goes beyond the scope of our work.

The force field parameters of our model is based on the full-atomistic model of Venkatnathan [Venkatnathan 2007] and adapted to the united-atom representation. The partial charge and the mass of each ionomer unit were assumed to be, respectively, the sum of the charges and masses of the constituent atoms. The polymer backbone is taken to be neutral, while the sulfonic acid head groups are assumed fully ionized. In order to preserve charge neutrality, flexible hydronium ions (H_3O^+) were added

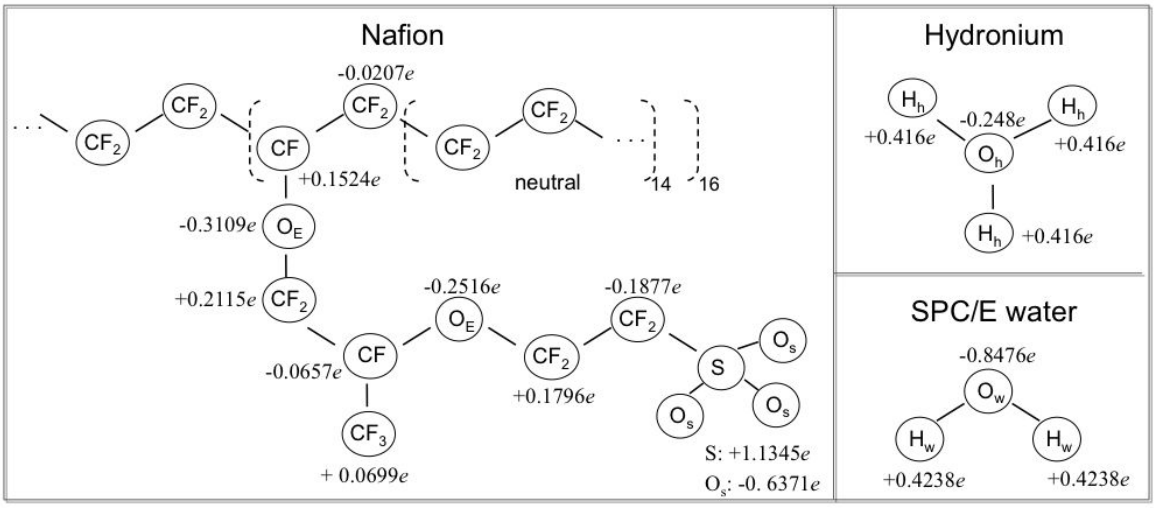

Figure 4.1: Fractional charges for ionized Nafion chain, hydronium ion and SPC/E water molecule.

in the simulation box. The force field parameters and partial charges for hydronium ions were taken from Kusaka *et al.* [Kusaka 1998] model. The water molecules were described by the rigid extended Simple Point Charge potential SPC/E of Berendsen *et al.* [Berendsen 1987]. Partial charges values of the system are shown in figure 4.1. All parameters used for the Nafion membrane, hydronium ion and water molecule are listed in tables 4.1 and 4.2 for both non-bonded and bonded interaction. The non-bonded potential takes into account interactions between pairs of atoms that are not permanently bonded to each other, either directly or via one or two intermediate bonds (1-5 interactions included). Lennard-Jones parameters for mixed interactions are obtained from the Lorentz-Berthelot mixing rules (equations 3.7b).

We remark here the main advantages of using such model. First, it assures a good computing performance by coarse-graining atomic charges. Next, it still allows a higher resolution description, at the atomic level, of particular system units that are expected to play crucial roles. For instance, with these simulations we are able to extract relevant information coming from orientation degrees of freedom of water molecules, hydronium ions and sulfonic acid groups, which can elucidate important properties of the Nafion film. Before going further with the interfacial model it is unavoidable to test the reliability of the ionomer model. Therefore, we performed several simulations of hydrated Nafion in the bulk membrane in order to check if the model is able to represent its main general features. The procedure to perform the

Bonded interaction

Bonds $U_b = k_b(r - r_0)^2$	$k_b(kcal/mol/\text{Å}^2)$	$r_o(nm)$	# of bonds
$S - O_s$	539.792	0.143	3
$CF_2 - S$	253.177	0.1770	1
$CF_n - CF_n$	309.305	0.1526	19
$CF_n - O$	318.859	0.1410	4
$O_h - H_h$ (hydronium)	553.285	0.0970	3
$O_w - H_w$ (water)	314.700	0.100	2

Angles $U_\theta = k_\theta(\theta - \theta_0)^2$	$k_\theta(kcal/mol/rad^2)$	$\theta_o(degrees)$	# of angles
$O_s - S - O_s$	74.520	119.93	3
$CF_2 - S - O_s$	66.518	108.42	3
$CF_2 - CF_2 - S$	62.339	112.00	1
$CF_n - CF_n - O_E$	57.323	109.57	4
$CF_n - O_E - CF_n$	40.007	109.50	2
$CF_n - CF_n - CF_n$ (backbone)	39.887	109.57	15
$H_h - O_h - H_h$ (hydronium)	36.567	111.65	3
$H_w - O_w - H_w$ (water)	322.75	109.47	1

Dihedrals $U_\phi = k_\phi[1 + dcos(n\phi)]$	$k_\phi(kcal/mol)$	$d = 1; n = 3$	# of dihedrals
$CF_2 - CF_2 - S - O_s$	0.69265		1
$O_E - CF_2 - CF_2 - S$	0.90761		1
$CF - O_E - CF_2 - CF_2$	0.90761		1
$CF - CF_2 - O_E - CF$	0.90761		1
$O_E - CF_2 - CF - CF_2$	0.90761		1
$CF_n - CF_n - CF_n - CF_n$ (backbone)	1.40919		17

Impropers $U_\chi = k_\chi(\chi - \chi_0)$	$k_\chi(kcal/mol/rad^2)$	$\chi_o(degrees)$	# of impropers
$O_s - S - O_s - O_s$	99.933123	35.3	1

Table 4.1: Bonded parameter sets and functional forms defining the potential energy of the ionomer/water system.

Non-bonded interaction		
Lennard-Jones $U_{LJ} = 4\varepsilon[(\sigma/r)^{12} - (\sigma/r)^{6}]$	$\varepsilon(kcal/mol)$	$\sigma(nm)$
S	0.250004	0.356362
O_s	0.210101	0.293994
CF_n	0.109468	0.340322
O_E	0.169911	0.302913
O_h (hydronium)	0.155333	0.316008
O_w (water)	0.155333	0.31666

Table 4.2: Non-bonded parameter sets and functional forms defining the potential energy of the ionomer/water system.

simulation is detailed in the next section.

4.2.3 Simulation details of Nafion membrane

Initial configurations were prepared by placing 10 polymer chains, 100 hydronium ions and N water molecules into a very large simulation box corresponding to very low mass density ($\sim 10^{-3}$ g/cm^3). N is set according to the desired water contents λ, defined by the number of water molecules per sulfonic acid group. The initial positions were determined by randomly placing the molecular center of mass inside the simulation box. In following, each molecule is rotated around its center of mass using three random rotation angle. Both single polymer chain topology, including correct positions, bonds, angles and dihedrals, and initial configurations have been generated by using an in-house developed C code. Periodic boundary conditions were imposed in all directions.

The system initially evolves in microcanonical ensemble (at constant number of particles N, volume V and energy E) with a very short integration time step ($\sim 10^{-7}$ fs) in order to avoid possible overlaps of atoms, which can amount in diverging interaction forces. Next, the system is equilibrated at constant temperature (T), using a Nose-Hoover thermostat with a relaxation time of 100 MD steps, and constant pressure (P), by using Berendsen barostat with relaxation time of 500 thousand MD steps. In the NPT ensemble, the volume of the system is allowed to isotropically fluctuate to match the desired pressure. Thus, the linear size of the cubic simulation box continuously varies in time.

The equations of motion were solved by using the Verlet scheme. The time step used for integration of the equation of motion is equal to $\delta t = 1$ fs for 300 K and 2.5 fs for 350 K. The short-range part of the Lennard-Jones and electrostatic potentials were truncated at 0.98 nm. In order to avoid the artefacts associated with truncation of electrostatic forces, the PPPM (Particle-Particle/Particle-Mesh) method was used for the calculation of the Coulomb long-range interactions (see section 3.3.2). Water molecules were treated as rigid bodies by applying the SHAKE algorithm [Ryckaert 1977], in order to keep the O-H distance fixed at $0.1nm$ and the H-O-H angle at 109.47°. The hydronium ions were considered flexible due to the limitation of computational package LAMMPS that does not accept fixing two types of molecules. The consequences of this choice in the energy conservation and in the equipartition of kinetic energy can be neglected due to the low amount of hydronium ions considered during the simulation.

Reaching thermodynamic equilibrium in very complex and big systems as those presented here often requires particular optimization tool. The system can be found in many possible equilibrium configurations, which correspond to local minima in the potential energy landscape. Increasing the temperature provides a way to overcame local energetic barriers, increasing the probability for the system to relax in a good energy minimum. This consideration is the base for simulated annealing methods, where the system is first equilibrated at a high temperature and then slowly cooled down to the desired temperature. In our case, the equilibrium was reached by performing repeated annealing in the NPT ensemble followed by very long trajectories at constant temperature. The annealing process consisted on linearly varying the temperature from 300/350 K to 800 K during a period of 0.5 ns, keep it at 800 K over additional 0.5 ns and, then, cool it down to 300/350 K over additional 0.5 ns. The annealing was repeated three times, then the barostat was removed and the system is run over additional 1 ns in the NVT ensemble.

Once the system was equilibrated at the desired temperature and at ambient pressure ($P = 1$ atm), the production runs were performed. In all cases, including annealing, equilibration and productions runs, the total simulation time was about 25 ns. Only the last 5 ns of the production trajectory were used for the analysis reported below. Snapshots of the entire system were saved for further analysis with a logarithmic time frequency. MD simulations were carried out using the software package LAMMPS (Large-scale Atomic/Molecular Massively Parallel Simulator), designed

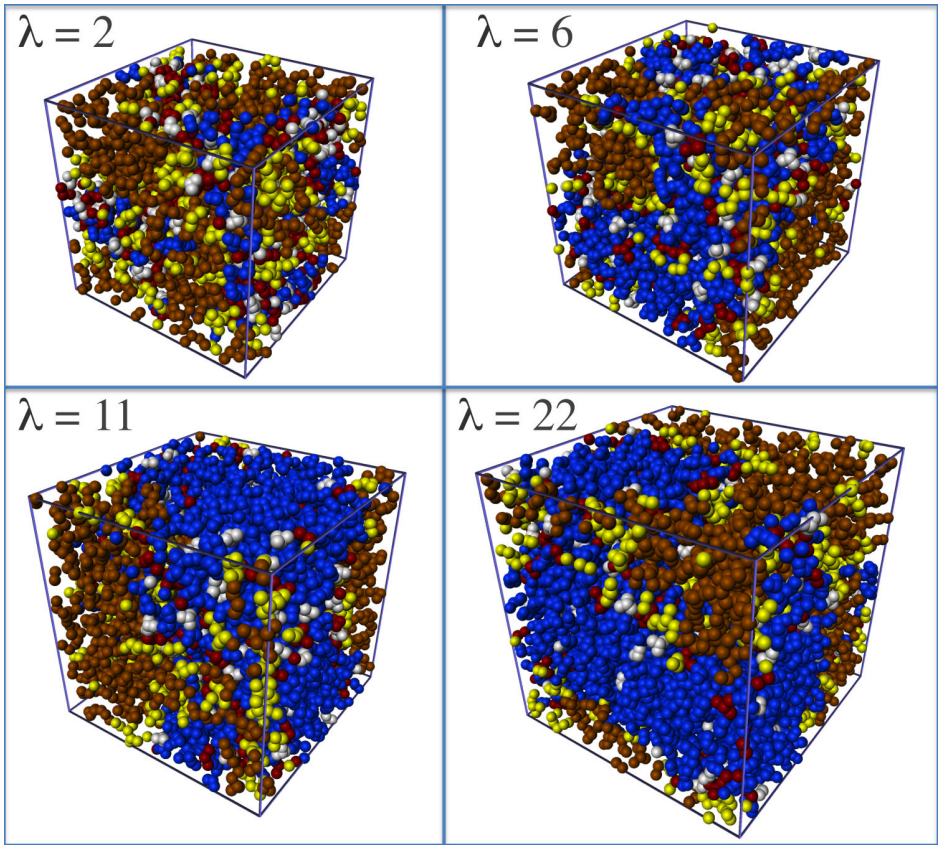

Figure 4.2: Snapshots of hydrated Nafion membrane at $T = 350$ K for different water content; The side-chain beads are shown in yellow, water molecules are in blue, hydronium ions in white, and Nafion backbones in brown

to run on parallel machines using MPI for parallel communication [Plimpton 1995].

4.3 Structure and dynamics of Nafion membrane

In this section, we examine the structure and dynamics of Nafion at different hydration levels in order to validate the ionomer model described in section 4.2. The equilibrated structures of hydrated Nafion have been characterized in terms of hydrophilic/hydrophobic phase segregation, mass density, radial distribution functions, and water molecules and hydronium ions self-diffusion. Our results were compared with available experimental work and computer simulation results.

4.3.1 Membrane structure

In figure 4.2 we show typical snapshots of hydrated Nafion equilibrated at $T = 350$ K for $\lambda = 2, 6, 11$ and 22. These snapshots confirm the general picture of heterogeneous Nafion morphology with well-defined phase separation of hydrophobic and hydrophilic domains. We can note that side-chains (yellow beads) are located at interfaces between backbone chains (brown beads) and water and hydronium ions (blue and white beads). The side-chains delimit the boundaries between the phases, which appear more evident at higher values of λ. The size of simulation box ($\sim$ 4-5 nm) is not large enough to characterize the geometrical shape and size of these hydrophilic and hydrophobic domains at larger length scales, as well as the connectivity between the hydrophilic clusters. However, it is evident that the shape and connectivity of both domains strongly depend on water content in agreement with mesoscale calculations found in the literature [Wescott 2006, Malek 2008].

In table 4.3 we report the polymer backbone mass densities obtained from the simulation at 300 and 350 K. The density gradually decreases while λ increases. This can be assigned to structural relaxation with increasing hydration, leading to a swelling of the membrane, which is more pronounced at high temperatures. The calculated densities are in a good agreement with the experimental values if one considers backbone masses only. The lack of accuracy on the total polymer density could be due to the fact that in this type of MD model the polymer chain has to be more flexible than in reality because of the limitation on the size of the simulation box. Nevertheless, we are convinced that the model is able to predict local structure of Nafion as it will be shown in the following.

Mass Density (g/cm^3)		
water contents (λ)	density ($T = 300$ K)	density ($T = 350$ K)
2	2.24	2.14
4	2.03	1.97
6	1.87	1.80
11	1.53	1.48
20	1.16	1.11
22	1.09	1.06

Table 4.3: Backbone mass density at different water contents and temperatures $T = 300$ K and 350 K.

In order to quantify the structure of hydrated Nafion, we have calculated the radial distribution function (RDF), also called pair correlation function. This quantity allows us to extract information about the local organization of the system. It is defined as being the relative probability of finding two particles at a distance r. It is determined by the equation:

$$g_{\alpha\beta}(r) = \frac{L^d}{F(r,d)N_\alpha N_\beta} \sum_{i\varepsilon|\alpha|} \sum_{j\varepsilon|\beta|} \langle \delta(r - r_{ij}) \rangle \,, \tag{4.1}$$

where N_α and N_β are the number of particles of type α and β respectively, d is the dimension of the space ($d = 1$, 2 or 3). $F(r,d)$ is the normalization factor defined as $F(r,1) = 2$, $F(r,2) = 2\pi r$ and $F(r,3) = 4\pi r^2$. At large values of r, $g_{\alpha\beta}(r)$ goes to 1, which means uniform probability (uniform distribution of particles). Values that differ from 1.0 indicate an enhanced or suppressed probability relative to a uniform distribution.

The $g_{\alpha\beta}(r)$ between different pairs, α and β, in hydrated ionomer at $T = 350$ K are shown in figure 4.3. The results at $T = 300$ K are qualitatively very similar. In figure 4.3.(a) and (b) we show $g_{SO_w}(r)$ and $g_{SO_h}(r)$ at indicated values of λ, which correspond to RDFs between the sulphur atom of the SO_3^- group and the oxygen atom of the H_2O and H_3O^+ , respectively. In both RDFs, the first peak occurs around 0.37 nm and this position does not depend on λ. This distance corresponds to the shortest distance between SO_3^- and the solvent molecule. The intensity of the first peak in $g_{SO_h}(r)$ is much higher than in $g_{SO_w}(r)$. Indeed, H_3O^+ are strongly correlated to SO_3^- , which means that H_3O^+ are mostly found close to sulphur atoms. This is attributed to the strong electrostatic interaction between the positively charged H_3O^+ and negatively charged sulfonate oxygen.

The intensity of the first peak in $g_{SO_h}(r)$ decreases by increasing λ. This indicates that fewer hydronium ions reside in the vicinity of the sulfonate groups when the membrane is well hydrated. In contrast, the number of water molecules around the sulfonate group should increase with the water content. At first glance, figure 4.3.(a) shows opposite trends (the magnitude of the peak decreases with increase water contents). One should consider that these magnitudes in part reflect the fact that RDF is normalized by the average water density, which changes with water content. One way to avoid wrong interpretation is to compute the first coordination number ($n_{\alpha\beta}$),

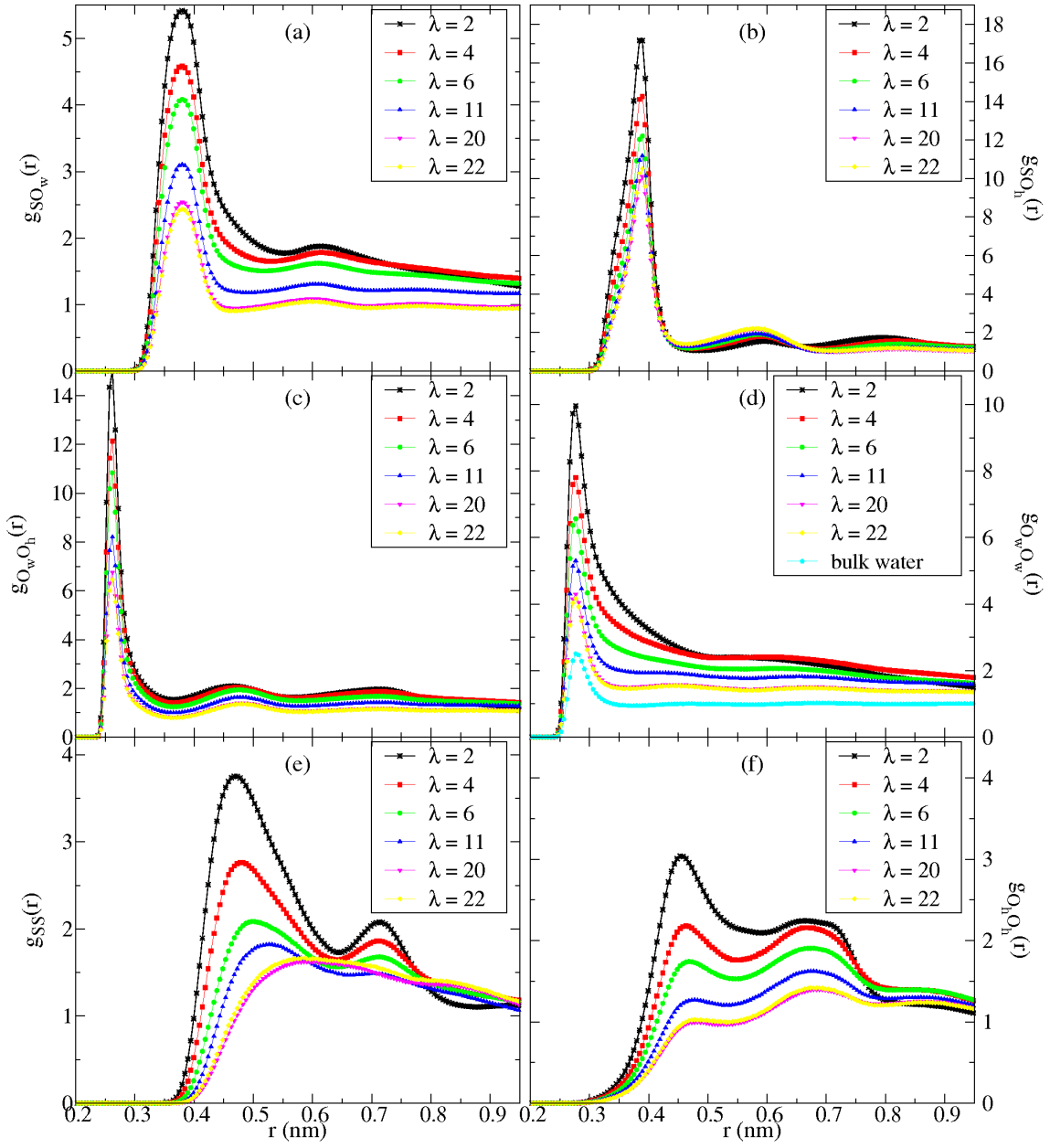

Figure 4.3: Radial distribution functions of different pairs in Nafion membrane at temperature $T = 350$ K and water content λ. S: sulphur of SO_3^- ; O_w: oxygen of H_2O ; O_h: oxygen of H_3O^+ ;

which is the average number of molecules of type β in the first interaction shell of molecules of type α. It is computed by the integral of radial distribution function,

$$n_{\alpha\beta} = 4\pi \int_0^{R_c} r^2 g_{\alpha\beta}(r)\rho \, \mathrm{d}r, \tag{4.2}$$

where $\rho = N_\beta/V$ is the number density. The limit of the integration R_c corresponds to the position of the first minimum in $g_{\alpha\beta}(r)$.

The table 4.4 show the first coordination numbers for different interacting pairs. These data confirm the augmentation of water molecules surrounding sulfonate groups with increasing water contents. In contrast the number of H_3O^+ increases to almost 3 ions per sulfonate groups at $\lambda = 2$, which means that H_3O^+ is shared by several sulfonic acids. These coordination numbers are slightly higher than those reported by Venkatnathan *et al.* [Venkatnathan 2007], which is consistent with higher mass densities obtained from our model.

In figure 4.3.(c) and (d) we show $g_{O_hO_w}(r)$ and $g_{O_wO_w}(r)$ corresponding to RDF between oxygen atoms of water-hydronium and water-water, respectively. Both RDFs show a first peak at 0.26 nm, which is related to the oxygen-oxygen distance in the first solvation shell. The $g_{O_hO_w}(r)$ shows strong correlation between water and hydronium. The number of H_2O surrounding H_3O^+ increases from 1.75 for $\lambda = 2$ to 4.42 for $\lambda = 22$. The $g_{O_wO_w}(r)$ exhibits similar trends. The coordination number of water molecules around each water molecule in the first solvation shell augments from 2.26 for $\lambda = 2$ to 4.64 for $\lambda = 22$. With increasing hydration level, the water molecules behave close to the bulk water molecules ($n^{bulk}_{O_wO_w} = 5.34$). This general features are similar to those previously observed in other publications [Devanathan 2007b, Venkatnathan 2007].

In figure 4.3.(e) and (f) we show the sulphur-sulphur and hydronium-hydronium RDFs respectively. The structure of $g_{OhOh}(r)$ is clearly governed by $g_{SS}(r)$. The first peak corresponds to the minimum distance between sulphur atoms. With increasing hydration, the first peak shifts from 0.47 nm for $\lambda = 2$ to 0.62 nm for $\lambda = 22$. When these values are compared with the distance between SO_3^- for the extended polymer chains ($\sim$ 2.2 nm), it makes evident that equilibrated hydrated Nafion chains agglomerate to form ionic clusters despite of electrostatic repulsion between SO_3^- groups. With increasing λ, the number of sulphur around each sulphur atom decreases from 3.67 to 0.94. This means that the sulfonate groups move away from each other, while water molecules move close to them. The trends in $g_{SS}(r)$ agree very well with Devanathan *et al.* [Devanathan 2007a].

Similar behaviour were found at lower temperature (T = 300 K) as shown in table 4.4. Finally, our model is in good agreement with other models found in the literature [Devanathan 2007a, Cui 2007, Venkatnathan 2007]. The slight differences

Coordination Number

water contents (λ)	$T = 300K$					$T = 350K$				
	n_{SO_w}	n_{SO_h}	$n_{O_hO_w}$	$n_{O_wO_w}$	n_{SS}	n_{SO_w}	n_{SO_h}	$n_{O_hO_w}$	$n_{O_wO_w}$	n_{SS}
2	3.16	2.96	1.74	2.56	3.75	3.23	2.99	1.75	2.26	3.67
4	4.81	2.31	2.63	3.52	2.74	4.90	2.28	2.74	3.27	2.69
6	5.52	1.93	3.17	3.98	2.37	5.81	1.78	3.33	3.63	1.99
11	6.57	1.35	3.90	4.35	1.52	6.57	1.33	3.90	4.28	1.45
20	7.29	0.83	4.50	4.66	1.01	7.13	0.93	4.39	4.55	0.95
22	7.21	0.95	4.38	4.79	1.09	7.17	0.92	4.42	4.64	0.94
SPC/E				5.36				5.34		

Table 4.4: First shell coordination numbers in the membrane at 300 K and 350 K. The R_c used where 0.45 nm for sulphur-water, 0.35 nm for water-water and water-hydronium and 0.64 nm for sulphur-sulphur, corresponding to different water contents λ.

in density and coordination numbers can be attributed to the coarse graining of the monomer of backbone chain. These differences do not have significant consequences on our results, which are therefore consistent and well describe the general local features in Nafion membrane.

4.3.2 Water and hydronium dynamics

In this section we show that the model can also provide interesting results on the dynamics of the water molecules and hydronium ions. First we have calculated the mean square displacement (MSD) that contains the information on molecular diffusivity. The MSD is a measure of the average distance a molecule travels in a given time interval. It is defined as,

$$\langle r^2(t)\rangle = \frac{1}{N}\sum_{i=1}^{N} |\vec{r_i}(t) - \vec{r_i}(0)|^2, \tag{4.3}$$

where $\vec{r_i}(t)$ is the position vector and $\langle ...\rangle$ denotes the average over all molecules and all configurations of the full trajectory as starting points. Figure 4.4 shows the MSD of water molecules at temperatures T = 300 K and 350 K. This function increases as a quadratic function for very small values of t. Indeed, in a sufficient short time interval the molecules behave as free particles, making the mean square displacement proportional to the square of time (t^2). Beyond this time, the motion of particle i is

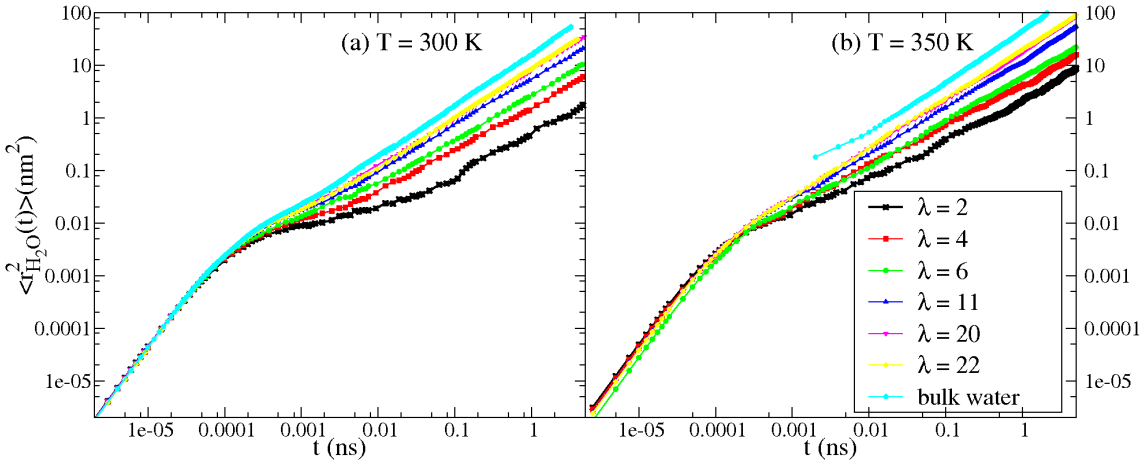

Figure 4.4: Mean squared displacement of water molecules at (a) $T = 300$ K and (b) 350 K

continuously impeded due to collisions with other molecules, thus the MSD increases only linearly with time. The rate of linear growth is related to molecular diffusion. Therefore, we can extract from MSD the self-diffusion coefficient D, which is defined by the Einstein relation,

$$D = \lim_{t\to\infty} \frac{1}{2dt} \langle r^2() \rangle, \tag{4.4}$$

where t is the time and d is the dimensionality of the system. In order to compute D, we performed a linear fit to the data in the region of a selected time interval. The interval is chosen in order to avoid the final part of MSD, where averages are calculated only over few uncorrelated system snapshots, and the initial rapidly increasing part. We therefore selected an interval of 2 ns in the middle of MSD curves.

In table 4.5, we show the values for the self-diffusion coefficient of water molecules and hydronium ions computed at different water contents and temperatures. The effects of membrane hydration and temperature are evident in figure 4.5. The water and hydronium diffusion clearly increase with water content and temperature. The water diffusion coefficient is significantly lower than in bulk water, due to confinement effects caused by the presence of the ionomer. When the membrane is highly hydrated the diffusion of water should indeed approach the diffusion of pure liquid water. The hydronium diffusion coefficient shows the same trends, and its value is about 3 times lower than the water diffusion coefficient. Our results are consistent and the diffu-

Diffusion Coefficient - D ($\times 10^{-5} cm^2/s$)				
	$T = 300K$		$T = 350K$	
water contents (λ)	D_{H_2O}	$D_{H_3O^+}$	D_{H_2O}	$D_{H_3O^+}$
2	0.05 ± 0.007	0.01 ± 0.001	0.28 ± 0.011	0.04 ± 0.005
4	0.21 ± 0.009	0.04 ± 0.005	0.54 ± 0.006	0.13 ± 0.007
6	0.36 ± 0.018	0.10 ± 0.014	0.80 ± 0.020	0.24 ± 0.016
11	0.75 ± 0.010	0.23 ± 0.021	1.81 ± 0.015	0.62 ± 0.013
20	1.21 ± 0.006	0.41 ± 0.024	2.87 ± 0.013	1.07 ± 0.028
22	1.34 ± 0.014	0.42 ± 0.032	2.94 ± 0.008	1.22 ± 0.020
SPC/E bulk	2.78 ± 0.002		7.88 ± 0.086	

Table 4.5: Self-diffusion coefficients for water and hydronium at temperatures $T = 300$ K and 350 K. *Good agreement with the values published by Mark *et al.* of 2.7(0.12)[Mark 2001]

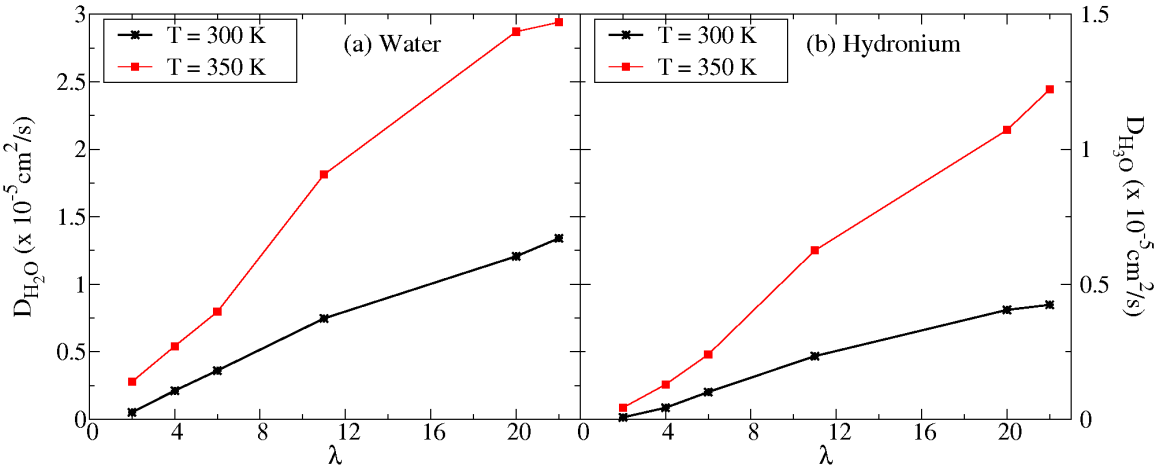

Figure 4.5: Self-diffusion coefficient of (a) water molecules and (b) hydronium ions as function of λ, at temperatures $T = 300$ K and 350 K

sion coefficients are found within the range reported in the review by Kreuer *et al.* [Kreuer 2004].

The computed diffusion coefficients of hydronium ions are substantially different from the proton diffusion measured by experimentalists. Since the model for hydronium ions does not include the transfer of protons between the hydronium ions and the water molecules (which has quantum mechanical origin), the diffusion coefficient for hydronium does not include the Grotthus mechanism but only vehicular diffusivity. Without the structural diffusion effect, the hydronium diffusion is significantly lower than that of water molecules. This is expected because of the strong electrostatic in-

teraction with the SO_3^- , which tends to bind the hydronium complexes, slowing down the diffusion of the ion.

4.4 Modelling the ionomer film in contact with hydrophobic/philic surface

4.4.1 Interfacial model

In the previous section we have shown that the model for representing ionomer, water molecules and hydronium ions, were found to be satisfactory for the representation of a real Nafion system. Next step consists in simulating this system when confined by any substrate characterized by different wetting properties. The hydrophobic or hydrophilic character of a surface is related to the microscopic principles, such as structure and polarity. One way to virtually control the surface hydrophobicity is modifying the surface polarity by rescaling partial atomic charges of the surface [Giovambattista 2007, Castrillón 2009]. In a simpler way, it has been shown that changing the covalent interactions between water molecules and the atoms of the surface is enough to modify wetting behaviour [Nijmeijer 1990].

Considering the complexity of our system, we needed a simple model that allows reducing computational cost without losing general wetting behaviour features. Therefore, the approach to mimic hydrophobic and hydrophilic surfaces does not take into account neither structure nor polarity of the surface. Instead, the substrate consists of an infinite flat and non-structured wall, and the interactions between system units and the wall are described via mean-field approach. This strategy has already been successfully applied in studies of molecular liquids at interfaces, like pure water in contact with perfectly smooth walls [Scheidler 2002, Spohr 1988].

Therefore, the interaction potential between the system unit and the wall was described by the 9-3 Lennard-Jones potential,

$$U_{LJ}^{93} = \varepsilon_{wall}\left[\frac{5}{12}\left(\frac{\sigma_{wall}}{z}\right)^9 - \left(\frac{\sigma_{wall}}{z}\right)^3\right]. \tag{4.5}$$

Here, z is the distance of the interacting unit from the wall and ε_{wall} and σ_{wall} are the potential parameters, to be properly tuned. The interaction potential depends only

on the distance z from the wall. U_{LJ}^{93} is derived by integrating over a 3D half-lattice of 12-6 Lennard-Jones particles [Abraham 1977]. It has, therefore, a repulsive part, where the distance of repulsion is controlled by σ_{wall}, and an attractive part, where the strength of attraction is controlled by ε_{wall} (see figure 4.6).

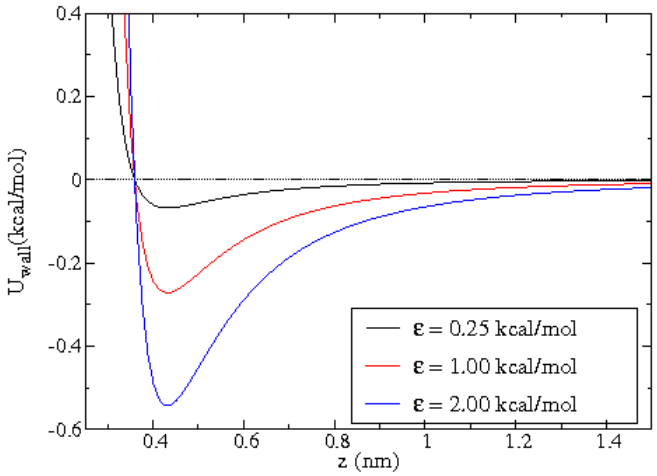

Figure 4.6: 9-3 Lennard-Jones potential function for different values of ε_{wall}, keeping $\sigma_{wall} = 0.32$ nm

In order to simulate the different wetting character, the wall affinity with water is easily controlled by changing the attraction strength via the energy parameter ε_{wall}. Of course, the interactions are not the same for all system units. Therefore, we define two types of interacting unit: hydrophilic, which includes oxygen atoms of H_2O , SO_3^- and H_3O^+ ; and hydrophobic, including the polymer beads excepted SO_3^- groups. Both unit types interact with the wall via the potential described by equation 4.5, but considering ε_{philic} and ε_{phobic} different. The hydrophobic interaction was fixed at $\varepsilon_{phobic} = 0.5$ kcal/mol, while ε_{philic} is systematically varied in the range 0.125 to 2.0 kcal/mol. The value of ε_{phobic} is the same order of magnitude as the typical interaction energy of polymer units and carbon sheet. For both unit types, the length scale σ_{wall} is fixed to 0.32 nm and the cutoff radius is equal to 1.5 nm. The value of σ_{wall} corresponds to the typical interaction size used for polymer units.

The reason behind our approach relies on the fact that the energy balance between water/wall and water/ionomer interaction should mostly control main features of Nafion thin-films. Therefore, we investigated the system only by changing water/wall interaction, while keeping the ionomer/wall interaction the same. Moreover,

a simple chemical adsorption can affect the surface polarity, and ultimately the affinity with water [Mashio 2010, Giovambattista 2007]. The polarity changes do not affect the interaction with the (apolar) backbone monomers at the same way as they affect interaction with water molecules. This supports the idea that changing the hydrophilicity of surface does not necessarily imply significant changes on ionomer backbone/surface interaction, which justifies keeping the same ε_{phobic} in our simulations. In what follows, we will show that the model indeed predict different water wetting behaviour. Moreover, we quantify the hydrophobic/hydrophilic character in terms of water droplet contact angles.

4.4.2 Surface hydrophilicity characterization through the water droplet contact angle

The hydrophobic or hydrophilic character of any surface can be characterized by studying the wetting phenomena occurring when a water droplet is gently deposited on the surface. In our model, the wetting behaviour should depend on the interaction parameters values ε_{philic}, described in equation 4.5. In order to associate a physical meaning to the adopted choice for ε_{philic}, we have performed MD simulations of water droplets in order to calculated the contact angle θ formed by these droplets. θ is defined as the angle formed between the wall and the tangent of the drop. By convention, the angle increases by decreasing hydrophilicity. It means that very hydrophilic surface, the drop spreads completely and $\theta \to 0$.

In order to trace the relation of liquid contact angle with ε_{philic}, a series of Molecular Dynamics simulations of water droplets on the surface were performed. In total of 3500 water molecules placed inside a huge volume of dimensions $20 \times 20 \times 20$ nm^3 were initially equilibrated at NVT ensemble by using canonical velocity-rescaling thermostat. A liquid water spherical cluster is formed at temperature $T = 300$ K. After equilibration the cluster was put in contact with the one 9-3 LJ wall. The whole system is shifted to have the wall placed at $z = 0.0$. Periodic boundary conditions were used only in xy directions. The simulation box size is large enough in order to prevent interactions with particles of image boxes. The same initial configuration is used in all simulations. The simulations were carried out for 2 ns with an integration time step of 1 fs.

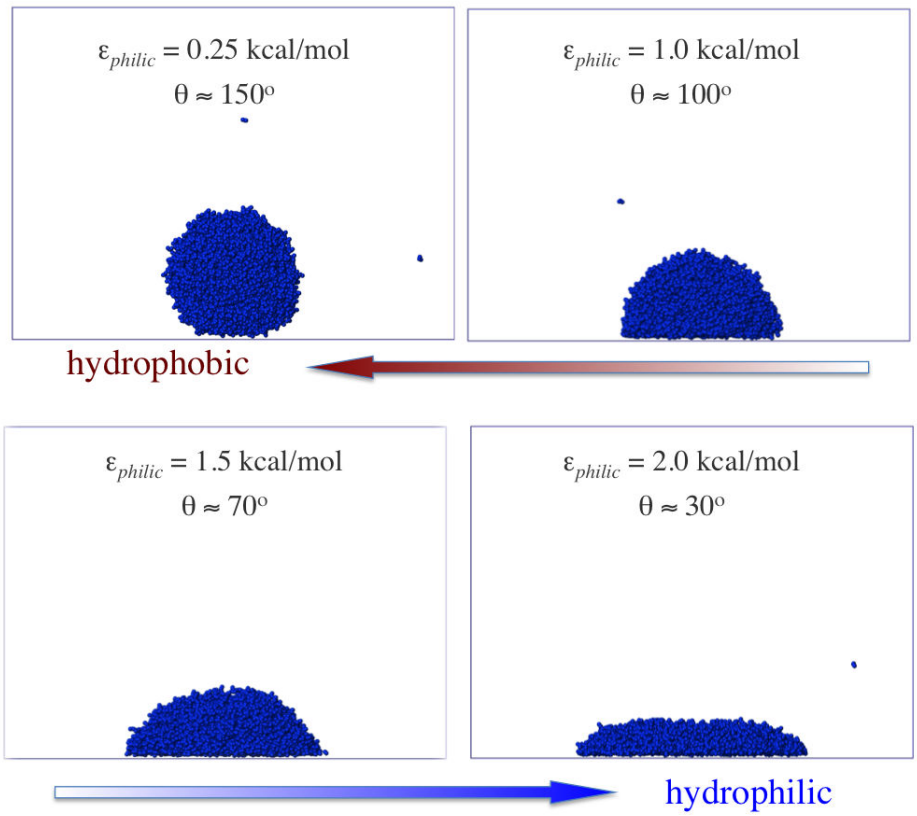

Figure 4.7: Snapshot: Molecular Dynamics simulations of 3500 water molecules placed on 9-3 LJ wall with different values of ε_{philic}. The associated water contact angles are indicated by θ.

Figure 4.7 shows the snapshots of equilibrated water droplets for 4 different values of ε_{philic} (0.25, 1.0, 1.5 and 2.0 kcal/mol). The snapshots clearly show the growth of wetting behaviour when increasing ε_{philic}. The transition from hydrophobic to hydrophilic surfaces is evident. Thus, we have estimated the contact angle by directly fitting the contour shape of the droplet. The contour is defined by the droplet profile, which is computed via the following procedure [Shi 2009, Werder 2003]: we introduce a cylindrical binning with the base on the wall and the axis passing through the droplet center of mass. The bins have a height of 0.5 nm separated vertically by 0.2 nm. For each bin, we calculate the horizontal mass density profile, that is the density in the slab as a function of the drop radius parallel to the wall. For each bin we associate a drop radius (drop boundaries), r_{drop}, given by the distance at which the horizontal density profile falls to 0.2 g/cm^3. The droplet profiles for different values of

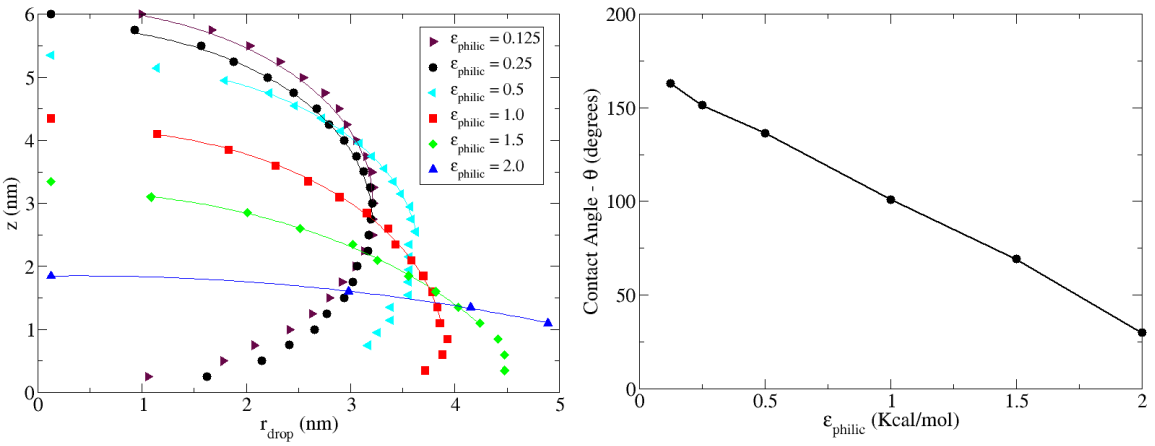

Figure 4.8: (a) Water droplet profiles for each case indicated by the parameter ε_{philic}. (b) Contact angles extracted from droplet profile via fitting method to a circular function. The contact angle varies linearly with ε_{philic}.

ε_{philic} are displayed in figure 4.8.

ε_{philic} (kcal/mol)	contact angle - θ (degrees)
0.125	163.02°
0.25	151.31°
0.5	136.34°
1.0	100.94°
1.5	69.09°
2.0	29.74°

Table 4.6: Water droplet contact angle for indicated values of ε_{philic}

To obtain the water contact angle from the drop profiles from figure 4.8, we assume that the curve forms a segment of a circumference or the droplet itself forms a partial sphere. Thus, a circular best fit through these points is extrapolated to the wall surface where the contact angle θ is measured. We compute θ for each value of ε_{philic}. Figure 4.8.(b) shows linear dependence of the contact angle with ε_{philic}. The precise values of θ are reported in table 4.6.

The plots in figure 4.8 prove that it is possible to change continuously from hydrophobic to hydrophilic wall only by increasing the energy interaction ε_{philic}. The associated contact angle to the ε_{philic} displayed in table 4.6 will be often referred during this manuscript. These values can, in principle, be compared to the literature in order

to find the type of material that better corresponds to the wall under consideration. For example, computer simulations of water droplet on a platinum surface shows a contact angle around 20-30° [Shi 2009]. In the case of carbon nanotubes the contact angle varies from 100 to 106°, while the carbon graphite varies from 110 to 115°, depending on the flexibility of the surface atoms [Werder 2003, Werder 2001]. For simulating Nafion films, we have chosen 4 values of θ, which correspond to the values showed in figure 4.7. In the following, we give details of the simulation procedures adopted.

4.4.3 Simulation details of Nafion film

Initial configurations were prepared by placing Nafion ionomer, hydronium ions, and water molecules on top of infinite non-structured 9-3 Lennard-Jones wall (9-3 LJ). The system is formed by 20 polymers chains, 200 hydronium ions and water molecules set according to the desired water content λ. The simulation box is schematically represented in figure 4.9. The lateral dimension has been fixed in order to generate a film of thickness $\delta z \sim 4 - 5$ nm at ambient pressure. Thus, for the considered water contents $\lambda = 6, 11$ and 22, we found $L_x = L_y = 6$, 6,8 and 8 nm, respectively. Periodic boundary conditions were imposed only in the plane containing the wall, while open boundaries were kept in the normal direction with the $L_z = 10$ nm. Adapted techniques have been used to properly evaluate long-range interactions in this anisotropic slab geometry [Yeh 1999], as discussed in section 3.3.2. A "mirror" wall is placed on the top of the simulation box to avoid molecules to escape from the box. Therefore, molecules attempting to cross the top of simulation box interact with the "mirror", which has the effect of reversing the sign of the z component of the molecule velocity.

The simulation was started from a random configuration and performed MD runs at NVE ensemble with very tiny timestep. The random configuration was generated by randomly placing the molecular center of mass close to the LJ wall. In following, each molecule is rotated around its center of mass using three random rotation angle. The initial velocities were created following a Gaussian distribution to produce the requested temperature. Thereafter, at NVT ensemble, the system were heated up at 500K over a period of 0.5 ns, followed by a quenching to 350 K. This procedure was repeated three times, always using Nose-Hoover thermostat with relaxation time equal

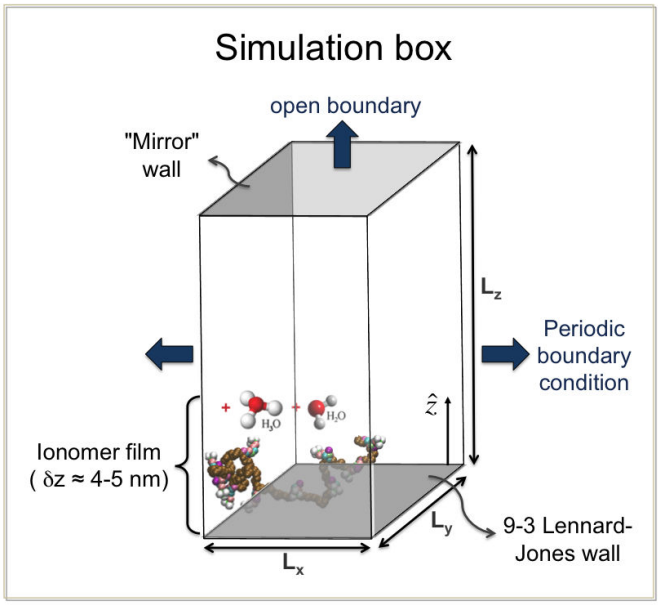

Figure 4.9: Scheme of simulation box used to simulate ionomer film

1.0 ps. During the heating, the system tends to be mixed over the 9-3 LJ wall. Only after quenching, the interaction with the wall pulls down the system. To avoid any effect from the mirror on the top of the box, the velocities were reset after quenching process. During the production run of 5 ns, equilibrated configurations were saved every 5 ps and used for the analysis.

4.5 Conclusions

In this chapter we have developed the model to mimic the ionomer film in contact with flat smooth surfaces (wall). We have explored the behaviour of a mixed united-atoms and all-atoms model for the ionomer, while the interaction with the surface has been described at the mean-field level. This model allows us to consider an integrated interaction, which only depends on the distance of the concerned unit from the wall, with a consequent significant decrease of computing time. The wall is supposed to mimic surfaces composed by different materials and consequently having different hydrophobic/hydrophilic characters. We have shown that it is possible to control the hydrophobic/hydrophilic character of the wall based on energy 9-3 LJ parameter only, with no reference to any particular chemical composition of the wall.

A precise physical meaning of interaction energy parameter was associated in terms of a well-defined contact angle. In conclusion, the main reason to use the above interfacial model is that we believe that the main features of ionomer thin films should ultimately be controlled by the global wetting properties of the surface. We are convinced our approach is a good choice to investigate general physical processes of ionomer films, preserving a significant degree of generality.

Chapter 5

Analysis of the structure of Nafion ultra-thin films

Contents

5.1 Introduction

A better understanding of the formation of Nafion ultra-thin films in contact with hydrophilic or hydrophobic surfaces is the main purpose of this chapter. In order to explore this issue, we consider the model discussed in the previous chapter, which allows us to switch continuously the hydrophilic/phobic character of the surface. Here, the surface is a perfectly flat wall characterized only by their global wetting properties through the measurement of the water droplet contact angle θ. In the context of PEMFC, we assume that these surfaces can mimic any type of substrate found inside the catalyst layer. For example, these surfaces could be related to the graphitized carbon sheet ($\theta \approx 110 - 115°$) [Werder 2003] used as catalyst support material as being one of hydrophobic cases while the Pt catalyst surface ($\theta \approx 20 - 30°$) [Shi 2009] as being the most hydrophilic. Moreover, a few studies have shown that graphitized carbon sheet functionalized with carboxyl or carbylate groups enhance the capacity of wetting the surface [Mashio 2010]. Also, the addition of organic solvent can enhance hydrophobicity of catalyst layer materials [Chun 1998].

In short, this chapter is dedicated to explore the self-assembly and nanostructure formation of the realistic model for the Nafion ionomer when deposited on hydrophobic or hydrophilic surfaces, under different hydration conditions. We have performed molecular dynamics simulations of 12 different cases, including 4 types of surfaces and 3 hydration levels. The films were always prepared as explained in section 4.4.1. All computed data in this chapter were obtained by averaging on 1000 configurations sampled on 5 ns trajectories. Snapshots of the system taken along the trajectory were analysed for each case in a number of different ways. Observables evaluated in this chapter include mass density distributions, radial distribution functions, ionic cluster sizes, water domain connectivity and ionomer orientation. Moreover, we discuss the adsorption of different species, including surface coverage and train fraction, followed by speculation of their impacts on the electrochemical processes at the vicinity of the catalyst surface. Finally, the film/vapour interface is characterized by measuring the surface roughness and surface hydrophobicity.

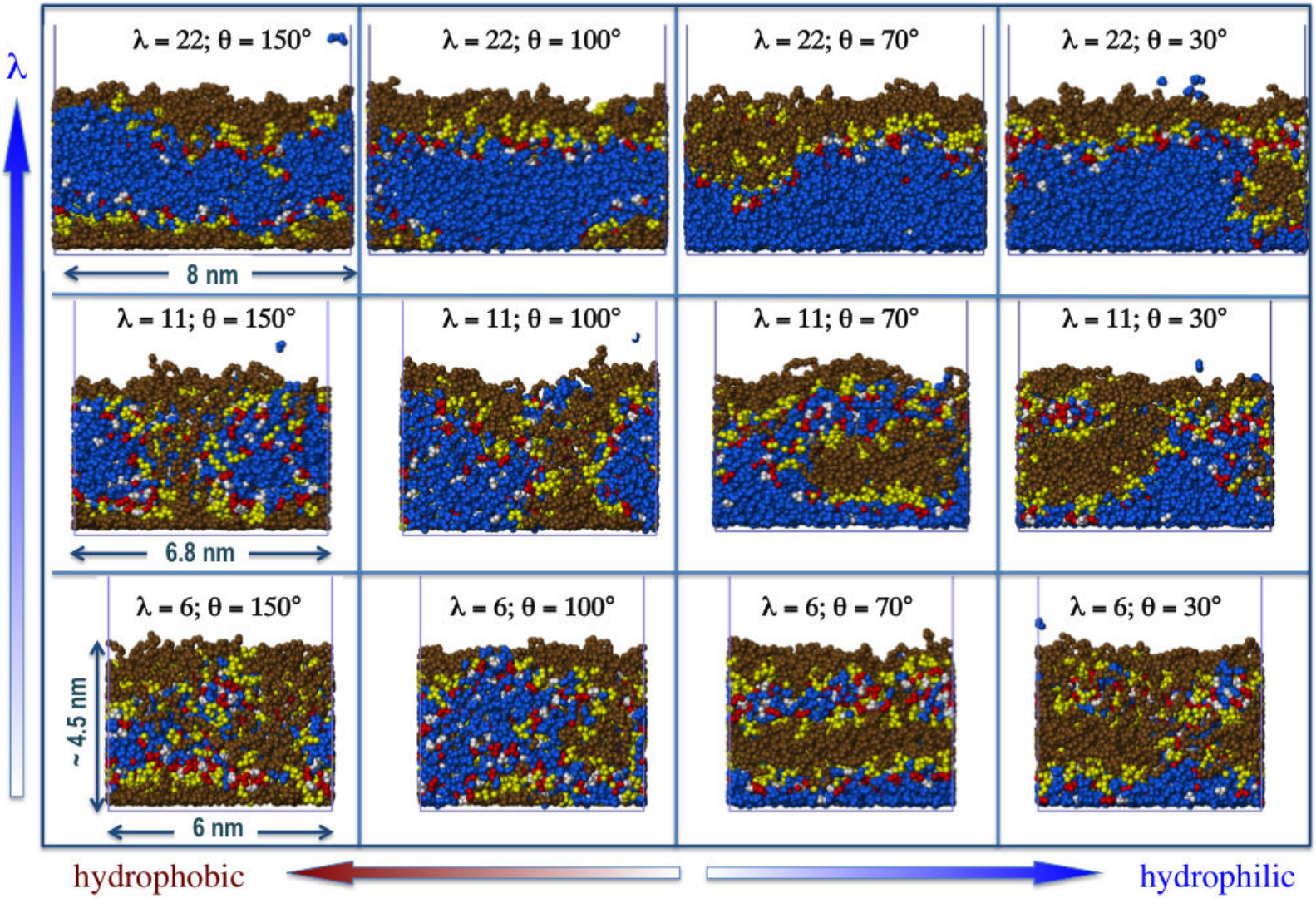

Figure 5.1: Lateral views of the equilibrated configuration of Nafion thin-films hydrated with $\lambda = 22$, 11 and 6, formed on surfaces with characteristic ranging from very hydrophobic ($\theta \approx 150°$) to very hydrophilic ($\theta \approx 30°$). The backbones beads are shown in brown, side-chains beads in yellow, SO_3^- in red, water molecules in blue and hydronium ions in white.

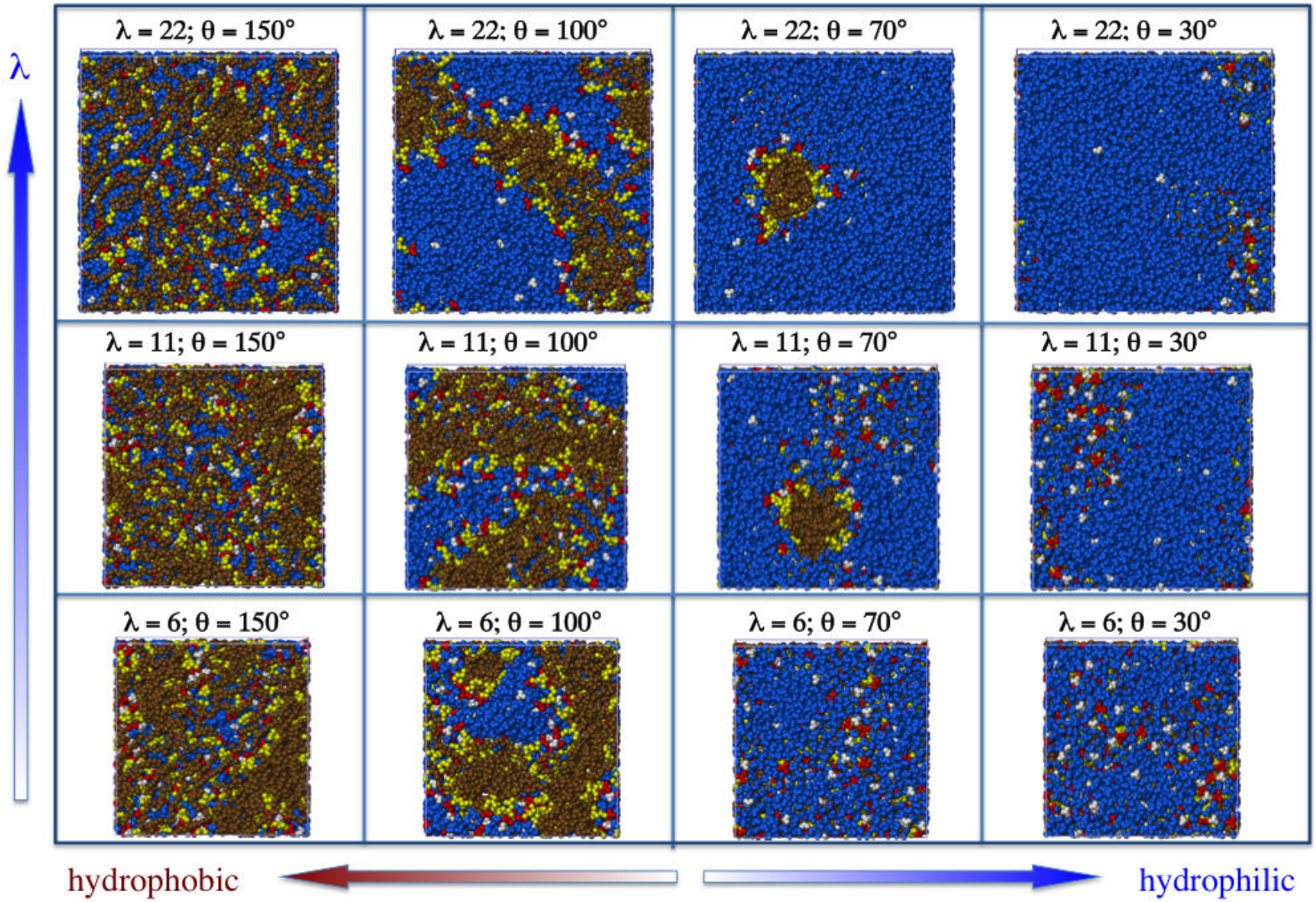

Figure 5.2: Bottom views of the equilibrated configuration of Nafion thin-films hydrated with $\lambda = 22$, 11 and 6, formed on surfaces with characteristic ranging from very hydrophobic ($\theta \approx 150°$) to very hydrophilic ($\theta \approx 30°$). The backbones beads are shown in brown, side-chains beads in yellow, SO_3^- in red, water molecules in blue and hydronium ions in white.

5.2 Morphology of the Ionomer thin-film

In figure 5.1 and 5.2 we show lateral and bottom views respectively of the equilibrated configuration of Nafion-films when deposited on hydrophobic and hydrophilic wall, under different hydration level. The snapshots at different hydration level correspond to the water contents $\lambda = 22$, 11 and 6. The hydrophilicity/hydrophobicity of each wall is identified by the contact angle introduced in the previous chapter. Four types of substrates have been studied: a) very hydrophobic, with a contact angle $\theta \approx 150°$; b) intermediate ($\theta \approx 100°$); c) hydrophilic ($\theta \approx 70°$); and d) strongly hydrophilic, corresponding to $\theta \approx 30°$. The contact angles correspond to interaction energy $\varepsilon_{philic} = 0.25$, 1.0, 1.5 and 2.0 kcal/mol respectively, as detailed in table 4.6. The thickness of all films is about $4.5 - 5$ nm, and the xy plane sizes depend on the water contents as shown in the figure. We choose to have different simulation box sizes in order to maintain approximately the same thickness for all films simulated.

These snapshots confirm, at first look, that the hydrophilicity of the substrate changes the general morphology of the film. It is evident that the distribution of water (blue beads) within the film, changes for each case of θ and λ. More details of the structure of every film will be discussed in this section.

5.2.1 Mass density distributions

The structure of the ionomer film is first analysed in terms of the mass density profiles along the z direction perpendicular to the wall. In figure 5.3 we show the polymer mass density distributions $\rho_{poly}(z)$ in the first column and the water mass density distributions $\rho_w(z)$ in the second column, computed for each film displayed in figure 5.1. These curves clearly show changes on the distribution of water and polymer impacted by the wall hydrophilicity θ. Also, the contrasting behaviour of $\rho_{poly}(z)$ and $\rho_w(z)$ is evident, *i.e.* the polymer density in contact with the surface decreases while water density increases and vice-versa.

First, we analyse the films on the top of strongly hydrophobic surfaces ($\theta = 150°$). In the highly hydrated film ($\lambda = 22$), at short distances from the surface, *i.e.* $z < 1$ nm, the presence of polymer is predominant, while $\rho_w(z)$ shows almost no presence of water at distances $z < 0.5$ nm (see figure 5.3.(a) and (b)). Still in this region, $\rho_{poly}(z)$ presents two well defined peaks. Based on additional analysis of

partial mass density distributions of polymer backbone and side-chains, we have found that the first peak is mainly due to contributions coming from the polymer backbone, while the second peak can be ascribed to the presence of side chains. In the middle of the film, *i.e.* at distance $1.0 < z < 3.0$ nm, the $\rho_w(z)$ is at a maximum, while the $\rho_{poly}(z)$ is minimum, which suggests the formation of water domains confined between polymer-rich layers localized on the bottom and top of the film. When decreasing the degree of hydration ($\lambda = 11$ and 6) this structure is less evident and the distribution of the polymer is less localized. As indicated in figure 5.3.(e) the polymer density profile has a shallow minimum.

In the case $\theta = 100°$, one starts to observe presence of water in direct contact with the substrate, as shown by the first peak of the water density profile. This suggests that the threshold marking the transition between completely hydrophobic and mixed hydrophilic/hydrophobic character of the substrate is intermediate between the cases $\theta \approx 100°$ and 150°. In contrast, the polymer density profile shows first and second peaks decreasing in intensities. Then, once the water start to wet the surface, the ionomer self-organizes in a different way. The polymer backbone should move upward and allow water to adsorb at the wall. As a result, both water and polymer are populating the substrate. With decreasing λ this balance is altered and the presence of polymer on the substrate is dominant.

In the more hydrophilic cases ($\theta = 70°$ and 30°), the polymer in direct contact with the substrate is strongly reduced. At $\lambda = 22$, the presence of ionomer is significant only at distance $z > 2.5$ nm. The large amount of water on the bottom pushes the polymer upward, forming an ionomer layer on the upper half of the film. When λ is lowered to 6, the ionomer starts to be found at distance around 1 nm from the substrate (see figure 5.3.(e). Almost no water are found in the middle of the film, say between $1.0 < z < 2.5$ nm far from the surface. Such a distance range corresponds also the broad peak on the polymer distribution. This suggests that at $\lambda = 6$ the water molecules can be found trapped in the region corresponding to the minimum of polymer density profile.

For all cases the position of the two well defined peaks in the vicinity of the wall for both polymer and water density distribution does not change neither with hydration nor with surface hydrophilicity. The fist and second peak appear at 0.29 and 0.55 nm for water while 0.33 and 0.76 nm for polymer. The distance of those

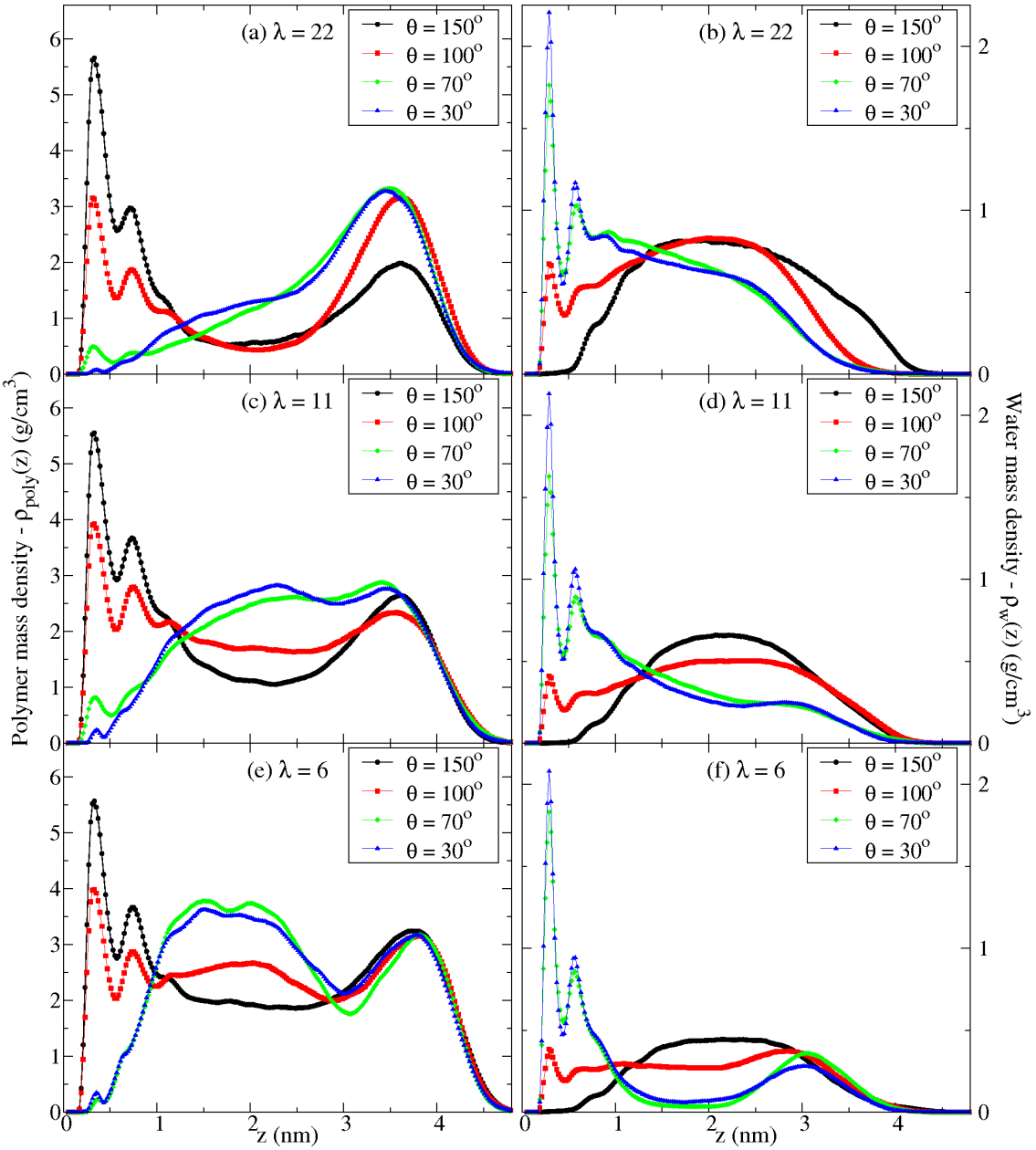

Figure 5.3: Mass density profile of polymer ($\rho_{poly}(z)$) and water ($\rho_w(z)$) of the ionomer films at $\lambda = 22$, 11 and 6. The hydrophilicity of the surface where the film is in contact is indicated by θ, where $\theta = 150°$ indicates the most hydrophobic and $\theta = 30°$ the most hydrophilic case.

peaks are controlled by the interaction with the wall, more precisely, by the parameter σ_{wall} of equation 4.5, which are the same value 0.32 nm for all cases. The distance between the two peaks around 0.26 nm and 0.46 nm are comparable with the minimum

distance between water-water molecules and between polymer beads and other species, respectively. This oscillatory density profile is typical behaviour found in liquids at interface with smooth walls [Spohr 1989, Lee 1994]. In other words, when a liquid makes contact with a solid wall, it is well known that the molecules will become layered adjacent to the wall.

From the above analysis we could see that modulating the interaction with the plate has indeed a strong impact on the local density profile. Although it is not surprising that the surface wetting grows due to the increasing hydrophilicity, the overall density profiles are not trivial. Consequently, more analysis, such as local structure, ionomer orientation, cluster distribution, are necessary to better understand the self-organization of these films. Therefore, the main conclusion we can obtain up to now is that the film morphology undergoes the changes according to the surface wettability and the hydration level. In other words, each simulated film exhibits a particular morphology.

5.2.2 Local structure

In this subsection, we aim to explore in details how the local structure depends on the wall hydrophilicity and the hydration level of the film. We have computed the (3D) radial distribution functions (RDFs) for each case studied according to the equation 4.1. The molecules close to the surface are included. The function is normalized by the volume of the film. Here, we focus on the RDF between water molecules, water and hydronium ions and the sulphur interacting with sulphur, water and hydronium. From the RDFs, we have also extracted the coordination numbers defined by equation 4.2.

Water Molecules and Hydronium Ions. Figure 5.4 shows the RDFs between water-water oxygen atoms ($g_{O_wO_w}(r)$) and water-hydronium oxygen atoms ($g_{O_wO_h}(r)$) at $\lambda = 22$, 11 and 6. The RDFs calculated for the bulk membrane are also shown in figure 5.4. As we can observe, the general features of these RDFs are similar to those for the bulk membrane in terms of position of the peaks. As in the bulk, the first peak in $g_{O_wO_w}(r)$ occurs at 0.27 nm, while in $g_{O_hO_w}(r)$ the first and second peaks occur at 0.26 nm and 0.47 nm, respectively. In terms of the intensity of these peaks, we can see that they decrease when increasing the hydrophilicy of the substrate. To

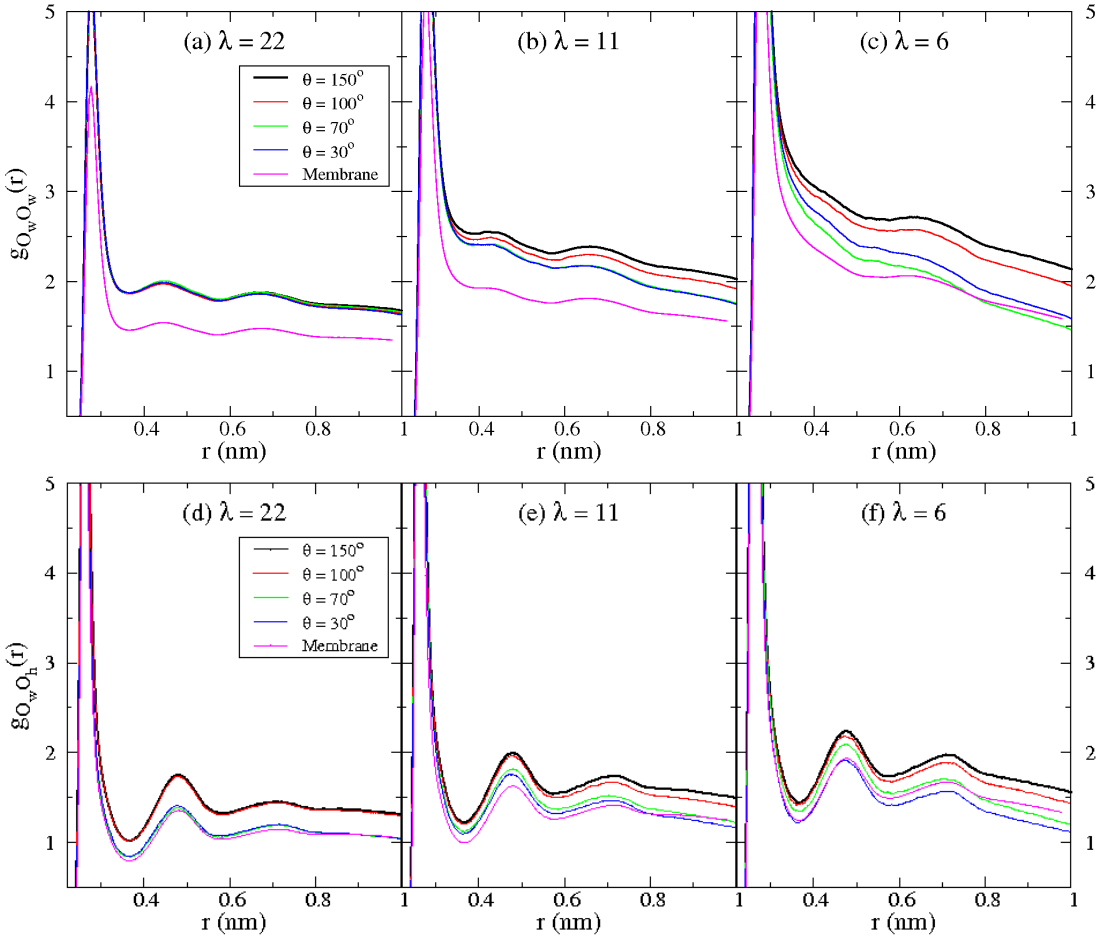

Figure 5.4: Radial distribution function of water-water oxygen atoms ($g_{O_wO_w}(r)$) and water-hydronium oxygen atoms ($g_{O_wO_h}(r)$) at $\lambda = 22$, 11 and 6 for the bulk membrane and for each ionomer film identified by the hydrophilicity of the substrate (θ).

better understand the meaning of this observation, we show in table 5.1 the first shell coordination numbers ($n_{O_wO_w}$ and $n_{O_hO_w}$). In all cases the coordination number is very close to the one found in the polymer membrane. Only for the film at $\lambda = 22$ a slight difference on the water coordination number around the hydronium is observed. In this case, $n_{O_hO_w}$ decreases from 4.37 for $\theta = 150°$ and in the bulk, to 3.66 for $\theta = 30°$. This means that less water molecules are found in the vicinities of hydronium ions for the films formed on hydrophilic surfaces.

Sulfunate groups. The RDFs between sulphur-sulphur atoms ($g_{SS}(r)$) are displayed in figure 5.5. In contrast to what we have found for water and hydroniun, the $g_{SS}(r)$

seems to be more sensitive to the ionomer film formation. Such sensibility is more accentuated at $\lambda = 22$ (see figure 5.5.a). In the case of $\theta = 30°$, the first peak is located at 0.48 nm and another clear peak exists around 0.7 nm. When the hydrophilicity decreases to $\theta = 100°$ and 150°, the first peak is shifted to 0.58 nm while the second becomes a shoulder and disappears almost completely, approaching the structureless $g_{SS}(r)$ found in the membrane. Then, we can affirm that the ionomer formed on a hydrophilic surface self-organizes in such a way to have their SO_3^- nearer to each other when compared with the one formed on hydrophobic surface or when compared with the membrane. The first shell coordination number also indicates that the number of SO_3^- ions residing in the vicinity of each other is larger in the case of $\theta = 30°$. The n_{SS} varies from 0.90 for $\theta = 150°$ to 1.66 for $\theta = 30°$, as shown in table 5.1. At hydration level $\lambda = 11$ and 6 the effect of the surface hydrophilicity is smaller. The position of the first peak around 0.48 nm is slightly smaller than that one in the bulk 0.51 nm. In other words, we suggest that when the film is highly hydrated ($\lambda = 22$) the interaction of the film with the surface can transform a bulk-like local structure, where SO_3^- groups are less constrained and more spaced, into a configuration where SO_3^- groups form compact ionic domains. Moreover, the $g_{SS}(r)$ approximates to the one in the corresponding bulk phase when decreasing the water contents and the surface hydrophilicity.

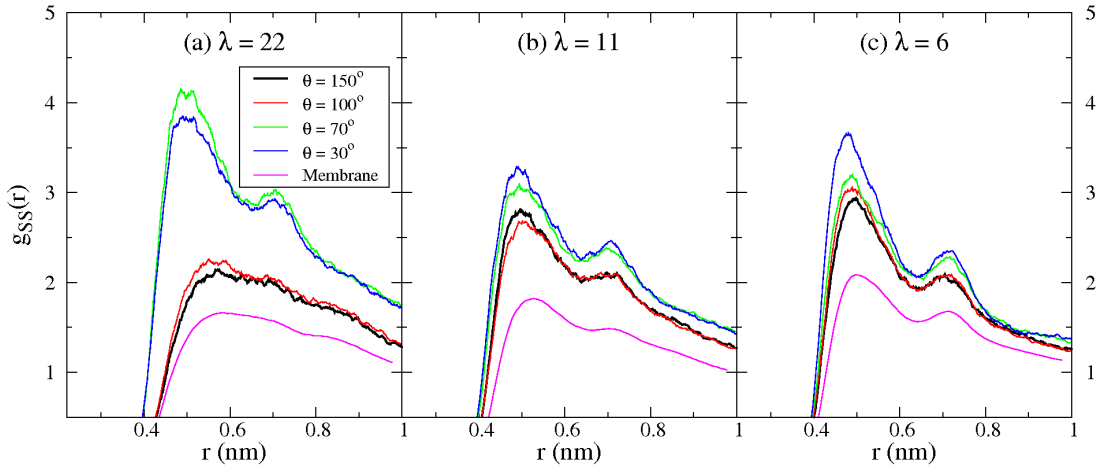

Figure 5.5: Radial distribution function of sulphur-sulphur atoms ($g_{SS}(r)$) for each film indicated at $\lambda = 22$, 11 and 6 for the bulk membrane and for each ionomer film identified by the hydrophilicity of the substrate (θ).

Coordination Number - $\lambda = 6$

θ (degree)	n_{SO_w}	n_{SO_h}	$n_{O_hO_w}$	$n_{O_wO_w}$	n_{SS}	$n_{O_hO_h}$
150°	5.29	1.90	3.09	3.66	2.14	1.93
100°	5.22	1.94	3.05	3.61	2.20	2.01
70°	5.30	1.96	3.04	3.46	2.31	2.08
30°	4.80	2.13	2.77	3.63	2.53	2.30

Coordination Number - $\lambda = 11$

θ (degree)	n_{SO_w}	n_{SO_h}	$n_{O_hO_w}$	$n_{O_wO_w}$	n_{SS}	$n_{O_hO_h}$
150°	6.01	1.48	3.63	4.20	1.63	1.36
100°	6.05	1.46	3.64	4.14	1.60	1.37
70°	5.78	1.62	3.45	4.13	1.83	1.63
30°	5.70	1.67	3.39	4.17	1.91	1.67

Coordination Number - $\lambda = 22$

θ (degree)	n_{SO_w}	n_{SO_h}	$n_{O_hO_w}$	$n_{O_wO_w}$	n_{SS}	$n_{O_hO_h}$
150°	6.94	0.90	4.37	4.52	0.90	0.72
100°	6.91	0.93	4.34	4.52	0.96	0.74
70°	5.91	1.51	3.59	4.60	1.74	1.37
30°	6.01	1.45	3.66	4.60	1.66	1.33

Table 5.1: First shell coordination numbers in the film. The cutoff radius R_c used where 0.45 nm for sulphur-water (n_{SO_w}) and sulphur-hydronium (n_{SO_h}), 0.35 nm for water-water ($n_{O_wO_w}$) and water-hydronium ($n_{O_hO_w}$) and 0.64 nm for sulphur-sulphur (n_{SS}) and hydronium-hydronium ($n_{O_hO_h}$).

Sulfonate groups with Water and Hydronium. The local structure around SO_3^- is also investigated via the RDFs of sulphur atoms with the water oxygen atoms ($g_{SO_w}(r)$) and hydronium oxygen atoms ($g_{SO_h}(r)$), as shown in figure 5.6. Both $g_{SO_w}(r)$ and $g_{SO_h}(r)$ exhibit strong correlation between the species similar to what we have observed in the bulk. The positions of the first and second peak are found around 0.38 and 0.60 nm and do not change neither with hydrophilicity of the surface nor with hydration level of the film. Only the amplitude of those peaks show some changes with

θ and λ. From the first shell coordination number of water molecules and hydronium ions around sulphur atom, we found that the number of water molecules surrounding the SO_3^- decreases when the hydrophilicity of the substrate increases, while the opposite trend was observed for the hydronium ions (see table 5.1). As we could expect, these changes are more evident at $\lambda = 22$, with water and hydronium coordination number varying, respectively, from 6.01 and 1.45 in hydrophilic case to 6.94 and 0.90 in the hydrophobic case. These findings are consistent with the RDFs for sulphur-sulphur atoms. The number of water and hydronium around sulphur atoms is always related to the SO_3^- agglomeration. In other words, when the sulfonate ions are less

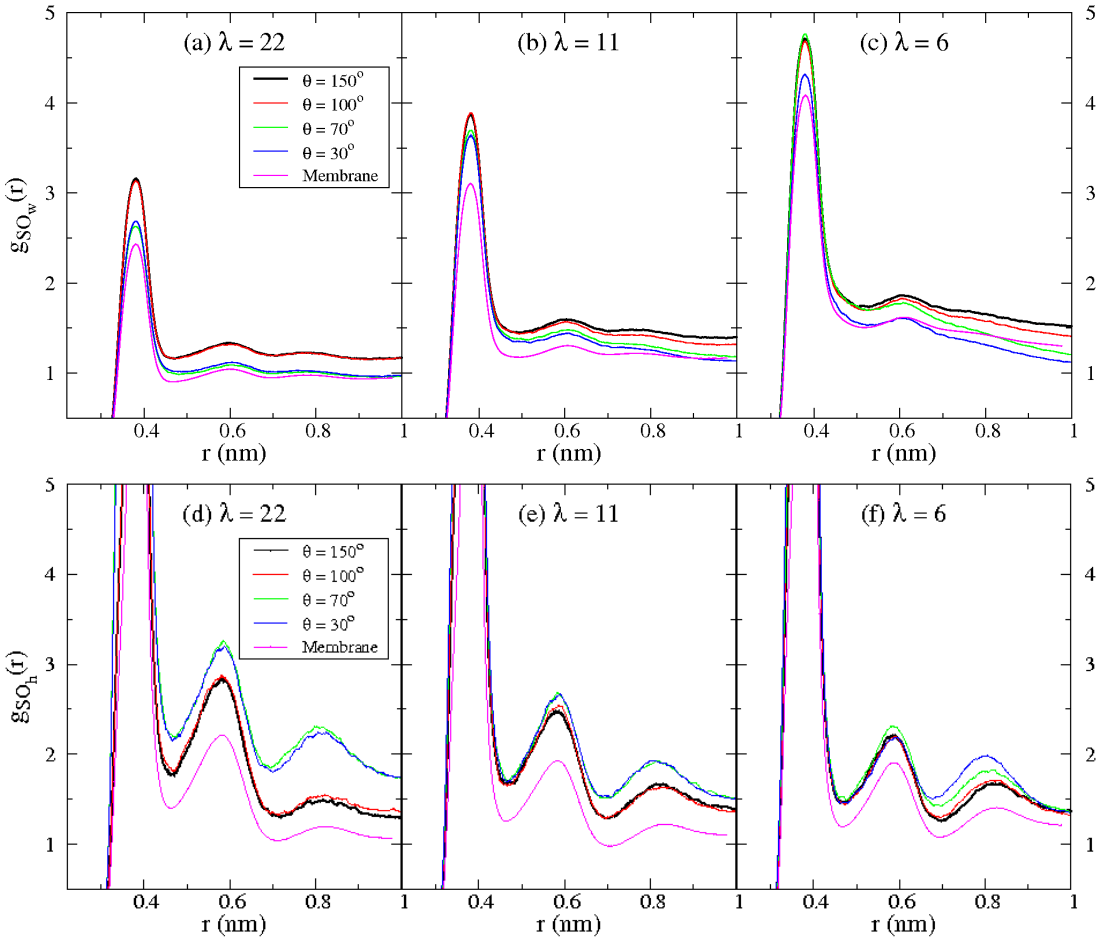

Figure 5.6: Radial distribution function of sulphur-water oxygen atoms ($g_{SO_w}(r)$) and sulphur-hydronium oxygen atoms ($g_{SO_h}(r)$) at $\lambda = 22$, 11 and 6 for the bulk membrane and for each ionomer film identified by the hydrophilicity of the substrate (θ).

agglomerated, they leave more available space for the water molecules to come near to the SO_3^- . Consequently, the hydronium ions become more dissolved.

In summary, the above analysis shows that the RDFs of the films exhibit qualitatively similar structure when compared with those in bulk membrane. Through the first shell coordination numbers we could measure the impact of surface hydrophilicity. We observe that for $\theta = 30°$ and $70°$ the sulphur atoms are found in compact agglomerates, consequently the number of water molecules decreases and the number of hydronium increases around SO_3^- groups. This effect is more evident for the highly hydrated films ($\lambda = 22$). Moreover, we observed that the more the film is hydrated the more it differs from the bulk membrane. For further analysis of the structure, in the next section we dedicate to an investigation of molecular orientation.

5.2.3 Molecular orientation profiles

To further elucidate both global and local structure of the film, we consider in this section the orientational order of water molecules and sulfonic acid groups inside the films. For each molecule, we have defined an orientation vector $\hat{u}_\chi$ and computed the angle ϕ_χ formed with the outer-pointing normal to the wall surface $\hat{z}$. The orientational order was analysed in terms of the distribution of $cos(\phi_\chi) = \hat{u}_\chi \cdot \hat{z}$. The distribution was calculated in different regions at a distance z from the wall. The film is therefore divided into overlapping "slices" parallel to the wall and of thickness chosen according to the number density of the molecule of interest. The molecular orientation dependence with the distance from the wall is crucial to elucidate the global ionomer orientation, as well as, the impact of surface interaction on the water molecules orientation.

5.2.3.1 Water molecule orientation

The spatial orientation of a water molecule can be identified via three unit vectors: $\hat{u}_{\hat{n}}$, the normal to the molecular plane; $\hat{u}_{\bar{OH}}$, the OH bond vector; and $\hat{u}_{\vec{\mu}}$ the molecular dipole moment vector. We analyse the orientation of these vectors in terms of $cos(\phi_\chi)$, where ϕ_χ corresponds to the angles $\phi_{\hat{n}}$, $\phi_{\bar{OH}}$ and ϕ_μ formed with $\hat{z}$. The probability distribution $P(cos(\phi_\chi))$ is computed within slabs at a given distance z from the surface and of thickness equal to 0.15 nm. The first slab starts from the

distance equal 0.14 nm, since smaller distances correspond to the inaccessible region due to the wall-film repulsion. In figure 5.7, we show $P(cos(\phi_\chi))$ in different slabs for 4 types of film at $\lambda = 22$. Very similar results were obtained for $\lambda = 11$ and 6, which indicates that the water content does not strongly influence the average orientation of the water molecule.

In figure 5.7 we first analyse the cosine distribution of $\phi_{\hat{n}}$ for the film $\theta = 30°$. Note that $P(cos(\phi_{\hat{n}}))$ produces a significant orientational anisotropy for the first and second slabs, which correspond to distance from the surface less than 0.36 nm. For instance, in the the first layer we can observe a strongly enhanced probability when $cos(\phi_{\hat{n}})$ approaches to the values 1 and -1. This means that the water molecules are likely to be found with their normal vectors forming an angle lower than 35° with the surface normal. Such orientational order decreases very quickly with increasing distance from the surface and the distribution became isotropic in the slabs in the center of the film, corresponding to $z > 0.51$ nm. When the wall surface is less hydrophilic ($\theta = 70°$ and 100°), the water-surface interaction is weaker and the molecular orientation order is less evident. Also in these cases, the orientational order can be affected by the presence of the ionomer in the first layer. In strongly hydrophobic case ($\theta = 150°$), water is not even in direct contact with the wall. Then, the probability distribution is shown starting from the forth layer ($z = 0.66$ nm), where one finds less orientational order when compared to the other cases.

For a more detailed analysis, we consider now the cosine distribution of $\phi_{\bar{OH}}$ and $\phi_{\vec{\mu}}$, also shown in figure 5.7. In the first layer, the $P(cos(\phi_{\bar{OH}}))$ and $P(cos(\phi_{\vec{\mu}}))$ maximums are close to 0°, which means that $\hat{u}_{\bar{OH}}$ and $\hat{u}_{\vec{\mu}}$ are roughly parallel to the surface. The distribution is not perfectly symmetric around zero, especially for $cos(\phi_{\bar{OH}})$. This means that the two OH bonds in H_2O molecule are not equally parallel to the surface. This supports the conclusion that the most probable configuration of water in the layer adjacent to the surface is one in which the oxygen atom is directed toward the surface and at least one hydrogen is slightly pointing outward the surface.

The orientational features change in the second layer. The maximum of the $P(cos(\phi_{\bar{OH}}))$ shifts to about -0.3 and a new maximum occurs at 1.0. Also, the $P(cos(\phi_{\vec{\mu}}))$ shifts toward zero with a shoulder around 0.5. These distributions result from the orientation where one hydrogen atom points away from the surface and the other one slightly toward it. This configuration means that the dipoles should form

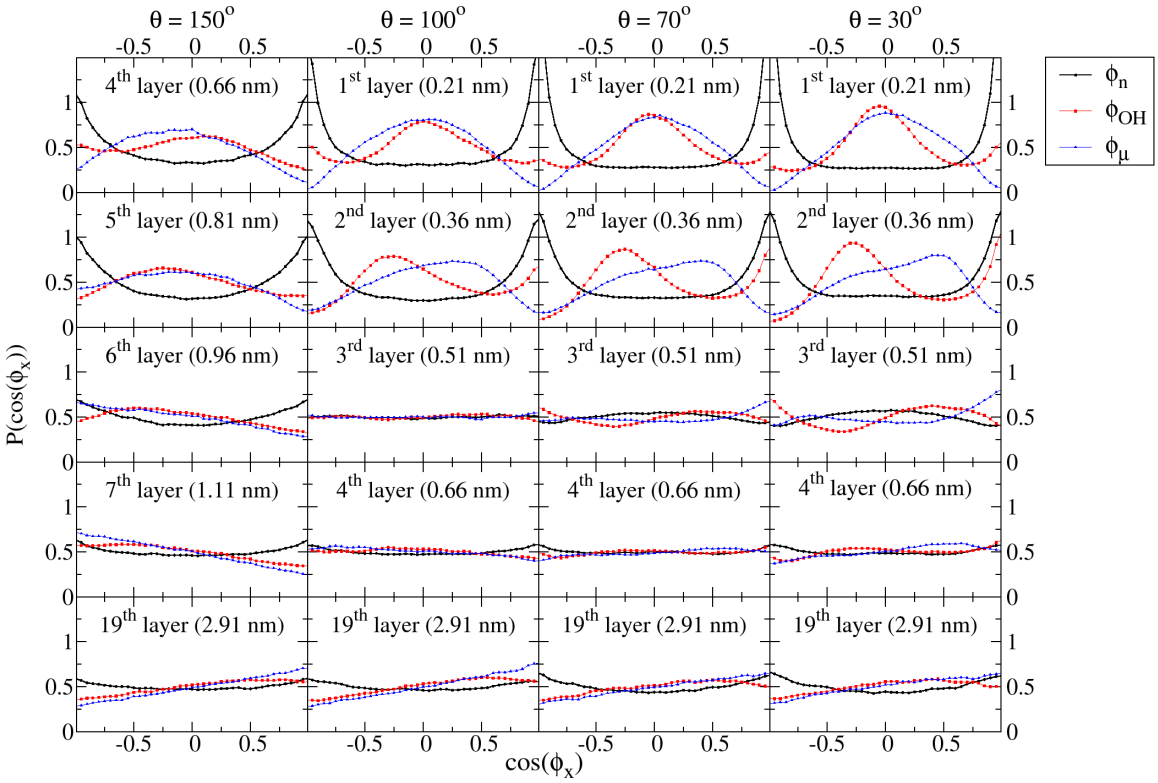

Figure 5.7: Probability function distribution of $cos(\phi_\chi)$, where ϕ_χ corresponds to the angles between the surface normal $\hat{z}$ and the normal vector to the water molecular plane $\hat{u}_{\hat{n}}$, OH bond $\hat{u}_{\vec{OH}}$ and dipole $\hat{u}_{\vec{\mu}}$. The distribution was calculated in slabs parallel to the wall, in the films with hydration level $\lambda = 22$ and wall hydrophilicity $\theta = 150°$, $100°$, $70°$ and $30°$.

an angle $\sim 60°$ with the normal surface. Identical orientations have been previously observed and well explained by Spohr [Spohr 1989], when he performed molecular dynamics simulation of water/Pt interface.

There is general agreement that the water dipole vectors near Lennard-Jones walls are preferentially oriented parallel to the surface [Spohr 1988]. This preference is explained through the water-surface interaction. Once the water molecules are attracted, they tend to form a 2D hydrogen-bonding network parallel to the surface. This configuration is also supported by experimental investigation of water molecules in contact with noble metal surfaces by using scanning tunnelling microscopy [Glebov 1997, Tatarkhanov 2009].

The main remark from our results is that ionomer does not play any important role on the water orientation profiles. The orientation is governed only by the water-

surface interaction. The intensity of this interaction determines the degree of order, *i.e.* the number of aligned water molecules. Since, in our model we are considering structureless wall and rigid water molecules, it is expected to find weaker orientation order if compared with other models [Spohr 1988, Spohr 1989]. We found orientational anisotropy only at short distances from the surface ($z < 0.5$ nm) and it does not strongly depend on water contents or surface hydrophilicity.

The main interest to understand the water orientation is concerning the configuration in the adsorbed region in catalyst surfaces. Franco *et al.* [Franco 2006, Franco 2007a] have shown that the orientation of water dipoles adsorbed on the top of PEMFC catalyst surfaces modulate the kinetic reaction equations. There, the authors assume water dipoles being aligned perpendicular to the surface. In the context of PEMFC, during operating system, the catalyst surface becomes electric charged and then, an electrical field at the vicinity of the surface is created. Thus, it is expected that the water molecule orientation be affected.

5.2.3.2 Sulfonic acid groups orientation

In the following, we investigate the sulfonic acid groups orientation in order to analyse the orientation of ionomer side chains. The SO_3^- orientation is given by the unit vector $\hat{u}_{SO_3^-}$ in the direction of the normal vector to the plane formed by the three oxygen atoms and pointing towards the sulphur atom. For instance, if the angle $\phi_{SO_3^-}$ formed with the wall normal vector is equal to zero, *i.e.* $cos(\phi_{SO_3^-}) = 1$, the SO_3^- configuration corresponds to the three oxygen atoms facing the plate and lying in the xy plane. To better visualize this configuration, we show $\hat{u}_{SO_3^-}$ in figure 5.8. Similar to what we have performed for water molecule, we compute the probability functions $P(cos(\phi_{SO_3^-}))$ on different slabs parallel to the surface. Here, each slab has thickness of 0.3 nm and the first layer corresponds to the

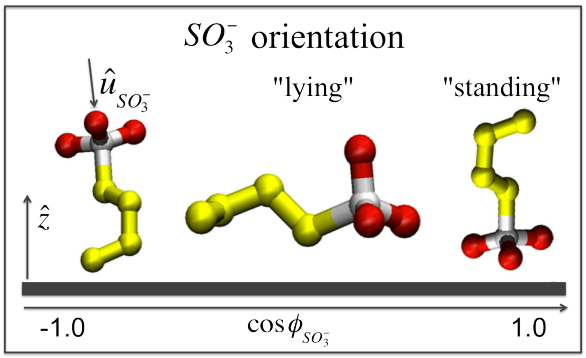

Figure 5.8: Orientation vector of SO_3^- group $\hat{u}_{SO_3^-}$ and $cos(\phi_{SO_3^-}) = \hat{u}_{SO_3^-} \cdot \hat{z}$. This figure illustrate the "standing" and "lying" configurations of the ionomer side-chain.

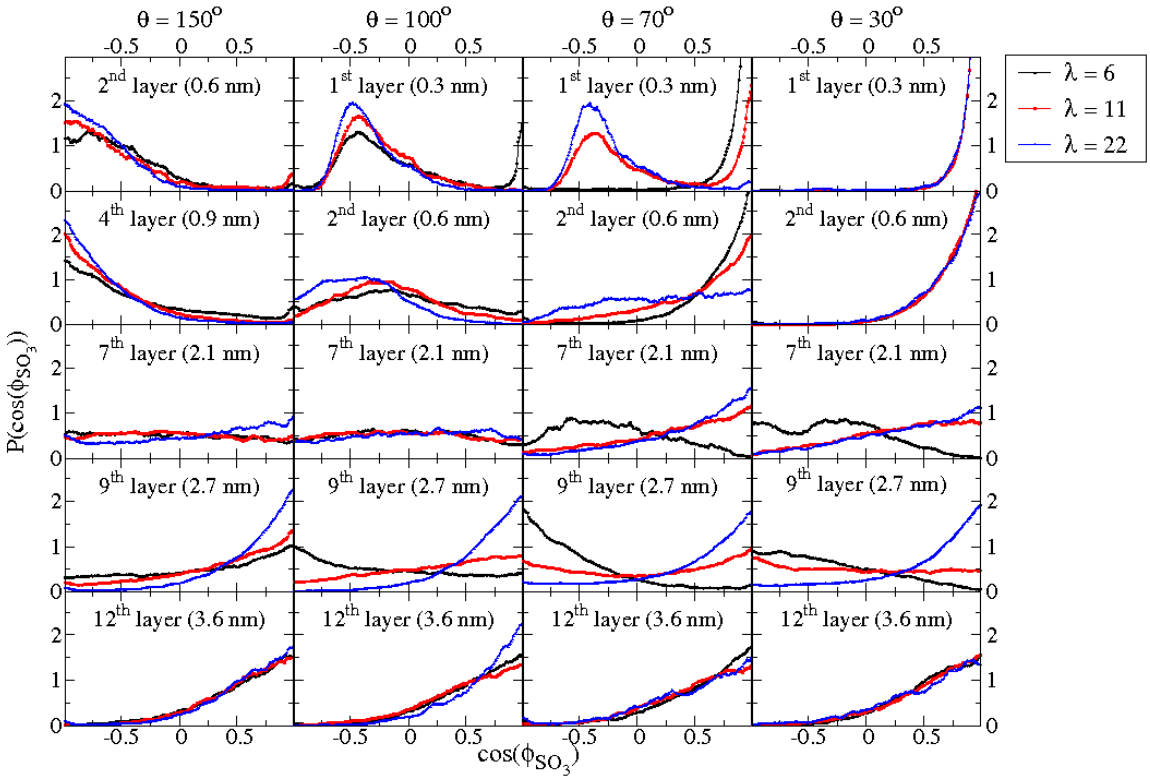

Figure 5.9: Probability function distribution of $cos(\phi_{SO_3^-})$, where $\phi_{SO_3^-}$ is the angle between the SO_3^- orientation vector $\hat{u}_{SO_3^-}$ and the surface normal $\hat{z}$. The distribution was calculated in slabs parallel to the wall of thickness 0.3 nm. In the first slab, one observes the inversion of SO_3^- orientation when changes the hydrophilicity θ.

range of $0.14 \leq z < 0.44$.

Figure 5.9 shows $P(cos(\phi_{SO_3^-}))$ computed for the films at each θ and at different hydration level. We observe that $P(cos(\phi_{SO_3^-}))$ depends on the hydrophilic character of the wall where the film is formed. Focusing on the first layer, it is evident that in the extreme cases, *i.e.* the most hydrophobic ($\theta = 150°$) and hydrophilic ($\theta = 30°$) cases, the SO_3^- are orientated in opposite directions. In the first case, the side chains tends to be aligned with the sulfonate groups, pointing outward to the wall, while in the second case, they are pointing toward the wall. In the intermediate cases ($\theta = 70°$ and $30°$), $P(cos(\phi_{SO_3^-}))$ have their maximum around -0.5. This means that, the oxygen atoms of SO_3^- tends to point in the direction of the ionomer, with the SO_3^- vector forming an angle of about $60°$ with the normal to the surface. This orientation is likely when the side-chains are aligned horizontally, as illustrated in figure 5.8. The

vertical and horizontal orientations of side-chains are called "standing" and "lying", respectively, and have been observed in previous simulations of ionomer on the top of platinum surface [Cheng 2010, Selvan 2008].

When decreasing the hydration of the film, the ionomer orientation is less ordered. It is interesting to see that in the case of $\theta = 70°$, the side-chains are first found in the "lying" position at $\lambda = 22$ and then gradually shift to "standing" when $\lambda = 6$. This indicates that the water contents also play an important role to determine the ionomer orientation. In this particular case, at low λ the majority of water molecules are found adjacent to the wall. Consequently the ionomer self-organizes in order to have SO_3^- groups at the interface with water. Hence, the optimal configuration is having sulfonate groups subsequent to the water layer adjacent to the wall. The shape of the interface between water and side-chains will be further discussed in the next sections.

Figure 5.9 also shows that SO_3^- groups have different preferential orientation in different regions within the film. In order to better visualize how the side-chains are orientated as a function of the distance z from the surface, we show in figure 5.10 the evolution of average $\langle cos(\phi_{SO_3^-})\rangle$ across the film thickness. Observe that in some cases, the side-chain orientation is inverted along z. This inversion is particular evident in the case of the films at $\lambda = 22$ formed on hydrophobic surfaces (see figure 5.10.(a)). For $\theta = 150°$ and $100°$, $\langle cos(\phi_{SO_3^-})\rangle$ is negative in the bottom half of the film and becomes positive in the top half. Other interesting cases are the films at $\lambda = 6$ placed on hydrophilic surfaces (see figure 5.10.(c)). For $\theta = 70°$ and $30°$ two inversions on side-chain orientation are observed. If we compare those plots with the water density profile in figure 5.3.(f) the minimum on $\langle cos(\phi_{SO_3^-})\rangle$ at z around 2.25-2.75 nm is found to be a region close to where is observed water "pools" formed between 2.5-3.5 nm. Indeed, this supports the idea that the side-chain orientation is governed by the distribution of water inside the film.

A relevant observation from figure 5.10 is that at distance larger than 3 nm from the wall, the side-chains always have sulfonic acid groups pointing toward the wall, independently on the type of the wall and hydration level. This side-chain alignment on the top is attributed in part to the interface of the film with the vapour phase. We will come back to this discussion in the next sections.

In summary, our results demonstrate that the interaction of water with the

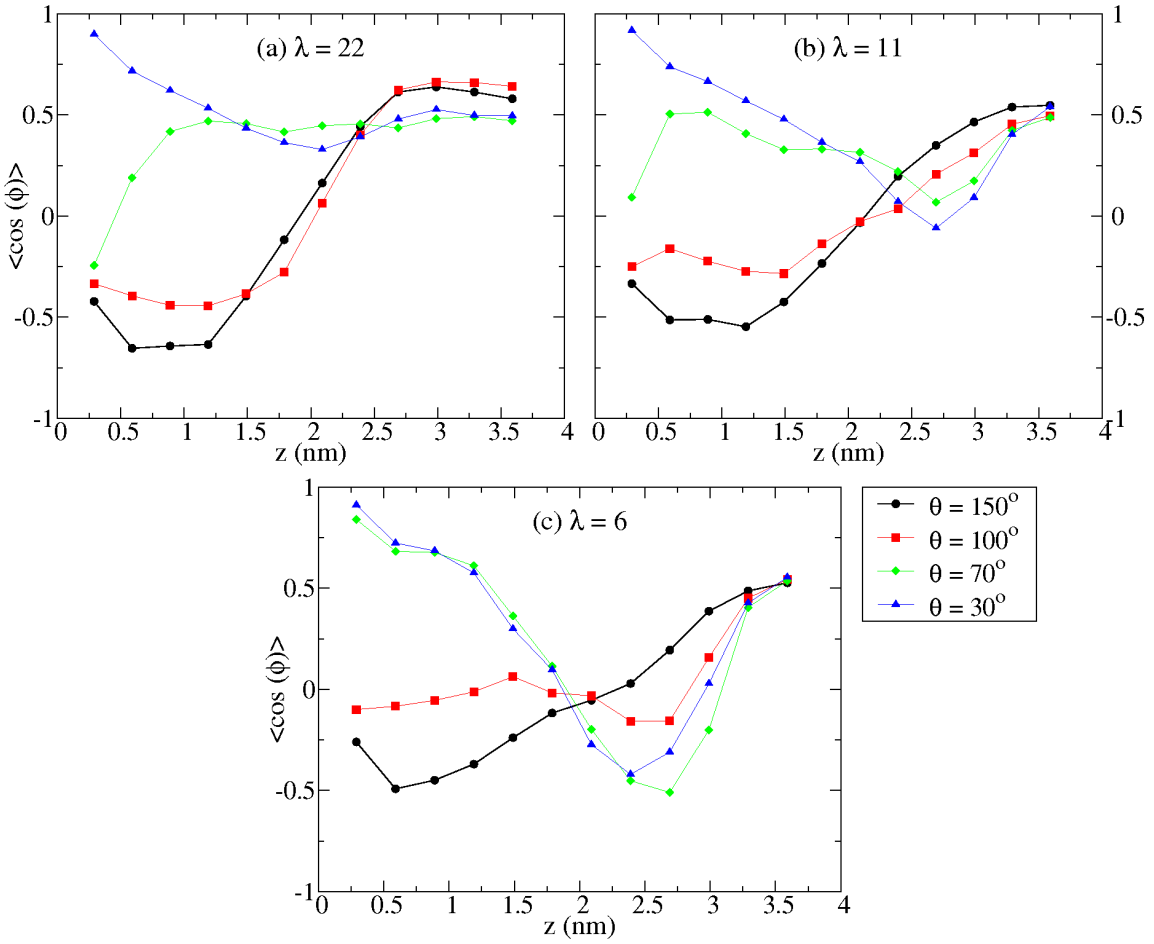

Figure 5.10: Average of $cos(\phi_{SO_3^-})$ as function of the distance from the surface in the films at (a) $\lambda = 22$, (b) 11 and (c) 6

wall is determinant for the side-chain orientation. The SO_3^- groups are embedded in the water domain, which makes the water content an important parameter on the ionomer orientation. Therefore, λ has no impact on orientational properties of water but has indeed impact on the side-chain orientation. The understanding of side-chain orientation will help us to figure out the Nafion film morphology for each hydrophobic/philic case and then identify any known patterns in the morphological models of Nafion. In the next section we dedicate to characterize the ionic clusters, in particular the SO_3^- agglomerations.

5.2.4 Formation of ionic cluster inside the film

In previous sections we have observed that the ionomer films present different SO_3^- packing, *i.e.* the coordination number and the minimum distances between SO_3^- groups are different for different case. Now we may include some analysis of ionic cluster distribution, which will be useful to figure out the global morphology of the films. We have identified the clusters by grouping SO_3^- groups within a cutoff distance of 0.64 nm. In other words, two SO_3^- groups are considered to belong to the same cluster if their sulphur atoms distance is smaller than the cutoff distance. This distance includes all SO_3^- groups in the first shell of the radial distribution function. The size of the cluster corresponds to the number of molecules that compose it. If a SO_3^- group has no neighbours within the cutoff distance, then it is a cluster with size equal 1.

In figure 5.11 we plot the normalized probability distribution of the cluster size n_S. In all cases, we observe a high probability to find small cluster sizes. n_S decays with S exponentially. This distribution can give wrong interpretation in terms of the distribution of molecules among clusters, since small clusters contain very few molecules. Therefore, we include in the insets the normalized number of molecules corresponding to a particular cluster size (*i.e.* $N_s = n_S S/N$, where N is the total number of molecules). Then, for instance in the film for $\lambda = 6$ showed in the inset of figure 5.11.(c), we can observe the peaks located at $S > 100$ in the cases $\theta = 70°$ and $30°$. They suggest that, although the incidence of such large clusters is low, it is high the probability to find a molecule that belong to them.

In table 5.2, we show the average cluster size for each film. We observe that the cluster size increases when decreases water contents. This is simply due to the effect of film swelling, which means that when the film is highly hydrated the water molecules intersperse among SO_3^- groups. In turn, SO_3^- groups form less compressed agglomerates and consequently they have higher probability to be found isolated (say, small cluster size). The hydrophobicity also impacts the average cluster size. For the case $\lambda = 22$, the hydrophilic cases $\theta = 70°$ and $30°$ show larger cluster size than the hydrophobic cases $\theta = 150°$ and $100°$. The opposite trend is found for $\lambda = 6$. In this case, the average clusters size is higher in the hydrophobic case than in hydrophilic cases. The dependence of the cluster size on the hydrophilicity is not trivial, and it

should depend on the particularity of the film morphology.

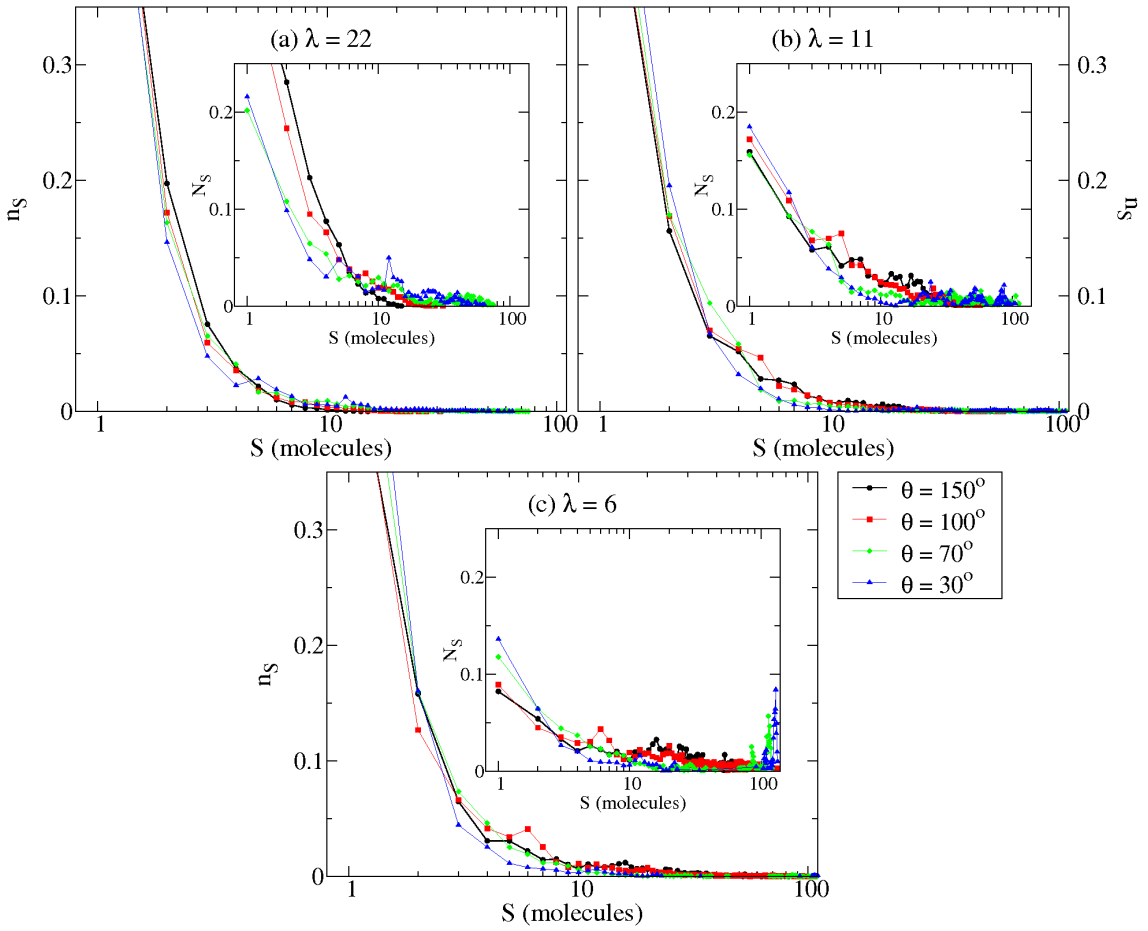

Figure 5.11: Cluster size distribution of SO_3^- groups, n_S . The insets display the probability of finding a SO_3^- groups in a cluster of a given size. The plots correspond to films for $\lambda =$ (a) 22 (b) 11 and (c) 6

Mean SO_3^- cluster size (molecules)			
θ (degree)	$\lambda = 22$	$\lambda = 11$	$\lambda = 6$
150°	1.71	3.38	5.85
100°	1.87	3.10	5.64
70°	3.02	3.65	4.96
30°	2.96	3.33	4.99

Table 5.2: Average cluster size of SO_3^- groups in the ionomer films.

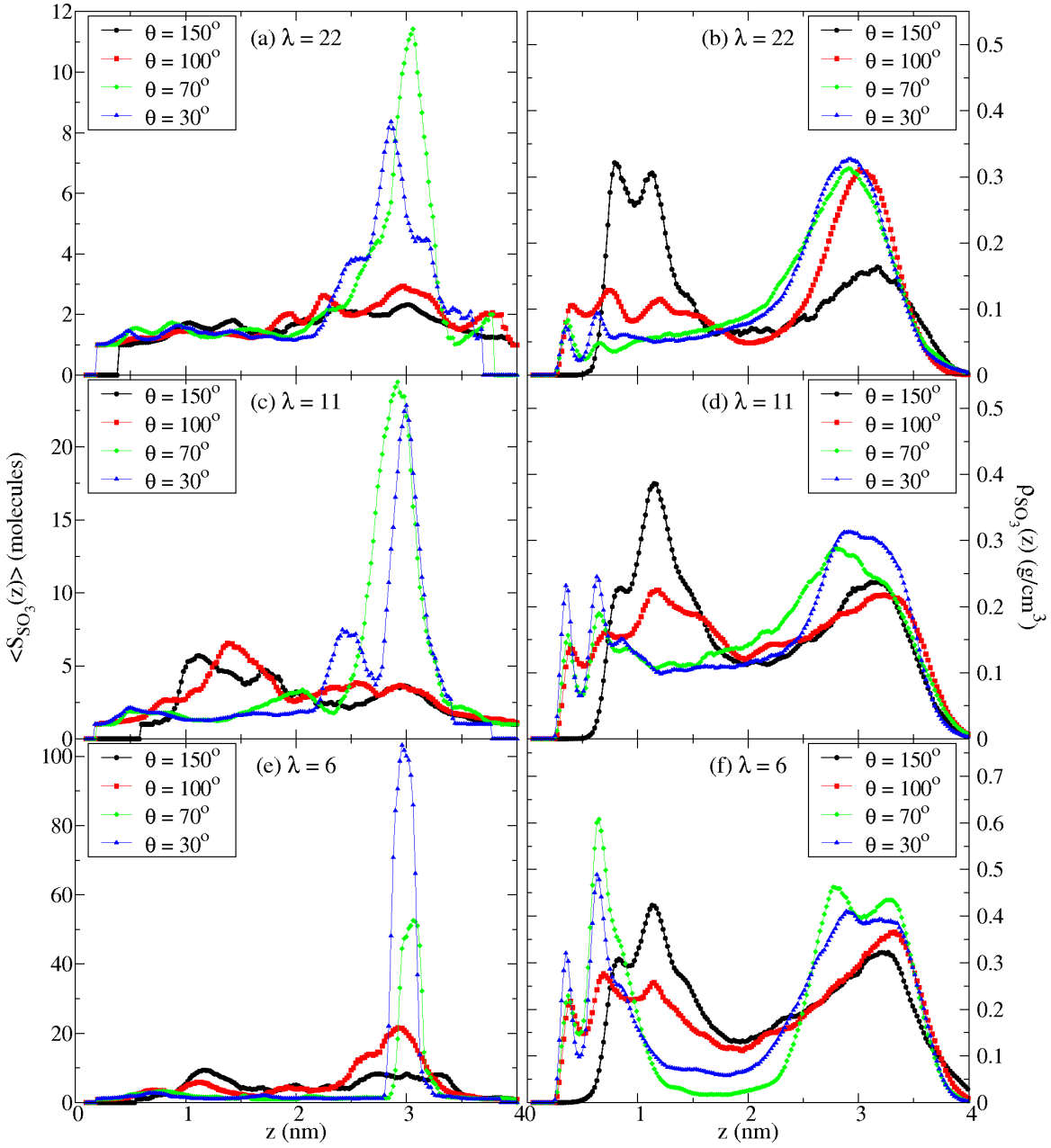

Figure 5.12: Average cluster size (left side) and SO_3^- density distribution (right side) as function of distance from the surface. The plots correspond to $\lambda =$ (a,b) 22 (c,d) 11 and (e,f) 6

In order to better understand ionic clustering in different region of the film, we compute the average cluster size as function of distance z from the surface. In figure 5.12 we plot the average cluster size $\langle S_{SO_3^-}(z)\rangle$ and the sulfonic acid mass density distribution $\rho_{SO_3^-}(z)$. For all values of λ and for the films $\theta = 30°$ and $70°$, the

$\langle S_{SO_3^-}(z)\rangle$ curves clearly indicate the formation of large clusters found at distance larger than 2 nm from the wall. The fact that the largest clusters are found at the top half of the film is consistent with the high SO_3^- mass density in this region. However, it is noticeable that for the films $\theta = 150°$ and 100° the distribution of average cluster size does not pronounced any relevant peak despite of the the maximums exhibited in $\rho_{SO_3^-}$ curves. In fact, the formation of SO_3^- agglomeration is not completely determined by the distribution of SO_3^- . For each film the SO_3^- agglomerates in different way.

The interesting point we want to emphasize here is that each film exhibits different SO_3^- agglomeration sizes. Later we will show that this ionic cluster play a crucial role on water dynamics. In general, the SO_3^- agglomeration has a vital impact on hydrogen binding between side-chains, it determines water binding and mechanisms of proton transport [Malek 2011b]. More details about the impact of ionomer cluster in the water and proton transport will be included in chapter 6.

5.2.5 Water clusters and connectivity

In this section, we focus on the water domains topology, in particular the shape and connectivity of these domains. We have previously shown water mass density distribution along the direction perpendicular to the films. Also, we have shown the orientation of ionomer side-chains and the distribution of SO_3^- clusters across the film. Now we are interested on the water cluster shapes. All these gathered informations will be used to develop a morphological model for each film we have simulated.

The water domains topology was investigated by computing the water mass density distribution in the plane parallel to the wall. We have partitioned the film in four slabs of thickness 1.2 nm and computed the water density distribution projecting on the xy plane. Our data are shown as 2D countour plots in figure 5.13, where lighter colors identify the regions where the density of water is higher. The ionomer and water are space-filling, therefore, the darker colors also identify where the presence of ionomers is significant. We emphasize, however, that the structure that we see in figure 5.13 is a "dynamic" one in the sense that it can only be found by averaging over the trajectories.

We first analyse the maps in figure 5.13 for the most hydrophobic case ($\theta = 150°$). We observer that water is concentrated in the second and third slabs. At $\lambda = 22$, the

homogeneous distribution suggests that water molecules form a unique layer parallel to the wall surface. Water is therefore confined between two ionomer layers separated by a distance of about $\sim$ 2 nm. The ionomer layers have the side-chains pointing toward the water layer. This indicates that Nafion adopts a "sandwich" morphology. In contrast, when decreasing the water content, the water pool tends to concentrate in the middle of xy plane with the ionomer around it. This is more visible for $\lambda = 6$, where water tends to form an elongated domain. We suggest the morphology of these films are similar to inverted micelles in the shape of ellipsoids or cylinders parallel to the wall surface.

In the intermediate case ($\theta = 100°$), we do not find any region with significant amount of water that we can consider as a water layer. Instead, the water can form agglomerates in any of the three slabs closer to the wall. In the case $\lambda = 6$, these water "pools" are well delimited and they are connected from one slab to the other. For $\lambda = 22$, the formation of "pools" is less clear. Indeed, water is more homogeneously distributed in all regions. Then, the ionomer are dissolved in the water. We can observe some ionomer "barriers" (indicated by darker colors in the middle of the maps) that connect the ionomer on top with the one on the bottom. In summary, the configurations are possible if the film adopts connected-cluster morphology with random shape.

In the hydrophilic cases, the films $\theta = 30°$ and $70°$ have similar water distributions. It is evident from these maps that the water domain is always mainly formed in contact with the surface. For $\lambda = 22$, the amount of water is also significant in the second slab, which suggests that water forms a thick continuous layer between the surface and the polymer on the top. As a result, these films adopt a bi-layer configuration. When λ decreases, except in the first layer, the water domains becomes less homogeneous and the formation of disconnected pools in the middle of the film is observed. For $\lambda = 6$, the water are concentrated mostly in the first and third slab. This suggests that the film consists in alternating layers of water and ionomer. Only a single narrow water channel is formed in the second slab making the connection between the two water domains. In this case, the film adopts a multilayer configuration. In all films, the fourth slab is not populated by water, which means that the top of the films is composed by mostly ionomer backbone with the side-chains pointing toward the wall.

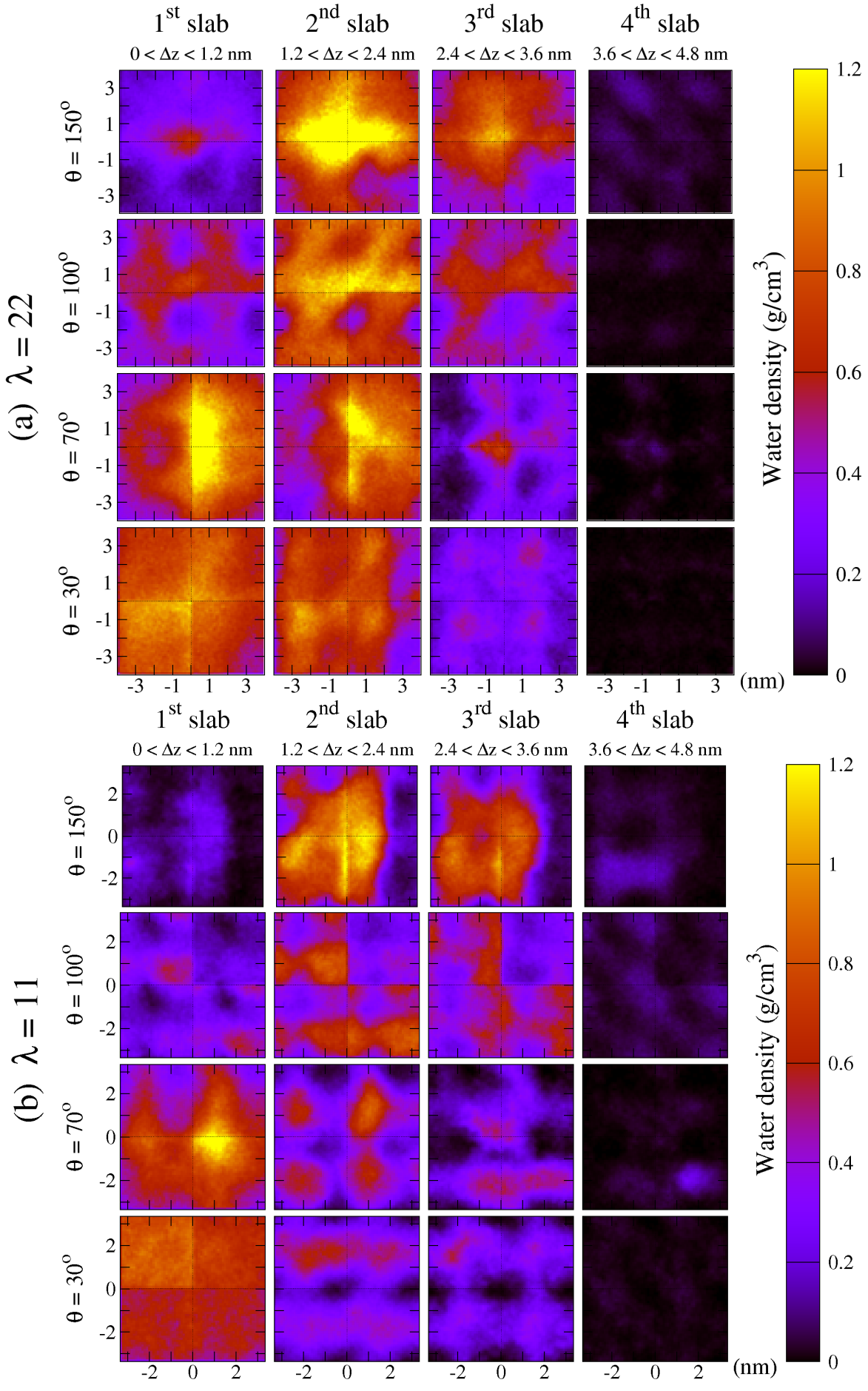
(a) λ = 22
1st slab
0 < Δz < 1.2 nm
2nd slab
1.2 < Δz < 2.4 nm
3rd slab
2.4 < Δz < 3.6 nm
4th slab
3.6 < Δz < 4.8 nm
θ = 150°
θ = 100°
θ = 70°
θ = 30°
Water density (g/cm3)
(nm)
(b) λ = 11

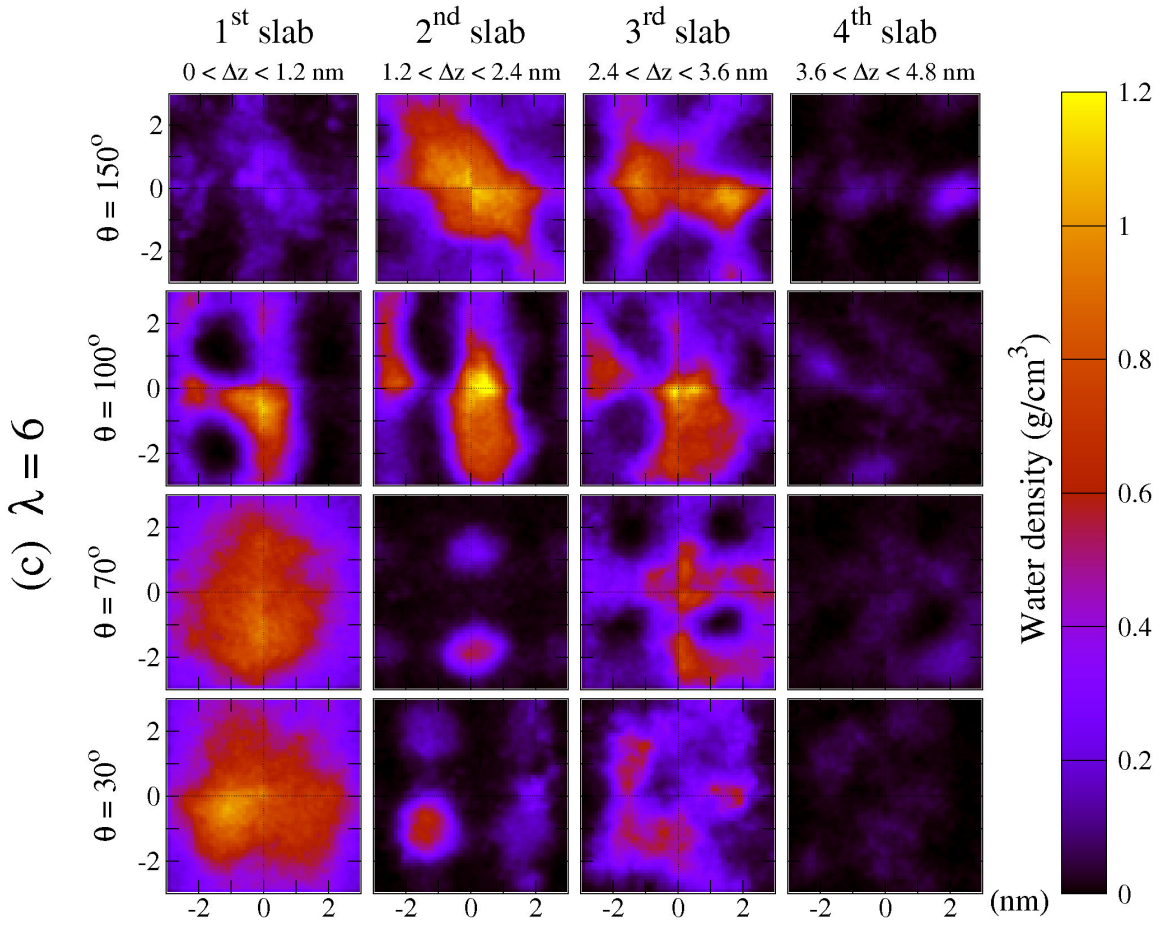

Figure 5.13: Contour plots of water density for λ equal (a) 22 (b) 11 and (c) 6

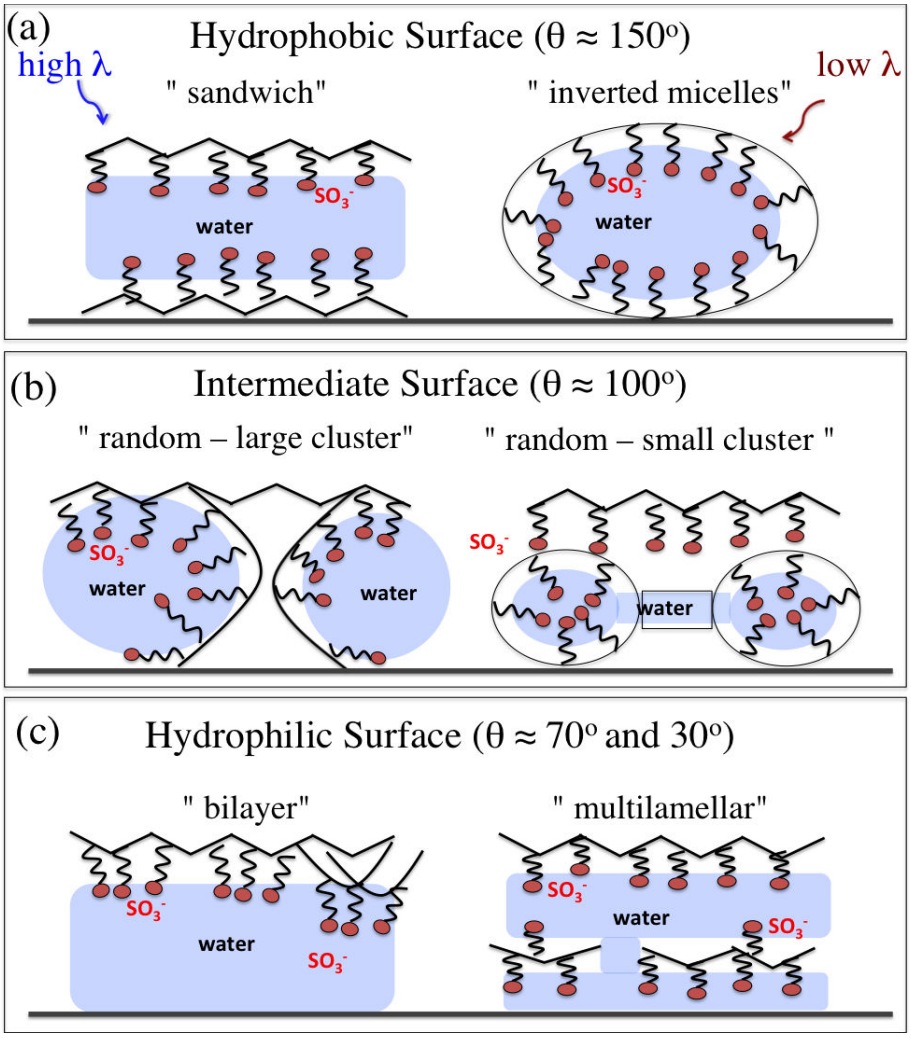

Figure 5.14: Illustration of the film morphologies. The left side corresponds to the films at high hydration, while the right side at low hydration.

Based on the water distribution maps and the ionomer orientation discussed in previous section, we can draw a general picture of the morphology of the films at different degree of hydration and nature of the support. In order to better visualize this, we schematically represent the backbone and side-chains orientation in figure 5.14. The SO_3^- groups are represented by red circle. In summary, we classify the films in three classes: *a) hydrophobic:* the film shows sandwich structure constituted by a sequence of layers: backbone, ionic groups, water, ionic groups and backbone. With less water, the ionomer folds around the water forming a inverted-micelles structure; *b) intermediate:* the film shows a random configuration with connected water "pools". In this case λ

influences the pools sizes; *c) hydrophilic:* the film shows two well separated water and ionomer layers. With less water inside the film, the ionomer approaches to the surface due the interaction of side chains with the water formed on the top of the substrate. Then, the film may adopt a multilamellar configuration. Finally, our findings are consistent with experimental observations found by Dura *et al.* [Dura 2009] and Wood *et al.* [Wood 2009]. In both works, was discovered a lamellar structures composed of thin alternating water-rich and Nafion-rich layers formed close to hydrophilic substrate.

5.3 Nafion film/wall interface

In the above section we have characterized the structure of the films from general point of view, as well as, the local structures, by studying the local organization of the different chemical species. Based on these analysis we have shown how the substrate can affect the ionomer morphology, but we have not yet addressed the adsorption of chemical species on the substrate. In this section we focus on characterizing the region immediately adjacent to the wall. The main interest in giving additional attention to this region is due to the fact that it could compose a typical scenario where the electrochemical reactions of PEM Fuel Cell take place. In a real system, two phenomena directly affect the reaction kinetics: adsorption of chemical species and the formation of electrochemical double layer. Detailed descriptions of these phenomena are not possible by considering our model. However we can speculate about the impact of ionomer organization on these phenomena. Therefore, we limit our investigation to explore how the ionomer local structure could directly or indirectly affect the reaction mechanisms inside the catalyst layer. The idea is to investigate the physical adsorption by focusing on the dependence of ionomer local structure, with no additional knowledge about the nature of the adsorption. In this section, we, first, quantify the overall coverage on each hydrophobic/philic surface and. Then, we discuss structural analysis of adsorbent species and distribution of charge in the vicinities of the surface.

5.3.1 Surface coverage and structure of adsorbed chemical species

The adsorption of polymer backbone, side-chains, sulfonate anions, water and hydronium ions are analysed in this subsection. Of course, in real system, the sub-

strate, especially catalyst surfaces (Pt and Pt alloy surface) can react with water, hydronium ions or other species [Subbaraman 2010b]. In this work, we have not included the chemical reactivity of the substrate, which would require sensibly more complex modelling. However, the overall surface coverage should be dependent on the ionomer distribution immediately adjacent to the substrate. Indeed, the directly adsorbed layer corresponds to the first peak in mass density profiles previously discussed in figure 5.3. Moreover, the ionomer adsorbed tends to adopt a particular conformation that can be explored by our model. Therefore, in this subsection, we first quantify the surface coverage and then we analyse the lateral conformation (say, 2D conformation) for each case of hydrophilicity and hydration level.

Surface coverage

The surface coverage for ionomer backbone, ionomer side-chains (without SO_3^-), H_2O , H_3O^+ and SO_3^- groups are plotted together in figure 5.15 for each film. This surface coverage is simply defined as the number of molecules within the adsorption region divided by the area of the xy dimensions of the simulation box. We consider the adsorption region as the region within the distance 0.55 nm from the surface. This distance is comparable to the position of the first minimum on the polymer density profiles.

The plots in figure 5.15 clearly show the inversion of surface coverage when it changes the hydrophilicity. In the hydrophobic case ($\theta = 150°$, which correspond to $\varepsilon_{philic} = 0.25$ kcal/mol), the adsorption of polymer backbone is predominant. On increasing the hydrophilicity of the substrate, the water coverage increases and backbones move upward allowing the adsorption of SO_3^- and H_3O^+ . The water content does not significantly change the backbone and water coverages. By decreasing water contents from $\lambda = 22$ to $\lambda = 6$, backbone coverage changes from 3.8 to 3.61 molecules/nm^2 for the most hydrophobic case, while water coverage reduces from 5.01 to 4.8 molecules/nm^2 for the most hydrophilic case. The reduction of water coverage is compensated by the increases of H_3O^+ and SO_3^- . Indeed, SO_3^- coverage increases from 0.02 to 0.09 molecules/nm^2 and H_3O^+ coverage from 0.08 to 0.28 molecules/nm^2.

In summary, figure 5.15 gives more evidence what we have already discussed the previous section, *i.e.* the transition of predominant backbone coverage to predominant

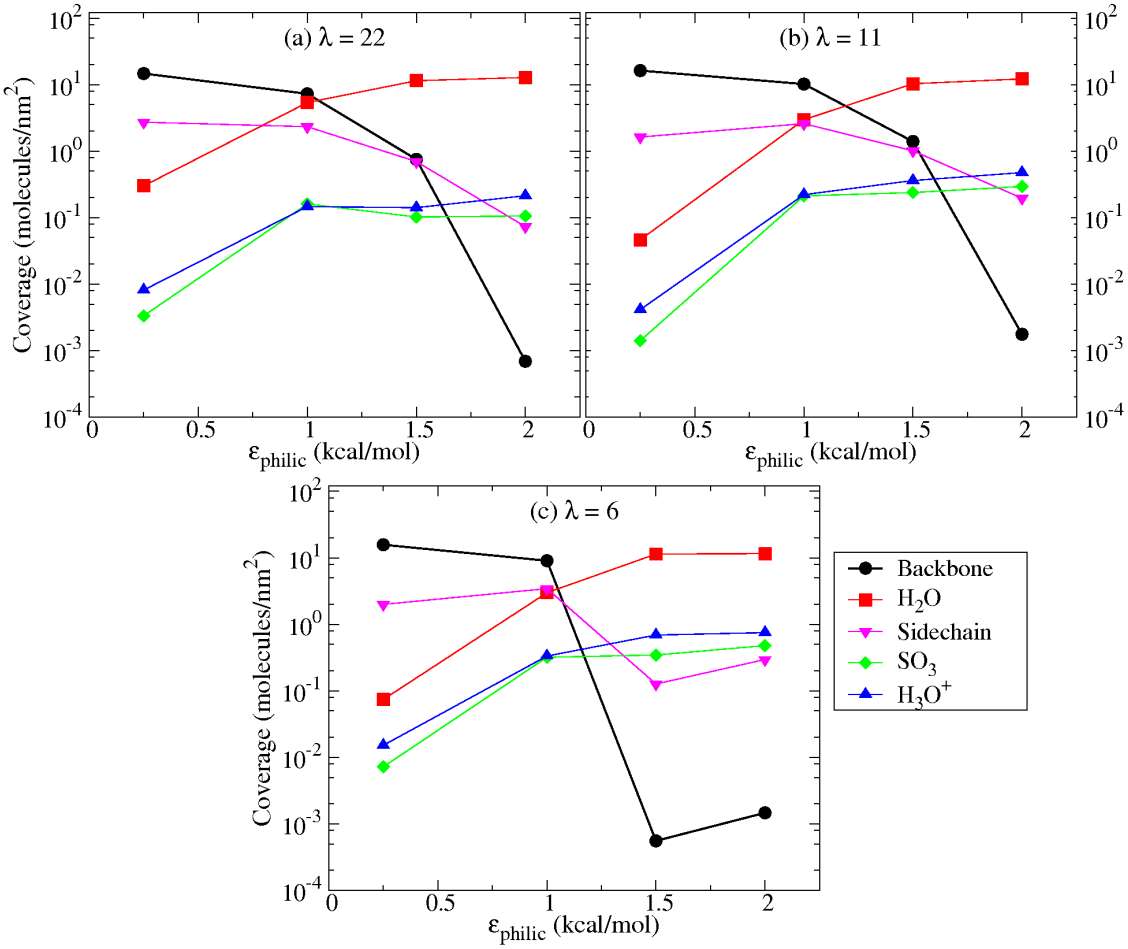

Figure 5.15: Ionomer backbone, water, side-chains, H_3O^+ and SO_3^- coverage on surfaces ranging from the most hydrophobic ($\varepsilon_{philic} = 0.25$ kcal/mol) to the most hydrophilic ($\varepsilon_{philic} = 2.0$ kcal/mol). The plots correspond to water contents λ equal (a) 22 (b) 11 and (c) 6

water coverage when switching from hydrophobic to hydrophilic surface. The adsorption of water, H_3O^+ and SO_3^- are negligible in the most hydrophobic case, however, even in the most hydrophilic cases, the adsorption of the ionomer is still observed. For hydrophilic surfaces, the SO_3^- and H_3O^+ have higher chances to be adsorbed when the hydration of the film is lower.

During the PEM Fuel Cell operation, the oxidation and reduction reactions occurring on the top of catalyst surfaces have strong dependence on the surface coverage [Franco 2006]. The adsorption of ionomer could block the adsorption of reactant species, reducing the area where the electrochemical reaction occurs. Our results sug-

gest that water molecules and hydronium ions can be found away from the catalyst surface when the surface hydrophilicity is not favourable. This is a phenomenon usually not considered when research is performed in order to increase platinum utilization in PEMFCs.

Ionomer Adsorption

The conformation of the ionomer adsorbed on the surface can be investigated by analysing the typical snapshot of the adsorption region (the region within the distance 0.55 nm from the surface). In polymer science the adsorption of polymers are common described by loop-train-tail model [Fleer 1993]. According to that, the adsorbed polymer chain consists of alternating sequences in direct contact with the surface, called trains, and no-direct contact with the surface that form loops and tails over the wall. Then one can compute a quantity measurable by experiments: the *train fraction*, which is defined as the amount of trains (in our case, the monomer within adsorption region defined above) divided by the total adsorbed chain (trains, loops and tails) [Fleer 1993, Nylander 2006]. In figure 5.16 we show typical snapshots of the adsorption region. They represent the trains of adsorbed ionomers.

In the case of hydrophobic surface ($\theta = 150°$) we can see the ionomer adsorbed mainly via the backbone (brown beads), as similarly observed in previous simulations of ionomer adsorbed on graphitized carbon sheets [Mashio 2010]. The trains display a extended 2D conformation without any apparent order. We compute the train fraction by accounting only for the monomers in the backbone, therefore the total number of monomers for each polymer chain adsorbed is equal to 160. The train fractions for the cases $\lambda = 22$, 11 and 6 are, respectively 0.56, 0.36 and 0.30. This means that in the case of $\lambda = 22$, the adsorbed ionomer is more flattened out on the wall. This is attributed to the water absorbed on the outer surface that compresses the ionomer toward the wall in a more efficient way than in the films with less amount of water.

For the case of intermediate hydrophilic/hydrophobic surface ($\theta = 100°$), the water molecules start to be significantly adsorbed on the surface and the polymer backbones move upward to also allow for adsorption of side-chains (yellow beads), with the backbone trains fraction 0.28, 0.23 and 0.16 for $\lambda = 22$, 11 and 6, respectively. These values are smaller than for the case $\theta = 150°$ because here, the side-chains are significantly more adsorbed, and they are not included in the train fraction. A balanced

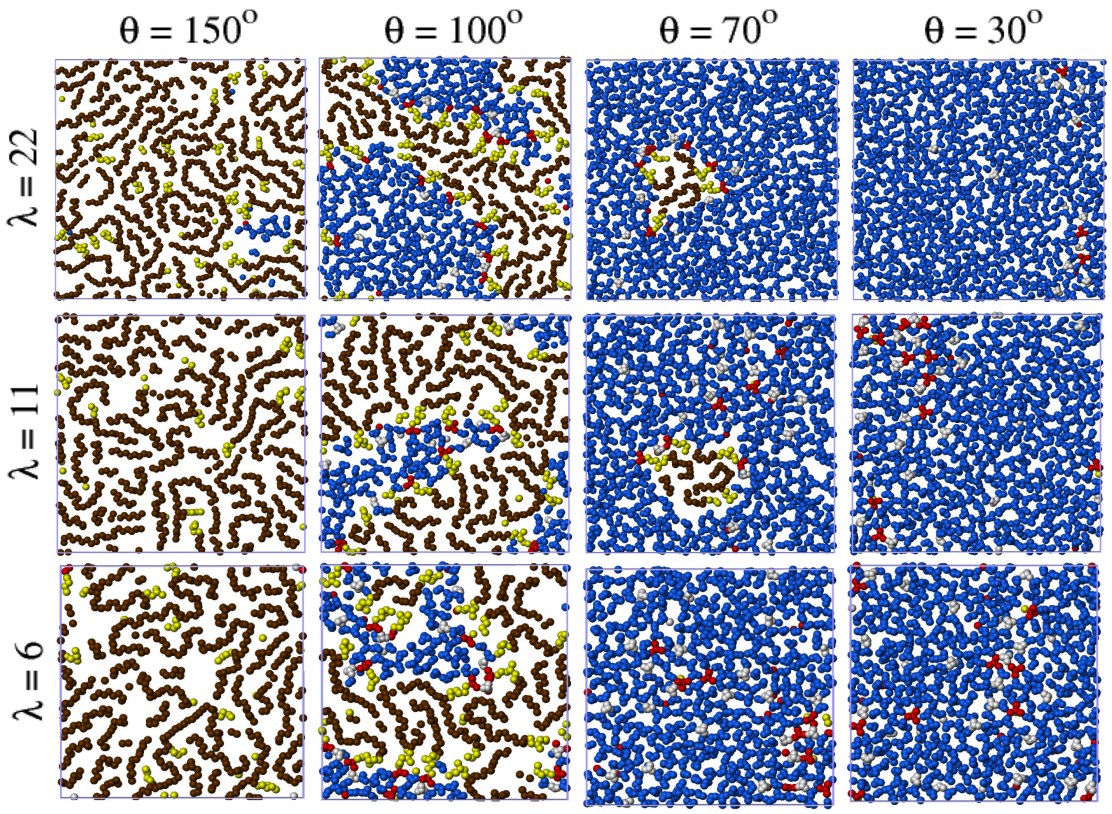

Figure 5.16: Snapshot of the adsorption region equivalent to 0.56 nm distance from the surface. The backbones trains are shown in brown, side-chains in yellow, SO_3^- in red, water molecules in blue and hydronium ions in white.

presence of water, backbone and side-chain is found for these intermediated cases, and, as evident from figure 5.16 ($\theta = 100°$), phase separation between two distinct domains occurs. The adsorbed backbone aggregates form a kind of wire of width about 1-4 nm and with the side chains perpendicular pointing outward the wire. Due the limited length scale of our simulation box, we cannot observe the conformation of these wires. Since the surface used in our model is perfectly flat, it is expected to observe random conformation. However, on structural surfaces this wires could unfold and extend into different conformations, as reported in experimental work of ionomer adsorbed on the HOPG surface [Masuda 2009], where aligned ribbon-like wires are observed.

In the hydrophilic case ($\theta = 70°$), adsorption of the ionomer is still observed. For $\lambda = 22$ and 11, the ionomer form island-like domains (globular structures), with agglomerations of chains surrounded by water molecules and hydronium ions (white

beads). The backbone trains fractions are 0.10 and 0.09 for $\lambda = 22$ and 11, respectively. For $\lambda = 6$ the backbone is no more adsorbed, instead of that, the ionomer adsorbs specially through its sulfonate groups (red bead). The same occurs for the most hydrophilic case ($\theta = 30°$). The SO_3^- groups are adsorbed with the three oxygen facing the wall (as previously shown by the orientation profiles of figure 5.9). Moreover, the number of adsorbed SO_3^- is higher for $\lambda = 6$ and 11, and they are more dispersed on the surface. In contrast, for $\lambda = 22$, SO_3^- tends to be agglomerated.

In the context of PEMFC, it has been observed that the adsorption of SO_3^- groups affects the electrochemical double layer formation at the vicinities of catalyst surface. Our results show that the probability of SO_3^- be chemically adsorbed on the hydrophilic surfaces is high when the film is low hydrated. Moreover, Subbaraman *et al.* [Subbaraman 2010b] have pointed various factors that can influence the chemical nature of the sulfonate adsorption. The factors include: nature of the counter cation, extent of SO_3^- agglomeration within the ionomer, length and spacing between side chains, *etc.* Our results show SO_3^- being adsorbed by forming different configurations, *e.g.* , clustering and dispersed. This should affect the chemical nature of the SO_3^- adsorption, and ultimately affect the electrochemical potential that drives the electrochemical reactions. In conclusion, although our results cannot predict how SO_3^- adsorptions affect kinetic reactions, we can suggest a non-uniform reaction rate inside the catalyst layer.

Water adsorption

We have previously discussed, in section 5.2, the orientation profile of water molecules inside the film. We have shown that the water molecules present anisotropic orientation distribution at the vicinities of any surface. This should strongly change the local organization of adsorbed water molecules. In order to investigate this point, we compute the 2D radial distribution functions $g^{2d}_{OwOw}(r)$ in the plane adjacent to the surface. The results are very similar for all values of λ, therefore we choose to show only the results for $\lambda = 22$.

Figure 5.17 shows the $g^{2d}_{OwOw}(r)$ of water within adsorption region for the cases $\theta = 30°$, 70° and 100°. For comparison we include the $g^{2d}_{OwOw}(r)$ in the region placed in the middle of the film. It is evident that the structure of water in the adsorption region is very different from the one in the middle, which in turn is comparable with the

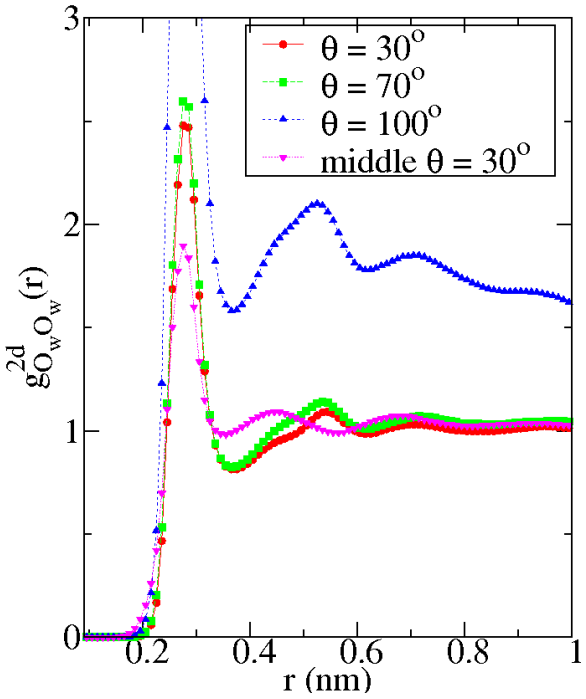

Figure 5.17: Water-water 2D radial distribution function in adsorption region for $\lambda = 22$;

structure of water in the bulk. The $g^{2d}_{OwOw}(r)$ in the adsorption region is characterized by a new maxima at about 0.54 nm together with a shoulder, which occurs around 0.43 nm. The third and fourth peaks around 0.7 and 0.94 nm respectively are very weak. For the hydrophilic cases $\theta = 30°$ and 70° the $g^{2d}_{OwOw}(r)$ curves are very similar. For the intermediate case ($\theta = 100°$), $g^{2d}_{OwOw}(r)$ is perturbed by the massive presence of the ionomer in the adsorption region.

These plots are just a consequence of the water orientation profile. If the surface were electrically charged or if the chemical adsorption of water molecule happen, the orientation of the molecules should be affected and consequently the rearrangement of the local structure. The water structure, *i.e.* orientation and local organization, in the region a few angstroms from the surface has important influence on electrical double layer formation [Franco 2006].

5.3.2 Effects of the presence of the ionomer on the charge distribution

In the previous discussion we have observed that the structure of the ionomer rules the overall surface coverage. Similarly, this structure governs the distribution of charge at the vicinity of the substrate. In order to clarify this point, we compute the net charge distribution across the film thickness. This distribution was computed by the difference of the SO_3^- and H_3O^+ concentrations.

From figure 5.18 we can see the effects of the presence of the ionomer on the charge distribution. The first peak corresponds to the hydronium concentration while the first well is due the sulfonate anion concentration. The intensity of the positive

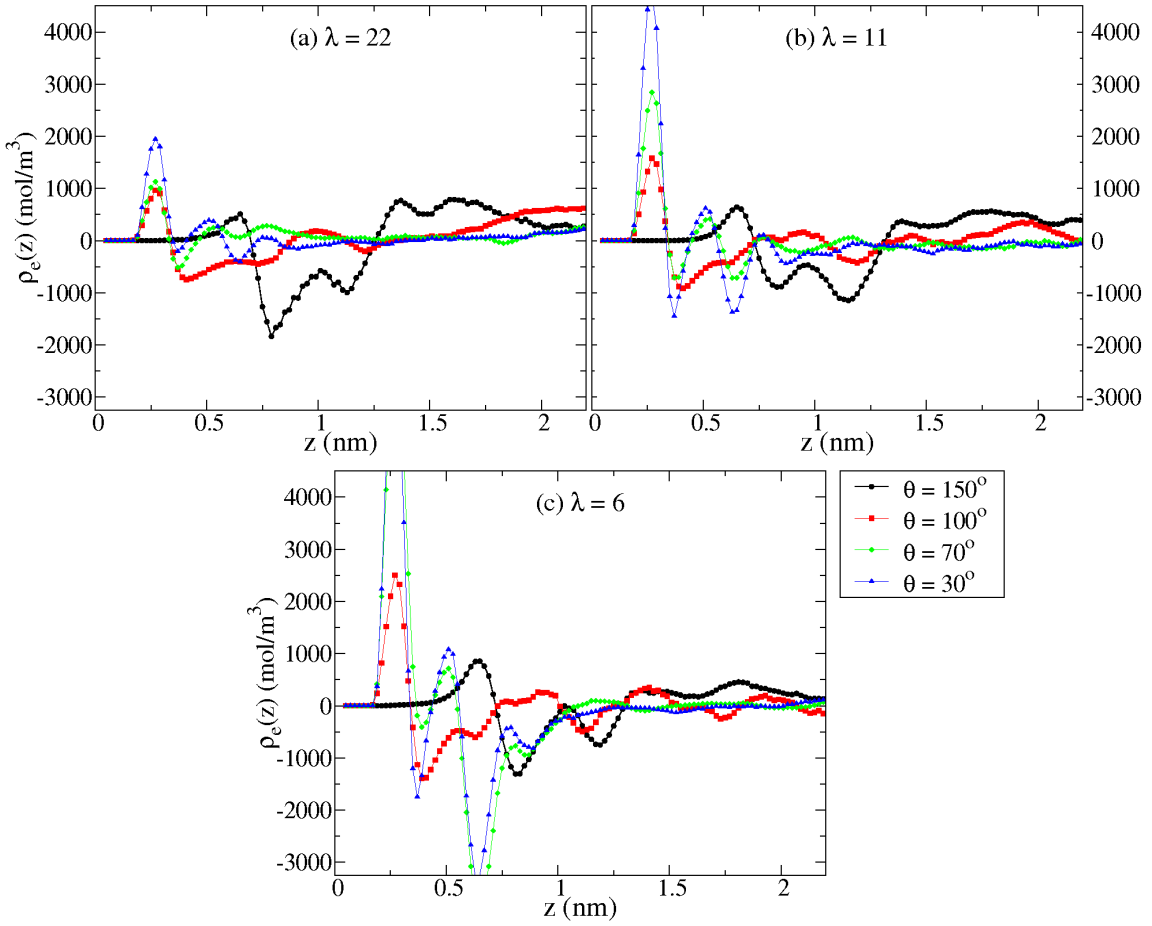

Figure 5.18: Net charge density distribution across the ionomer thin-film at $\lambda = 22$, 11 and 6

peak decreases when decreasing hydrophilicity. This is explained by the fact that the adsorbed ionomer chains can inhibit access of protons to the surface. Regarding the catalyst surface, this prevention will affect the electrochemical double layer formation. The charge distribution showed on this graph determines the proton concentration at the reaction plane as well as the electric potential profile across the film. Therefore, the formation of the electrochemical double layer will be clearly affected by the hydrophilicity of the catalyst surface.

5.4 Nafion film/vapor interface

The Nafion/vapour interfacial morphology has received special attention due to its importance in ionomer water uptake [Bass 2011]. This interface consists of the hydrophobic backbones exposed to the gas phase, and the hydrophilic side-chains buried under them. This interfacial configuration is deemed responsible for Schroeder's paradox, *i.e.* different Nafion water uptake of a liquid solvent and its vapour [Freger 2009, Choi 2003]. A physical explanation for this configuration is due to the different surface tensions of water and polymer [Bass 2010, Bass 2011]. In other words, the surface tension of water is much higher than that of hydrophobic matrix, then, the matrix phase must "spread" over the polymer, while the hydrophilic domains "sink" below the surface. In result, the free (top) surface of the ionomer film should have a significant hydrophobic character. In this section, we have characterized the Nafion film/vapor interface in terms of hydrophobicity and the roughness.

5.4.1 Hydrophobicity of the Nafion film surface

In order to analyse the hydrophobicity of the film surface, we have mapped the distribution of hydrophobic and hydrophilic units present at top of the film. We have considered the ionomer/vapour interface comprising the region located from 3.0 to 4.5 nm far from the wall. The hydrophobic species are the atoms of polymer except the sulfonate groups. The hydrophilic species include sulfonate groups, water molecules and hydronium ions. The interface was therefore divided in a grid with bits of volume $0.2 \times 0.2 \times 1.5$ nm for all cases. Each map corresponds to an average over 1000 configurations. For each bit, it is attributed a value n_i corresponding to the

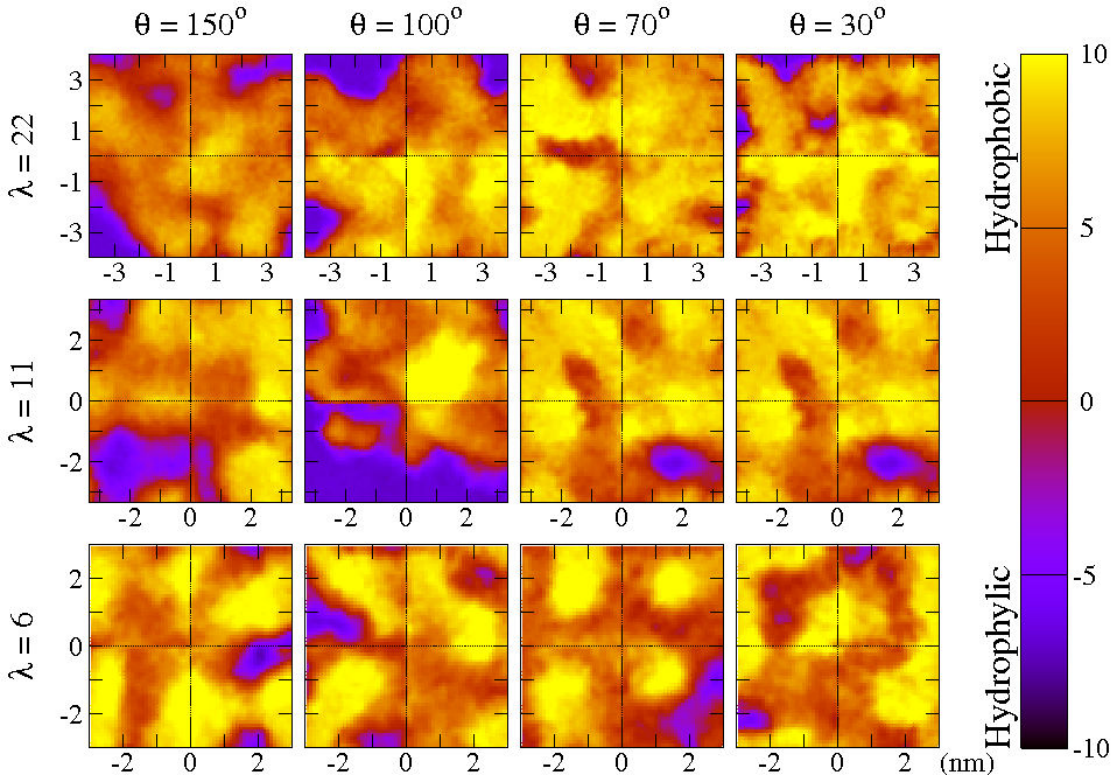

Figure 5.19: Density maps of the hydrophobicity of Nafion thin-film surface. The yellow color represent hydrophobic regions while the blue color represent hydrophilic regions

difference of the volume of hydrophobic and hydrophilic atoms occupying the same bit, *i.e.* $n_i = V^i_{phobic} - V^i_{philic}$. The volume of each atom is computed by using the LJ parameter σ as the "radius" of the atom. Therefore, a negative value corresponds to hydrophilic bits while positive values identify hydrophobic bits.

Figure 5.19 shows the maps for each film considered in this work. The yellow color represent hydrophobic regions while the blue one are the hydrophilic ones. The blue region formed on the maps, especially for the films $\theta = 150°$ and $100°$ at high λ, probably result from the water molecules present immediately below the polymer backbone. In contrast, the films with $\theta = 70°$ and $30°$ present significantly less blue regions, which means that the film has a massive hydrophobic layer on the top. In other words, this suggests that hydrophobicity is highly pronounced, in the case of films formed on hydrophilic wall. When decreasing water content, the films present similar surface hydrophobicity.

Our observations suggest that tuning the film/wall interactions can also modify

Nafion film/vapour morphology. For instance, the substrate with $\theta = 30°$ leads to a film configuration where the entire water content is confined under the polymer, whereas the ionomer backbone forms a "crust" hydrophobic layer. This "crust" should present high resistance to deformation, which could decrease water uptake. During PEMFC operation, this "crust" on the top could lead to transport losses. It could obstruct reactants (*e.g.* O_2 and H_2), coming from the CL pores, to cross the thin-film for reaching the catalyst sites. In contrast, the films formed on the substrate with $\theta = 150°$, show a configuration where a fraction of the ionomer backbone is in direct contact with the substrate. This reduces the concentration of polymer backbone on the top and, then, increases the presence of water. Clearly, this interface should be more favourable for water absorption. This observation is contrary to the one reported by Modestino *et al.* [Modestino 2012]. We can ascribe this difference to thin-films that were around 20 times thicker than the ones considered in our work.

5.4.2 Surface roughness

At the ionomer/vapour interface, the ionomer tends to flatten. In order to compare the flattening topography, we have investigated the surface roughness of each film. The roughness is often quantified by the vertical deviations of the real surface from its ideal form (say, the average vertical position). Thus, a Root Mean Square (RMS) value R_q is defined as

$$R_q = \sqrt{\frac{\sum_{i=1}^{N}(Z_i - \bar{Z})^2}{N}}, \tag{5.1}$$

where Z_i denotes the height of the i^{th} exposed atom on the film surface, $\bar{Z}$ is the mean height of all the surface atoms, and N is the number of the surface atoms [Huang 2012]. The surface atoms are defined as those having no other atoms in a square prism of edge 0.1 nm and height 5 nm above them. The surface of the film is mapped through the time average height of exposed polymer atoms (see figure 5.20)

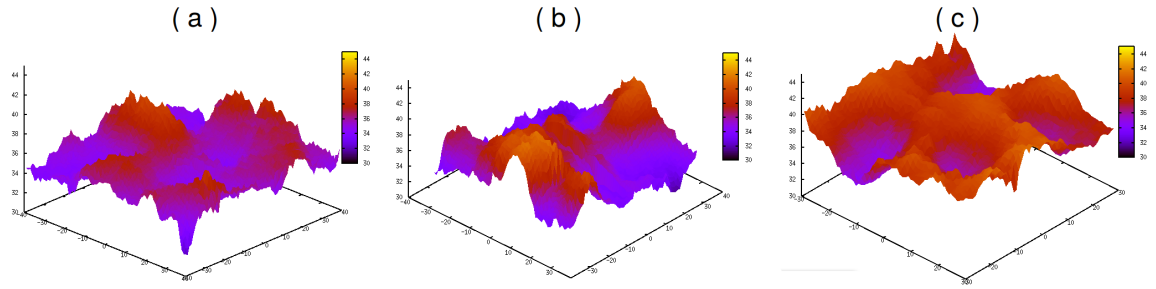

Figure 5.20: XY map of surface atoms position for thin-films $\theta = 70°$ and λ equal (a) 22, (b) 11 and (c) 6

Table 5.3 shows the values of RMS for each film studied. The roughness of the films surface are between 0.13-0.55 nm. Experimental measurement of RMS of Nafion surface in ambient air is found to be 0.35 [Bass 2010]. Interestingly, the roughness of the films at intermediate cases ($\theta = 100°$) are slightly higher when compared with other films. This can be attributed to their random cluster configuration. In contrast, for the cases $\theta = 150°$, 70° and 30°, the films approach to lamellar configurations.

Root Mean Square - RMS

θ (degree)	$\lambda = 22$	$\lambda = 11$	$\lambda = 6$
150°	0.16	0.25	0.29
100°	0.21	0.56	0.29
70°	0.13	0.46	0.24
30°	0.25	0.44	0.30

Table 5.3: Root mean square calculated using equation 5.1

According to Bass *et al.* [Bass 2010], the morphology of these interfaces is stable as far as the water vapour is not saturated. After that, the hydrophobic layer should deform and the buried hydrophilic groups eventually migrate to the surface. However, when the surface is initially hydrophobic (especially on low water contents), the high energetic and kinetic barriers associated with rearranging many groups may effectively keep the polymer kinetically trapped in this state for very long time [Bass 2010].

5.5 Conclusions

In this chapter we have investigated in detail the structure of Nafion thin-films formed on hydrophilic and hydrophobic surfaces. We have considered four types of

substrate: strong hydrophobic ($\theta = 150°$), intermediate ($\theta = 100°$), hydrophilic ($\theta = 70°$) and strong hydrophilic ($\theta = 30°$). Based on our structural analysis, we have proposed three classes of film, depending on the hydrophilic character of the substrate. The basic film morphologies are: *i)* sandwich (high λ) and inverted micelles (low λ) for the case of most hydrophobic surface; *ii)* connected cluster for intermediate; *iii)* bilayer (high λ) and multilamellar (low λ) for the hydrophilic and most hydrophilic surfaces. Moreover, we have shown that the local structure in films at $\lambda = 22$ appears to be the most sensitive to the wettability property of the substrate. In other words, the sandwich and bilayer film structure present particularly different SO_3^- and H_3O^+ solvation structure. We have discovered that, in contrast to the sandwich structure, the bilayer structure shows large and compact SO_3^- agglomerates, resulting in a poor hydration of H_3O^+ and SO_3^- .

We believe that these morphologies could be present in a wide range of PEMFC catalyst layers across a range of operating conditions. When fuel cell is operating at high currents, the important production of water in the cathode fills the catalyst layer pores, humidifying the impregnated ionomer. In these conditions, the ionomer on the top of the catalyst layer might be found in bilayer configuration, whereas on the supports, it might be organized in sandwich or connected-cluster configurations. Changes of the hydration condition and the substrate wettability properties during PEMFC operation could imply a rearrangement of the film, affecting its stability.

The reaction kinetic on catalyst surfaces should also be affected by the wettability of the surface. The adsorption of SO_3^- and coverage of other species can inactivate the catalyst surface. Our results have shown that SO_3^- groups can be adsorbed even when the hydrophilicity is favourable. This adsorption is more likely at low hydration conditions. Regarding the character of the ionomer/vapour interfaces, our results have shown that when the substrate is hydrophilic, the ionomer top surface tends to be more hydrophobic due to the formation of dense ionomer backbone. This would prevent reactants being absorbed by the ionomer film.

In conclusion, our results clearly show that water is the main active factor determining ionomer morphology. Changing the water/substrate interactions causes a redistribution of water, leading to ionomer reorganization. The implications of the nano-structure on the performance of PEMFC catalyst layers are mainly related to the efficiency on transport properties it can provide. Therefore, the next chapter is

dedicated to study the water and hydronium ions dynamics for each film presented above.

Chapter 6

Water and hydronium dynamics in Nafion ultra-thin films

Contents

6.1 Introduction

In order to understand the transport mechanisms occurring near the catalyst and catalyst support surfaces inside the PEMFC catalyst layer, a molecular level study of dynamics of water molecules and (positive) charges carriers in ionomer thin-films is essential. In hydrated Nafion, the ionomer chains have very slow dynamics, which means that its atoms vibrate around their equilibrium positions and no further configuration changes are observed on the typical timescale of a MD simulation (< 10 ns). In contrast, the dynamics of water molecules and protons are fast and they are of major interest when studying these kind of systems. In particular, proton dynamics is a combination of classical mass motion and structural diffusion mechanism via quantum processes [Kreuer 2000]. Referring to classical motion, the water and hydronium dynamics remind a liquid confined in a soft charged matrix, which can be fully investigated via classical models. However, a detailed description of proton transport requires more detailed models that include quantum effects. This goes beyond the scope of this work and it constitutes the most evident limit of our discussions.

In the previous chapter, we have shown how the hydrophilicity of the substrate where the Nafion thin-film is coated determines the morphology of the film. It is reasonable to expect that the substrate also affect the transport properties. In this chapter, we focus on exploring the impact of substrate hydrophilicity on the dynamics of water and hydronium inside hydrated ionomer films. We show that, indeed the film conformation is the determinant factor in transport properties. Therefore, we aim to clarify how the water channels, ionic clusters, and hydrophobic polymer barriers affect the movement of water and hydronium inside the films.

The main observables considered in this chapter include mean squared displacement, intermediate scattering functions, rotational correlation functions and residence time. We analyse the diffusion of water and hydronium ions for Nafion films discussed in the chapter 5 in both directions parallel and normal to the support. Moreover, we investigate the dynamics as a function of the distance from the surface in order to associate the dynamics with the organization of the ionomer. At last, we report a discussion of structural proton diffusion limited to a qualitative description of the local environment that could affect proton conductivity.

6.2 Translational dynamics

6.2.1 Mean-squared displacement

The vehicular diffusion of water molecules and hydronium ions was first analysed by calculating the mean-squared displacement (MSD) defined in equation 4.3. We have considered the trajectories during a total time interval of 5 ns for each film described in chapter 5. Snapshots of the systems have been stored every 50 ps for analysis. In order to avoid contributions coming from molecules in the gas phase, the MSD was calculated considering only the molecules inside the Nafion film. Therefore, only molecules diffusing in the region within 5 nm from the surface were taken into account. From this quantity, we have extracted the diffusion coefficients for each film and compared with the case of the ionomer in the bulk membrane.

Before going further in the MSD analysis, it is important to point out a general remark concerning the diffusion along x, y and z directions inside the films. Considering the film $\theta = 30°$ as an example, figure 6.1 shows the 1D contributions in the three dimensions (xyz) to the MSD for water and hydronium. Similar behaviour is found for all films. The plots clearly show the difference between the x and y components and the z component. Because of the finite thickness of the film, the molecules are not

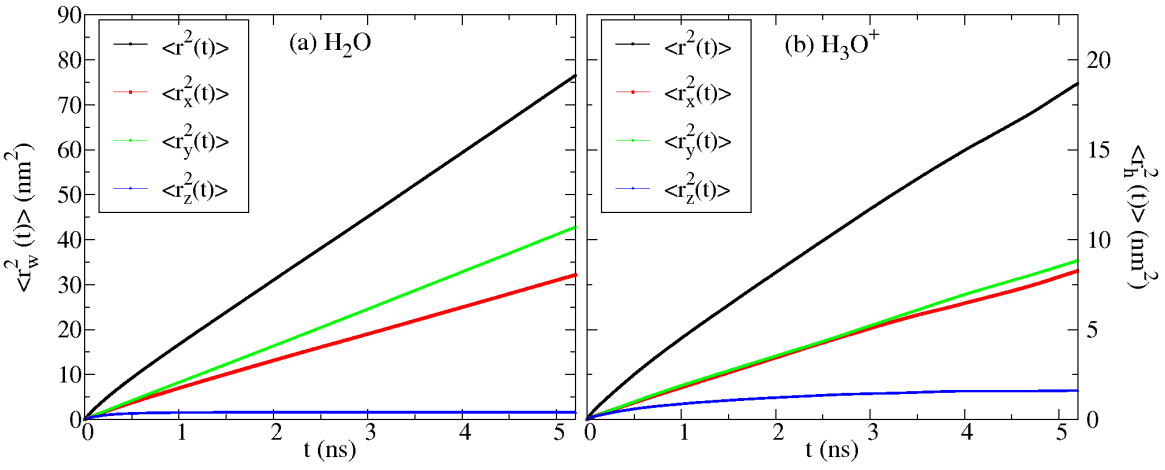

Figure 6.1: Mean-squared displacement of (a) water molecules and (b) hydronium ions in x, y and z direction at $\lambda = 22$ and hydrophilicity $\theta = 30°$. The mean-squared displacements normal to the surface are lower than those parallel to the surface.

diffusive in the direction normal to the surface, as we will explain in more details below. The z component significantly reduces the global MSD, which becomes inappropriate to be directly compared with the 3D MSD in the bulk membrane. Therefore, in the following we will distinguish displacements in different directions, namely $\langle r_{\parallel}^2(t)\rangle = \langle r_x^2(t)\rangle + \langle r_y^2(t)\rangle$ parallel to the surface (in-plane) and $\langle r_{\perp}^2(t)\rangle = \langle r_z^2(t)\rangle$ normal to the surface.

6.2.1.1 In-plane Mean-Squared Displacement

The in-plane mean-squared displacement for water molecules and hydronium ions calculated for each film are shown in figure 6.2. We recall that θ is the water droplet contact angle that varies from $\theta = 30°$ (hydrophilic wall) to $\theta = 150°$ (hydrophobic wall). The first evidence from figure 6.2 is that the time dependence of both water and hydronium displacements are affected by hydrophilicity of the wall where the film is deposited. For example, figure 6.2.(a) shows the MSDs of water molecules inside highly hydrated films ($\lambda = 22$). We observe that the water molecules have faster displacement in the cases $\theta = 70°$ and 150°, wherein the last one corresponds to the most hydrophobic surface. In contrast, in the case of $\theta = 100°$, where the surface is still hydrophobic, the water MSD is found to be the lowest one.

In order to better compare the MSDs curves, we have calculated the in-plane self-diffusion coefficients, as shown in figure 6.3. The diffusion coefficients for water ($D_{\parallel,w}$) and hydronium ($D_{\parallel,h}$) were calculated through the Einstein's relation defined in equation 4.4, using the slope of the MSD curves determined in the time interval from 1.5 to 2.5 ns, using $d = 2$ (2D diffusion coefficient). Figure 6.3 shows the diffusion coefficients for each value of ε_{philic} (the corresponding values of θ are indicated in the figure caption). By way of comparison, the diffusion coefficients for the bulk membrane at the corresponding values of λ are included in the graphs (dashed lines). For water content $\lambda = 22$, the water molecules inside the films have faster diffusion than inside the membrane. In contrast, the hydronium diffusion is found slower than in the membrane. When the water content decreases, both water and hydronium diffusion coefficients can be either higher or lower than in the membrane.

It is evident from figures 6.2 and 6.3 that, although some kind of modulation of diffusion with θ, we cannot conclude any continuous dependence of diffusion on the degree of hydrophilicity of the wall. This behaviour suggests that the molecular

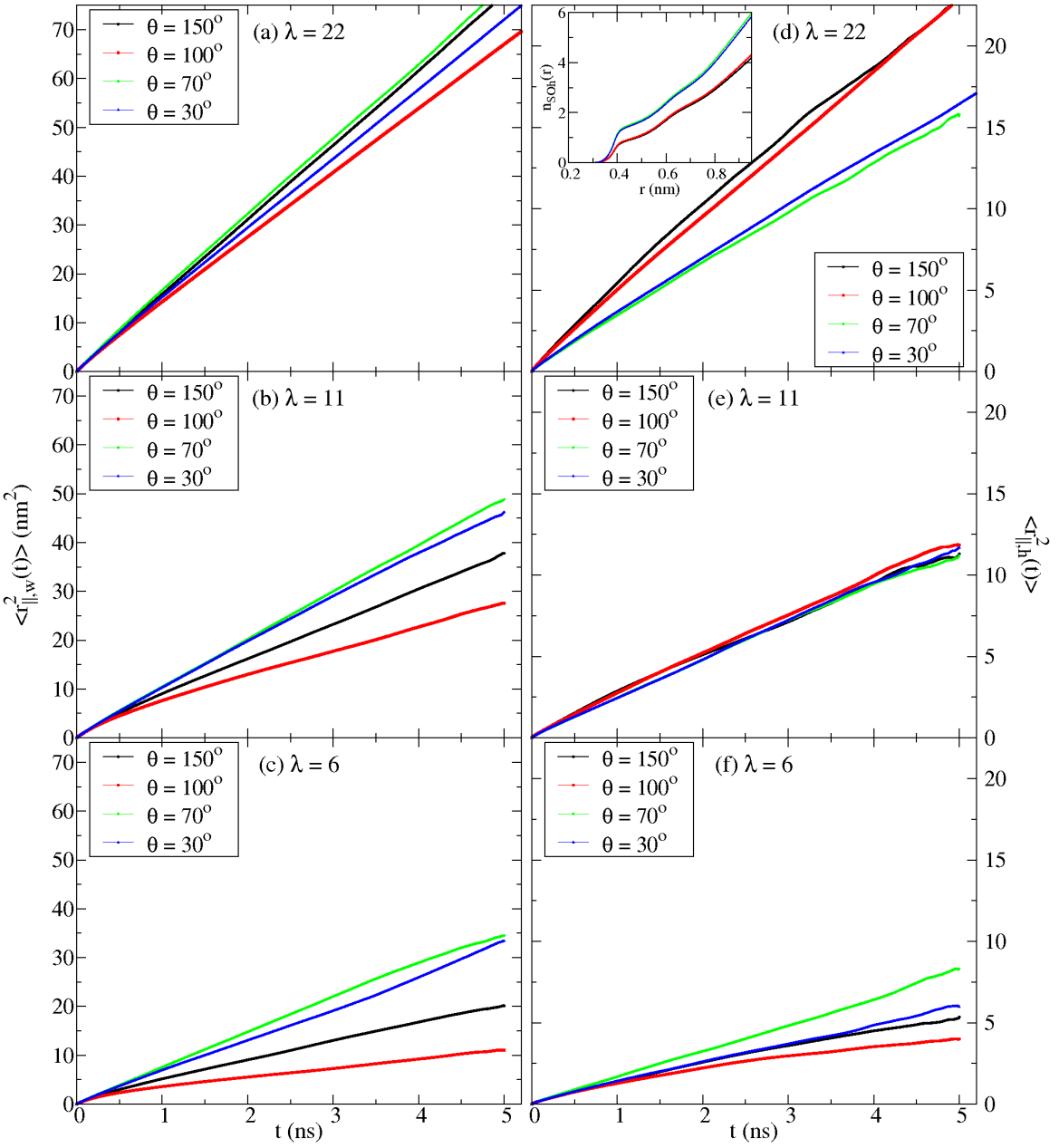

Figure 6.2: In-plane mean-squared displacement of (a,b,c) water and (d,e,f) hydronium inside the films indicated by θ, and hydration level λ equal (a,d) 22 (b,e) 11 and (c,f) 6.

motion is not directly governed by the strength of the interaction with the wall, but only indirectly, via the details of the film morphology. In order to better understand how the organization of ionomer affects the diffusion of water molecules, one must refer to the scheme of the film morphology shown in figure 5.14 of previous chapter.

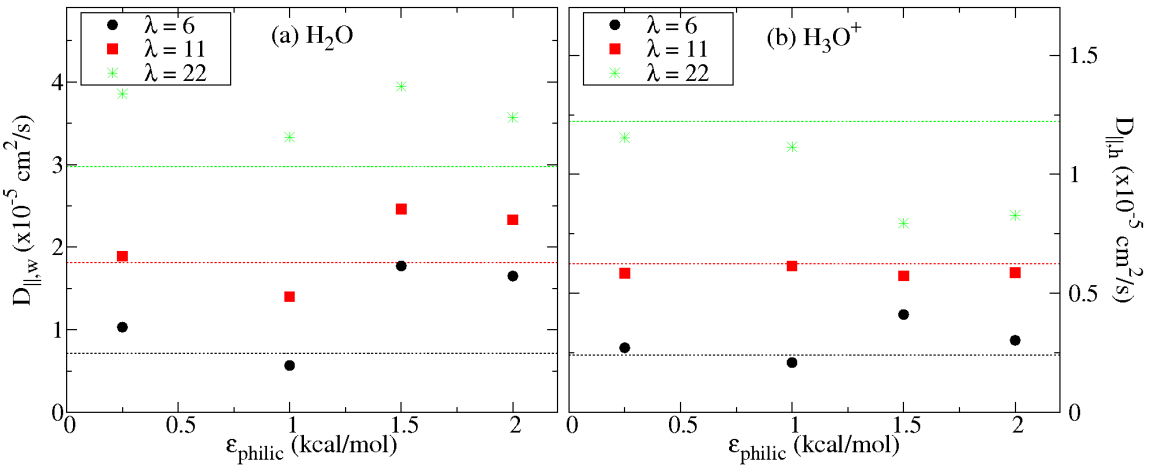

Figure 6.3: Water and hydronium in-plane diffusion coefficient for each film at $\lambda = 22$, 11 and 6. The dashed lines correspond to the values in the membrane for the respective λ. $\varepsilon_{philic} = 0.25$, 1.0, 1.5 and 1.5 correspond to $\theta = 150°$, $100°$, $70°$ and $30°$, respectively.

First, when the film presents a "sandwich" structure ($\theta = 150°$) or "bilayer" structure ($\theta = 70°$ and $30°$), the water-rich layer formed in the middle of the film or between the substrate and the polymer should provide favourable conditions for a relatively bulk-like diffusion of water molecules. In other words, these two types of morphology should enhance water displacement, as we observe in figure 6.2.(a). On the other hand, the intermediate case ($\theta = 100°$) displays a "random" structure, where the water molecules are able to diffuse inside water pools connected by narrow channels, reducing the water displacement.

When decreasing λ to 11, the dynamics becomes slower and the impact of the film morphology is even more evident (see figure 6.2.(b)). In the case of hydrophobic surface ($\theta = 150°$) the "sandwich" converts to a more "inverted micelles" structure. This structure leaves less room for water diffusion, and as a consequence the water MSD is lower when compared to "bilayer" structure ($\theta = 70°$ and $30°$). For the intermediate case, the "random" structure, the hydration level will influence the size of the water pools and ultimately the diffusion of water. Similar effects are observed for λ equal 6. In the hydrophilic cases, the formation of "multilamellar" structures also enhance water mobility, as shown in the figure 6.2.(c).

The hydronium diffusion is about 3 times slower than the diffusion of water molecules. In contrast to what we found for water, the impact of hydrophilicity is

more evident when the film is at high hydration. In other words, when decreasing λ, the MSDs seem to be not strongly affected by θ and the diffusion coefficients are close to the values for bulk membrane (see figure 6.3.(b)). This suggests that the morphology of the film does not play the same role on hydronium diffusion as in the water case. Indeed, the hydronium ions motion must be more hampered by the electrostatic attraction with SO_3^- groups than water molecules. For example, figure 6.2.(d) clearly shows two well distinguished cases for the MSD: larger MSD for the case of hydrophobic surface and lower for hydrophilic surface. This difference fully depends on the hydration structure of H_3O^+ around SO_3^- . As shown in the inset of figure 6.2.(d), the coordination number ($n_{SO_h}(r)$) of hydronium oxygen atoms around sulfur atoms of sulfonate groups are higher for the hydrophilic cases. Therefore, a larger number of H_3O^+ at the vicinities of SO_3^- groups implies a lower global hydronium diffusion inside the film.

In summary, the formation of water-rich layer in the films placed on hydrophilic surfaces and in hydrophobic at high hydration level, enhance in plane water diffusion of water molecules. The effects of the water domains shape has not the same importance for hydronium diffusion, which is primarily associated to the local structure of SO_3^- groups. Next, we will discuss the diffusion in the direction normal to the surface.

6.2.1.2 Normal Mean Square Displacement

The molecular motion normal to the surface was analysed through the water and hydronium MSDs in $\hat{z}$ direction, as displayed in figure 6.4. An obvious constraint exists for the diffusion, imposed by the finite thickness of the water domain in the $\hat{z}$ direction. We therefore expect that $\langle r_\perp^2(t)\rangle$ saturates to a finite value at long time. In figure 6.4.(a), we can observe this effect in the $\langle r_\perp^2(t)\rangle$ of water molecules for the case $\lambda = 22$. Here, the water molecules move fast enough to reach the boundaries of the film. Notice that the molecule does not reach the diffusive limit, *i.e.* the MSD is never a linear function with time. The constant $\langle r_\perp^2(t)\rangle$ values observed at time larger than 0.5 ns is approximately equal to the square size of the confinements in $\hat{z}$ direction. Hence, the water layers thickness can be estimated for the "sandwich" and "bilayer" films as 1.11 nm for the case $\theta = 150°$ and 1.17 and 1.24 nm for the cases $\theta = 70°$ and 30°, respectively. For the intermediate case ($\theta = 100°$), the thickness of the water domain extend up to 1.19 nm.

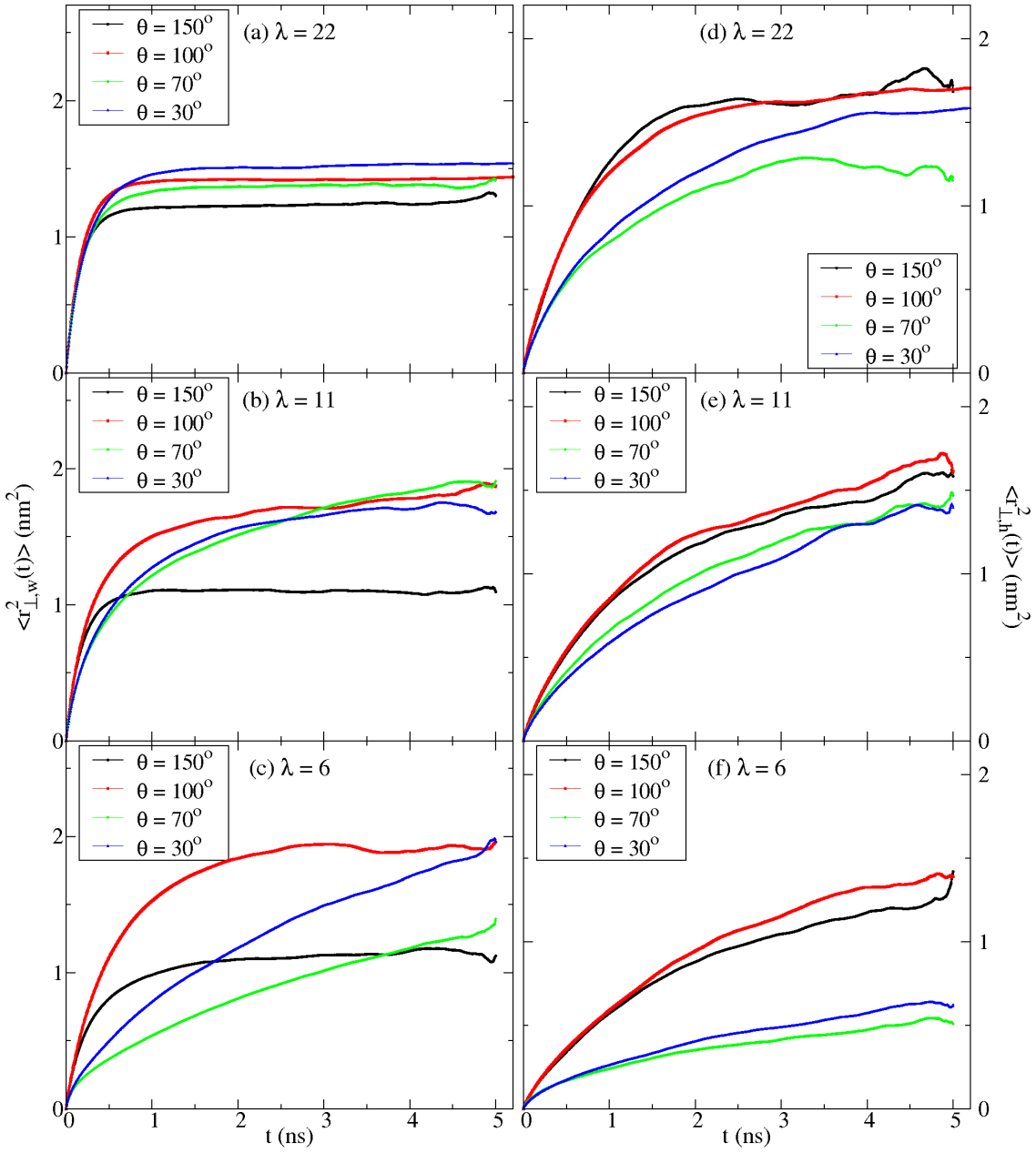

Figure 6.4: Normal mean square displacement of (a,b,c) water and (d,e,f) hydronium inside the films indicated by θ with hydration level λ equal (a,d) 22 (b,e) 11 and (c,f) 6.

When decreasing water content, the diffusion of water is slower and the saturation is no longer observed in hydrophilic cases ($\theta = 70°$ and $30°$). Also, the maximum displacement $\langle r_\perp^2(t)\rangle$ is higher at low λ, which means that water domain extends in z direction instead of being completely confined as a thin layer inside the film. More-

over, in the hydrophobic cases the water diffusion tends always to be faster than for hydrophilic cases independently of λ. One explanation is that on hydrophilic surfaces water is more attracted by the surface and then its mobility is reduced. Another interpretation could rely on the analysis of the distribution of SO_3^- groups inside the film (we will come back on this discussion later). At $\lambda = 6$, the perpendicular water motion is reduced also because in such films the water domains are poorly connected in $\hat{z}$ direction.

Similar behaviour is found for the hydronium ions diffusivity (see figure 6.4.(d), (e) and (f)). The hydronium ions tend to cross the film thickness more rapidly in the hydrophobic cases than in the hydrophilic cases. The main reason for that can be attributed to the spatial disposition of SO_3^- agglomerates. For instance, in a "bilayer" film, the SO_3^- are massively found at distance around 3 nm from the surface. Then, hydronium would hardly move away from the SO_3^- layer in the direction to the wall. In the context of PEMFC, this should have implication on motion of proton carriers inside the cathode. For instance, the proton carriers could be trapped close to SO_3^- groups, which mitigate the access of the proton on the catalyst sites for participating in the oxygen reduction reaction (ORR).

In conclusion, both lateral and perpendicular diffusions of water and hydronium appears to be governed by the film morphology, while their direct interaction with the substrate plays an indirect role only. Thus, we found that diffusion does not depend on the wettability of the surface following any simple relation, which makes the understanding of the dynamics a complex issue. Also, the number of cases studied is not sufficiently extended to trace a function of diffusion versus θ. However, we are convinced that the sample of the films above are enough to explore the local dynamics and then identify the factors that can enhance or mitigate water diffusion. In the next section, we analyse in more details the diffusion of water molecules in different regions within the film.

6.2.2 Water diffusion across the film thickness

Due to the strong structural heterogeneities observed inside the ionomer film (see chapter 5), we expect that the transport of water and hydronium is not isotropic. The film may have some regions where the molecular mobility is more prominent. In

particular, the diffusion may depend on the molecule distance z from the surface. To quantify space-dependent transport, we restrict to the xy-plane, slice the film in overlapping slabs of width 0.5 nm with spacing between them equal to 0.1 nm, and consider the following generalized form of the mean-squared displacement [Scheidler 2004] :

$$\langle r_{\parallel}^2(z,t)\rangle = \frac{1}{N}\sum_{i=1}^{N}\left\langle |\vec{r}_i(t)-\vec{r}_i(0)|^2\delta(z_i(0)-z)\right\rangle . \tag{6.1}$$

Here $\langle ...\rangle$ is the thermodynamic average and $\vec{r}_i(t)$ is the xy projection of the three-dimensional position vector of the oxygen atom of water molecule $i = 1, ..., N$. Equation 6.1 considers only molecules that at $t = 0$ had a distance z from the wall. Nevertheless, the statistical uncertainty might still be relatively large, specially in the slabs containing few number of water molecules (for example in polymer-rich slabs). Next, we define a z-dependent diffusion coefficient ($D_{\parallel,w}(z) = \langle r_{\parallel}^2(z,t)\rangle/4t$), via the Einstein relation. This strategy has been demonstrated to properly characterize space-dependent translational diffusion in confined geometries [Scheidler 2000, Scheidler 2002, Scheidler 2004].

Figure 6.5 shows the obtained diffusion coefficients as a function of the distance from the surface for each film. For $\theta = 150°$ and 100°, $D_{\parallel,w}(z)$ is quite uniform across the film, and everywhere close to the average total values. In contrast, for $\theta = 70°$ and 30° dramatic changes are visible, following the accumulation of the ionomer at intermediate and large distance, with the consequent formation of pure water layers at small z (the films display bilayer structures). Diffusion becomes strongly heterogeneous, steadily decreasing at distances $z > 2.5$ nm. In the region close to the wall, diffusion is enhanced compared to the integrated value, as also reported in the case of simple liquids confined by smooth boundaries [Scheidler 2000, Scheidler 2002, Scheidler 2004]. $D_{\parallel,w}(z)$ becoming strongly suppressed at higher distances, where interactions with polymer backbones and sulfonate groups are very strong.

Although in principle, the formation of water-rich layers with the polymer on the top can justify the decreasing of $D_w^{\parallel}(z)$ for hydrophilic cases, knowledge of the water and ionomer distributions only is not sufficient to completely explain the behaviour of $D_w^{\parallel}(z)$. For example, the water-rich layer is also formed in the case of $\theta = 150°$ at $\lambda = 22$, but the diffusion coefficient does not show any strong decay. Indeed, the modulation of $D_w^{\parallel}(z)$ should depend on the local environment across the film. In order

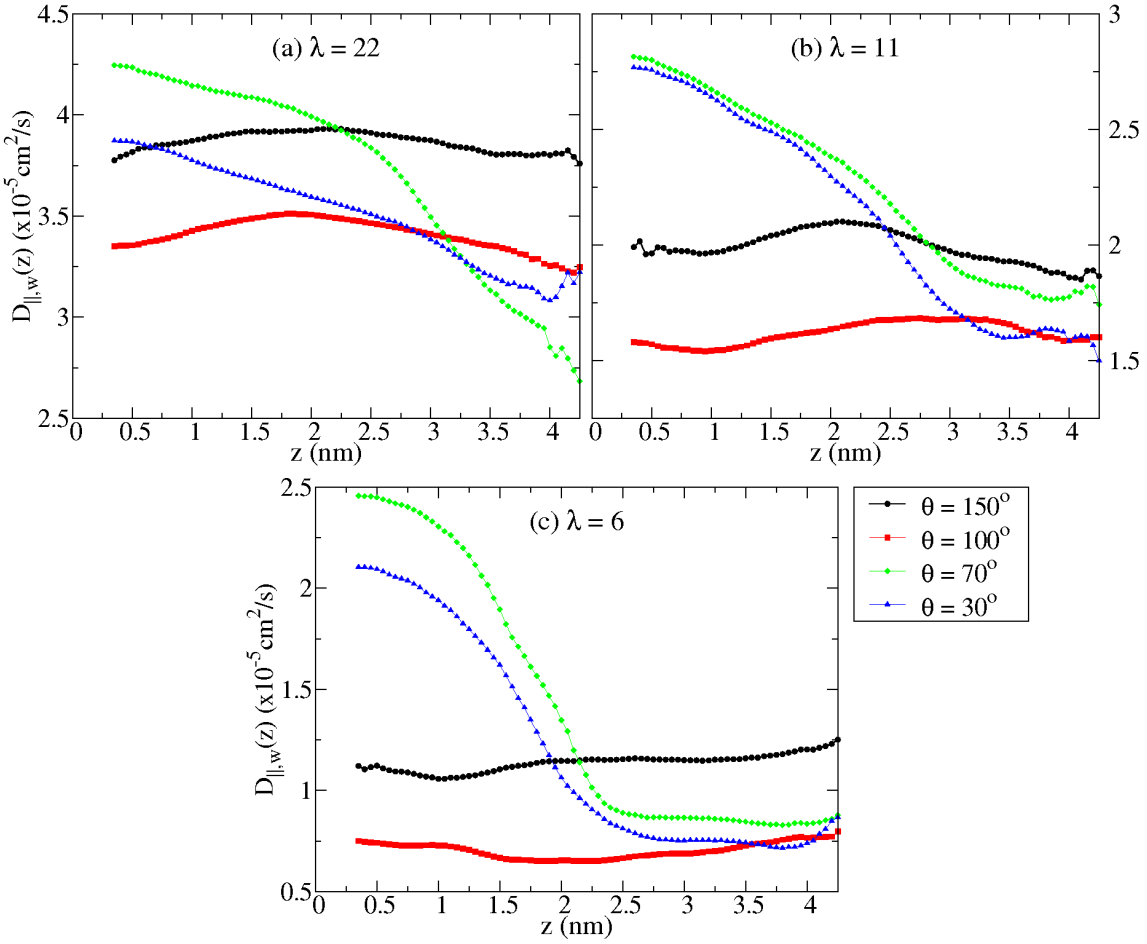

Figure 6.5: In-plane diffusion coefficient of water as a function of the distance z from the surface for diverse films with hydration level (a) $\lambda = 22$, (b)11 and (c) 6.

to find the relation between $D_w^{\|}(z)$ and the ionomer structure, we turn our attention to the SO_3^- cluster distribution discussed in figure 5.12. The pronounced peaks between 2.25 - 3.5 nm for $\lambda = 22$ and 11 and between 2.75 - 3.25 nm for $\lambda = 6$ observed for hydrophilic cases strongly suggest that the water dynamics is also governed by the formation of SO_3^- agglomerates. For hydrophobic cases the SO_3^- clusters are more homogeneously distributed inside the film with a lower average size, which explains the fact that the diffusion coefficient remains almost constant across the film. Therefore, it is important to emphasize that the water dynamics is affected by the structural configuration of SO_3^- clusters and not by mere SO_3^- presence.

In conclusion, the fact that water self-diffusion is reduced by interactions with

sulfonate groups sites has been largely reported in the literature [Paddison 2000, Kreuer 2000]. The water molecules are classified as bounded (slow), loosely bounded and free water (fast) to SO_3^- [Kim 2003]. The additional contribution coming from our observations is that spatial distribution of the SO_3^- groups, whether they are agglomerated or dispersed, is a crucial factor for local diffusion. Indeed, the formation of large and compact SO_3^- clusters requires the presence of water molecules and hydronium ions that screen the repulsion between SO_3^- groups. This configuration should be stable, consequently, this keeps the water at low motion. Therefore, more compact the SO_3^- groups agglomerates, more important in their impact on the global water dynamics. Concluding, from our observations we propose two main factors that govern the overall diffusion of water inside film: water domains shape and the degree of SO_3^- aggregates.

6.3 Relaxation dynamics

6.3.1 Self-intermediate scattering function

Having characterized in detail the vehicular diffusion of water molecules inside the ionomer films, we now perform a similar investigation for the structural relaxation dynamics. We have focused on the intermediate scattering function $F(\vec{q},t)$, defined as

$$F(\vec{q},t) = \frac{1}{N}\sum_{i=1}^{N}\sum_{j=1}^{N}\langle exp\left[-i\vec{q}\cdot(\vec{r}_i(t)-\vec{r}_j(0))\right]\rangle\,. \tag{6.2}$$

Here, $\vec{r}_i(t)$ is the vector position at time t and $\vec{q}$ is the wave vector $\vec{q} = \frac{2\pi}{L}(n_x, n_y, n_z)$, where n_i are integers and L is the size of the simulation box. The self intermediate scattering function, $F_s(\vec{q},t)$, which contains information about single particle motion, is obtained by restricting the double summation of equation 6.2 to the terms with $i = j$:

$$F_s(\vec{q},t) = \frac{1}{N}\sum_{i=1}^{N}\langle exp\left[-i\vec{q}\cdot(\vec{r}_i(t)-\vec{r}_i(0))\right]\rangle\,. \tag{6.3}$$

The physical interest for computing these quantities is related to the fact that coherent and incoherent neutron scattering experiments provide information related to the total

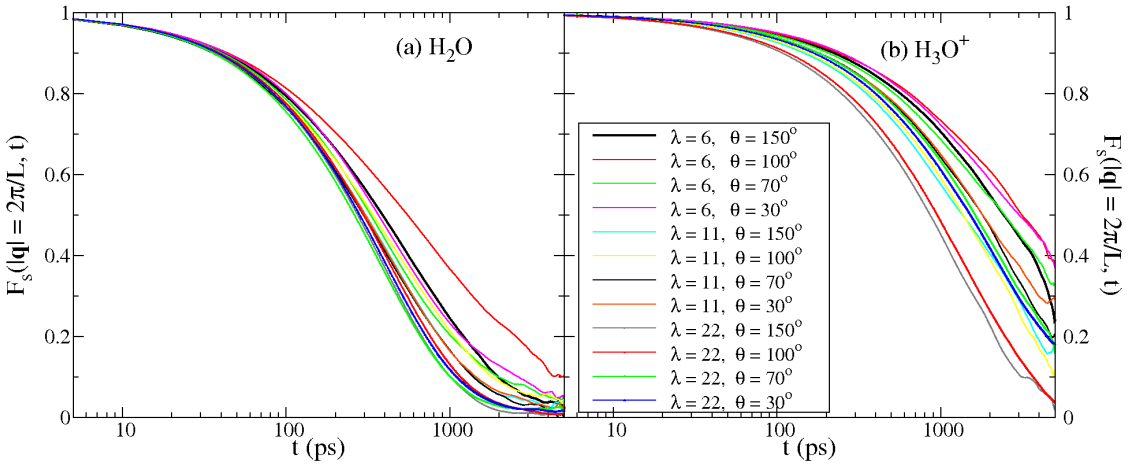

Figure 6.6: Incoherent (self) intermediate scattering functions $F_s(\vec{q},t)$ at $|\vec{q}| = 1.05$, 0.92 and 0.78 nm^{-1} for $\lambda = 6$, 11 and 22 respectively calculated for (a) water and (b) hydronium.

and self-intermediate scattering functions, respectively. The $F_s(\vec{q},t)$ provides information regarding the temporal decay density fluctuations as a function of the spatial scale (monitored by the wave vector $\vec{q}$). In this section we explore for each ionomer film, the time dependence of self-intermediate scattering function at given wave-vector. We concentrate on $F_s^{\parallel}(\vec{q},t)$ for a $\vec{q}$-vector parallel to the wall. For simplicity, we consider the smallest wave vectors $\vec{q} = \frac{2\pi}{L}(1,0,0)$ and $\frac{2\pi}{L}(0,1,0)$. We note that the value of L is dependent on the values of λ, thus, $|\vec{q}|$ varies for each λ, with $|\vec{q}| = 1.05$, 0.92 and 0.78 nm^{-1} for $\lambda = 6$, 11 and 22, respectively.

In figure 6.6 we show the self-intermediate scattering functions for water molecules and hydronium ions in each film. The shape of the curves is not exponential. However, being interested in a qualitative dependence of relaxation time τ_q on θ and λ, we impose a generic exponential relaxation $F_s(2\pi/L,t) \approx exp(-t/\tau_q)$ and extract a relaxation time as $F_s(2\pi/L,\tau_q) = e^{-1}$. We show in table 6.1 extracted from the data in figure 6.6. Since the decay of $F_s(\vec{q},t)$ depends on the magnitude of wave vector $\vec{q}$, we restrict our comparison to films at the same hydration level.

As expected, the values of τ_q presented in table 6.1 confirm a non-trivial dependence on θ, as found for diffusion coefficient. The water relaxation times are the highest for films $\theta = 100°$, while hydronium relaxation times are the highest for $\theta = 70°$ and 30°. This observation is qualitatively similar to those reported in the translation diffusion, which means the lowest water dynamics is in the films that present random

Structural relaxation time of H_2O : τ_q (ps)

	$\lambda = 6$	$\lambda = 11$	$\lambda = 22$
θ (degree)	$\|\vec{q}\| = 1.05$ nm^{-1}	$\|\vec{q}\| = 0.92$ nm^{-1}	$\|\vec{q}\| = 0.78$ nm^{-1}
150°	0.628×10^3	0.478×10^3	0.404×10^3
100°	0.998×10^3	0.552×10^3	0.441×10^3
70°	0.514×10^3	0.463×10^3	0.389×10^3
30°	0.583×10^3	0.473×10^3	0.421×10^3

Structural relaxation time of H_3O^+ : τ_q (ps)

	$\lambda = 6$	$\lambda = 11$	$\lambda = 22$
θ (degree)	$\|\vec{q}\| = 1.05$ nm^{-1}	$\|\vec{q}\| = 0.92$ nm^{-1}	$\|\vec{q}\| = 0.78$ nm^{-1}
150°	3.977×10^3	2.318×10^3	1.281×10^3
100°	5.174×10^3	2.156×10^3	1.443×10^3
70°	3.277×10^3	2.724×10^3	2.528×10^3
30°	5.043×10^3	3.104×10^3	2.368×10^3

Table 6.1: Relaxation time $\tau_q$for the self-intermediate scattering functions showed in figure 6.6 calculated by the threshold method $F(q, \tau_q) = e^{-1}$.

configurations ($\theta = 100°$), while the lowest H_3O^+ dynamics is result of large SO_3^- clusters formed on the films for hydrophilic cases ($\theta = 70°$ and 30°). Next, we will discuss the local relaxation dynamics as a function of the distance from the surface, similar to what have been reported for self-diffusion coefficient.

6.3.2 Relaxation time *vs.* distance from the surface

We now investigate the space-dependent structural relaxation time, τq, from a generalized self-intermediate scattering function,

$$F_s(\vec{q}, z, t) = \frac{1}{N} \sum_{i=1}^{N} \langle exp\left[-i\vec{q} \cdot (\vec{r_i}(t) - \vec{r_i}(0))\right] \delta(z_i(0) - z) \rangle \tag{6.4}$$

where $F_s(\vec{q}, z, t)$ considers only particles that at initial time $t = t_0$ had a distance z from the surface [Scheidler 2002]. We only present results for the water molecules. Indeed, poor statistic for hydroniums does not allow us to extract reliable information. The function is averaged over wave vectors $\vec{q}$ parallel to the wall, as considered in the previous calculation. Next, we calculate $\tau_q(z)$, the relaxation time as function of z, by imposing $F_s(\vec{q}, z, \tau_q) = e^{-1}$.

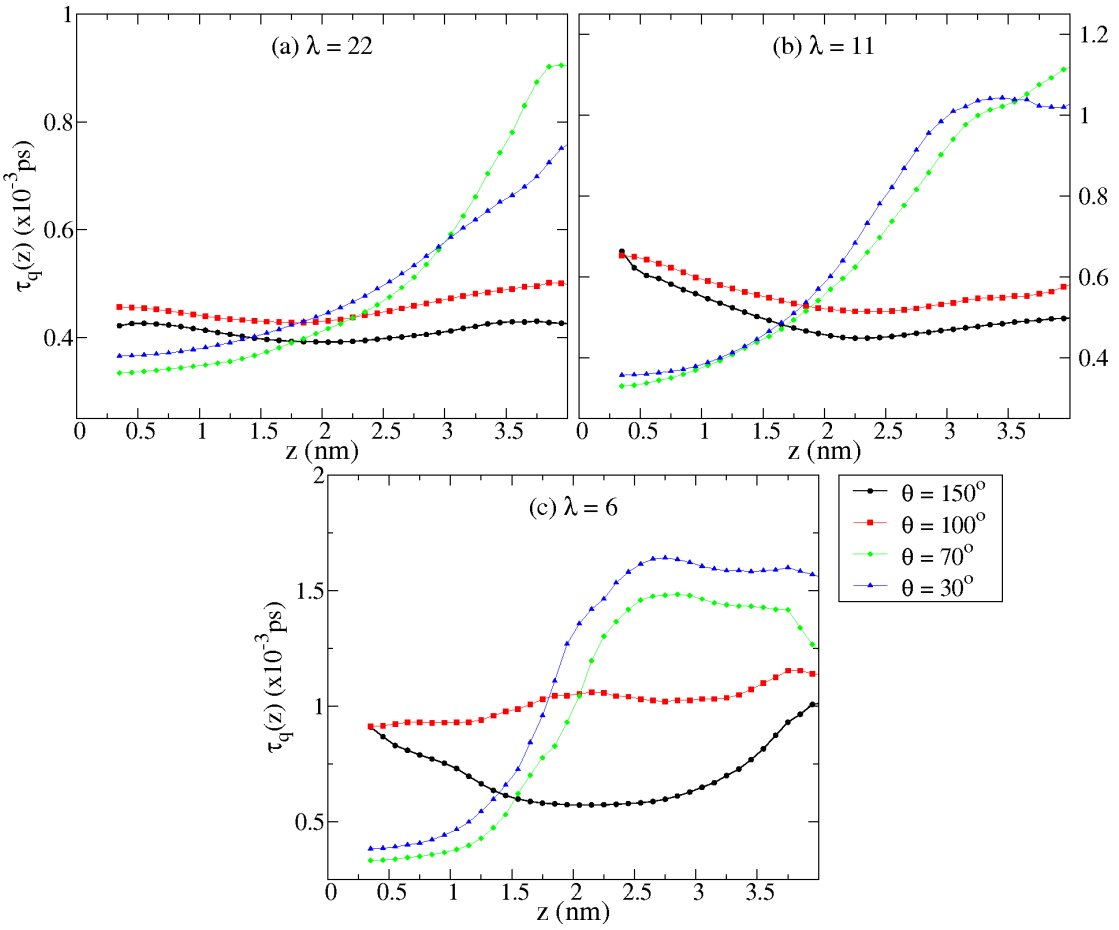

Figure 6.7: Structural relaxation time $\tau_q(z)$ of water molecules as a function of distance z from the surface calculated by the threshold method $F_s(\vec{q}, z, \tau_q) = e^{-1}$.

Figure 6.7 shows $\tau_q(z)$ for the different indicated values of θ and λ. For the hydrophilic cases ($\theta = 70°$ and $30°$), $\tau_q(z)$ increases with distance z from the wall, which means that the dynamics of water molecules far from the wall is suppressed. These results are consistent to what we have observed for the self-diffusion coefficient $D_{\|,w}(z)$, and therefore, they are attributed mainly due the formation of large SO_3^- in the top half of the film. The apparent modulation of $\tau_q(z)$ in the film $\theta = 150°$ at $\lambda = 6$ (see figure 6.7.(c)) can be ascribed to difficult sampling for low λ, with no qualitative impact on our conclusions.

To conclude, by implying a more involved analysis of self-diffusion and structural relaxation at different distances from the wall, we have discovered that water dynamics

is highly heterogeneous across the films with "bilayer" and "multilamella" structures. In a much simpler way than in the studies of Nafion membrane, we have explored how sulfonic acid groups configurations can affect the dynamics of water. Therefore, we have characterized the main contributions arising from the heterogeneity of water dynamics in Nafion. Next, we will complete our discussion by considering the molecular rotational dynamics.

6.4 Rotational dynamics

6.4.1 Rotational autocorrelation function

The molecular rotational dynamics of water molecules and hydronium ions has a concrete physical connection to the translational diffusion and the structural relaxation. Another particular interest on studying this dynamics is relation with the dynamics of formation and breaking of hydrogen bonds formed between water-hydronium and water-water molecules, important for proton transport. In this section we therefore have dedicated to study the orientational autocorrelation function of water and hydronium. Here, we have defined the molecular orientation vector $\hat{u}_i(t)$ in the same way we have done in section 5.2. For water molecules we choose $\hat{u}_i(t)$ as the normal vector of the H_2O plane, *i.e.* normal to the plane formed by oxygen-hydrogen bonds. For hydronium ions the orientation vector is the normal to the plane formed by the three hydrogen atoms. The orientational motion behaviour is accessible via the dynamics of the Legendre polynomials calculated from the orientation vectors. Some of these polynomials are directly related to the response functions detected by different experimental techniques [Simon 1990]. These techniques generally measure an autocorrelation function of the unit vector $\hat{u}_i$ given by

$$C_l(t) = \frac{1}{N}\left\langle \sum_{i=1}^{N} P_l(\vec{u}_i(t)\cdot\vec{u}_i(0)) \right\rangle, \tag{6.5}$$

where P_l is Legendre polynomial of order l, where $P_1 = x$ and $P_2 = \frac{1}{2}(3x^2-1)$ for $l = 1$ and 2, respectively. The time scale of rotational relaxation is short (less than 2 ps). Therefore, $C_l(t)$ were calculated considering short trajectories of time interval equal 100 ps with snapshots stored with a frequency of every 0.5 ps. The rotational

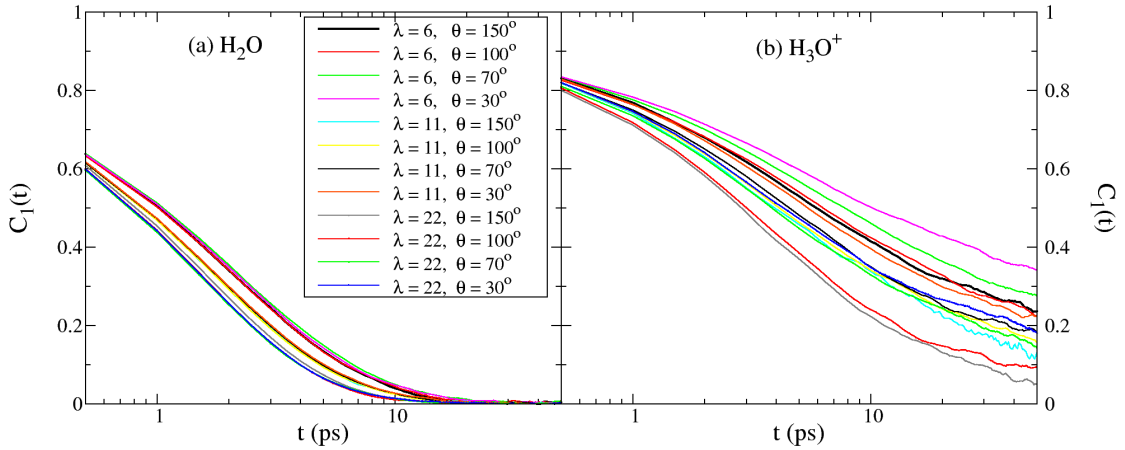

Figure 6.8: Rotational autocorrelation functions of the Legendre polynomials of order 1 calculated for (a) water and (b) hydronium.

autocorrelation function of polynomial of order 1 for water and hydronium are shown in figure 6.8. We have estimated the rotation relaxation time τ_l by the threshold method $C_l(\tau_l) = e^{-1}$, imposing $C_l(t) \approx exp(-t/\tau_l)$.

Table 6.2 lists the rotational relaxation time τ_l of the Legendre polynomials of order $l = 1$ and 2. By comparing the films at the same hydration level, we observe that in the case of H_3O^+ , the values of τ_l are always higher for the hydrophilic cases ($\theta = 70°$ and $30°$), *i.e.* the ion rotation motions are slower. This is related to the fact that for these cases, there are more hydronium ions close to SO_3^- groups, as indicated by the coordination number n_{SOh} (see table 5.1). Also, we recall that the SO_3^- groups are more compact in the hydrophilic case. This is possible because H_3O^+ intersperse SO_3^- groups and they are orientated in a way to have the minimum electrostatic energy. This orientation should be relatively stable and, therefore, the rotation motion of H_3O^+ is hampered.

In contrast, the water molecule rotation is not strongly sensitive to the hydrophilicity of the wall θ. We observe a slight difference for the values of τ_l among films with the same hydration level. When it is compared with τ_l in the membrane, the rotational dynamics is always slightly faster in the films. Also, the τ_l increases with water content, approaching to the limit of bulk-like water, as expected. Nevertheless, the rotational dynamics should depend on the local organization of the film, as observed for self-diffusion and structural relaxation. Therefore, in the following, we analyse the water rotational relaxation time as function of the distance from the

Rotational relaxation time of H_2O : τ_l (ps)

	$\lambda = 6$		$\lambda = 11$		$\lambda = 22$	
θ (degree)	τ_1	τ_2	τ_1	τ_2	τ_1	τ_2
150°	1.81	0.53	1.50	0.48	1.41	0.47
100°	1.81	0.53	1.50	0.48	1.35	0.46
70°	1.91	0.59	1.53	0.49	1.32	0.46
30°	1.87	0.57	1.54	0.48	1.34	0.47
membrane	2.001	0.64	1.69	0.50	1.38	0.47

Rotational relaxation time of H_3O^+ : τ_l (ps)

	$\lambda = 6$		$\lambda = 11$		$\lambda = 22$	
θ (degree)	τ_1	τ_2	τ_1	τ_2	τ_1	τ_2
150°	13.58	3.03	8.31	1.96	5.05	1.44
100°	15.12	3.12	8.55	1.90	5.41	1.43
70°	19.34	3.66	9.05	2.21	7.99	1.95
30°	35.04	4.94	11.95	2.51	9.05	2.07
membrane	8.23	2.40	7.31	1.97	4.47	1.40

Table 6.2: Rotational relaxation time (τ_l) of water and hydronium calculated from the correlation function $C_l(t)$ of the Legendre polynomials of order $l = 1$ and 2 (see equation 6.5). τ_l is estimated by the threshold method $C_l(\tau_l) = e^{-1}$.

surface, similar to the translational cases considered above.

6.4.2 Rotational relaxation time *vs.* distance from the surface

The water rotational dynamics as function of distance from the surface was calculated via a generalization of equation 6.5:

$$C_l(t,z) = \frac{1}{N}\left\langle \sum_{i=1}^{N} P_l(\vec{u}_i(t)\cdot\vec{u}_i(0))\delta(z_i(0)-z)\right\rangle, \tag{6.6}$$

$C_l(t,z)$ considers molecules found in the slab centred at distance z at initial time t_0. We compute the local rotational relaxation time, $\tau_l(z)$, by fitting a stretched exponential $exp(-t/\tau_l(z))$ to $C_l(\tau_l,z)$. Here we will show only results of Legendre polynomials of order $l = 1$. Similar qualitatively results are found for $l = 2$.

Figure 6.9 shows $\tau_1(z)$ for every film indicated by θ and λ. In contrast to what we observed for diffusion coefficient $D_w^{\parallel}(z)$ and structural relaxation time $\tau_q(z)$, $\tau_1(z)$

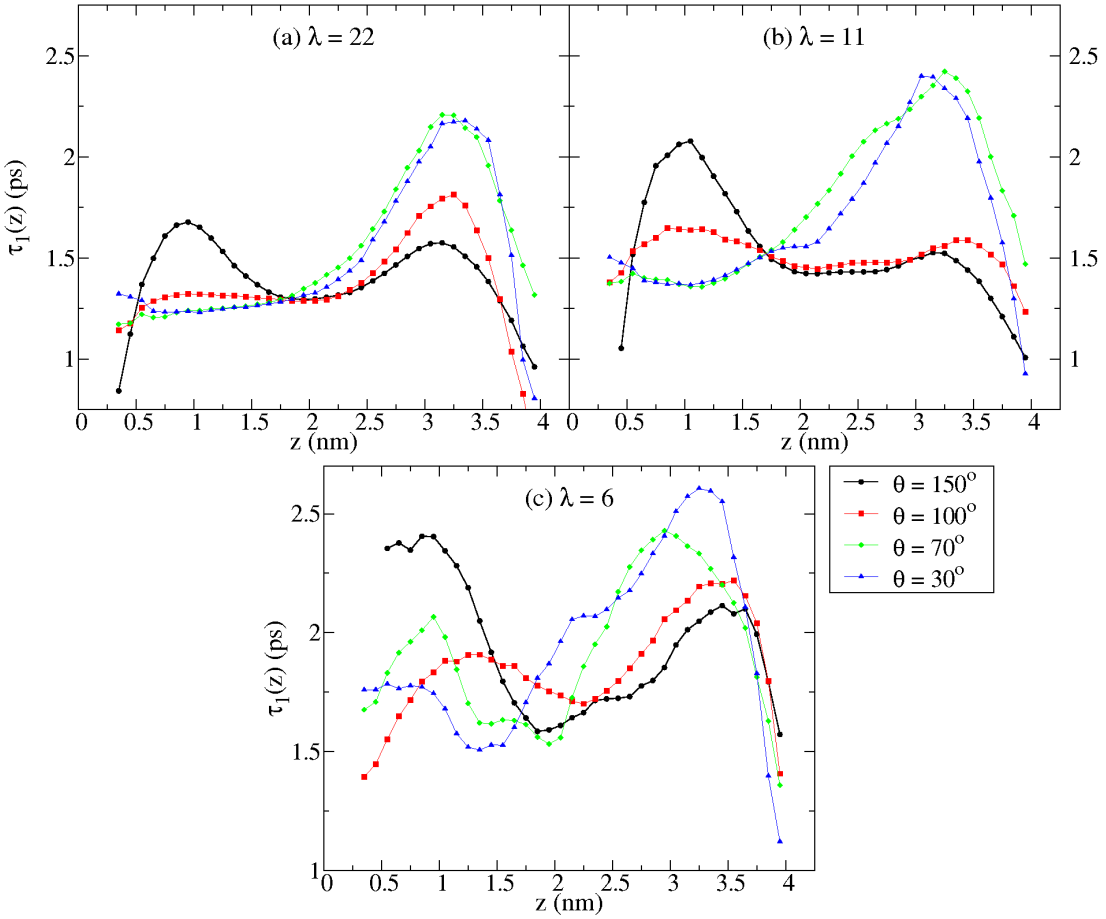

Figure 6.9: Rotation relaxation time for the water normal rotational correlation function of Legendre polynomials of the order $l = 1$ as function of the distance z from the surface.

is isotropic in both hydrophilic and hydrophobic cases. In figure 6.9.(a), we clearly observe two well-defined maximums for the case $\theta = 150°$. This modulation is fully coupled with the SO_3^- density profile $\rho_{SO_3^-}(z)$ discussed in figure 5.12. The maxima found in $\tau_l(z)$ (around 0.9 nm and 3.1 nm) correspond to the maxima of $\rho_{SO_3^-}(z)$. The same trend is observed for all the films. This suggests that the effect of the interaction of water molecule dipoles with sulfonate groups is striking. Consequently, we observe a non-monotonic modulation of the rotational relaxation time, which strictly follows the SO_3^- mass density distributions.

In conclusion, we have found that the rotational motion is more sensitive to the local structure than the translational motion. The fact of having SO_3^- agglomerates

more compact or disperse seems to not have influence on the relaxation time. Therefore, we can conclude that the rotational dynamics is governed only by the presence of SO_3^- groups, without given relevance to the configuration of ionic clusters.

6.5 Mean residence time

In our previous analysis we have shown that SO_3^- clusters strongly influence solvent dynamics. In order to shed more light on dynamical behaviour in the vicinity of SO_3^- groups, we use the definition of mean residence time to directly investigate the mobility of water and hydronium at SO_3^- groups solvation shell. Also, we will use the same approach for investigating water mobility in H_3O^+ hydration shell.

The mean residence time of a molecule is defined as being the time span during which the molecule stays in a given region or hydration shell. An approach commonly used in the literature is to define this time based on the idea of persisting coordination. Therefore, the lifetime of molecules near the ionic groups or near the wall is estimated by considering the residence correlation function [Lee 1994],

$$R(r,t) = \frac{1}{N_r(t)} \sum_{i=1}^{N} \left[h_i(r,t) \cdot h_i(r,0) \right], \tag{6.7}$$

where $h_i(r,t)$ is a Boolean variable that is 1 if molecule i is in a region r at time t and 0 otherwise, and $N_r(t)$ is the average number of molecules in the region r at time t. The mean residence time τ_{MR} is therefore obtained by fitting $R(r,t)$ to an exponential function $exp(-t/\tau_{MR})$.

6.5.1 Mean residence time near sulfonate groups and hydronium ions

The mean residence times of water molecules and hydronium ions (τ_{MR}) around SO_3^- groups were computed depending on the distance from the SO_3^- groups. Figure 6.10 shows these values calculated for the distance 0.2-0.4 nm from the SO_3^- groups belonging to the films at different λ and θ. The residence time in the membrane at the corresponding values of λ are included in the graphs (dashed lines) for comparison. The complete list of residence time, corresponding to the distance 0.4-0.6 nm and

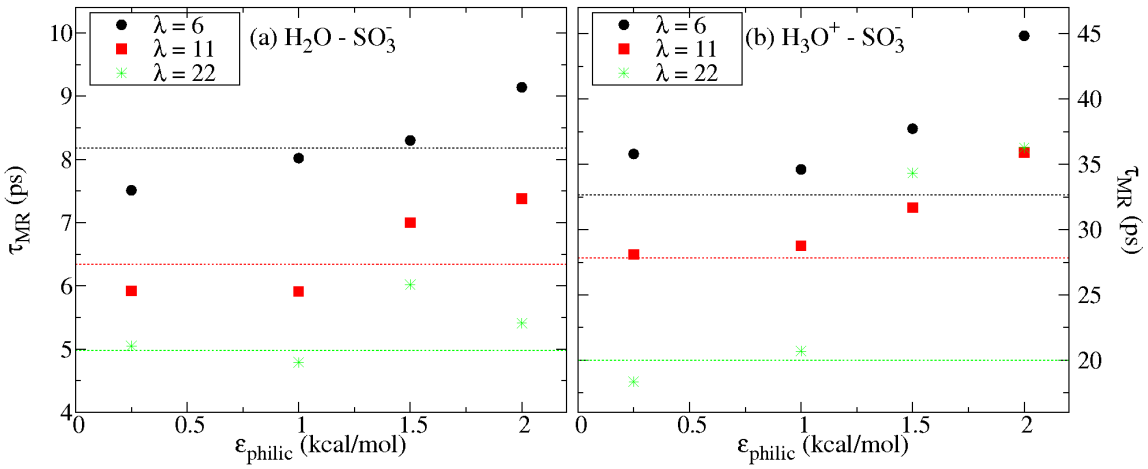

Figure 6.10: Mean residence time of (a) water molecules and (b) hydronium ions at distance from 0.2 to 0.4 nm from SO_3^- group.

0.6-0.8 nm are shown in table 6.3.

Table 6.3 shows that hydronium ions have residence time more than 3 times longer than water around the sulfonate groups. This property depends on effective interactions between sulfonate groups and the solvent molecules. A high residence time indicates low mobility of hydronium ions as a result of their strong electrostatic interactions with fixed sulfonate groups. From figure 6.10 we see that both water and hydronium have high residence times in the films $\theta = 30°$ and $70°$. For these cases, water and hydronium molecules are trapped on the SO_3^- groups. Notice also that for $\lambda = 22$, the residence time of H_3O^+ is almost twice as long for hydrophilic case than for the hydrophobic case. We attribute this observation to the size of SO_3^- clusters formed in each film. The larger the SO_3^- clusters, the longer the time the solvent stays close to SO_3^- .

In figure 6.11 we show the residence time of water near hydronium ions. We observe the same trends for the residence time of water near sulfonate groups, *i.e.* the residence times of hydronium are longer for the case $\theta = 30°$ and $70°$. Indeed, most H_3O^+ are found close to SO_3^- groups, which explains the similar behaviour of water around SO_3^- and H_3O^+ . Interestingly, the lifetime of water in the first hydration shell of H_3O^+ is longer than that on SO_3^- . This phenomenon can be attributed to the formation of hydrogen bonds network between water molecules and hydronium ions. We will come back to this discussion in the next section.

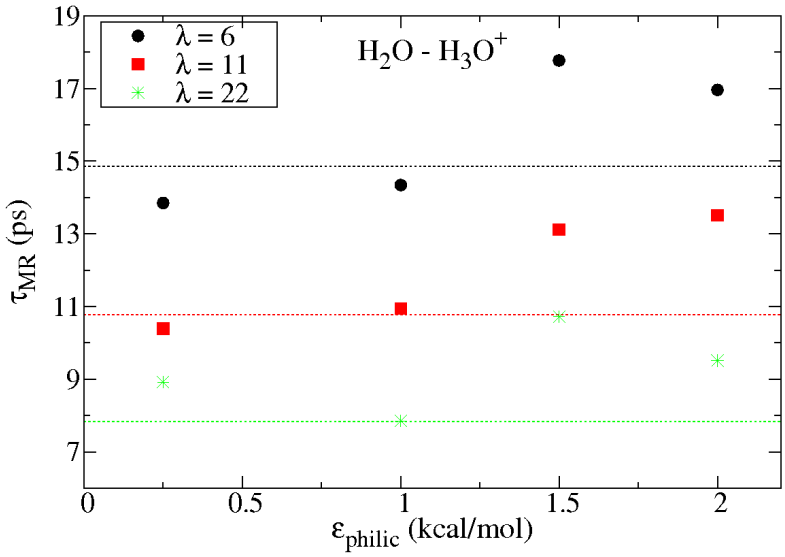

Figure 6.11: Mean residence time of water molecules near hydronium ions.

Mean residence time of H_2O near SO_3^- : τ_{MR} (ps)

	$\lambda = 6$			$\lambda = 11$			$\lambda = 22$		
θ (degree)	2-4 Å	4-6 Å	6-8 Å	2-4 Å	4-6 Å	6-8 Å	2-4 Å	4-6 Å	6-8 Å
150°	7.51	9.47	7.46	5.92	7.26	5.45	5.05	5.78	4.3
100°	8.02	9.85	8.34	5.91	6.84	5.49	4.79	5.48	4.35
70°	8.3	11.13	9.42	7.0	7.99	6.33	6.02	6.69	4.92
30°	9.14	11.15	9.85	7.38	8.80	6.83	5.41	6.34	4.81
membrane	8.18	9.93	8.04	6.34	7.4	5.88	4.98	5.41	4.32

Mean residence time of H_3O^+ near SO_3^- : τ_{MR} (ps)

	$\lambda = 6$			$\lambda = 11$			$\lambda = 22$		
θ (degree)	2-4 Å	4-6 Å	6-8 Å	2-4 Å	4-6 Å	6-8 Å	2-4 Å	4-6 Å	6-8 Å
150°	35.79	13.94	14.83	28.1	12.09	10.01	18.35	11.63	6.77
100°	34.61	14.29	14.02	28.77	12.54	10.31	20.69	10.87	6.92
70°	37.73	16.77	19.88	31.68	13.43	13.6	34.33	13.42	15.95
30°	44.84	19.84	28.78	35.92	15.5	18.38	36.26	14.81	15.69
membrane	32.67	13.57	12.03	27.81	13.13	9.63	19.99	8.64	7.04

Table 6.3: Mean residence time depending on the distance from the sulfonic acid

Mean residence time of H_2O near H_3O^+ : τ_{MR} (ps)

	$\lambda = 6$			$\lambda = 11$			$\lambda = 22$		
θ (degree)	2-4 Å	4-6 Å	6-8 Å	2-4 Å	4-6 Å	6-8 Å	2-4 Å	4-6 Å	6-8 Å
150°	13.85	6.92	6.84	10.39	5.23	4.67	8.92	4.34	3.54
100°	14.34	7.53	7.6	10.94	5.55	4.69	7.85	4.52	3.48
70°	17.77	8.29	8.83	13.11	6.3	5.87	10.72	5.02	4.27
30°	16.96	8.89	9.14	13.51	6.34	5.95	9.51	4.62	4.04
membrane	14.86	7.59	7.39	10.78	5.6	4.88	7.83	4.34	3.48

Table 6.4: Residence time (τ_{MR}) depending on the distance from the nearest sulfonic acid

6.6 Implications on the Structural Proton transport

So far, we have discussed the molecular transport properties, taking into account only classical physics phenomena. We recall that the ionomer proton conductivity is characterized by two mechanisms: vehicular and structural diffusion. In spite of our model using a non-reactive potential, we can still obtain information relevant to the structural diffusion by exploring the description of the local environment that can enhance or mitigate short and long-range proton transfer. In this section we aim to discuss the possible impacts on the structural diffusion due to the structure and dynamics of the ionomer films discussed above.

The structural proton diffusion is the combination of the Grotthuss mechanism, occurring mainly in bulk-like water, and the surface diffusion, occurring at the water/polymer interface. The Grotthuss mechanism involves protons shuttling from molecule to molecule via hydrogen bonds, whereas surface diffusion involves protons hopping from one SO_3^- to another via water bridges. It is generally accepted that the Grotthus mechanisms depend on the proton solvation structure, which is idealized in terms of structures: Zundel ion, $H_5O_2^+$, where the proton is placed between the two water molecules in the hydrogen bond; and Eigen ion, $H_9O_4^+$, where the hydronium ion is hydrogen-bonded to three water molecules. In the case of surface diffusion, it has been observed that proton-transfer depends on the presence of weakly bound water molecules to the SO_3^- . Also, the flexibility of the side-chain and separation between

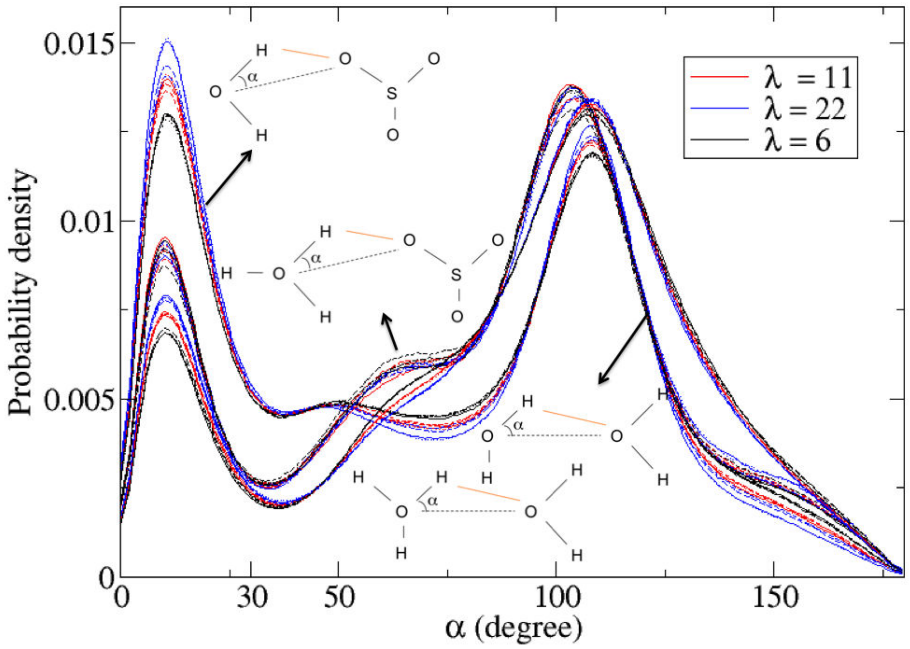

Figure 6.12: Distribution of α, where α is the angle between the intramolecular oxygen-hydrogen vector and the oxygen-oxygen vector for O-O distance less than 0.35 nm.

SO_3^- groups have shown to be important parameters [Roudgar 2006, Tuckerman 2010].

Focusing on the importance of hydrogen bonding in facilitating the proton-transfer, we have investigated the formation of hydrogen bonds inside Nafion films. Two molecules are considered as "hydrogen bonded" if the distance between two oxygen atoms is lower than 0.35 nm and the angle, α, formed between the intramolecular O-H vector (OH of donor molecule) and the intermolecular O-O vector (O atoms of donor and receptor) is smaller than 30°. Figure 6.12 shows the probability distribution of angle α, of H-bonds formed between the following receptor-donor pairs: H_2O-H_2O, H_2O-H_3O^+, H_2O-SO_3^- and H_3O^+-SO_3^-, as defined in the figure. The area where $\alpha < 30°$ indicates high probability of forming hydrogen bond. The wide peak around 104° contains the contribution from the angle involving the other hydrogen atom of the donor. From the H-bond distributions we estimate that about 30% of solvent molecule pairs are hydrogen bonded, which indicates the formation of a hydrogen bond network in the solvent. Interestingly, the distribution in different films at the same hydration level is nearly unchanged, except for H_2O -SO_3^- that appears

to be more sensitive to ionomer structure. When decreasing the water content, the probability of hydrogen bond formation decreases.

Average number of hydrogen bonds per H_3O^+

θ (degree)	$\lambda = 6$	$\lambda = 11$	$\lambda = 22$
150°	1.63	1.89	2.27
100°	1.61	1.93	2.27
70°	1.62	1.82	1.87
30°	1.49	1.80	1.92

Table 6.5: Average number of hydrogen bonds per H_3O^+ formed between H_3O^+ and H_2O .

In table 6.5, we show the average number of hydrogen bonds per H_3O^+ , n_{Hbond}. The n_{Hbond}, is strictly related to the hydration of H_3O^+ , $n_{O_hO_h}$, (see first coordination number of H_2O around H_3O^+ discussed in table 5.1 in chapter 5). Both n_{Hbond} and $n_{O_hO_w}$ decreases with λ and they have slight variation with θ, except for $\lambda = 22$. Focusing on films at $\lambda = 22$, we have investigated the evolution of n_{Hbond} and $n_{O_hO_h}$ with the distance, z from the surface. It is evident from figure 6.13 the decay of $n_{Hbond}(z)$ at distance $z > 2.0$ nm for films on hydrophilic surfaces ($\theta = 70°$ and 30°). We recall that this region corresponds to the water/polymer interface, with the formation of large and compact SO_3^- clusters. Indeed, the configuration where SO_3^- groups are strongly agglomerated is possible only if some water molecules and hydronium ions intersperse among SO_3^- groups in order to screen the electrostatic repulsion. This configuration is quite stable and gives no space for additional water molecules to come near, consequently the hydration of SO_3^- and H_3O^+ remains poor. Under such conditions (*e.g.* low degree of hydration and low number of hydrongen bond formed), the proton structural diffusion would be likely suppressed [Roudgar 2006].

Although strong hydrogen bonding is considered to be a precursor of proton-transfer reactions, the long-range proton transport also requires rapid process of breaking and formation of hydrogen bonds [Kreuer 2000, Kreuer 2004]. This process relies on the rearrangement of hydrogen-bond network, which depends on the orientational behaviour of water molecules and hydronium ions. Therefore, any constraint to the rotational dynamics would decrease mobility of the protons. Focusing on that, the ro-

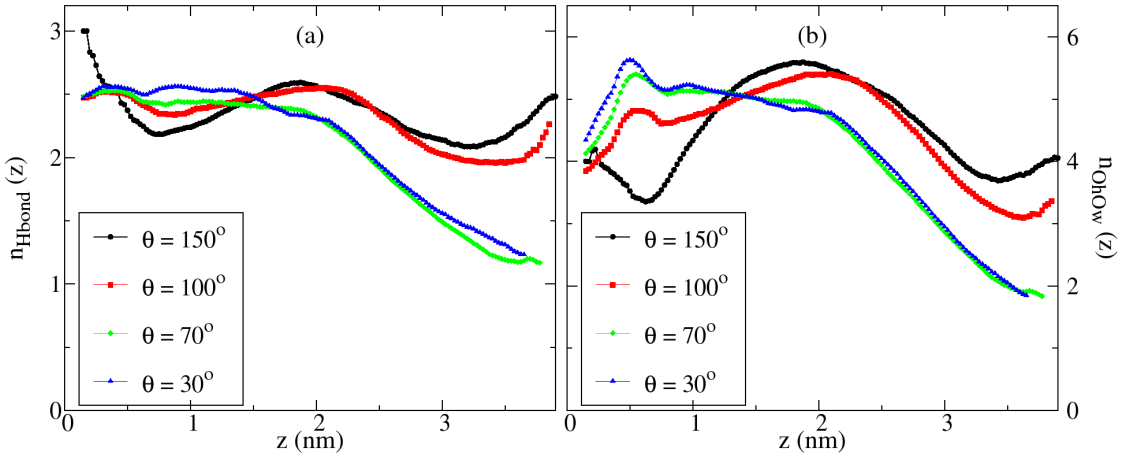

Figure 6.13: Number of hydrogen-bonds per H_3O^+ $n_{Hbond}(z)$ and number of first neighbours $n_{O_hO_w}(z)$ as a function of the distance z from the wall.

tational dynamics investigated in previous sections could suggest probable interfacial effects on proton mobility. For example, we have reported that the rotational relaxation times of hydronium ions are higher in hydrophilic cases ($\theta = 70°$ and $30°$). Slow rotation suggests long hydrogen bond lifetime, which could hamper proton shuttling at long range.

The three proton transport mechanisms (*i.e.* vehicular, Grotthuss and surface structural diffusion) contribute to the ionomer proton conductivity. The importance of each mechanism depends on the ionomer conformation and hydration level [Kreuer 2004]. Comparing the films at $\lambda = 22$ for two extreme cases, *i.e.* sandwich-like film ($\theta = 150°$) and bi-layer-like film ($\theta = 70°$ and $30°$), we can speculate the interplay among these three mechanisms. For the bi-layer structure the hydronium ions are found strong correlated to SO_3^- groups, hampering its self-diffusion and surface structural diffusion. Therefore, the dominant mechanism should be the self-diffusion and Grotthuss mechanism occurring in the rich-water layer between the wall and the polymer ($z < 2.0$ nm). In contrast, the conductivity in the sandwich film should have an important contribution from the surface structural diffusion. This is supported by figure 6.13, showing the enhancement of $n_{hbond}(z)$ for $z < 0.7$ nm, which corresponds to the distance between adsorbed polymer backbone and the side-chain terminal SO_3^- . $n_{hbond}(z)$ reaches its maximum, *i.e.* 3 hydrogen bonds per H_3O^+ , which means formation of Eigen ions, characterized by strong hydrogen bonds with 3 water molecules. In

addition, the sandwich-like film also presents water-rich layers, which facilitate Grotthuss mechanism and hydronium self-diffusion. In conclusion, we would suggest that the conductivity for sandwich film should be the higher than for bi-layer film.

6.7 Conclusions

In this chapter we have investigated the water and hydronium molecular dynamics inside the ionomer thin-films discussed in the chapter 5. Our results have shown that the molecular motion is not directly governed by the hydrophilicity of the substrate, but only indirectly, via the details of the film morphology. Moreover, we have found that the dynamics is highly heterogeneous across the film. A detailed study of such heterogeneity allowed us in a simple way to understand how sulfonic acid groups aggregates can affect the local dynamics of water and hydronium, which could have similar implications in the bulk membrane.

Main conclusions of this chapter include the following assertions:

- the formation of water-rich layers inside films of (multi)lamellar structure enhances in-plane water diffusion, but does not have important effects on hydronium diffusion, which is mainly associated to the local structure of SO_3^- clusters;
- the diffusion in the normal direction to the substrate is higher in the hydrophobic than hydrophilic case; in the hydrophilic cases, the attractions with the substrate and with SO_3^- -rich layers prevent molecules crossing the film thickness;
- strong heterogeneity of water diffusion is attributed mainly to the degree of SO_3^- agglomerates;
- the rotational dynamics of water molecules appears to be heterogeneous for all cases; we have identified a very close correlation between rotational dynamics and spatial sulfonate groups distribution;
- the residence time of water and hydronium around SO_3^- and water around H_3O^+ is higher in the hyrophilic than hydrophobic cases.
- the proton conductivity in the films with sandwich-like structure is probably higher than in the bilayer structure

The results reported in this chapter have direct implications on the PEMFC technologies. The PEMFC performances can be optimized with reducing proton, water and reactants transport losses inside Nafion ultra-thin films. We have shown that the ionomer film at high hydration level, formed on a very hydrophobic surface, provides the most favourable environment for proton and water transport. When decreasing water content, this feature is strongly suppressed and the ionomer approaches to the transport properties found in the membrane. When the hydrophilicity of the catalyst particles is favourable, we showed that the ionomer film will present high heterogeneous dynamics due to high degree of SO_3^- groups aggregates. These agglomerates trap water molecules and hydronium ions, preventing short displacement such as crossing the film thickness. On the other hand, these films provide good in-plane diffusion and favourable environment of Grotthuss mechanisms. In conclusion, Nafion ultra-thin films with sandwich-like structure coating catalyst-support and bilayer structure coating catalyst surface should be a promising solution for transport inside catalyst layer.

Chapter 7

Conclusions and Perspectives

We have studied by Molecular Dynamics simulations the formation of Nafion ultra-thin films at the interface with unstructured flat wall, characterized by their global wetting properties only. By tuning a single control parameter, ε_{philic}, we have been able to investigate in an unique framework a variety of environments peculiar of the PEMFC catalyst layer, ranging from hydrophobic (carbon) to hydrophilic (platinum). The hydrophilicity degree was estimated by computing the contact angle of a water droplet gently deposited on the wall. In total, four types of substrates (wall) were considered: strong hydrophobic, intermediate, hydrophilic and strong hydrophilic. Moreover, three hydration levels were considered in order to investigate the role of water content. The well-thermalized thin-film configurations were described in details in terms of their structural and dynamical properties.

Our results have shown that the change of hydrophilic character of the substrate has a strong impact on the film morphology, which ranges from a sandwich structure (where an extended water pool is sandwiched by ionomer sheets) to a bilayer configuration (where water flood the interface with the substrate and polymers accumulate at the top). By decreasing water content, the films convert into inverted micelles and multilamellar, for hydrophobic and hydrophilic surfaces, respectively. We also have discovered that, in contrast to the sandwich structure, the bilayer structure shows large and compact SO_3^- agglomerates, resulting in a poor hydration of H_3O^+ and SO_3^- . Analysis of surface coverage showed a clear transition from predominant backbone coverage to predominant water coverage, when switching from hydrophobic to hydrophilic surface. Interestingly, the SO_3^- coverage on hydrophilic substrate is high when the film is low hydrated, suggesting high probability to be specific adsorbed. Finally, we have shown that tuning the hydrophilicity of the substrate possibly modifies the film/vapour interface.

The changes in the film morphology have shown an impact in the transport fea-

tures of water molecules and hydronium ions. The first evidence we could observe was related to the water cluster shape. Water in-plane diffusion is enhanced by the formation of water-rich layers in the (multi)lamellar and sandwich morphologies. Performing a more involved analysis of diffusion at different distances from the substrate, we have discovered that dynamics is highly heterogeneous across the film. This heterogeneity arises from the structural configuration of SO_3^- clusters. We have shown that the degree of SO_3^- agglomerates influences the local water and hydronium transport. The SO_3^- groups should be found more dispersed in order to enhance water diffusion at the water/polymer interface, as well as, to facilitate surface structural proton transport. Finally, we have suggested that the sandwich structure should present higher proton conductivity than the bilayer structure.

The main results of our work could be of major interest for the development of PEMFC technology. We have shown the possibility to control the film morphology only by changing the wetting properties of the substrate. Therefore, the use of an appropriate substrate could be highly attractive for controlling the SO_3^- clusters size and the water cluster shape, in order to enhance water transport and proton conductivity. We have shown that lamellar morphologies appear to be best solution for reducing transport losses inside CL. Finally, we are convinced that our results would contribute in view of optimisation of CL performance.

However, our work has presented some limitations, which could be partially overcome in the near future. Firstly, the limited number of substrate has restricted us to obtain a global conclusion about the film properties depending on the substrate hydrophilicity, θ. Therefore, the next step would be to account for an extended number of θ, in order to find a continuous dependence of the film properties with hydrophilicity. Another limitation is to have neglected effects of Grotthuss mechanism for proton transport. This impeded us to have a quantitative description of the film proton conductivity. In order to account structural diffusion, the following step would be to use an alternative model, such as empirical valence bond theory (EVB) algorithms within standard MD [Schmitt 1998, Day 2002].

The computation limitations of MD simulations should also be taken into account. Complex systems like the Nafion thin-films require a very long time to be fully equilibrated. Moreover, the system can be trapped in a configuration of local energy minimum for a very long time. Consequently, initial configurations and pre-

equilibration processes (*e.g.* annealing, quenching) could affect the final configuration. In order to partially overcame this limitation, we propose for the future to sample the configurational space by averaging over several simulations stemming from different, but equivalent, starting conditions.

Finally, as perspectives for our work, many issues about thin-films on PEMFC catalyst layer could be investigated. Indeed, the approach used in our work is suitable for exploring several different systems. Among the numerous ideas to complement our work, we would highlight the following: *i)* we could perform systematic studies of the effect of the film thickness, which is non-homogeneous inside CL. *ii)* we could account for different external conditions, such as temperature and presence of a constant electric field. In particular, it is questioning if electric field could affect ionomer side-chain orientation and, ultimately ionomer film morphology; *iii)* we could include in our simulation the reactants molecules, *e.g.* O_2 and H_2. The study of their diffusions across the film might be important for elucidating CL transport losses; *iv)* we could consider heterogeneous hydrophilicicty of the substrate by delimiting hydrophobic and hydrophilic regions on the wall. This should be important to elucidate the organization of the film coating both catalyst and catalyst-support surfaces; *v)* we could mimic ionomer degradation processes, by simply detaching side-chains from the backbone [Malek 2011a].

Moreover, we acknowledge that development of the CL component requires smart solutions to an intrinsically multiscale problem. Therefore, it remains challenging to integrate molecular details into macroscopic properties. Future theoretical works on CL systems should use combinations of different methods at different length and time scales. One possibility could be to use the non-equilibrium thermodynamics MEMEPhys®approach developed by Franco's group, which could allow to simulate the impact of the nanostructure on the PEMFC observables response [Franco 2006].

Résumé en Français

La demande croissante d'énergie parallèlement à l'augmentation de la conscience environnementale encourage de nos jours les scientifiques et les industriels à investir dans les technologies innovantes pour la production de nouvelles énergies. Durant les dernières décennies, des efforts importants ont été déployés dans la quête d'une alternative à la diminution des ressources naturelles de carburant fossile. Dans le cadre du développement de ces nouvelles technologies, la quantité d'énergie pouvant être produite, le coût, et l'impact environnemental (particulièrement la quantité d'émission de CO_2) sont alors des enjeux essentiels. Ces nouvelles technologies se doivent d'être compétitives pour le large panel d'applications mettant en jeu des dispositifs à conversion d'énergie: les transports (en particulier le marché automobile), la génération de puissance stationnaire (pour les résidences ou les immeubles publics par exemple) et les applications portables (telles que les téléphone cellulaires, les ordinateurs portables, les unités de puissances auxiliaires des voitures, *etc.*).

Les piles à combustibles sont aujourd'hui considérées comme étant l'un des dispositifs à conversion d'énergie parmi les plus prometteurs. Leur principe de fonctionnement de base a été établi par Schoenbein et Grove en 1839 quand ils sont parvenus à générer de l'électricité à partir d'hydrogène et d'oxygène en reversant le principe de l'électrolyse de l'eau[Schoenbein 1839, Grove 1839]. Durant près d'un siècle, il n'y eu quasiment aucun progrès significatif concernant le développement de cette technologie. Ce ne fut que dans les années 1950 que W. Thomas Grubb modifia la pile à combustible originale par l'utilisation d'une membrane d'échange d'ion en Polytyrene sulfoné comme électrolyte [Grubb 1959]. Par la suite, Leonard Niedrach fut le premier à concevoir une technique de dépôts de platine sur la membrane servant de catalyseur aux réactions essentielles de la cellule[Niedrach 1967]. A ce moment, la première utilisation d'une pile à combustible en tant que source de puissance auxiliaire lors des vols spatiaux Gemini de la NASA, fut accomplie.

Parmi les technologies de piles à combustible, les *piles à combustible à membrane échangeuse de protons (PEMFC)*, également appelées *piles à combustible à membrane électrolyte polymère* sont une classe importante. Ce type de pile à combustible a une densité de puissance élevée et de nombreux avantages (*e.g.* la température relativement

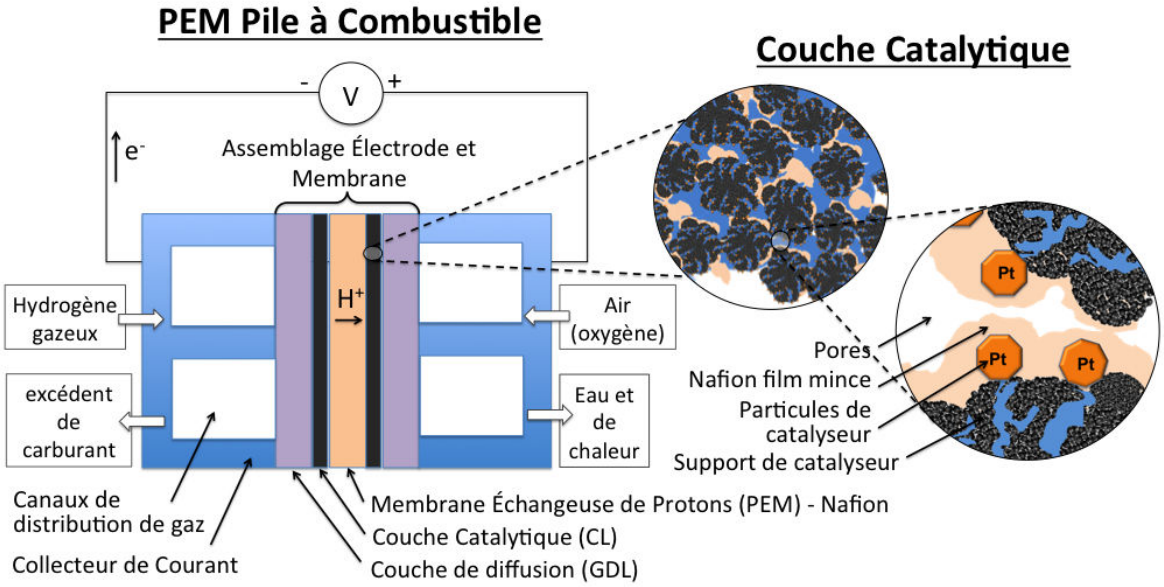

Figure 1: Schéma représentant une cellule typique de pile à combustible à membrane échangeuse de proton. La structure de la couche active (CL) comprend: des particules de carbone ou agglomérats décorées avec des particules de catalyseur (Pt/C); ionomère Nafion dispersé sur Pt/C, et la phase poreuse.

basse de fonctionnement, un faible poids, *etc.*) par rapport aux autres. Généralement, les composants d'une pile à combustible sont l'assemblage électrode/membrane (MEA) qui consiste en deux électrodes (anode et cathode) séparées par la membrane électrolyte, et les canaux de gaz placés sur chaque côté de la MEA (voir figure 1). Les composants d'électrode sont les suivants: la couche catalytique (CL), où interviennent les réactions électrochimiques, et la couche de diffusion de gaz (GDL), à travers laquelle les réactifs sont diffusés depuis les canaux de gaz vers des sites actifs de la CL.

Le fonctionnement d'une pile à combustible consiste à convertir, en continu, l'énergie chimique provenant d'une réaction de réduction en énergie électrique tant que du combustible et de l'oxydant sont fournis. Son fonctionnement est le suivant: le combustible hydrogène est fourni à l'anode (terminaison négative) pendant que l'oxygène est fourni à la cathode (terminaison positive). Par une réaction d'oxydation l'hydrogène se divise en un électron (production d'électricité) et un proton. Les protons traversent la membrane électrolyte et atteignent la cathode, où ils réagissent avec les électrons et l'oxygène pour former de l'eau via un mécanisme de réduction.

Une étape importante de l'histoire des PEMFC fut atteinte en 1960 lorsque le *Nafion*, un polymère conducteur protonique inventé par la société DuPont a été introduit comme membrane électrolyte [Connolly 1966]. Ce polymère fait preuve d'une excellente conductivité protonique lorsqu'il est hydraté et d'une exceptionnelle stabilité chimique. A cette époque, les piles à combustible à haute puissance et des densités d'énergie ont été réalisées avec des coûts de fabrication extrêmement élevés en raison de la forte utilisation du platine. Cet inconvénient fut la principale limitation d'une plus large utilisation de cette technologie. Des progrès plus significatifs ne sont devenus possibles qu'après les années 1980, lorsque de nouvelles avancées ont permis une reconfiguration importante des composants de la cellule.

De nos jours, les nouveaux développements sur les PEMFC sont surtout orientés dans le but d'explorer de nouveaux matériaux pour chaque composant. En particulier, les membranes en Nafion ont reçu beaucoup d'attention en raison de la haute complexité de leur structure au niveau nanométrique. Ce polymère est le résultat de la copolymérisation d'une chaîne de tétrafluoréthylène (Téflon) et d'une chaîne latérale formée de groupes de perfluorovinyle-éther terminés par des groupes sulfonés. La principale caractéristique de la structure du Nafion est l'hétérogénéité à l'échelle nanométrique. En présence d'eau, les chaînes latérales pendantes sont capables d'introduire un changement de phase hydrophobe/hydrophile. Plusieurs modèles, tels que les micelles inversées, le réseau de grappes ou le faisceau de polymère ont été proposés pour décrire la morphologie de la membrane ionomère en présence d'eau [Mauritz 2004]. Cependant, ces modèles sont très souvent inefficaces et contradictoires, et, par conséquent, la structure du Nafion reste incertaine. De plus, il existe toujours un débat sur la relation de Nafion nanostructure à ses propriétés de transport, tels que la conduction de protons et de gestion de l'eau à l'intérieur de la membrane [Kreuer 2004].

La couche catalytique (CL) présente également une structure très hétérogène et complexe. Les méthodes actuelles de fabrication de CL sont très empiriques et utilisent mal les méthodes de traitement contrôlées. Le résultat est une structure hétérogène aléatoire formée par des nanoparticules de platine dispersées sur une matrice de carbone imprégnée par l'ionomère de Nafion (voir figure 1). Le Nafion a été présenté comme l'un de ses constituants pour deux raisons: tout d'abord, au cours du processus de fabrication le Nafion agit comme un liant, ayant un rôle important sur la

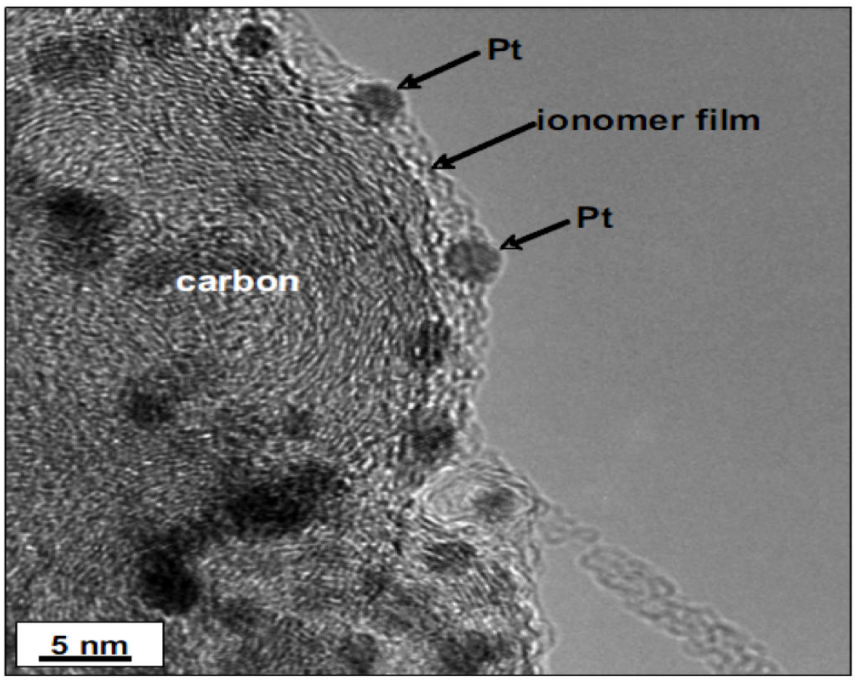

Figure 2: Image TEM montrant les interfaces Pt/ionomère/C. Cette image montre clairement la formation d'une mince pellicule d'ionomère recouvrant les particules de Pt et de carbone. Figure de référence [More 2006].

dispersion des agrégats Pt/C et, par conséquent, sur l'utilisation du platine. En second lieu, lors du fonctionnement de la pile à combustible, il forme un réseau important pour la conduction de proton à partir de/vers la membrane de/vers les sites catalytiques. Le Nafion présente une phase non-homogène et non-continue à l'intérieur du CL. Il peut se présenter comme un *film ultra-mince* à la surface des supports de carbone et de particules de Pt (voir figure 2). Typiquement, ce film n'est pas uniformément distribué et son épaisseur s'étend d'environ 4 à 20 nm [More 2006].

La formation de films-minces de Nafion dans la couche catalytique fut ces dernières années un des sujets "chaud" du développement des piles à combustible. La structure et les propriétés de ces films peuvent différer significativement de ceux de la membrane ionomère [Paul 2011a]. En se concentrant sur l'hétérogénéité de la couche catalytique, le film-mince du ionomère va s'auto-organiser selon différentes formes, dépendant des propriétés du substrat avec lequel il interagit. Cela doit dépendre de la composition chimique (*e.g.* , les états d'oxydation des matériaux de Pt et de C), de la géométrie (courbure) et, finalement, des propriétés de mouillabilité de la surface

[Modestino 2012]. En particulier, il existe des preuves expérimentales que les modifications des propriétés hydrophobique du substrat sont suffisantes pour affecter la morphologie de film de Nafion [Wood 2009]. Comprendre les effets de telles interactions dans la morphologie de l'ionomère est une étape cruciale vers le contrôle des propriétés fonctionnelles, telles que la conductivité protonique et le transport de l'eau à l'intérieur de la CL.

L'adsorption effective de l'ionomère sur la surface catalytique a été l'objet de nombreuses études. Jusqu'à récemment, les visions les plus admises considèrent le Nafion comme un électrolyte non-adsorbant dans les couches catalytiques des PEMFC. Cette image générale fut changée quand il a été démontré que l'adsorption spécifique des groupes sulfonés sur le catalyseur peut arriver et peut fortement affecter la réactivité et la stabilité des mécanismes de réduction de l'oxygène [Subbaraman 2010a, Ma 2007, Ohma 2011]. De plus, la nature de l'adsorption de l'ionomère peut être en partie dépendante de son organisation, comme la formation d'agrégats ioniques dans la région très proche de la surface. Enfin, l'adsorption dépend fortement des propriétés du substrat, comme par exemple le caractère hydrophobe/hydrophile.

La surface de la couche catalytique a des caractères hydrophile/hydrophobe inhomogènes. En effet, la surface de platine est plus hydrophile alors que les supports de carbone tendent à être plutôt hydrophobes. Parallèlement, les propriétés de mouillabilité de ces surfaces peuvent être affectées pendant le fonctionnement de la pile à combustible. Les variations des potentiels à l'anode et de la cathode peuvent changer plusieurs propriétés des matériaux, telles que le degré de recouvrement de surface du platine et du carbone ainsi que l'hydrophilicité des surfaces [Borup 2007]. De la même façon, les mécanismes de dégradation de ces matériaux incluant le fractionnement et les changements de composition du catalyseur à cause de la corrosion, l'empoisonnement du catalyseur par des impuretés adsorbées, le vieillissement de la membrane échangeuse de proton et des modifications des propriétés hydrophobe/hydrophile des surfaces des couches catalytiques [Chen 2006, Wang 2009].

Dans ce contexte global, une simple question surgit: que se passe-t-il avec le film-mince de Nafion lorsqu'il se dépose sur des surfaces de caractères hydrophobe/hydrophile différents? Une discussion particulièrement intéressante est de savoir s'il existe une association préférée des domaines hydrophobes ou hydrophiles du Nafion avec la surface. Quel type de structure l'ionomère peut former dépendant seulement de la mouil-

labilité de la surface? En effet, si la morphologie de l'ionomère est sensible à ce paramètre, la suite sera d'étudier comment cette forme pourrait affecter les propriétés fonctionnelles importantes, comme la conduction protonique, le transport de l'eau, l'adsorption de l'ionomère. Ces questions peuvent être adressées en effectuant des simulations numériques. Les méthodes de calcul essentielles ici sont les approches de type Monte Carlo (MC) et de Dynamique Moléculaire (MD), leur principal avantage étant la dépendance en temps.

L'objectif de ma thèse de doctorat est d'effectuer une étude en profondeur des effets du substrat sur la morphologie du film ultra-mince de l'ionomère pour différents niveaux d'hydratation lorsque l'on considère seulement les propriétés de mouillabilité du système. La méthode choisie pour ce travail est basée sur des simulations de dynamique moléculaire classique. L'étude de tels systèmes à travers des simulations numériques représente un défi important. Le système devant être suffisamment grand pour représenter les dimensions du film, cela va devoir impliquer des ressources informatiques couteuses. Dans ce but, nous avons développé un modèle simple d'approche champ moyen qui permet de changer continuellement l'hydrophilicité du substrat en contact avec le film tout en gagnant du temps de simulation.

L'objectif de la thèse est aussi de comprendre la structure des films minces de Nafion sur la surface de n'importe quel substrat. De par l'aspect très général de ce travail, nous pensons que la contribution de nos résultats peut aller au-delà des applications des piles à combustible PEM. Ces études peuvent aider à comprendre la formation de film-minces de Nafion sur plusieurs substrats tels que Au, Pt(hkl), Ru(hkl), SiO_2, et communément utilisés dans des électrodes d'ionomère modifiés pour divers dispositifs électrochimiques.

La thèse

Le but de ma thèse de doctorat est d'effectuer des simulations numériques sur la formation d'un film-ultra-mince de Nafion polyélectrolyte hydraté lorsqu'il est en contact avec des surfaces hydrophobe/hydrophile. Les propriétés physiques de tels systèmes, incluant l'auto-organisation et la dynamique du polymère et du complexe d'eau ont été étudiées par des simulations de Dynamique Moléculaire. L'ensemble du travail, comprenant l'étude de la bibliographique, l'utilisation de la méthode et les

résultats ainsi que les conclusions pertinentes est reporté selon le plan suivant:

Chapitre 2: Contexte expérimental et théorique

L'objectif de ce chapitre est de faire une sélection des travaux expérimentaux et théorique que nous avons jugés nécessaire afin de rendre le lecteur conscient du contexte dans lequel notre travail est inséré. Nous comptons introduire les concepts généraux au sujet du Nafion et des couches catalytiques des PEMFC. Puis, nous présenterons l'état de l'art du Nafion à l'interface des points de vue expérimentaux et théoriques.

Chapitre 3: Méthodes computationnelles

Les méthodes computationnelles utilisées dans ce travail sont décrites dans le chapitre 3. Nous y détaillons les idées principales derrière les simulations de dynamique moléculaire, incluant les algorithmes et les concepts de physique statistique. Nous donnerons également des informations pratiques, utiles pour la simulation de systèmes polymères.

Chapitre 4: Le modèle

Ce chapitre est dédié à la description du modèle de dynamique moléculaire adopté pour simuler le Nafion et l'eau, incluant les paramètres et les détails de simulation. Nous avons développé le modèle pour simuler un film d'ionomère en contact avec des surfaces planes et lisses (mur). Nous avons adopté un mélange des modèles "united-atom" et "all-atom" pour la représentation des chaînes d'ionomère, tandis que l'interaction avec la surface a été décrite au niveau du champ moyen. Ce modèle nous permet de prendre en compte une interaction avec le substrat qui ne dépend que de la distance avec le mur, et ainsi de bénéficier d'un diminution significative du temps de calcul. Le mur est censé imiter la surface composée par différents matériaux et ayant par conséquent des caractères hydrophobe/hydrophile différents. Nous avons montré qu'il est possible de contrôler ce caractère hydrophobe/hydrophile de la paroi avec seulement les paramètres du potentiel du type Lennard-Jones 9-3, sans aucune référence à une composition chimique particulière du mur. La signification physique précise du paramètre représentant l'énergie d'interaction est associée à la

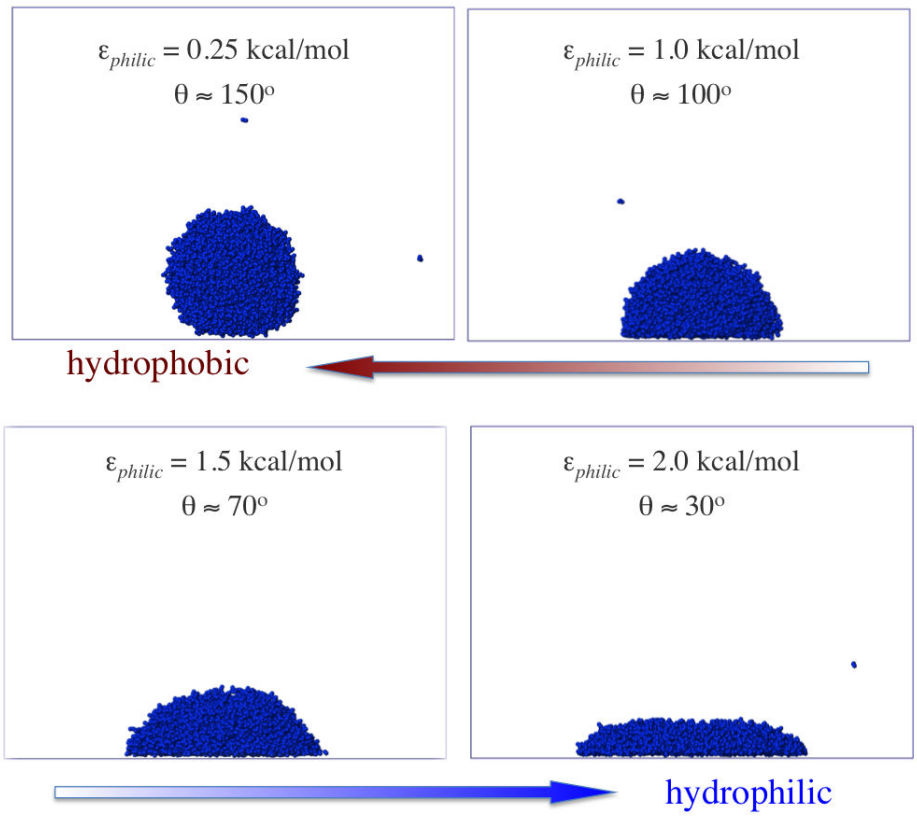

Figure 3: Snapshot: simulations de dynamique moléculaire de 3500 molécules d'eau placées sur un mur 9-3 LJ avec différentes valeurs de ε_{philic}. Les angles de contact d'eau associés sont signalés par θ.

définition de l'angle de mouillage (voir figure 3). En conclusion, la principale raison d'utiliser ce modèle d'interface est que nous croyons que les caractéristiques essentielles de l'ionomère devraient finalement être contrôlées par les propriétés globales de mouillage de la surface. Nous sommes convaincus que notre approche est un bon choix pour étudier les processus physiques du film d'ionomère, en préservant un degré élevé de généralité.

Chapitre 5: Analyse structurale de films ultra-minces de Nafion

Dans ce chapitre, nous explorons l'auto-assemblage et la formation de nanostructure dans un modèle réaliste pour l'ionomère Nafion (introduit au chapitre 4) quand il est déposé sur des surfaces avec des secteurs hydrophobes et hydrophiles. Nous avons examiné quatre types de substrats: fortement hydrophobe ($\theta = 150°$), intermédiaire

($\theta = 100°$), hydrophile ($\theta = 70°$) et fortement hydrophile ($\theta = 30°$). Sur la base de notre analyse structurale, nous avons proposé trois catégories de films, selon le caractère hydrophile du substrat. Les morphologies des films de base sont: *i)* "Sandwichs" (haute λ) et micelles inversées (faible λ) pour le cas de la plupart des surfaces hydrophobes; *ii)* agrégats ioniques ("cluster") connectés pour le cas intermédiaire; *iii)* bicouches (haute λ) et multilamellaires (faible λ) pour les surfaces hydrophiles (voir figure 4). Par ailleurs, nous avons montré que la structure locale dans les films à $\lambda = 22$ semble être le plus sensible à la propriété de mouillabilité du substrat. En d'autres termes, les couches de solvatation de SO_3^- et H_3O^+ sont particulièrement différentes pour les films avec des structures sandwich et bicouche. Nous avons découvert que, contrairement à la structure sandwich, la structure bicouche montre des agglomérats de SO_3^- grands et compactés, ce qui entraîne une mauvaise hydratation de H_3O^+ et SO_3^-.

La cinétique des réactions sur les surfaces catalytiques devrait également être affectée par la mouillabilité de la surface. L'adsorption de SO_3^- et le recouvrement d'autres espèces peuvent inactiver la surface du catalyseur. Nos résultats ont montré que les groupes de SO_3^- peuvent être absorbés même lorsque le caractère hydrophile est favorable. Cette adsorption est plus susceptible d'apparaître dans des conditions de faible hydratation. En ce qui concerne le caractère des interfaces ionomère/vapeur, nos résultats ont montré que lorsque le substrat est hydrophile, la surface supérieure du film a tendance à être plus hydrophobe en raison de la formation d'une couche dense formée par la chaîne hydrophobe de l'ionomère. Cela permettrait d'éviter que les réactifs soient absorbés par la couche d'ionomère.

Chapitre 6: Dynamique de l'eau et de l'hydronium dans les films de Nafion ultra-minces

Dans ce chapitre nous poursuivons notre discussion en nous concentrant sur l'exploration de l'effet de la morphologie du film sur la dynamique de l'eau et des protons au sein du film d'ionomère hydraté. Nos résultats ont montré que le mouvement moléculaire n'est pas directement régi par le caractère hydrophile du substrat, mais seulement indirectement, via les caractéristiques de la morphologie du film. Par ailleurs, nous avons constaté que la dynamique est très hétérogène à travers le film.

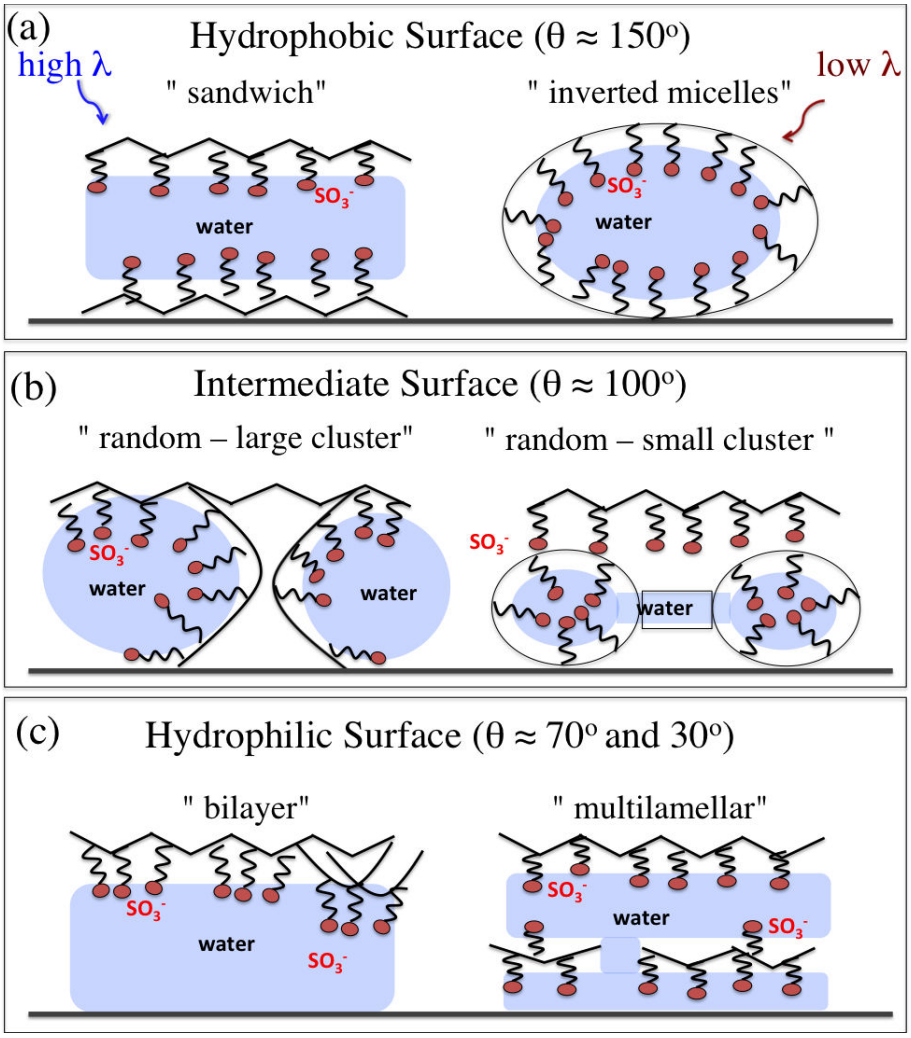

Figure 4: Illustration de la morphologie du film. La partie gauche correspond à des films à haute hydratation, alors que le côté droit à la basse hydratation.

Une étude détaillée de cette hétérogénéité nous a permis d'une manière simple de comprendre comment les agrégats de SO_3^- peuvent affecter la dynamique locale de l'eau et de l'hydronium, ce qui pourrait avoir des répercussions semblables dans la membrane.

Les principales conclusions de ce chapitre comprennent les affirmations suivantes: *i)* la formation de couches riches en eau à l'intérieur des films de structure multi lamellaire améliore la diffusion de l'eau dans le plan, mais ne semble pas avoir des effets importants sur la diffusion de l'hydronium, qui est principalement associée à la structure locale des agrégats de SO_3^- ; *ii)* la diffusion dans la direction normale au

substrat est plus élevée dans le cas hydrophobe; dans les cas hydrophiles, le substrat et les couches riches en SO_3^- empêchent les molécules qui traversent l'épaisseur du film de sortir; *iii)* la forte hétérogénéité de la diffusion de l'eau est principalement attribuable à la présence d'agglomérats de SO_3^- ; *iv)* la dynamique des molécules d'eau en rotation semble être hétérogène dans tous les cas, nous avons identifié une corrélation très étroite entre la dynamique de rotation et la distribution spatiale des groupes sulfonés; *v)* le temps de résidence de l'eau et de l'hydronium autour des SO_3^- et de l'eau autour des H_3O^+ est plus élevée dans le cas hydrophile que dans le cas hydrophobe. *vi)* la conductivité protonique dans les films de structure de type sandwich est probablement plus élevée que dans la structure bicouche

En conclusion, les principaux résultats de nos travaux pourraient être d'un intérêt majeur pour le développement de la technologie PEMFC. Nous avons montré la possibilité de contrôler la morphologie du film seulement en changeant les propriétés de mouillage du substrat. Par conséquent, l'utilisation d'un substrat approprié pourrait être très attrayante pour contrôler la taille des agglomérats de SO_3^- et la forme des agglomérats d'eau, afin d'améliorer le transport de l'eau et la conductivité protonique. Nous avons montré que les morphologies lamellaires semblent être la meilleure solution pour réduire les pertes de transport à l'intérieur des CL. Enfin, nous sommes convaincus que nos résultats contribueront à l'optimisation des performances des CL.

Bibliography

[Abraham 1977] F. F. Abraham and Y. Singh. *The structure of a hard-sphere fluid in contact with a soft repulsive wall.* Journal of Chemical Physics, vol. 67, page 2384, 1977. (Cited on page 76.)

[Allahyarov 2009] E. Allahyarov, P. L. Taylor and H. Löwen. *Simulation study of sulfonate cluster swelling in ionomers.* Physical Review E, vol. 80, page 061802, 2009. (Cited on page 20.)

[Allahyarov 2011] E. Allahyarov and P. L Taylor. *Simulation study of the equilibrium morphology in inomers with different architectures.* Journal of Polymer Science Part B: Polymer Physics, vol. 49, pages 368–376, 2011. (Cited on page 21.)

[Allen 1989] M. P. Allen and D. J. Tildesley. Computer Simulation of Liquids. 1989. (Cited on page 45.)

[Andersen 1980] H. C. Andersen. *Molecular dynamics simulations at constant pressure and/or temperature.* Journal of Chemical Physics, vol. 72, page 2384, 1980. (Cited on page 57.)

[Arnold 2002] A. Arnold, J. de Joannis and C. Holm. *Electrostatics in periodic slab geometries I.* Journal of Chemical Physics, vol. 117, page 2496, 2002. (Cited on page 55.)

[Balbuena 2005] P Balbuena, E Lamas and Y Wang. *Molecular modeling studies of polymer electrolytes for power sources.* Electrochimica Acta, vol. 50, pages 3788–3795, 2005. (Cited on page 39.)

[Bass 2010] M. Bass, A. Berman, A. Singh, O. Konovalov and V. Freger. *Surface structure of Nafion in vapor and liquid.* The Journal of Physical Chemistry B, vol. 114, pages 3784–90, 2010. (Cited on pages 40, 119 and 122.)

[Bass 2011] M. Bass, A. Berman, A. Singh, O. Konovalov and V. Freger. *Surface-Induced Micelle Orientation in Nafion Films.* Macromolecules, vol. 44, pages 2893–2899, 2011. (Cited on pages 36 and 119.)

[Berendsen 1984] H. J. C. Berendsen, J. P. M. Postma, A. DiNola and J. R. Haak. *Molecular dynamics with coupling to an external bath.* Journal of Chemical Physics, vol. 81, pages 3684–3690, 1984. (Cited on pages 56 and 58.)

[Berendsen 1987] H. J. C. Berendsen, J. R. Grigera and T. P. Straatsma. *The missing term in effective pair potentials.* The Journal of Physical Chemistry, vol. 91, pages 6269–6271, 1987. (Cited on page 63.)

[Berthelot 1898] Daniel Berthelot. *Sur le mélange des gaz.* Comptes rendus hebdomadaires des séances de l'Académie des Sciences, vol. 126, pages 1703–1855, 1898. (Cited on page 49.)

[Borup 2007] R. Borup, J. Meyers, B. Pivovar, Y. S. Kim, R. Mukundan, N. Garland, D. Myers, M. Wilson, F. Garzon, D. Wood, P. Zelenay, K. More, K. Stroh, T. Zawodzinski, J. Boncella, J. E. McGrath, M. Inaba, K. Miyatake, M. Hori, K. Ota, Z. Ogumi, S. Miyata, A. Nishikata, Z. Siroma, Y. Uchimoto, K. Yasuda, K.-I. Kimijima and N. Iwashita. *Scientific aspects of polymer electrolyte fuel cell durability and degradation.* Chemical Reviews, vol. 107, pages 3904–51, 2007. (Cited on pages 4 and 163.)

[Bussi 2007] G. Bussi, D. Donadio and M. Parrinello. *Canonical sampling through velocity rescaling.* Journal of Chemical Physics, vol. 126, page 014101, 2007. (Cited on page 56.)

[Castrillón 2009] S. R.-V. Castrillón, N. Giovambattista, I. Aksay and P. G. Debenedetti. *Effect of surface polarity on the structure and dynamics of water in nanoscale confinement.* The Journal of Physical Chemistry B, vol. 113, pages 1438–1446, 2009. (Cited on page 75.)

[Chen 2006] Weimin Chen, Gongquan Sun, Junsong Guo, Xinsheng Zhao, Shiyou Yan, Juan Tian, Shuihua Tang, Zhenhua Zhou and Qin Xin. *Test on the degradation of direct methanol fuel cell.* Electrochimica Acta, vol. 51, pages 2391–2399, 2006. (Cited on pages 4 and 163.)

[Cheng 2010] C.H. Cheng, K. Malek, P.C. Sui and N. Djilali. *Effect of Pt nano-particle size on the microstructure of PEM fuel cell catalyst layers: Insights from molec-*

ular dynamics simulations. Electrochimica Acta, vol. 55, pages 1588–1597, 2010. (Cited on page 101.)

[Choi 2003] P. Choi and R. Datta. *Sorption in Proton-Exchange Membranes.* Journal of The Electrochemical Society, vol. 150, no. 12, page E601, 2003. (Cited on page 119.)

[Choi 2005] P. Choi, N. H. Jalani and R. Datta. *Thermodynamics and proton transport in Nafion: II. proton diffusion mechanisms and conductivity.* Journal of the Electrochemical Society, vol. 152, page E123, 2005. (Cited on page 25.)

[Chun 1998] Y. G. Chun, C. S. Kim, D. H. Peck and D. R. Shin. *Performance of a polymer electrolyte membrane fuel cell with thin film catalyst electrodes.* Journal of Power Sources, vol. 71, pages 174–178, 1998. (Cited on pages 31 and 85.)

[Connolly 1966] D.J. Connolly, Longwood and W. F. Gresham. *Fluorocarbon Vinyl Ether Polymers. U.S. Patent*, 1966. (Cited on pages 3 and 161.)

[Coulon 2012] R. Coulon. *Modélisation de la dégradation chimique de membranes dans les piles à combustibles à membrane électrolyte polymère* . PhD thesis, Université de Grenoble, 2012. (Cited on page 13.)

[Cui 2007] S. Cui, J. Liu, M. E. Selvan, D. J. Keffer, B. J. Edwards and W. V. Steele. *A molecular dynamics study of a nafion polyelectrolyte membrane and the aqueous phase structure for proton transport.* The Journal of Physical Chemistry B, vol. 111, pages 2208–2218, 2007. (Cited on pages 20, 21 and 71.)

[Damjanovic 1967] A. Damjanovic and V. Brusic. *Electrode kinetics of oxygen reduction on oxide-free platinum electrodes.* Electrochimica Acta, vol. 12, pages 615–628, 1967. (Cited on page 26.)

[Darden 1993] T. Darden, D. York and L. Pedersen. *Particle mesh Ewald: An Nlog(N) method for Ewald sums in large systems.* The Journal of Chemical Physics, vol. 98, pages 10089–10092, 1993. (Cited on page 53.)

[Day 2002] T.J.F. Day, A.V. Soudackov, M. Cuma and G. A. Schmitt U.W.; Voth. *A second generation multistate empirical valence bond model for proton transport*

in aqueous systems. The Journal of Chemical Physics, vol. 117, pages 5839–5849, 2002. (Cited on page 156.)

[de Joannis 2002] J. de Joannis, A. Arnold and C. Holm. *Electrostatics in periodic slab geometries II.* Journal of Chemical Physics, vol. 117, page 2503, 2002. (Cited on page 55.)

[de Morais 2011a] R. F. de Morais. *Study of the Stability and the Reactivity of Pt and Pt_3Ni Model Catalyst for PEM Fuel Cells: An Ab-initio Based Multiscale Modeling Approach.* PhD thesis, Ecole Doctorale de Chimie de Lyon ED206,, 2011. (Cited on page 26.)

[de Morais 2011b] R. F. de Morais, Ph. Sautet, D. Loffreda and A. A. Franco. *A multiscale theoretical methodology for the calculation of electrochemical observables from ab initio data: Application to the oxygen reduction reaction in a Pt(111)-based polymer electrolyte membrane fuel cell.* Electrochimica Acta, vol. 56, pages 10842–10856, 2011. (Cited on page 26.)

[Devanathan 2007a] R. Devanathan, A. Venkatnathan and M. Dupuis. *Atomistic simulation of Nafion membrane: 1. Effect of hydration on membrane nanostructure.* The Journal of Physical Chemistry B, vol. 111, pages 8069–79, 2007. (Cited on pages 20 and 71.)

[Devanathan 2007b] R. Devanathan, A. Venkatnathan and M. Dupuis. *Atomistic simulation of Nafion membrane: 2. Dynamics of water molecules and hydronium ions.* The Journal of Physical Chemistry B, vol. 111, pages 13006–13013, 2007. (Cited on page 71.)

[Devanathan 2010] R. Devanathan, A. Venkatnathan, R. Rousseau, M. Dupuis, T. Frigato, W. Gu and V. Helms. *Atomistic simulation of water percolation and proton hopping in Nafion fuel cell membrane.* The Journal of Physical Chemistry B, vol. 114, pages 13681–90, 2010. (Cited on page 20.)

[Devanathan 2012] R. Devanathan and M. Dupuis. *Insight from molecular modelling: does the polymer side chain length matter for transport properties of perfluorosulfonic acid membranes?* Physical Chemistry Chemical Physics, vol. 14, pages 11281–95, 2012. (Cited on page 21.)

[Dorenbos 2009] G. Dorenbos and Y. Suga. *Simulation of equivalent weight dependence of Nafion morphologies and predicted trends regarding water diffusion.* Journal of Membrane Science, vol. 330, pages 5–20, 2009. (Cited on page 22.)

[Dura 2009] J. A. Dura, V. S. Murthi, M. Hartman, S. K. Satija and C. F. Majkrzak. *Multilamellar interface structures in Nafion.* Macromolecules, vol. 42, pages 4769–4774, 2009. (Cited on pages 35 and 111.)

[Eastman 2012] S. A. Eastman, S. Kim, B. W. Page K. A.and Rowe, S. Kang and C. L. Soles. *Effect of confinement on structure, water solubility, and water transport in Nafion thin films.* Macromolecules, vol. 45, pages 7920–7930, 2012. (Cited on page 34.)

[Eastwood 1974] J. W. Eastwood and R. W. Hockney. *Shaping the force law in two-dimensional particle mesh models.* Journal of Computational Physics, vol. 16, pages 342–359, 1974. (Cited on page 53.)

[Eikerling 2009] M. H. Eikerling and K. Malek. Proton Exchange Membrane Fuel Cells: Materials Properties and Performance, chapitre Physical Modeling of Materials for PEFCs: A Balancing Act of Water and Complex Morphologies, pages 343–435. CRC Press, 2009. (Cited on page 20.)

[Elliott 2011] James A. Elliott, Dongsheng Wu, Stephen J. Paddison and Robert B. Moore. *A unified morphological description of Nafion membranes from SAXS and mesoscale simulations.* Soft Matter, vol. 7, pages 6820–6827, 2011. (Cited on page 18.)

[Essmann 1995] U. Essmann, L. Perera, M. L. Berkowitz, T. Darden, H. Lee and L. Pedersen. *A smooth particle mesh Ewald method.* Journal of Chemical Physics, vol. 103, pages 8577–8593, 1995. (Cited on page 53.)

[Fleer 1993] G. J. Fleer. Polymers at interfaces. Springer, 1993. (Cited on page 114.)

[Franco 2005] A.A. Franco. PhD thesis, Université Claude Bernard Lyon 1, 2005. (Cited on page 37.)

[Franco 2006] A. A. Franco, P. Schott, C. Jallut and B. Maschke. *A dynamic mechanistic model of an electrochemical interface.* Journal of the Electrochemical

Society, vol. 153, pages A1053–A1061, 2006. (Cited on pages 37, 99, 113, 117 and 157.)

[Franco 2007a] A. A.. Franco, P. Schott, C. Jallut and B. Maschke. *A multi-scale dynamic mechanistic model for the transient analysis of PEFCs.* Fuel Cells, vol. 7, pages 99–117, 2007. (Cited on page 99.)

[Franco 2007b] A. A. Franco and M. Tembely. *Transient multiscale modeling of aging mechanisms in a PEFC cathode.* Journal of the Electrochemical Society, vol. 154, pages B712–B723, 2007. (Cited on page 37.)

[Freger 2009] V. Freger. *Hydration of ionomers and Schroeder's paradox in Nafion.* The Journal of Physical Chemistry B, vol. 113, pages 24–36, 2009. (Cited on page 119.)

[Frenkel 2002] D. Frenkel and B. Smit. Understanding Molecular Simulation: From Algorithms to Applications. Academic Press, 2002. (Cited on page 45.)

[Gebel 2000a] G Gebel. *Structural evolution of water swollen perfluorosulfonated ionomers from dry membrane to solution.* Polymer, vol. 41, pages 5829–5838, 2000. (Cited on pages xiii and 17.)

[Gebel 2000b] G. Gebel and R. B. Moore. *Small-angle scattering study of short pendant chain perfuorosulfonated ionomer membranes.* Macromolecules, vol. 33, pages 4850–4855, 2000. (Cited on page 15.)

[Gierke 1981] T. D. Gierke, G.E. Munn and F. C. Wilson. *The morphology in Nafion perfluorinated membrane products, as determined by wide- and small- angle X-Ray studies.* Journal of Polymer Science: Polymer Physics Edition, vol. 19, pages 1687–1704, 1981. (Cited on pages xiii, 14 and 15.)

[Giovambattista 2007] N. Giovambattista, P. G. Debenedetti and P. J. Rossky. *Effect of surface polarity on water contact angle and interfacial hydration structure.* The Journal of Physical Chemistry B, vol. 111, pages 9581–9587, 2007. (Cited on pages 75 and 77.)

[Glebov 1997] A. Glebov, A. P. Graham, A. Menzel and J. P. Toennies. *Orientational ordering of two-dimensional ice on Pt(111).* Journal of Chemical Physics, vol. 106, page 9382, 1997. (Cited on page 98.)

[Grove 1839] W. R. Grove. *On voltaic series and the combination of gases by platinum.* The London and Edinburgh Philosophical Magazine and Journal of Science, vol. 14, pages 127–130, 1839. (Cited on pages 1 and 159.)

[Grubb 1959] W.T Grubb. *Fuel Cell*, 1959. (Cited on pages 1 and 159.)

[Harvey 1998] S.C. Harvey, Tan R.K.Z. and Cheatham T.E. *The flying ice cube: Velocity rescaling in molecular dynamics leads to violation of energy equipartition.* Journal of Computational Chemistry, vol. 19, pages 726–740, 1998. (Cited on page 56.)

[Haubold 2001] H.-G. Haubold, Th. Vad, H. Jungbluth and P. Hiller. *Nano structure of NAFION: A SAXS study.* Electrochimica Acta, vol. 46, pages 1559–1563, 2001. (Cited on pages xiii and 16.)

[Hoover 1985] W. G. Hoover. *Canonical dynamics: equilibrium phase-space distributions.* Physical Review A, vol. 31, pages 1695–1697, 1985. (Cited on page 57.)

[Hsu 1983] W. Y. Hsu and T. D. Gierke. *Ion transport and clustering in nafion perfluorinated membranes.* Journal of Membrane Science, vol. 13, pages 307–326, 1983. (Cited on pages xiii and 14.)

[Huang 2012] J. Huang D.and Pu, Z. Lu and Q. Xue. *Microstructure and surface roughness of graphite-like carbon films deposited on silicon substrate by molecular dynamic simulation.* Surface and Interface Analysis, vol. 44, pages 837–843, 2012. (Cited on page 121.)

[Iden 2008] H. Iden, A. Ohma and K. Shinohara. *Analysis of proton transport in pseudo catalyst layers.* ECS Transactions, vol. 16, pages 1751–1762, 2008. (Cited on page 36.)

[Jacob 2003] T. Jacob, R. P. Muller and Goddard. W. A. *Chemisorption of atomic oxygen on Pt(111) from DFT studies of Pt-clusters.* The Journal of Physical Chemistry B, vol. 107, pages 9465–9476, 2003. (Cited on page 26.)

[Jang 2004] S. S. Jang, V. Molinero, T. Cagin and W. A. Goddard. *Nanophase-segregation and transport in Nafion 117 from molecular dynamics simulations: Effect of monomeric sequence.* The Journal of Physical Chemistry B, vol. 108, pages 3149–3157, 2004. (Cited on page 21.)

[Jiang 2004] J. Jiang and A. Kucernak. *Investigations of fuel cell reactions at the composite microelectrode/solid polymer electrolyte interface. I. Hydrogen oxidation at the nanostructured Pt/Nafion® membrane interface.* Journal of Electroanalytical Chemistry, vol. 567, pages 123–137, 2004. (Cited on page 37.)

[Kendrick 2010] I. Kendrick, D. Kumari, A. Yakaboski, N. Dimakis and E. S. Smotkin. *Elucidating the ionomer-electrified metal interface.* Journal of the American Chemical Society, vol. 132, pages 17611–17616, 2010. (Cited on page 38.)

[Kim 2003] Y.S. Kim, L.M. Dong, M.A. Hickner, T.E. Glass, V. Webb and J. E. McGrath. *State of water in disulfonated poly(arylene ether sulfone) copolymers and a perfluorosulfonic acid copolymer (Nafion) and its effect on physical and electrochemical properties.* Macromolecules, vol. 36, pages 6281–6284, 2003. (Cited on pages 24 and 137.)

[Kinoshita 1988] K. Kinoshita. Carbon: electrochemical and physicochemical properties. Wiley-Interscience;, 1988. (Cited on page 32.)

[Knox 2010] C. K. Knox and G. A. Voth. *Probing selected morphological models of hydrated Nafion using large-scale molecular dynamics simulations.* The Journal of Physical Chemistry B, vol. 114, pages 3205–3218, 2010. (Cited on page 22.)

[Koestner 2011] R. Koestner, Y. Roiter, I. Kozhinova and S. Minko. *AFM imaging of adsorbed Nafion polymer on mica and graphite at molecular level.* Langmuir, vol. 27, pages 10157–10166, 2011. (Cited on page 34.)

[Kreuer 2000] K. D. Kreuer. *On the complexity of proton conduction phenomena.* Solid State Ionics, vol. 136-137, pages 149–160, 2000. (Cited on pages 23, 25, 127, 137 and 150.)

[Kreuer 2004] Klaus-Dieter Kreuer, Stephen J Paddison, Eckhard Spohr and Michael Schuster. *Transport in proton conductors for fuel-cell applications: simulations,*

elementary reactions, and phenomenology. Chemical Reviews, vol. 104, pages 4637–78, 2004. (Cited on pages 3, 25, 74, 150, 151 and 161.)

[Kreuer 2008] K. D. Kreuer, M. Schuster, B. Obliers, O. Diat, U. Traub, A. Fuchs, U. Klock, S. J. Paddison and J. Maier. *Short-side-chain proton conducting perfluorosulfonic acid ionomers: Why they perform better in PEM fuel cells.* Journal of Power Sources, vol. 178, pages 499–509, 2008. (Cited on pages 22 and 25.)

[Kusaka 1998] I. Kusaka, Wang Z. G. and Seinfeld J. H. *Direct evaluation of the equilibrium distribution of physical clusters by a grand canonical Monte Carlo simulation* . Journal of Chemical Physics, vol. 108, page 6829, 1998. (Cited on page 63.)

[Lamas 2006] E. Lamas and P. Balbuena. *Molecular dynamics studies of a model polymer–catalyst–carbon interface.* Electrochimica Acta, vol. 51, pages 5904–5911, 2006. (Cited on page 39.)

[Lee 1994] S. H. Lee and P. J. Rossky. *A comparison of the structure and dynamics of liquid water at hydrophobic and hydrophilic surfaces - A molecular dynamics simulation study.* Journal of Chemical Physics, vol. 100, page 3334, 1994. (Cited on pages 91 and 145.)

[Li 2009] A Li and S. H. Chan. *Anti-flooding cathode catalyst layer for high performance PEM fuel cel.* Electrochemistry Communications, vol. 11, pages 897–900, 2009. (Cited on page 32.)

[Li 2010] A. Li, M. Han, S. H. Chan and N. T. Nguyen. *Effects of hydrophobicity of the cathode catalyst layer on the performance of a PEM fuel cell.* Electrochimica Acta, vol. 55, pages 2706–2711, 2010. (Cited on page 32.)

[Lim 2008] D. H. Lim, W. D. Lee, D. H. Choi, D. R. Park and H. I. Lee. *Preparation of platinum nanoparticles on carbon black with mixed binary surfactants: Characterization and evaluation as anode catalyst for low-temperature fuel cell.* Journal of Power Sources, vol. 185, pages 159–165, 2008. (Cited on page 31.)

[Litster 2004] S. Litster and G. McLean. *PEM fuel cell electrodes.* Journal of Power Sources, vol. 130, pages 61–76, 2004. (Cited on page 28.)

[Litt 1997] M. H. Litt. *A reevaluation of Nafion morphology.* Polymer Preprints (American Chemical Society, Division of Polymer Chemistry), vol. 38, page 80, 1997. (Cited on page 15.)

[Liu 2008] J. Liu, M. E. Selvan, S. Cui, B. J. Edwards, D. J. Keffer and W. V. Steele. *Molecular-level modeling of the structure and wetting of electrode/electrolyte interfaces in hydrogen fuel cells.* The Journal of Physical Chemistry C, vol. 112, pages 1985–1993, 2008. (Cited on page 39.)

[Lorentz 1881] H. A. Lorentz. *Ueber die anwendung des satzes vom virial in der kinetischen theorie der gase.* Annalen der Physik, vol. 12, pages 127–136, 1881. (Cited on page 49.)

[Lustig 1998] R. Lustig. *Microcanonical Monte Carlo simulation of thermodynamic properties.* The Journal of Chemical Physics, vol. 109, pages 8816–8828, 1998. (Cited on page 52.)

[Ma 2007] S Ma, Q Chen, F Jogensen, P Stein and E Skou. *$^{1}9F$ NMR studies of Nafion^{T}M ionomer adsorption on PEMFC catalysts and supporting carbons.* Solid State Ionics, vol. 178, pages 1568–1575, 2007. (Cited on pages 4, 34 and 163.)

[Malek 2007] K. Malek, M. Eikerling, Q. Wang, T. Navessin and Z. Liu. *Self-Organization in Catalyst Layers of Polymer Electrolyte Fuel Cells.* The Journal of Physical Chemistry C, vol. 111, pages 13627–13634, 2007. (Cited on page 32.)

[Malek 2008] K. Malek, M. Eikerling, Q. Wang, Z. Liu, S. Otsuka, K. Akizuki and M. Abe. *Nanophase segregation and water dynamics in hydrated Nafion: molecular modeling and experimental validation.* Journal of Chemical Physics, vol. 129, page 204702, 2008. (Cited on pages 22 and 68.)

[Malek 2011a] K. Malek and A. A. Franco. *Microstructure-based modeling of aging mechanisms in catalyst layers of polymer electrolyte fuel cells.* The Journal of Physical Chemistry B, vol. 115, pages 8088–101, 2011. (Cited on page 157.)

[Malek 2011b] K Malek, T. Mashio and M. Eikerling. *Microstructure of Catalyst Layers in PEM Fuel Cells Redefined: A Computational Approach.* Electrocatalysis, vol. 2, pages 141–157, 2011. (Cited on pages 32, 33 and 106.)

[Mark 2001] P. Mark and L. Nilsson. *Structure and Dynamics of the TIP3P, SPC, and SPC/E Water Models at 298 K.* The Journal of Physical Chemistry A, vol. 105, pages 9954–9960, 2001. (Cited on pages xix and 74.)

[Maruyama 1998] J. Maruyama, M. Inaba, K. Katakura, Z. Ogumi and Z. Takehara. *Influence of Nafion film on the kinetics of anodic hydrogen oxidation.* Journal of Electroanalytical Chemistry, vol. 447, pages 201–209, 1998. (Cited on page 37.)

[Mashio 2010] T. Mashio, K. Malek, M. Eikerling, A. Ohma, H. Kanesaka and K. Shinohara. *Molecular dynamics study of ionomer and water adsorption at carbon support materials.* The Journal of Physical Chemistry C, vol. 114, pages 13739–13745, 2010. (Cited on pages 33, 40, 77, 85 and 114.)

[Masuda 2009] T. Masuda, H. Naohara, S. Takakusagi, P. R. Singh and K. Uosaki. *Formation and structure of perfluorosulfonated ionomer thin film on a graphite surface.* Chemistry Letters, vol. 38, pages 884–885, 2009. (Cited on pages 34 and 115.)

[Mauritz 2004] K. A. Mauritz and R. B. Moore. *State of understanding of Nafion.* Chemical Reviews, vol. 104, pages 4535–4585, 2004. (Cited on pages xiii, 3, 13, 14 and 161.)

[Modestino 2012] M. A. Modestino, A. Kusoglu, A. Hexemer, A. Z. Weber and R. A. Segalman. *Controlling Nafion structure and properties via wetting interactions.* Macromolecules, vol. 45, pages 4681–4688, 2012. (Cited on pages 4, 35, 121 and 163.)

[More 2006] K. More, R. Borup and K. Reeves. *Identifying contributing degradation phenomena in PEM fuel cell membrane electride assemblies via electron microscopy.* ECS Transactions, vol. 3, pages 717–733, 2006. (Cited on pages xiv, 3, 30 and 162.)

[Niedrach 1967] L.W Niedrach. *Electrode Structure and Fuel Cell Incorporating the Same*, 1967. (Cited on pages 1 and 159.)

[Nijmeijer 1990] M. J. P. Nijmeijer, C. Bruin, A. F. Bakker and J. M. J. van Leeuwen. *Wetting and drying of an inert wall by a fluid in a molecular dynamics simulation.* Physical Review, vol. 42, page 6052, 1990. (Cited on page 75.)

[Nose 1984] S. Nose. *A molecular dynamics method for simulations in the canonical ensemble.* Molecular Physics, vol. 52, pages 255–268, 1984. (Cited on page 57.)

[Nylander 2006] T. Nylander, Y. Samoshina and B. Lindman. *Formation of polyelectrolyte-surfactant complexes on surfaces.* Advances in Colloid and Interface Science, vol. 123-126, pages 105–123, 2006. (Cited on page 114.)

[Ohma 2011] A. Ohma, T. Mashio, K. Sato, H. Iden, Y. Ono, K. Sakai, K. Akizuki, S. Takaichi and K. Shinohara. *Analysis of proton exchange membrane fuel cell catalyst layers for reduction of platinum loading at Nissan.* Electrochimica Acta, vol. 56, pages 10832–10841, 2011. (Cited on pages 4 and 163.)

[Paddison 2000] S. J. Paddison, R. Paul and T. A. Zawodzinski. *A statistical mechanical model of proton and water transport in a proton exchange membrane.* Journal of the Electrochemical Society, vol. 147, page 617, 2000. (Cited on page 137.)

[Paddison 2003] S. J. Paddison. *Proton conduction mechanisms at low degrees of hydration in sulfonic acid-based polymer electrolyte membranes.* Annual Review of Materials Research, vol. 33, pages 289–319, 2003. (Cited on page 25.)

[Paganin 1996] Ticianelli E. A. Gonzalez E. R. Paganin V. A. *Development and electrochemical studies of gas diffusion electrodes for polymer electrolyte fuel cells.* Journal of Applied Electrochemistry, vol. 26, pages 297–304, 1996. (Cited on page 31.)

[Parry 1975] D. E. Parry. *The electrostatic potential in the surface region of an ionic crystal.* Surface Science, vol. 49, pages 433–440, 1975. (Cited on page 55.)

[Paul 2011a] D. K. Paul, A. Fraser and K. Karan. *Towards the understanding of proton conduction mechanism in PEMFC catalyst layer: Conductivity of adsorbed*

Nafion films. Electrochemistry Communications, vol. 13, pages 774–777, 2011. (Cited on pages 4, 36 and 162.)

[Paul 2011b] D. K. Paul, A. Fraser, J. Pearce and K. Karan. *Understanding the ionomer structure and the proton conduction mechanism in PEFC catalyst layer: Adsorbed Nafion on model substrate.* ECS Transactions, vol. 41, pages 1393–1406, 2011. (Cited on page 36.)

[Plimpton 1995] S. Plimpton. *Fast Parallel Algorithms for Short-Range Molecular Dynamics.* Journal Computer Physics, vol. 117, pages 1–19, 1995. (Cited on pages 45 and 67.)

[Rapaport 2009] D.C Rapaport. The Art of Molecular Dynamics Simulation. Cambridge University Press, 2009. (Cited on page 45.)

[Roudgar 2006] A. Roudgar, S. P. Narasimachary and M. Eikerling. *Hydrated arrays of acidic surface groups as model systems for interfacial structure and mechanisms in PEMs.* The Journal of Physical Chemistry B, vol. 110, pages 20469–20477, 2006. (Cited on pages 25, 149 and 150.)

[Rubatat 2002] L. Rubatat, A. L. Rollet, G. Gebel and O. Diat. *Evidence of elongated polymeric aggregates in Nafion.* Macromolecules, vol. 35, pages 4050–4055, 2002. (Cited on page 17.)

[Rubatat 2004] L. Rubatat, G. Gebel and O. Diat. *Fibrillar structure of Nafion : matching fourier and real space studies of corresponding films and solutions.* Macromolecules, vol. 37, pages 7772–7783, 2004. (Cited on pages xiii, 17 and 18.)

[Ryckaert 1977] J.-P. Ryckaert, G. Ciccotti and H. J. C Berendsen. *Numerical integration of the cartesian equations of motion of a system with constraints: molecular dynamics of n-alkanes.* Journal of Computational Physics, vol. 23, pages 327–341, 1977. (Cited on page 66.)

[Scheidler 2000] P. Scheidler, W. Kob and K. Binder. *The relaxation dynamics of a simple glass former confined in a pore.* Europhysics Letters, vol. 52, pages 277–283, 2000. (Cited on page 135.)

[Scheidler 2002] P. Scheidler, W. Kob and K. Binder. *Cooperative motion and growing length scales in supercooled confined liquids.* Europhysics Letters, vol. 59, pages 701–707, 2002. (Cited on pages 75, 135 and 139.)

[Scheidler 2004] P. Scheidler, W. Kob and K. Binder. *The Relaxation Dynamics of a Supercooled Liquid Confined by Rough Walls.* The Journal of Physical Chemistry B, vol. 108, pages 6673–6686, 2004. (Cited on page 135.)

[Schmidt-Rohr 2008] K. Schmidt-Rohr and Q. Chen. *Parallel cylindrical water nanochannels in Nafion fuel-cell membranes.* Nature Materials, vol. 7, pages 75–83, 2008. (Cited on pages xiii, 18 and 19.)

[Schmitt 1998] U.W. Schmitt and G.A. Voth. *Multistate Empirical Valence Bond Model for Proton Transport in Water.* The Journal of Physical Chemistry B, vol. 102, pages 5547–5551, 1998. (Cited on page 156.)

[Schoenbein 1839] C. F. Schoenbein. *On the voltaic polarization of certain solid and fluid substances.* The London and Edinburgh Philosophical Magazine and Journal of Science, vol. 14, pages 43–45, 1839. (Cited on pages 1 and 159.)

[Selvan 2008] M. E. Selvan, J. Liu, D. J. Keffer, S. Cui, B. J. Edwards and W. V. Steele. *Molecular dynamics study of structure and transport of water and hydronium ions at the membrane/Vapor interface of Nafion.* The Journal of Physical Chemistry C, vol. 112, pages 1975–1984, 2008. (Cited on pages 39 and 101.)

[Selvan 2011] M. E. Selvan, E. Calvo-Munoz and D. J. Keffer. *Toward a Predictive Understanding of Water and Charge Transport in Proton Exchange Membranes.* The Journal of Physical Chemistry B, vol. 115, pages 3052–3061, 2011. (Cited on page 24.)

[Selvan 2012] M. E. Selvan, Q. He, E. M. Calvo-mun and D. J. Keffer. *Molecular dynamic simulations of the effect on the hydration of Nafion in the presence of a platinum nanoparticle.* The Journal of Physical Chemistry C, vol. 116, pages 12890–12899, 2012. (Cited on page 40.)

[Shi 2009] B. Shi and V. K. Dhir. *Molecular dynamics simulation of the contact angle of liquids on solid surfaces.* Journal of Chemical Physics, vol. 130, page 034705, 2009. (Cited on pages 78, 80 and 85.)

[Shin 2002] S. J. Shin, J. K. Lee, H. Y. Ha, S. A. Hong, H. S. Chun and I. H. Oh. *Effect of the catalytic ink preparation method on the performance of polymer electrolyte membrane fuel cells.* Journal of Power Sources, vol. 106, pages 146–152, 2002. (Cited on page 31.)

[Simon 1990] J.D. Simon. *Solvation dynamics: new insights into chemical reaction and relaxation processes.* Pure and Applied Chemistry, vol. 62, pages 2243–2250, 1990. (Cited on page 141.)

[Siroma 2009] Z. Siroma, R. Kakitsubo, N. Fujiwara, T. Ioroi, S. Yamazaki and K. Yasuda. *Depression of proton conductivity in recast Nafion® film measured on flat substrate.* Journal of Power Sources, vol. 189, pages 994–998, 2009. (Cited on page 36.)

[Song 2001] J. M. Song, S. Y. Cha and W. M. Lee. *Optimal composition of polymer electrolyte fuel cell electrodes determined by the AC impedance method.* Journal of Power Sources, vol. 94, pages 78–84, 2001. (Cited on page 31.)

[Sonsudin 2010] F. Sonsudin, T. Masuda, K. Ikeda, H. Naohara and K. Uosaki. *Effect of coating by perfluorosulfonated ionomer film on electrochemical behaviors of Pt(111) electrode in acidic solutions.* Chemistry Letters, vol. 39, pages 286–287, 2010. (Cited on page 38.)

[Spohr 1988] E. Spohr and K. Heinzinger. *Computer simulations of water and aqueous electrolyte solutions at interfaces.* Electrochimica Acta, vol. 33, pages 1211–222, 1988. (Cited on pages 75, 98 and 99.)

[Spohr 1989] E. Spohr. *Computer simulation of the water/platinum interface.* The Journal of Physical Chemistry, vol. 93, pages 6171–6180, 1989. (Cited on pages 91, 98 and 99.)

[Spohr 2002] E. Spohr, P. Commer and A. A. Kornyshev. *Enhancing proton mobility in polymer electrolyte membrane: Lessons from molecular dynamic simulation.*

The Journal of Physical Chemistry B, vol. 106, pages 10560–10569, 2002. (Cited on page 25.)

[Stamenkovic 2007] V. R. Stamenkovic, B. Fowler, B. S. Mun, G. Wang, P. N. Ross, C. A. Lucas and N. M. Marković. *Improved oxygen reduction activity on $Pt_3Ni(111)$ via increased surface site availability.* Science, vol. 315, pages 493–497, 2007. (Cited on page 27.)

[Subbaraman 2010a] R. Subbaraman, D. Strmcnik, A. P. Paulikas, V. R. Stamenkovic and N. M. Markovic. *Oxygen reduction reaction at three-phase interfaces.* ChemPhysChem, vol. 11, pages 2825–33, 2010. (Cited on pages 4, 38 and 163.)

[Subbaraman 2010b] R. Subbaraman, D. Strmcnik, V. Stamenkovic and N. M Markovic. *Three phase interfaces at electrified metal-solid electrolyte systems 1 . Study of the Pt(hkl) -Nafion interface.* The Journal of Physical Chemistry C, vol. 114, pages 8414–8422, 2010. (Cited on pages 38, 112 and 116.)

[Tatarkhanov 2009] M. Tatarkhanov, D. F. Ogletree, F. Rose, T. Mitsui, E. Fomin, S. Maier, M. Rose, J. I. Cerdá and M. Salmeron. *Metal- and hydrogen-bonding competition during water adsorption on Pd(111) and Ru(0001).* Journal of the American Chemical Society, vol. 131, pages 18425–18434, 2009. (Cited on page 98.)

[Tuckerman 2010] Mark E Tuckerman, Amalendu Chandra and Dominik Marx. *A statistical mechanical theory of proton transport kinetics in hydrogen-bonded networks based on population correlation functions with applications to acids and bases.* The Journal of chemical physics, vol. 133, no. 12, page 124108, September 2010. (Cited on page 149.)

[Urata 2005] S. Urata, J. Irisawa, A. Takada, W. Shinoda, S. Tsuzuki and M. Mikami. *Molecular dynamics simulation of swollen membrane of perfluorinated ionomer.* The Journal of Physical Chemistry B, vol. 109, pages 4269–78, 2005. (Cited on pages 21, 24 and 62.)

[Venkatnathan 2007] A. Venkatnathan, R. Devanathan and M. Dupuis. *Atomistic simulations of hydrated nafion and temperature effects on hydronium ion mobility.*

The Journal of Physical Chemistry B, vol. 111, pages 7234–7244, 2007. (Cited on pages 20, 62 and 71.)

[Vishnyakov 2001a] A. Vishnyakov and A. V. Neimark. *Molecular dynamics simulation of microstructure and molecular mobilities in swollen Nafion membranes.* The Journal of Physical Chemistry B, vol. 105, pages 9586–9594, 2001. (Cited on page 20.)

[Vishnyakov 2001b] A. Vishnyakov and A. V. Neimark. *Molecular dynamics simulation of Nafion oligomer solvation in equimolar methanol-water mixture.* The Journal of Physical Chemistry B, vol. 105, pages 7834–7834, 2001. (Cited on page 20.)

[Wang 2009] Z. B. Wang, P. J. Zuo, Y. Y. Chu, Y. Y. Shao and G. P. Yin. *Durability studies on performance degradation of Pt/C catalysts of proton exchange membrane fuel cell.* International Journal of Hydrogen Energy, vol. 34, pages 4387–4394, 2009. (Cited on pages 4 and 163.)

[Werder 2001] Thomas Werder, Jens H. Walther, Richard L. Jaffe, Timur Halicioglu, Flavio Noca and Petros Koumoutsakos. *Molecular Dynamics Simulation of Contact Angles of Water Droplets in Carbon Nanotubes.* Nano Letters, vol. 1, no. 12, pages 697–702, December 2001. (Cited on page 80.)

[Werder 2003] T. Werder, J. H. Walther, R. L. Jaffe, T. Halicioglu and P. Koumoutsakos. *On the water-carbon interaction for use in molecular dynamics simulations of graphite and carbon nanotubes.* The Journal of Physical Chemistry B, vol. 107, pages 1345–1352, 2003. (Cited on pages 78, 80 and 85.)

[Wescott 2006] J. T. Wescott, Y. Qi, L. Subramanian and T. W. Capehart. *Mesoscale simulation of morphology in hydrated perfluorosulfonic acid membranes.* Journal of Chemical Physics, vol. 124, page 134702, 2006. (Cited on page 68.)

[Wilson 1993] Mahlon S. Wilson. *Membrane catalyst layer for fuel cells*, 1993. (Cited on page 28.)

[Wilson 1995] M. S. Wilson, J. A. Valerio and S. Gottesfeld. *Low platinum loading electrodes for polymer electrolyte fuel cells fabricated using thermoplastic ionomers.* Electrochimica Acta, vol. 40, pages 355–363, 1995. (Cited on page 28.)

[Wood 2009] D. L. Wood, J. Chlistunoff, J. Majewski and R. L. Borup. *Nafion structural phenomena at platinum and carbon interfaces.* Journal of the American Chemical Society, vol. 131, pages 18096–104, 2009. (Cited on pages 4, 33, 35, 111 and 163.)

[Xiao 2012] Y. Xiao, M. Dou, J. Yuan, M. Hou, W. Song and B. Sundén. *Fabrication process simulation of a PEM fuel cell catalyst layer and its microscopic structure characteristics.* Journal of the Electrochemical Society, vol. 159, page B308, 2012. (Cited on page 28.)

[Xie 2010] J. Xie, F. Xu, D. L. Wood, K. L. More, T. Zawodzinski and W. H. Smith. *Influence of ionomer content on the structure and performance of PEFC membrane electrode assemblies.* Electrochimica Acta, vol. 55, pages 7404–7412, 2010. (Cited on pages xiv and 29.)

[Yang 2010] L. Yang, W. Li, X. Du and Y. Yang. *Effect of Hydrophobicity in Cathode Porous Media on PEM Fuel Cell Performance.* Journal of Fuel Cell Science and Technology, vol. 7, no. 6, page 061012, 2010. (Cited on page 32.)

[Yeager 1981] H. L Yeager and A. Stek. *Cation and water diffusion in Nafion ion exchange membranes: Influence of polymer structure.* Journal of the Electrochemical Society, vol. 128, pages 1980–1984, 1981. (Cited on pages xiii, 14 and 15.)

[Yeh 1999] I. C. Yeh and M. L. Berkowitz. *Ewald summation for systems with slab geometry.* Journal of Chemical Physics, vol. 111, page 3155, 1999. (Cited on pages 55 and 80.)

[Young 2002] S. K. Young, S. F. Trevino and N. C. Beck Tan. *Small-angle neutron scattering investigation of structural changes in nafion membranes induced by swelling with various solvents.* Journal of Polymer Science Part B: Polymer Physics, vol. 40, pages 387–400, 2002. (Cited on page 15.)

[Yu 2006] H. Yu, C. Ziegler, M. Oszcipok, M. Zobel and C. Hebling. *Hydrophilicity and hydrophobicity study of catalyst layers in proton exchange membrane fuel cells.* Electrochimica Acta, vol. 51, pages 1199–1207, 2006. (Cited on page 32.)

[Yu 2011] X. Yu, J. Yuan and B. Sundén. *Review on the properties of nano-microstructures in the catalyst layer of PEMFC.* Journal of Fuel Cell Science and Technology, vol. 8, page 034001, 2011. (Cited on page 28.)

[Zembala 2004] M. Zembala. *Electrokinetics of heterogeneous interfaces.* Advances in Colloid and Interface Science, vol. 112, pages 59–92, 2004. (Cited on page 27.)

[Zeng 2012] J. Zeng, D. I. Jean, C. Ji and S. Zou. *In situ surface-enhanced Raman spectroscopic studies of Nafion adsorption on Au and Pt electrodes.* Langmuir, vol. 28, pages 957–964, 2012. (Cited on page 38.)

[Zhao 2011] Q. Zhao, P. Majsztrik and J. Benziger. *Diffusion and interfacial transport of water in Nafion.* The Journal of Physical Chemistry B, vol. 115, pages 2717–2727, 2011. (Cited on page 23.)

[Zhdanov 2004] V. p. Zhdanov and B. Kasemo. *Towards the understanding of the specifics of reactions in polymer-electrolyte fuel cells.* Surface Science, vol. 554, pages 103–108, 2004. (Cited on page 37.)

[Zhdanov 2006] V. Zhdanov and B. Kasemo. *Kinetics of electrochemical O_2 reduction on Pt.* Electrochemistry Communications, vol. 8, pages 1132–1136, 2006. (Cited on page 37.)